JOURNAL OF RESEARCH

OF THE U.S. GEOLOGICAL SURVEY

NOVEMBER–DECEMBER 1976
VOLUME 4, NUMBER 6

Scientific notes and summaries of investigations in geology, hydrology, and related fields

U.S. DEPARTMENT OF THE INTERIOR

UNITED STATES DEPARTMENT OF THE INTERIOR
THOMAS S. KLEPPE, Secretary
GEOLOGICAL SURVEY
V. E. McKelvey, Director

For sale by the Superintendent of Documents, U.S. Government Printing Office, Washington, DC 20402. Annual subscription rate $18.90 (plus $4.75 for foreign mailing). Make checks or money orders payable to the Superintendent of Documents.

Send all subscription inquiries and address changes to the Superintendent of Documents at the above address.

Purchase orders should not be sent to the U.S. Geological Survey library.

Library of Congress Catalog-card No. 72-600241.

The Journal of Research is published every 2 months by the U.S. Geological Survey. It contains papers by members of the Geological Survey and their professional colleagues on geologic, hydrologic, topographic, and other scientific and technical subjects.

Correspondence and inquiries concerning the Journal (other than subscription inquiries and address changes) should be directed to Anna M. Orellana, Managing Editor, Journal of Research, Publications Division, U.S. Geological Survey, 321 National Center, Reston, VA 22092.

Papers for the Journal should be submitted through regular Division publication channels.

The Secretary of the Interior has determined that the publication of this periodical is necessary in the transaction of the public business required by law of this Department. Use of funds for printing this periodical has been approved by the Director of the Office of Management and Budget through June 30, 1980.

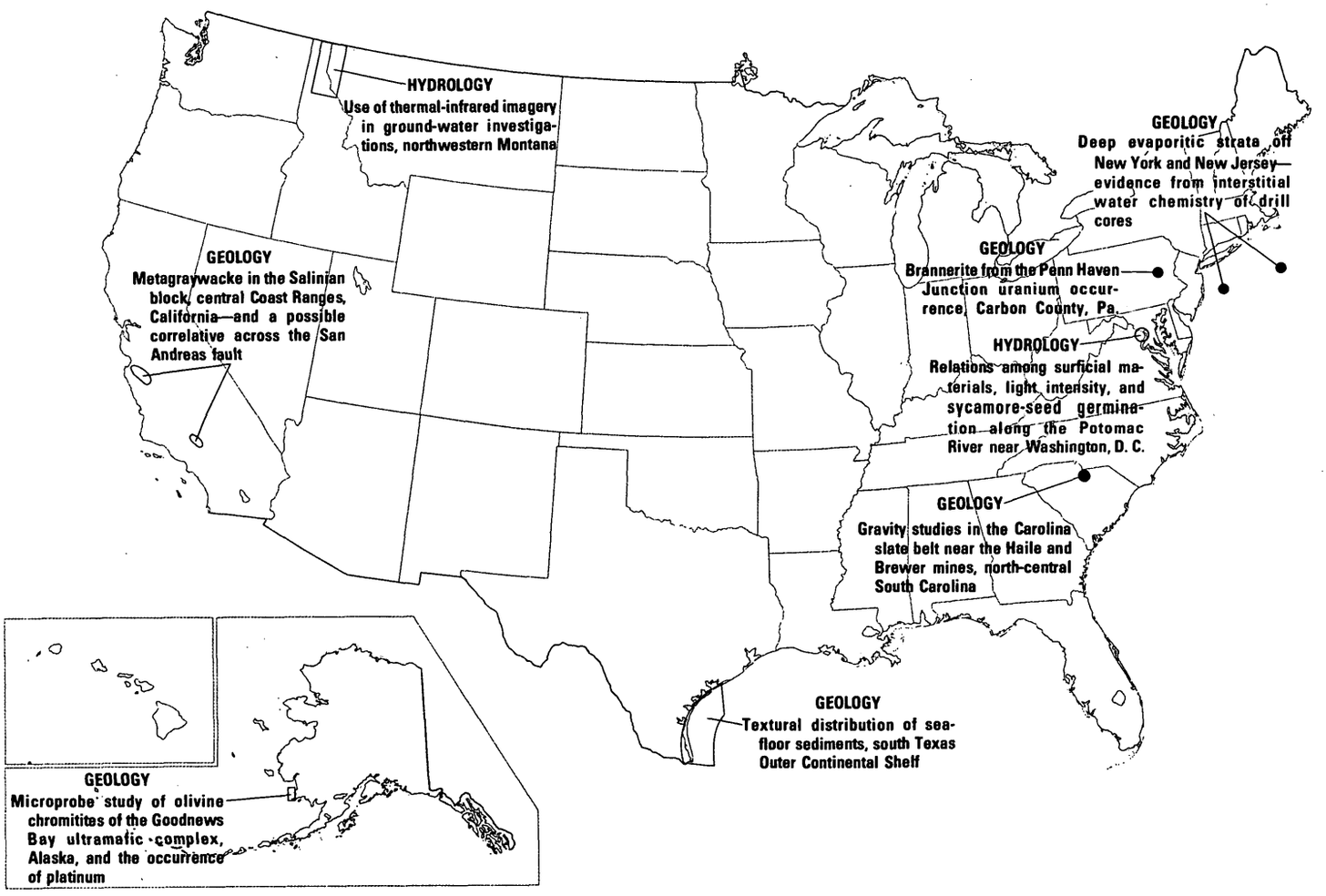

GEOGRAPHIC INDEX TO ARTICLES

See "Contents" for articles concerning areas outside the United States and articles without geographic orientation.

JOURNAL OF RESEARCH

of the

U.S. Geological Survey

Vol 4 No. 6 Nov.–Dec. 1976

CONTENTS

SI UNITS AND U.S. CUSTOMARY EQUIVALENTS

[SI, International System of Units, a modernized metric system of measurement. All values have been rounded to four significant digits except 0.01 bar, which is the exact equivalent of 1 kPa. Use of hectare (ha) as an alternative name for square hectometer (hm^2) is restricted to measurement of land or water areas. Use of liter (L) as a special name for cubic decimeter (dm^3) is restricted to the measurement of liquids and gases; no prefix other than milli should be used with liter. Metric ton (t) as a name for megagram (Mg) should be restricted to commercial usage, and no prefixes should be used with it. Note that the style of meter^2 rather than square meter has been used for convenience in finding units in this table. Where the units are spelled out in text, Survey style is to use square meter]

SI unit		U.S. customary equivalent	
Length			
millimeter (mm)	=	0.039 37	inch (in)
meter (m)	=	3.281	feet (ft)
	=	1.094	yards (yd)
kilometer (km)	=	0.621 4	mile (mi)
	=	0.540 0	mile, nautical (nmi)
Area			
centimeter^2 (cm^2)	=	0.155 0	inch^2 (in^2)
meter^2 (m^2)	=	10.76	feet^2 (ft^2)
	=	1.196	yards^2 (yd^2)
	=	0.000 247 1	acre
hectometer^2 (hm^2)	=	2.471	acres
	=	0.003 861	section (640 acres or 1 mi^2)
kilometer^2 (km^2)	=	0.386 1	mile^2 (mi^2)
Volume			
centimeter^3 (cm^3)	=	0.061 02	inch^3 (in^3)
decimeter^3 (dm^3)	=	61.02	inches^3 (in^3)
	=	2.113	pints (pt)
	=	1.057	quarts (qt)
	=	0.264 2	gallon (gal)
	=	0.035 31	foot^3 (ft^3)
meter^3 (m^3)	=	35.31	feet^3 (ft^3)
	=	1.308	yards^3 (yd^3)
	=	264.2	gallons (gal)
	=	6.290	barrels (bbl) (petroleum, 1 bbl=42 gal)
	=	0.000 810 7	acre-foot (acre-ft)
hectometer^3 (hm^3)	=	810.7	acre-feet (acre-ft)
kilometer^3 (km^3)	=	0.239 9	mile^3 (mi^3)
Volume per unit time (includes flow)			
decimeter^3 per second (dm^3/s)	=	0.035 31	foot^3 per second (ft^3/s)
	=	2.119	feet^3 per minute (ft^3/min)
Volume per unit time (includes flow)—Continued			
	=	15.85	gallons per minute (gal/min)
	=	543.4	barrels per day (bbl/d) (petroleum, 1 bbl=42 gal)
meter^3 per second (m^3/s)	=	35.31	feet^3 per second (ft^3/s)
	=	15 850	gallons per minute (gal/min)
Mass			
gram (g)	=	0.035 27	ounce avoirdupois (oz avdp)
kilogram (kg)	=	2.205	pounds avoirdupois (lb avdp)
megagram (Mg)	=	1.102	tons, short (2 000 lb)
	=	0.9842	ton, long (2 240 lb)
Mass per unit volume (includes density)			
kilogram per meter^3 (kg/m^3)	=	0.062 43	pound per foot^3 (lb/ft^3)
Pressure			
kilopascal (kPa)	=	0.145 0	pound-force per inch^2 (lbf/in^2)
	=	0.009 869	atmosphere, standard (atm)
	=	0.01	bar
	=	0.296 1	inch of mercury at 60°F (in Hg)
Temperature			
temp kelvin (K)	=	[temp deg Fahrenheit (°F)+459.67]/1.8	
temp deg Celsius (°C)	=	[temp deg Fahrenheit (°F)−32]/1.8	

Any use of trade names and trademarks in this publication is for descriptive purposes only and does not constitute endorsement by the U.S. Geological Survey.

Jour. Research U.S. Geol. Survey
Vol. 4, No. 6, Nov.-Dec. 1976, p. 631–644

THE HEAT CAPACITIES OF CALORIMETRY CONFERENCE COPPER AND OF MUSCOVITE $KAl_2(AlSi_3)O_{10}(OH)_2$, PYROPHYLLITE $Al_2Si_4O_{10}(OH)_2$, AND ILLITE $K_3(Al_7Mg)(Si_{14}Al_2)O_{40}(OH)_8$ BETWEEN 15 AND 375 K AND THEIR STANDARD ENTROPIES AT 298.15 K

By RICHARD A. ROBIE, BRUCE S. HEMINGWAY, and
WILLIAM H. WILSON, Reston, Va.

Abstract.—The heat capacities of Calorimetry Conference copper and of muscovite, pyrophyllite, and illite were measured between 15 and 375 K using an adiabatic calorimeter. Tables of the thermodynamic functions C_p°, $(H_T^\circ - H_0^\circ)/T$, $(G_T^\circ - H_0^\circ)/T$, and $S_T^\circ - S_0^\circ$ are presented for these phases at integral temperatures from 0 to 370 K. At 298.15 K (25.0°C), $S_T^\circ - S_0^\circ$ is 33.12±0.06, 287.7±0.6, 239.4±0.4, and 1,104.2±0.6 J/(mol·K) for copper, muscovite, pyrophyllite, and illite, respectively. The operation of a semiautomatic data-acquisition system for calorimetric measurements at low temperatures is also described, together with a description of a miniature calorimeter having a novel closure seal.

The heat capacities (C_p°) of muscovite, pyrophyllite, illite, and the Calorimetry Conference sample of copper (Osborne, Flotow, and Schreiner, 1967) have been measured between 15 and 375 kelvins using an adiabatic calorimeter to obtain their standard entropies. The heat capacity of muscovite was previously measured by Weller and King (1963) between 52 and 296 K; Pankratz (1964) has measured $H_T^\circ - H_{298}^\circ$ for this same muscovite up to 903 K. King and Weller (1970) determined the heat capacity of pyrophyllite between 52 and 296 K. Earlier measurements of the heat capacity of copper have been critically examined by Furukawa, Saba, and Reilly (1968). Because the previous data for muscovite and pyrophyllite had a low temperature limit of only 52 K, new measurements extending to lower temperatures are needed to reduce the uncertainty in the entropy caused by the rather long extrapolation of C_p° below 52 K.

The heat capacity of the Calorimetry Conference copper sample was measured to compare the accuracy of our procedures with the accuracy of several earlier investigations on this same sample, particularly for temperatures below 25 K. No previous low-temperature heat capacity data exist for illite.

Acknowledgments.—We wish to thank H. W. Flotow of the Argonne National Laboratory for supplying us with the Calorimetry Conference copper sample; Prof. D. L. Graf, University of Illinois, for the illite; Prof. C. S. Hurlbut, Jr., Harvard University, for the Methuen Township muscovite; and E-an Zen, U.S. Geological Survey, for the pyrophyllite from North Carolina.

We are also indebted to our U.S. Geological Survey colleagues R. O. Fournier and M. L. Smith for the X-ray studies on the muscovite and pyrophyllite and to E. J. Dwornik and R. R. Larson for their electron microscopic study of the illite sample used in the calorimetry. Kenneth Krupka kindly allowed us the use of the high-temperature heat-capacity data for pyrophyllite.

These studies were supported in part by the Advanced Research Project Agency, U.S. Department of Defense (A.R.P.A. order 1813), and by the Office of Saline Waters, U.S. Department of the Interior (agreement No. 14–30–3040), to whom we are most grateful.

MATERIALS

Copper

The 1965 Calorimetry Conference copper sample (Osborne and others, 1967), as received, was in the form of a right-circular cylinder 3.18 centimetres in diameter, 5.34 cm in length, and 376.2 grams in weight. The sample designation was T 7.2.

The cylindrical sample was machined to a length of 5.08 cm and an outside diameter of 2.94 cm, and a 0.574-cm-diameter hole was drilled axially the length of the cylinder. The sample was sawed parallel to the axis of the cylinder into 90° segments by means of a

0.04-cm-thick milling cutter. After being machined, the sample was cleaned of cutting fluid, given a 4-minute etch in 6 N HNO_3 to remove surface cold work, rinsed in distilled water, and vacuum dried at room temperature. This procedure removed a surface layer approximately 0.3 millimetre thick. The calorimetric sample weighed 242.669 g (in vacuo). The 1971 atomic weight (Commission on Atomic Weights, 1972) for copper, 63.54_6 was used for our calculations. For the measurements on copper, the sample holder contributed 10 percent of the total observed heat capacity (sample plus sample holder) and was almost independent of temperature, as more than 90 percent of the mass of the sample holder is copper.

Muscovite, $KAl_2(AlSi_3)O_{10}(OH)_2$

The chemistry and crystallography of the muscovite sample from Methuen Township, Ontario, had previously been studied by Hurlbut (1956). The crystals were separated into cleavage flakes approximately 0.2 mm thick. Those flakes that had inclusions were discarded. The central part of each flake was trimmed to an approximately square cross section by using surgical scissors, and the selvages were discarded. A chemical analysis of the sample used in the calorimetric studies is given in table 1. When corrections were made for impurities, the sample was assumed to have the composition of analysis 5, table 1. A three-dimensional refinement of the crystal structure of this muscovite is in progress (Eric Dowty, oral commun., October 1974).

TABLE 1.—*Chemical analyses, in weight percent, of muscovite used for low-temperture heat-capacity measurements*

Sample	1	2	3	4	5	6
SiO_2	45.27	45.87	45.20	44.0	46.29	45.79
Al_2O_3	38.39	38.69	38.46	35.0	35.82	33.47
Fe_2O_3	----	----	.25	2.2	----	3.22
FeO	----	----	----	.26	2.27	.47
MgO	----	.10	.00	.57	.65	.79
CaO	----	----	----	.22	----	----
Na_2O	----	.64	.59	.72	.45	.99
K_2O	11.82	10.08	10.5	9.6	10.25	10.73
H_2O+	4.52	4.67	4.64	5.6	4.27	4.47
H_2O-	----	----	.08	2.0		----
TiO_2	----	----	----	.13	----	.08
P_2O_5	----	----	.02	.01	----	----
MnO	----	----	----	.07	----	----
CO_2	----	----	----	.01	----	----
F	----	----	----	.29	----	----
Total	100.00	100.05	99.74	100.68	100.00	100.01

1. $KAl_2(AlSi_3)O_{10}(OH)_2$ (ideal muscovite).
2. Muscovite from Methuen Township, Ontario, (Hurlbut, 1956). Analyst, F. A. Gonyer.
3. Muscovite from Methuen Township, Ontario (65–WG–27) (Eugster and others, 1972). Analyst, J. J. Fahey, U.S. Geol. Survey.
4. Muscovite from Methuen Township, Ontario (W–179493). Rapid rock analysis by method of Shapiro (1967). Analyst, Hezekiah Smith, U.S. Geol. Survey.
5. Muscovite from Methuen Township, Ontario. Average of three analyses. H_2O obtained by difference. Microprobe analysis by Toby Wiggins, U.S. Geol. Survey. Total iron as FeO.
6. Muscovite used by Weller and King (1963).

The unit-cell parameters for this muscovite, determined by Robert Fournier, U.S. Geological Survey, are $a=5.203\pm0.005$ angstroms, $b=9.003\pm0.01$ A, $c=20.031\pm0.001$ A, $\beta=94.47°\pm0.17°$, using fluorite, $a=5.4626$ A, as an internal standard. The calorimeter was loaded with 22.941 g (in vacuo) of muscovite. The formula weight used for muscovite, 398.309 grams·mole^{-1}, is based on the 1971 atomic weights.

Pyrophyllite, $Al_2Si_4O_{10}(OH)_2$

The sample used for the heat-capacity measurements was collected from Staley, N.C., by E-an Zen of the U.S. Geological Survey (Zen, 1961). It was in the form of radial growths of lath-shaped crystals. The individual crystal blades were approximately 10 mm long by 1 mm wide and of varying thickness. The crystals had a very pale green tint. The aggregates were chipped into equant fragments approximately 0.5 cm on edge, using a hardened-steel scribe point. The sample was purposely not ground in a mortar because we did not wish to introduce dislocations into this very soft material. Chemical analyses of the calorimetric sample are given in table 2, analyses 2 and 3. The results of analysis 3 were used to make the impurity correction. The formula weight used in our calculations was 360.316 g·mol^{-1}.

Unit-cell parameters for this material, determined by M. L. Smith of the U.S. Geological Survey, are $a=5.18$ A, $b=8.93$ A, $c=18.67$ A, and $\beta=99.83°$. These values agree with the data of Rayner and Brown (1964), who refined the structure of a pyrophyllite from Graves Mountain, Ga. The calorimetric sample weighed 31.726 g (in vacuo). Taylor and Bell (1971) have measured the thermal expansion of the Staley, N.C., pyrophyllite between 295 and 657 K. For the unit-cell parameters at 22°C, they obtained $a=5.169\pm0.004$ A, $b=8.931\pm0.002$ A, $c=18.639\pm0.003$ A, and $\beta=99.91°\pm0.02°$.

Illite $K_3(Al_7Mg)(Si_{14}Al_2)O_{40}(OH)_8$

The sample of illite, from Marblehead, Wis., used for our low-temperature heat-capacity studies was kindly provided by Prof. Donald L. Graf of the University of Illinois, who also furnished the following description of its preparation.

One-half kilogram of illite was placed in 12 liters of distilled water and allowed to sit for 5 days except for occasional stirring. Twelve hundred and fifty millilitres of this suspension was centrifuged for 10 minutes at 3,000 r/min (revolutions per minute). This step removed excess electrolytes from the clay so that flocculation no longer occurred. The supernatant was

TABLE 2.—*Chemical analyses, in weight percent, of pyrophyllite and illite used for low-temperature heat-capacity measurements*

Sample	1	2	3	4	5	6	7	8
SiO_2	66.70	66.4	66.32	65.78	54.14	52.0	51.62	52.87
Al_2O_3	28.30	28.5	28.27	28.22	29.53	24.9	23.96	24.90
Fe_2O_3	-----	.42	.32	.34	-----	1.9	1.63	.78
FeO	-----	.07	.03	-----	-----	.07	.29	1.19
MgO	-----	.01	.07	.22	2.60	3.9	3.83	3.60
CaO	-----	.01	-----	-----	-----	.42	.47	.69
Na_2O	-----	.05	.05	-----	-----	.09	.14	.22
K_2O	-----	.05	.02	-----	9.09	7.8	8.12	7.98
H_2O+	5.00	4.7	4.94	5.26	4.64	5.4	5.00	4.61
H_2O-	-----	.13	-----	-----	-----	2.9	2.90	1.75
TiO_2	-----	-----	.01	.14	-----	.95	.92	1.02
P_2O_5	-----	.01	-----	-----	-----	.13	.09	-----
MnO	-----	-----	-----	-----	-----	-----	.01	-----
CO_2	-----	.01	-----	-----	-----	.01	-----	-----
F	-----	.03	-----	-----	-----	.76	.74	-----
Subtotal	100.00	100.39	100.03	99.96	100.00	101.23	99.72	99.61
Less O	-----	.02	-----	-----	-----	.32	.31	-----
Total	100.00	100.37	100.03	99.96	100.00	100.91	99.41	99.61

1. $Al_2Si_4O_{10}(OH)_2$ (ideal pyrophyllite).
2. Pyrophyllite from Staley, N. C. (W–179494). Rapid rock analysis by method of Shapiro (1967). Analyst, Hezekiah Smith, U.S. Geol. Survey.
3. Pyrophyllite from Staley, N. C. (D–103758). Conventional rock analysis. Analyst, V. C. Smith, U.S. Geol. Survey.
4. Pyrophyllite used by King and Weller (1970).
5. $K_3(Al_7Mg)(Si_{14}Al_2)O_{40}(OH)_8$ (ideal illite).
6. Illite from Marblehead, Wis. (W–179495). Rapid rock analysis by method of Shapiro (1967). Analyst, Hezekiah Smith, U.S. Geol. Survey.
7. Illite from Marblehead, Wis. (D–103757). Conventional rock analysis. Analyst, V. C. Smith, U.S. Geol. Survey.
8. Illite from Marblehead, Wis. (Gaudette, 1965). Analyst, J. Witters, Illinois State Geol. Survey.

discarded, and the sediment was washed and resuspended in distilled water.

This suspension was again centrifuged for 10 min at 3,000 r/min in a Sorvall 55–3 automatic centrifuge. The solid sediment was saved after the supernatant suspension was discarded. All particles in the saved part were less than 0.25 μm (micrometre) (equivalent hydraulic sphere diameter assuming a density of 2.6). This sediment was washed and resuspended in distilled water.

The resultant suspension was centrifuged at 1,000 r/min for 80 seconds. The supernatant suspension was saved, and the sediment at the bottom of the centrifuge tube was discarded.

The supernatant suspension was centrifuged for 10 min at 3,000 r/min. After centrifugation, the supernatant was discarded and the sediment was saved. This step tended to remove some of the particles less than 0.25 μm in size, though many small (possibly colloidal) particles remained in the sample. The sediment was washed and resuspended, and the suspension was evaporated to dryness at 80°C. The procedure outlined above was repeated several times until sufficient sample was accumulated. Two chemical analyses of this material are given in table 2. In correcting our data for impurities, we have used the results of analysis 7, table 2.

The calorimetric sample weighed 29.058 g (in vacuo) and included 0.465 g of adsorbed water. The adsorbed water was determined by weighing part of the sample immediately after opening the calorimeter and then heating this part to 115°C for 2 hours and immediately reweighing. The formula weight for ideal illite, $K_3(Al_7Mg)(Si_{14}Al_2)O_{40}(OH)_8$, used in our calculations is 1,553.671 $g \cdot mol^{-1}$.

The Marblehead illite was originally described by Gaudette (1965), who determined the unit-cell parameters and refractive indices and presented a chemical analysis (see table 2, analysis 8). Gaudette, Eades, and Grim (1966) have compared the Marblehead illite with several other well-crystallized illites and have discussed the proper assignment of the atoms in the unit cell.

Guven (1972) has studied the Marblehead illite by X-ray, electron diffraction, and electron microscopy and has prepared an indexed powder pattern. His cell parameters are in good agreement with those of Gaudette (1965). Guven (1970) has also discussed compositional and structural relationships between phengite (Ernst, 1963), illite, and muscovite. Reesman (1974) has measured the aqueous solubility of the Marblehead illite and has calculated a value for the Gibbs free energy of formation.

APPARATUS AND TECHNIQUES

The cryostat used for these measurements has been described by Robie and Hemingway (1972). For this investigation, a new miniature sample holder was constructed (fig. 1).

Miniature calorimeter

The body of the calorimeter (*e*) was fabricated from oxygen-free high-conductivity (OFHC) copper rod, and the single joint at the throat of the reentrant well

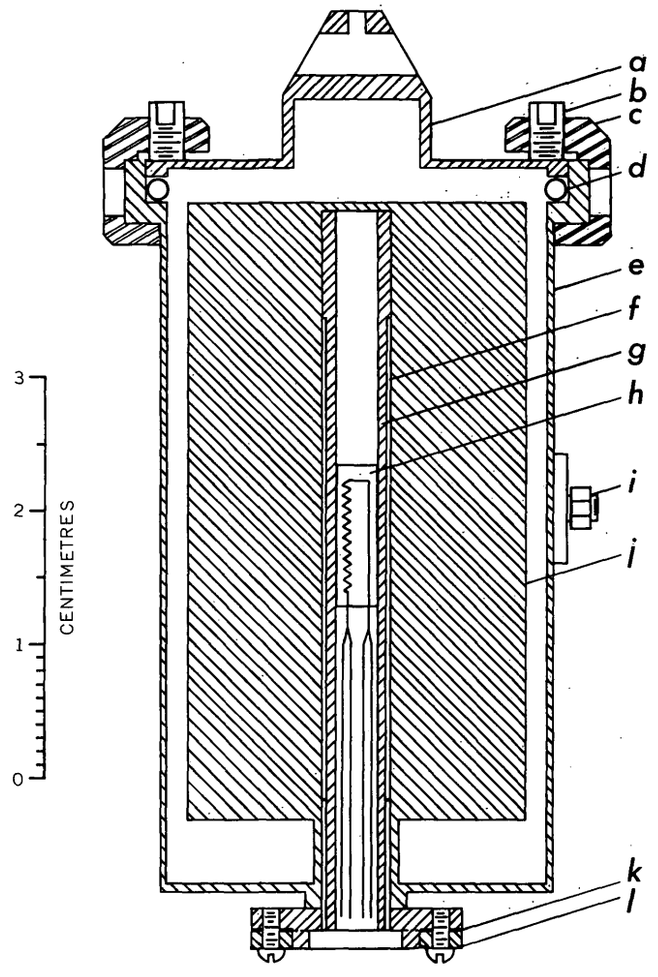

FIGURE 1.—Heat-capacity calorimeter. *a*, Calorimeter top; *b*, steel 4–40 set screws; *c*, gold-plated aluminum clamping ring; *d*, Teflon-coated hollow metal O-ring (Advanced Metal Products 1250); *e*, calorimeter body; *f*, reentrant well for thermometer-heater bobbin; *g*, thermometer-heater bobbin; *h*, platinum-resistance thermometer (Minco S–1059); *i*, screw stud anchor for differential thermocouple; *j*, heat-dispersal fins; *k*, mica disk insulators; *l*, holddown ring for lead wires.

(*f*) for the thermometer-heater bobbin was autogenously arc welded. The top (*a*) is made of a beryllium-copper alloy (Berylco 25) and hardened to 40 Rockwell C. The outer surface of the calorimeter was electroplated with gold, 0.0002 cm thick.

The calorimeter is sealed by either a Teflon-coated hollow metal O-ring (*d*) or V-ring (Parker Seal 8812–2003–0125) and a two-piece, gold-plated, aluminum clamping ring (*c*). The calorimeter has an inside diameter of 2.94 cm, an inside depth of 5.08 cm, and a wall thickness of 0.032 cm. The central reentrant well is 5.08 cm deep, has an inside diameter of 0.53 cm, and has four 0.04-cm-thick fins (*j*) to promote rapid heat dispersal.

A copper bobbin (*g*) upon whose outer surface is wound a 172-ohm heater of fiberglass-insulated American Wire Gauge No. 36 Evanohm wire and within which is mounted a miniature platinum-resistance thermometer (*h*) slip-fits within this well and is brought into thermal contact with the calorimeter by using Apiezon T stopcock grease. Provision was made in the design of the heater bobbin for the addition, at a future date, of a germanium-resistance thermometer to extend the range of our measurements down to 5 K. The calorimeter has an internal volume of 30.0 cm^3 and a heat capacity of 28.5 $J \cdot K^{-1}$ (joules per kelvin) at 300 K.

The strain-free miniature platinum-resistance thermometer (Minco–S1059–1) was calibrated by the Temperature Measurements Section of the U.S. National Bureau of Standards between 13.8 and 505 K on the IPTS (International Practical Temperature Scale) of 1968 (Comité International des Poids et Mesures, 1969). The thermometer has a resistance at 273.15 K (0.0°C) of 100.015 ohms and a dR/dT of 0.4 ohm$\cdot K^{-1}$ at this temperature. Between 50 and 380 K, the thermometer current is maintained at approximately 0.0008 amperes and the maximum power dissipated is always less than 90 μW (microwatts). Below 50 K, the thermometer current is increased to 0.002 mA (milliampere) to increase the temperature sensitivity. At these thermometer currents, the temperature sensitivity is better than ± 0.4 mK (millikelvin) at all temperatures above 24 K and decreases to ± 2 mK at 15 K.

The gold-2.1 atomic percent cobalt versus copper differential thermocouple used in earlier measurements (Robie and Hemingway, 1972) was replaced by one of gold-0.07 atomic percent iron versus Chromel (Rosenbaum, 1968; Sparks and Powell, 1972) to improve the sensitivity of the adiabatic shield control at the lowest temperatures.

The empty calorimeter is weighed, filled with the sample, and weighed again to determine the mass of the sample. It is then placed in a special clamp which is attached to the base plate of a vacuum bell jar (fig. 2).

The top of the calorimeter is attached to the fixed arm (*b*) of the clamp with a 4–40 machine screw, and the body of the calorimeter rests upon the movable arm of the clamp (*e*). In this position, a gap of about 0.5 mm exists between the top of the calorimeter and the metal O-ring. The bell jar (*a*) is then sealed and evacuated to 0.0004 pascal (3×10^{-6} mm Hg). Pure helium gas at about 10^5 Pa, or less pressure, is then let into the bell jar through an activated charcoal trap cooled to 77 K, and the body of the calorimeter is then pressed up against the top of the calorimeter by means of the

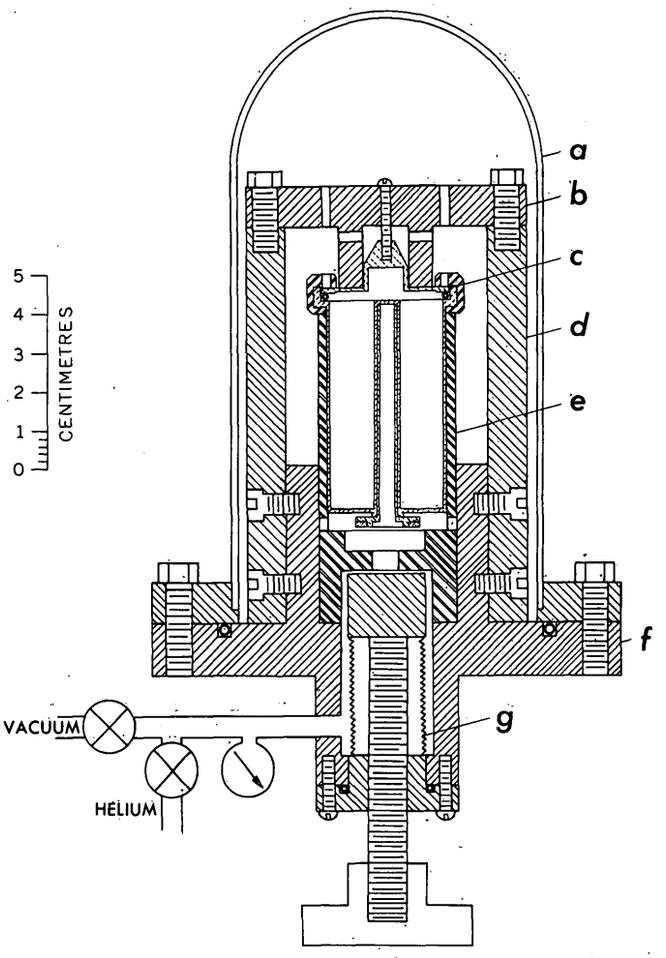

FIGURE 2.—Vacuum bell jar and sealing clamp for miniature calorimeter. *a*, Bell jar; *b*, fixed arm of clamp; *c*, calorimeter top; *d*, tie rods; *e*, movable arm of clamp; *f*, base attached to bench top; *g*, bellow-sealed driver rod.

movable arm of the clamp. This compresses the hollow-metal O-ring and seals the calorimeter with helium gas inside. The helium gas is necessary to provide heat exchange between the sample and the calorimeter.

The bell jar is removed and, while still clamped shut, the top and body of the calorimeter are locked together by tightening the six screws (mounted in the aluminum clamping ring) against the top of the calorimeter. The calorimeter is then removed from the clamp and is mounted within the cryostat.

This type of seal permits the calorimeter to be sealed repeatedly without having to make corrections for differences in the weights of solder and Teflon between the empty and filled calorimeter, as was previously required (Robie and Hemingway, 1972, p. 11). The seal also allows the helium gas to be sealed within the calorimeter at reduced pressure, thus reducing the possibility of adsorption of the gas at the lowest temperature.

The calorimeter is operated under quasi-adiabatic conditions using intermittent heating. For the "worst case" situation (that of an empty calorimeter), the percentage correction for the deviation from true adiabatic conditions—zero heat exchange between the calorimeter and its surroundings—amounts to 0.3 percent at 374 K, is less than 0.1 percent between 343 and 45 K, and increases to 1.0 percent at 20 K. For a filled calorimeter, these corrections are ordinarily less than one-third of the above values.

Inasmuch as the thermometer current is on continuously, the joule heating of the platinum-resistance thermometer is the same in the rating periods as in the heating period and accordingly does not enter into the method of correcting for the small deviations from adiabaticity; that is, by linearly extrapolating the fore- and after-rating-period temperatures to the midtime of the heating period to obtain the corrected value of the temperature rise.

Data-acquisition system

For the studies presented in this report, the calorimetric measurement circuit described by Robie and Hemingway (1972, fig. 4) was modified to permit the automatic transfer of data to a Teletype (ASR 33) or to a magnetic tape cassette–typewriter computer terminal[1] (Memorex 1280) and to measure automatically the heater energy (fig. 3). The potentiometer and selector switch were modified by the addition of digital encoders that convert the decimal information (dials and range) from the potentiometer, and the channel number from the selector switch, into +8−4−2−1 BCD (binary coded decimal) coding compatible with a Hewlett Packard 2547A digital coupler. The encoder was fabricated from Digital Equipment Corporation K-series logic modules.

Although the data-acquisition system shown in figure 3 still requires the manual operation of the selector switch (channel) and balancing of the potentiometer dials, it does provide a major saving of time and reduction of errors, in that all data are recorded on a tape that permits direct entry into a computer by eliminating manual transfer of data.

The function of the coupler is to transfer the readings of the potentiometer, null detector, DVM (digital voltmeter), and counter at given time intervals (normally every 2 min) to a Teletype-like recorder. The coupler provides the time in hours, minutes, and sec-

[1] The magnetic tape–typewriter terminal provides a higher storage density of the raw data than does the Teletype punched tape and permits a sixfold increase in the rate of transmission (via a standard telephone line) to a distant computer.

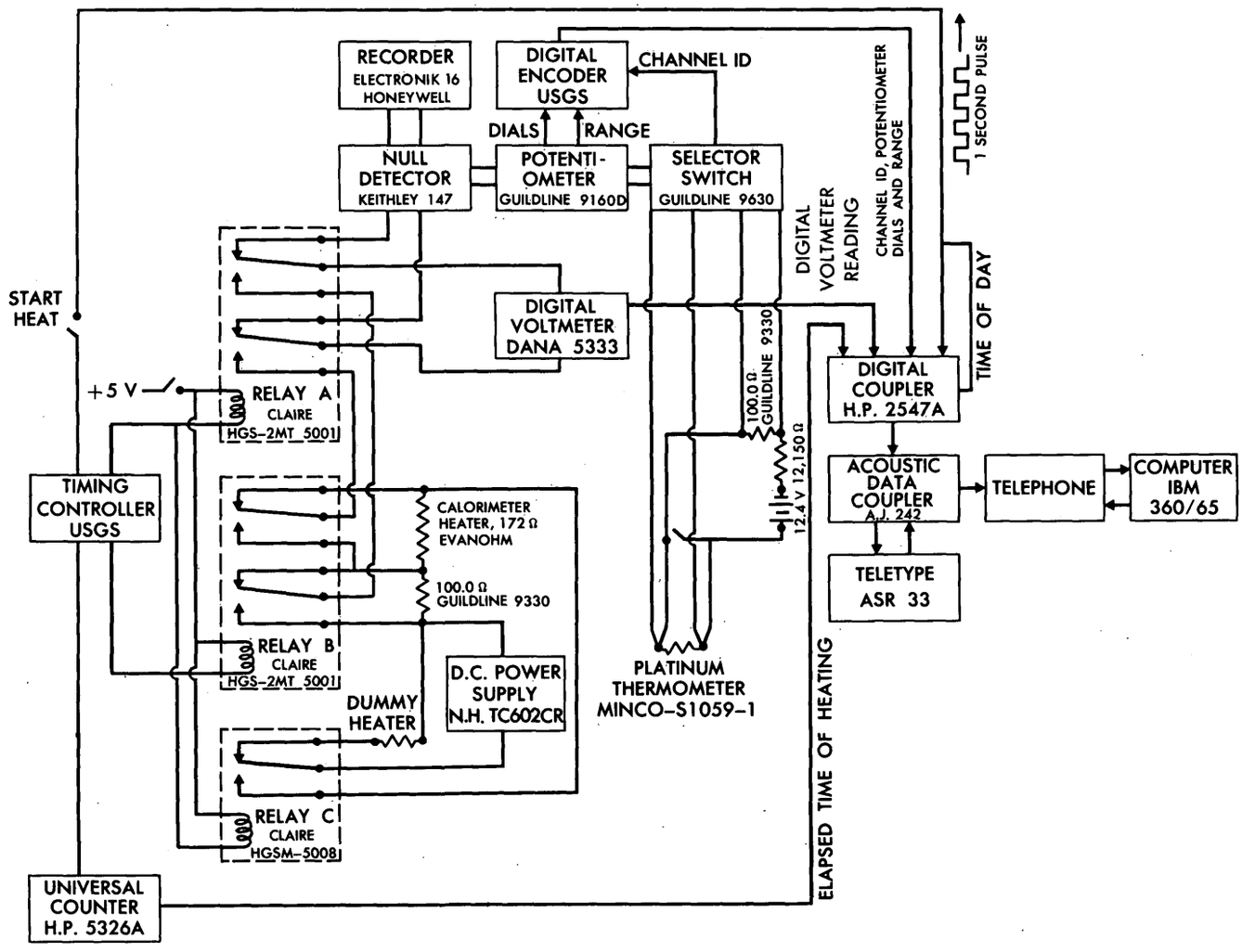

FIGURE 3.—Semiautomatic data-acquisition system for low-temperature calorimetry.

onds from an internal quartz-crystal-based clock and also furnishes a 1-second output pulse (accurate to $\pm 1 \times 10^{-7}$ second), which is used to control the elapsed time of energy input to the calorimeter heater and to program the opening or closing of the three relays. The coupler serializes the data from the digital encoder, together with the readings from the digital clock, DVM, and elapsed time counter (H.P. 5326A), whose outputs are already BCD encoded, and transmits the results to the typewriter terminal in ASCI–II code. The terminal generates a simultaneous printed record and punched-paper-tape or magnetic-tape log of the data.

The total time of heating is controlled by a preset counter, which counts the 1-second pulses, and a digital divider, which opens a switch after an exact (± 0.0001) number of seconds has elapsed. The desired heating time is preset on a three-deck digital thumbwheel switch (Digitran 28000 series) and can be varied from 1 to 999 seconds. The elapsed time of heating is measured by means of a 50-MHz (megahertz) counter (H.P. 5326A). The mercury contact relays (Claire HGS–5000 series) have a throw time of 900 μs (microseconds), and the voltage drop across the relay contacts is 25 μV (microvolts) constant to ± 5 μV. The relay closure time was checked by using a 50-MHz counter, and the voltage drop across the contacts of the relay was checked with a Keithley nanovolt null detector.

Experimental procedures

At the beginning of a heating period, the switch marked "Start heat" is depressed. This action starts the counter and simultaneously diverts the electrical power, supplied by the North Hills 602C power sup-

ply, from a dummy heater to the calorimeter heater through an SPDT (single-pole double-throw) mercury contact relay (relay C) within 0.9 millisecond. The energizing coil of relay C is connected in parallel with the energizing coil of a DPDT (double-pole double-throw) mercury-wetted contact relay (A). The output voltage of the Keithley nanovolt null detector (±1.0-volt full scale, 0.1 percent linearity) is connected with the normally closed contacts of this relay. A 5½-digit digital voltmeter (Dana 5333) is connected across the movable contacts of this relay. The normally open contacts are connected with the movable contacts of a second DPDT relay (B). The function of relay B is to alternately connect the voltage drop across the calorimeter heater and across a series-connected 100.0-ohm resistor with the input of the digital voltmeter during the time that electrical power is introduced into the calorimeter heater. During the heating period the digital voltmeter measures these two voltages at successive 30-second intervals controlled by the programer, that is activated by the 1-second pulses of the digital clock. During a rating period the digital voltmeter continuously measures the output of the null detector.

The power supply for the calorimeter heater has ±0.0001-percent line and load regulation and ±0.001-percent stability. During the heating interval, the heater voltage changes linearly by about 0.02 percent because of the small change in the lead-wire resistance.

The digital voltmeter has a calibrated accuracy of 0.004 percent over a period of 6 months after calibration, has an input impedance of 10^{10} ohms on the 0.1-, 1.0-, and 10-V ranges, and is routinely checked at the beginning and end of each workday by direct measurement of the voltage of a saturated standard cell (Guideline M2A) thermostated at 32.0±0.02°C. The 100.0-ohm current shunt (Guildline 9330) has a U.S. National Bureau of Standards traceable certification accurate to $\pm 1.0\times10^{-7}$ ohm. From the above observations, it can be seen that the electrical energy used to heat the calorimeter,

$$E=\int_{t_i}^{t_f} V\cdot I\,dt,$$

can be measured automatically with an accuracy of about 0.01 percent.

An entire day's record of data can be stored on a single magnetic tape cassette. At the completion of 7 hours of measurements (13 heat capacities and 500 lines of data at 40 characters/line), the data are read into the computer (Remote Entry Batch Processing) using the tape reading capability of the computer terminal and a standard telephone line equipped with a Bell System DAA (Data Access Arrangement). Input of the data tape requires about 10 min. The computer calculates the heat capacities, using a stored program, and lists the results on command at the remote terminal. It also converts the raw input data (40 characters/line) into punched cards containing two data lines/card. The cards are retained at the central computer location for later batch processing of all measurements on a particular phase.

EXPERIMENTAL RESULTS

Copper

Eighty-five measurements of the heat capacity of the Calorimetry Conference sample of copper were made between 15 and 380 K. The data are listed in their chronological order of measurement in table 3.

Furukawa and others (1968) made a comprehensive survey of earlier low-temperature heat-capacity measurements on copper and have presented a table of "best" values between 0 and 300 K. Osborn and others

TABLE 3.—*Experimental heat capacites of 63.546 g of the 1965 Calorimetry Conference copper sample*

Temperature in K	Heat capacity in J/(mol·K)	Temperature in K	Heat capacity in J/(mol·K)	Temperature in K	Heat capacity in J/(mol·K)
SERIES 4		SERIES 10		SERIES 17	
305.90	24.53	186.21	22.11	127.52	18.92
312.54	24.61	193.43	22.36	135.81	19.56
		200.50	22.58	151.88	20.58
SERIES 5		207.50	22.78		
306.40	24.54			SERIES 18	
313.11	24.61	SERIES 11		15.36	0.1981
319.91	24.68	206.96	22.76	17.39	0.2995
326.56	24.76	213.90	22.94		
333.14	24.84	221.23	23.12	SERIES 19	
339.71	24.89	228.92	23.30	19.52	0.4221
346.24	24.96	236.55	23.47	21.70	0.5995
352.76	25.02			24.25	0.8632
		SERIES 12		26.95	1.210
SERIES 6		237.82	23.44	29.58	1.610
359.47	25.08	245.47	23.63	32.51	2.133
366.13	25.15	253.00	23.79	35.94	2.824
372.70	25.20			39.77	3.671
379.26	25.25	SERIES 13		44.02	4.680
		260.68	23.88	48.38	5.764
SERIES 7		268.12	24.01		
59.10	8.452	275.53	24.13	SERIES 20	
64.41	9.683	282.89	24.24	295.34	24.41
69.47	10.81	290.22	24.36	302.69	24.50
74.71	11.90	297.53	24.43	309.92	24.58
80.17	12.90				
		SERIES 14			
SERIES 8		306.65	24.54		
117.81	18.04				
122.33	18.47	SERIES 15			
127.33	18.92	56.68	7.851		
132.42	19.30	62.65	9.273		
137.54	19.68	67.82	10.43		
142.96	20.05	73.04	11.54		
		78.39	12.59		
SERIES 9		83.87	13.59		
143.76	20.09				
151.22	20.53	SERIES 16			
158.67	20.94	87.08	14.13		
166.21	21.30	92.57	14.99		
173.62	21.63	100.23	16.06		
180.93	21.93	109.86	17.22		
		118.90	18.15		

(1967) have described the preparation of the 1965 Calorimetry Conference sample of copper (99.99+, annealed) and have summarized the results of some previous investigations of the heat capacity for 99.99+ copper between 1 and 25 K. Holste, Cetas, and Swenson (1972) have summarized the more recent C_p° data for temperatures below 30 K. Martin (1973) has remeasured the C_p° of copper between 2.5 and 30 K, and Hurley and Gerstein (1974) have measured the C_p° of the Calorimetry Conference sample below 30 K.

Of the 60 sets of heat-capacity measurements for copper considered by Furukawa and others (1968), the only results directly comparable with ours, for the range 30 to 300 K with respect to purity of sample and the ability to intercompare the temperature scale used, are those of Martin (1960).

Our results for the heat capacity of the 1965 Calorimetry Conference copper sample are shown in figure 4 as deviations from the "best" values adopted by Furukawa and others (1968). The results of Martin (1960) are also shown in figure 4. It should be noted that our results refer to the IPTS 1968, whereas the data of Martin (1960) were based upon the IPTS 1948, and the values adopted by Furukawa and others (1968) are not, strictly speaking, on either temperature scale. The "best" values of Furukawa and others (1968) are a selected average of several earlier investigations which have a scatter greater than 2.5 percent (see Furukawa and others, 1968, fig. 2a), and of which there are only two studies for the temperature range 20 to 300 K less than 30 years old (Sandenaw, 1959; Martin, 1960). Furthermore, Sandenaw (1959) gave three sets of measurements that differ amongst themselves by an average of 0.5 percent.

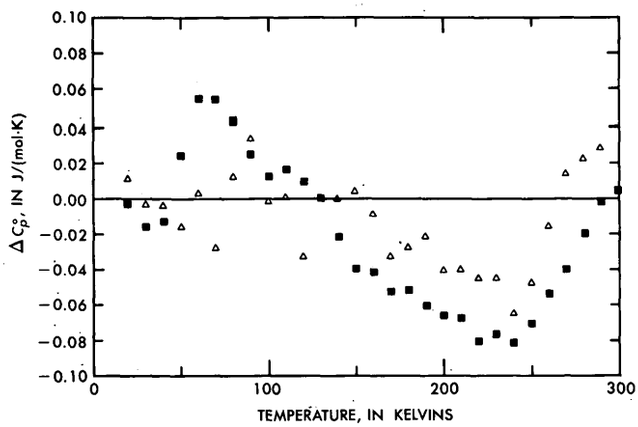

FIGURE 4.—Deviation plot of heat-capacity measurements of copper from the reference values adopted by Furukawa and others (1968). Open triangles, results of Martin (1960); solid squares, this investigation on the Calormetry Conference sample of copper.

Our results deviate systematically from the values selected by Furukawa and others (1968) by as much as 0.5 percent between 70 and 300 K. However, the values of Martin (1960), the only other data for a sample comparable to the Calorimetry Conference sample, also show deviation (parallel to ours) from the values of Furukawa and others (1968).

Muscovite

Our measurements for the heat capacity of muscovite, uncorrected for deviations from the formula $KAl_2(AlSi_3)O_{10}(OH)_2$, are listed in their chronological order of measurement in table 4 and are shown graphically in figure 5. Weller and King's (1963) results are also shown in figure 5.

Our corrected values for C_p° of muscovite are systematically higher than those of Weller and King (1963) by about 1.0 percent between 100 and 300 K and are 1.0 percent lower than their extrapolated value

TABLE 4.—*Experimental heat capacities of 398.309 g of muscovite not corrected for impurities*

Temperature in K	Heat capacity in J/(mol·K)	Temperature in K	Heat capacity in J/(mol·K)
SERIES 1		SERIES 5	
295.64	321.3	152.38	178.7
302.98	326.4	159.27	187.5
310.85	332.2	166.28	196.3
319.35	337.9	173.49	205.1
		180.77	213.8
SERIES 2		188.01	222.1
303.12	326.5	195.34	230.2
311.58	332.3	202.90	238.4
320.08	338.0	210.56	246.3
328.49	343.5	218.32	254.2
336.83	348.9	226.07	261.9
345.10	354.0	233.69	269.1
353.29	358.8	241.20	276.2
361.43	363.5		
369.50	367.8	SERIES 6	
377.51	372.3	234.38	269.9
385.47	377.6	241.92	276.8
		249.55	283.7
SERIES 3		257.07	290.2
54.69	39.33	264.51	296.4
59.07	45.39	271.97	302.6
63.22	51.16	279.60	308.8
67.56	57.35	287.24	314.7
72.08	63.94	294.80	320.4
76.51	70.55		
80.88	77.07	SERIES 7	
		13.29	0.5823
SERIES 4		14.83	0.5823
79.47	75.00	16.40	1.482
84.70	82.83	17.82	1.965
90.16	90.98	19.23	2.579
101.67	108.0	22.43	4.310
107.74	116.8	24.43	5.651
120.30	135.0	29.49	9.661
126.55	143.9	32.53	12.70
133.07	152.9	36.01	16.27
139.87	162.2	39.94	20.55
146.70	171.3	44.38	25.68
153.31	179.9	49.22	31.64
159.74	188.1	54.19	38.43
166.74	196.2		

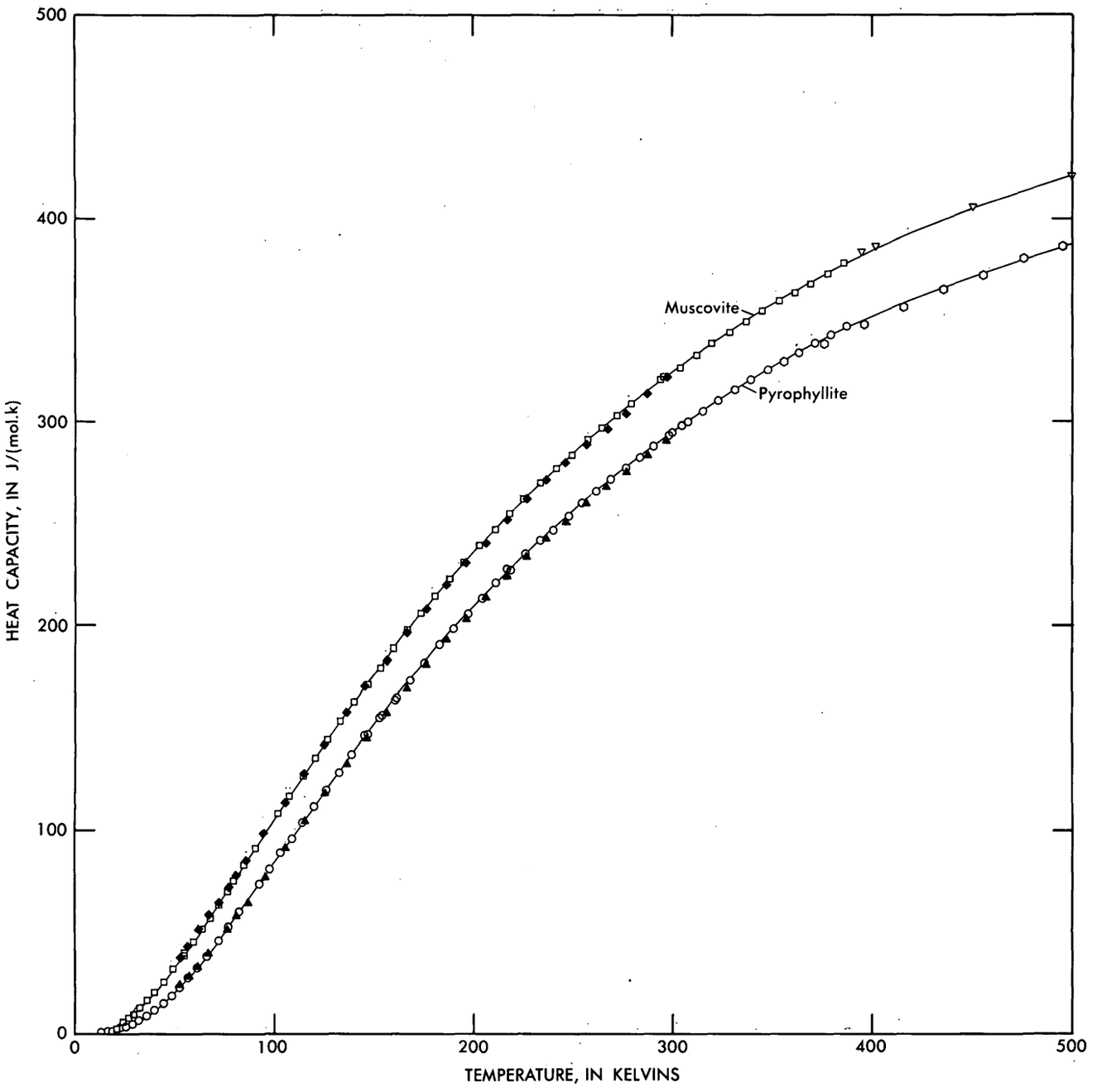

FIGURE 5.—Heat capacities of muscovite and pyrophyllite, uncorrected for impurities. Open squares, muscovite, this investigation; solid diamonds, data of Weller and King (1963) for muscovite; inverted triangles, calculated from the $H_T^\circ - H_{298}^\circ$ data of Pankratz (1964) on muscovite; open circles, pyrophyllite, this investigation; open hexagons, unpublished measurements from this laboratory by differential scanning calorimetry; solid triangles, measurements of King and Weller (1970) for pyrophyllite.

at 50 K. Although the sample used by Weller and King (1963) was considerably less ideal than the material used for our measurements, they did not attempt to correct their results for the deviation of their sample from stoichiometry but assumed that the effect of the impurities on the heat capacity "should be partially compensated." Most of the difference is probably due to the much larger amount of Fe^{+3} in their sample, which is more properly described as a phengite (tetrahedral Si/Al>3) rather than as a muscovite (tetrahedral Si/Al=3) (Deer, Howie and Zussman, 1962, p. 14; Ernst, 1963). In figure 5, we also have included

several high-temperature heat-capacity values for muscovite obtained from the $H_T^\circ - H_{298}^\circ$, drop-calorimeter measurements of Pankratz (1964).

The measured heat capacities of muscovite, pyrophyllite, and illite were corrected for deviations from their stoichiometric formulas, as follows: The heat capacity of that mass of sample having the composition given in table 1 (or 2) and containing exactly one gram formula weight (mole) of the ideal formula was calculated, and the excess oxides were combined into normative phases for which low-temperature heat-capacity data are available. For muscovite having the composition of analysis 4, table 1, a sample mass of 459.548 grams was assumed to consist of $KAl_2(AlSi_3)O_{10}(OH)_2$ and 9.18 g of $Al_2Si_4O_{10}(OH)_2$, 17.50 g of $NaAlSi_3O_8$ (low albite), 14.50 g of $MgFe_2O_4$, 10.98 g of quartz, 9.015 g of Al_2SiO_5 (andalusite), and 0.06 g of MgO. The heat capacities of these impurities were subtracted from the heat capacity of 459.548 g of our muscovite sample to obtain values for $KAl_2(AlSi_3)O_{10}(OH)_2$.

The sum of the heat capacities of the oxide constituents of the muscovite exceeded that of muscovite by 15.4 percent at 50 K and by less than 4 percent at temperatures above 100 K. The difference between the corrected (assuming additivity of oxide heat capacities) and the uncorrected heat capacities per gram of our muscovite sample is −1.3 percent at 50 K and −1.0 percent or less between 100 and 370 K. Thus, our correction procedure should not introduce errors of greater than 0.3 percent at 50 K and 0.04 percent above 100 K to the smoothed C_p°'s of ideal $KAl_2(AlSi_3)O_{10}(OH)_2$. Because the entropy at 50 K is only 5 percent of that at 298.15 K, the impurity correction should introduce errors no greater than 0.1 percent to $S_{298.15}^\circ$ over that due to the measurement uncertainty of ±0.15 percent. Robie (1957, p. 34) and Furukawa and Saba (1965) have previously made similar observations. This method of correction would fail badly for paramagnetic impurities (see Kittel, 1957, p. 138) below 10 K.

Pyrophyllite

The heat capacity of pyrophyllite from Staley, N.C., uncorrected for deviations from the formula $Al_2Si_4O_{10}(OH)_2$, is listed in table 5 and shown in figure 5. In figure 5, we have also included our unpublished heat-capacity measurements, between 350 and 500 K, for this pyrophyllite obtained by using a differential-scanning calorimeter. The heat-capacity data of King and Weller (1970) for pyrophyllite (location not specified) differ from our results by −0.7 percent at 300 K to −0.6 percent at 100 K. The sum of the heat capacities of α–Al_2O_3 (corundum), $4SiO_2$ (α-quartz), and H_2O (ice) is greater than the heat capacity of pyrophyllite by 0.8 percent at 300 K, by 8.5 percent at 100 K, and by 39 percent at 60 K.

For pyrophyllite, the difference between the corrected and uncorrected heat capacities is −0.5 percent at 50 K and is always less than 0.2 percent between 100 and 370 K; the impurity correction, therefore, makes a negligible (0.05 percent) contribution to the probable error in $S_{298.15}^\circ$ of pyrophyllite.

TABLE 5.—*Experimental heat capacities of 360.316 g of pyrophyllite not corrected for impurities*

Temperature in K	Heat capacity in J/(mol·K)	Temperature in K	Heat capacity in J/(mol·K)
SERIES 1		SERIES 6	
299.82	294.4	147.04	147.4
307.30	299.8	154.21	156.3
315.00	305.0	161.32	165.1
322.83	310.1	168.45	173.6
		175.61	181.9
SERIES 2		182.81	190.1
330.92	315.3		
339.14	320.3	SERIES 7	
347.27	325.1	189.95	197.9
355.34	329.7	197.05	205.5
363.33	333.9	204.22	212.9
371.26	338.3	211.46	220.1
379.12	342.4	218.79	227.3
386.93	346.9	226.20	234.3
		233.71	241.3
SERIES 3			
32.23	6.981	SERIES 8	
35.93	9.218	217.69	226.2
39.87	11.80	225.02	233.3
44.02	14.98	232.33	240.0
48.32	18.92	239.75	246.8
52.78	23.61	247.28	253.6
		254.84	259.9
SERIES 4			
52.24	22.95	SERIES 9	
56.49	27.55	261.66	265.5
60.97	32.60	268.92	271.4
65.72	38.32	276.16	277.2
71.02	44.97	283.31	282.5
76.68	52.35	290.43	287.9
82.56	60.26	297.53	292.9
		304.62	297.9
SERIES 5			
80.67	57.70	SERIES 10	
86.65	65.85	12.66	0.3508
92.18	73.44	13.89	0.5577
97.55	80.85	15.29	0.7407
102.93	88.28	16.83	1.004
108.45	95.93	18.27	1.351
114.12	103.8	19.67	1.661
119.95	111.8	21.09	2.043
125.93	119.9	22.51	2.467
132.20	128.2	23.84	2.936
138.96	137.1	25.82	3.676
146.07	146.2	28.70	4.885
153.21	155.1	31.96	6.715
160.24	163.7	35.60	8.965
		39.77	11.73
		44.11	15.12
		48.39	18.90
		52.84	23.44
		57.52	28.57

Illite

Our experimental results for the heat capacity of illite from Marblehead, Wisc., between 15 and 380 K, are listed in table 6. The data were corrected for 1.59-

TABLE 6.—*Experimental heat capacities of 1,553.671 g of illite from Marblehead, Wis., corrected for adsorbed water but not for other impurities*

Temperature in K	Heat capacity in J/(mol·K)	Temperature in K	Heat capacity in J/(mol·K)	Temperature in K	Heat capacity in J/(mol·K)
SERIES 1		SERIES 5		SERIES 8	
298.20	1304.7	143.78	659.2	15.32	7.451
308.10	1330.7	151.28	698.6	16.39	8.778
317.54	1354.2	157.47	730.6	17.77	12.29
326.86	1377.7	157.62	732.0	19.30	16.13
336.07	1399.2	164.00	764.8	21.12	20.63
345.18	1420.9	170.33	796.3	23.22	26.16
		176.90	829.2	25.52	32.35
SERIES 2		183.84	863.0	28.19	39.97
354.18	1441.0	190.96	897.1		
363.13	1459.7	198.15	930.4	SERIES 9	
371.98	1481.2	205.64	964.3	31.44	50.83
380.74	1503.0	213.44	999.1	35.05	64.82
		221.30	1032.4	39.11	80.59
SERIES 3				43.43	99.45
52.24	143.0	SERIES 6		47.87	119.8
55.66	161.0	222.71	1038.9	52.59	144.3
59.66	182.6	230.40	1071.2		
64.53	208.9	237.96	1101.6		
70.08	239.8	245.39	1130.7		
75.70	272.2	252.70	1157.4		
		259.92	1183.9		
SERIES 4		267.03	1208.8		
75.66	271.8	272.31	1226.7		
80.82	302.0	275.80	1238.3		
86.22	333.6	280.99	1254.4		
92.30	369.1	287.86	1275.5		
98.66	406.0	294.76	1294.9		
105.20	443.9				
111.59	480.6	SERIES 7			
117.64	515.2	299.70	1308.8		
123.53	548.7	306.68	1327.1		
129.29	580.6	313.53	1344.3		
134.94	611.6	321.16	1359.6		
140.71	642.7	329.56	1382.2		
146.69	674.6	337.88	1403.6		
152.90	706.8	346.12	1422.5		
		354.29	1441.0		
		362.39	1458.7		
		370.42	1477.5		

weight-percent adsorbed water by using the C_p° values of Giauque and Stout (1936) for ice below 273 K and the data of Osborne, Stinson, and Ginnings (1939) for water above 273 K, but were not corrected for other impurities. Illite is a 2:1 dioctahedral phyllosilicate having the general formula $K_{x+y}(Al_{4-y}Mg_y^{+2})(Si_{8-x}Al_x)O_{20}(OH)_4$. Of the four well-characterized $2M_1$-illites described by Gaudette, Eades, and Grim (1966), all have more than 1 magnesium atom for the 40 oxygens per unit cell. For this reason, we have adopted $K_3(Al_7Mg)(Si_{14}Al_2)O_{40}(OH)_8$ as the ideal formula for illite.

The impurity correction necessary to convert our measurements on the Marblehead illite to C_p°'s of $K_3(Al_7Mg)(Si_{14}Al_2)O_{40}(OH)_8$ is an order of magnitude larger than that for muscovite or pyrophyllite. The difference between the corrected and uncorrected heat capacities per gram amounts to 12 percent at 50 K and decreases to 5 percent at 300 K. Because of the approximate nature of the additivity assumption, our derived values for C_p° of ideal illite, $K_3(Al_7\ Mg)\ (Si_{14}Al_2)O_{40}(OH)_8$, might be in error by as much as 0.5 percent at 300 K and 1.5 percent at 50 K. The resultant error in $S_{298}^\circ - S_0^\circ$, however, could amount to no more than 1 percent.

THERMODYNAMIC PROPERTIES OF COPPER, MUSCOVITE, PYROPHYLLITE, AND ILLITE

Smoothed values for the thermodynamic functions C_p°, $S_T^\circ - S_0^\circ$, $(H_T^\circ - H_0^\circ)/T$, and $(G_T^\circ - H_0^\circ)/T$ for Cu, $KAl_2(AlSi_3)O_{10}(OH)_2$, $Al_2Si_4O_{10}(OH)_2$, and $K_3(Al_7Mg)(Si_{14}Al_2)O_{40}(OH)_8$ are listed at integral temperatures in tables 7 through 10.

At 298.15 K, the entropy changes $S_{298}^\circ - S_0^\circ$ for copper, muscovite, pyrophyllite, and illite are 33.12 ± 0.06, 287.7 ± 0.6, 239.4 ± 0.4, and $1{,}104.2 \pm 6.0$ J/(mol·K), respectively. The values for muscovite and illite include fairly appreciable corrections to the measured heat

TABLE 7.—*Molar thermodynamic properties of Calorimetry Conference copper*

[Formula weight = 63.546 g·mol^{-1}]

Temperature, T, in kelvins	Heat capacity, C_p°, in J/(mol·K)	Entropy $(S_T^\circ - S_0^\circ)$, in J/(mol·K)	Enthalpy function $(H_T^\circ - H_0^\circ)/T$, in J/(mol·K)	Gibbs energy function $-(G_T^\circ - H_0^\circ)/T$, in J/(mol·K)
5	0.007	0.005	0.003	0.002
10	0.054	0.021	0.017	0.004
15	0.182	0.063	0.052	0.011
20	0.458	0.149	0.122	0.026
25	0.953	0.300	0.245	0.055
30	1.683	0.535	0.433	0.102
35	2.628	0.863	0.691	0.172
40	3.716	1.284	1.014	0.270
45	4.918	1.789	1.392	0.397
50	5.920	2.362	1.810	0.552
60	8.643	3.708	2.744	0.963
70	10.91	5.214	3.752	1.462
80	12.89	6.803	4.774	2.029
90	14.59	8.423	5.773	2.650
100	16.03	10.04	6.729	3.308
110	17.24	11.62	7.631	3.992
120	18.26	13.17	8.475	4.693
130	19.12	14.66	9.262	5.402
140	19.85	16.11	9.993	6.116
150	20.47	17.50	10.67	6.829
160	21.01	18.84	11.30	7.538
170	21.48	20.13	11.89	8.241
180	21.89	21.37	12.43	8.936
190	22.25	22.56	12.94	9.621
200	22.56	23.71	13.41	10.30
210	22.84	24.82	13.85	10.96
220	23.09	25.89	14.27	11.62
230	23.31	26.92	14.66	12.26
240	23.52	27.91	15.02	12.89
250	23.71	28.88	15.37	13.51
260	23.89	29.81	15.69	14.12
270	24.05	30.72	16.00	14.72
280	24.20	31.59	16.29	15.31
290	24.34	32.44	16.56	15.88
300	24.47	33.27	16.82	16.45
310	24.58	34.08	17.07	17.00
320	24.69	34.86	17.31	17.55
330	24.79	35.62	17.53	18.09
340	24.90	36.36	17.75	18.61
350	25.00	37.08	17.95	19.13
360	25.09	37.79	18.15	19.64
370	25.18	38.48	18.34	20.14
273.15	24.10	30.99	16.09	14.90
298.15	24.44	33.12	16.78	16.34

TABLE 8.—*Molar thermodynamic properties of muscovite,* $KAl_2(AlSi_3)O_{10}(OH)_2$

[Formula weight = 398.309 g·mol^{-1}]

Temperature, T, in kelvins	Heat capacity, C_p°, in J/(mol·K)	Entropy $(S_T^\circ - S_0^\circ)$, in J/(mol·K)	Enthalpy function $(H_T^\circ - H_0^\circ)/T$, in J/(mol·K)	Gibbs energy function $-(G_T^\circ - H_0^\circ)/T$, in J/(mol·K)
5	0.0334	0.0108	0.0080	0.0028
10	0.2871	0.0904	0.0681	0.0223
15	1.108	0.3330	0.2535	0.0795
20	2.998	0.8778	0.6744	0.2034
25	6.136	1.861	1.432	0.4289
30	10.37	3.336	2.553	0.7839
35	15.43	5.306	4.023	1.284
40	20.89	7.719	5.786	1.933
45	26.93	10.52	7.787	2.728
50	33.34	13.69	10.07	3.663
60	47.05	20.95	15.03	5.923
70	61.72	29.30	20.64	8.654
80	76.69	38.51	26.71	11.80
90	91.70	48.41	33.10	15.32
100	106.7	58.85	39.71	19.14
110	121.5	69.71	46.47	23.24
120	136.0	80.91	53.33	27.58
130	150.2	92.36	60.24	32.12
140	163.9	104.0	67.15	36.84
150	177.2	115.8	74.05	41.71
160	190.2	127.6	80.90	46.71
170	202.7	139.5	87.70	51.81
180	214.8	151.4	94.43	57.02
190	226.4	163.4	101.1	62.30
200	237.4	175.3	107.6	67.65
210	248.0	187.1	114.1	73.06
220	258.2	198.9	120.4	78.51
230	268.1	210.6	126.6	84.00
240	277.6	222.2	132.7	89.52
250	286.8	233.7	138.7	95.06
260	295.5	245.1	144.5	100.6
270	303.8	256.4	150.3	106.2
280	312.0	267.6	155.9	111.7
290	319.9	278.7	161.4	117.3
300	327.4	289.7	166.8	122.9
310	334.6	300.6	172.1	128.4
320	341.4	311.3	177.3	134.0
330	348.0	321.9	182.4	139.5
340	354.5	332.4	187.4	145.0
350	360.8	342.8	192.2	150.5
360	366.8	353.0	197.0	156.0
370	372.4	363.1	201.7	161.5
273.15	306.4	260.0	152.1	107.9
298.15	326.1	287.7	165.8	121.8

TABLE 9.—*Molar thermodynamic properties of pyrophyllite,* $Al_2Si_4O_{10}(OH)_2$

[Formula weight = 360.316 g·mol^{-1}]

Temperature, T, in kelvins	Heat capacity, C_p°, in J/(mol·K)	Entropy $(S_T^\circ - S_0^\circ)$, in J/(mol·K)	Enthalpy function $(H_T^\circ - H_0^\circ)/T$, in J/(mol·K)	Gibbs energy function $-(G_T^\circ - H_0^\circ)/T$, in J/(mol·K)
5	0.0263	0.0084	0.0062	0.0022
10	0.2020	0.0666	0.0497	0.0169
15	0.6992	0.2275	0.1707	0.0568
20	1.713	0.5536	0.4173	0.1363
25	3.309	1.095	0.8244	0.2701
30	5.597	1.887	1.417	0.4699
35	8.499	2.964	2.217	0.7461
40	11.80	4.308	3.203	1.105
45	15.76	5.919	4.371	1.548
50	20.51	7.818	5.741	2.077
60	31.35	12.49	9.079	3.408
70	43.63	18.23	13.12	5.103
80	56.74	24.90	17.75	7.152
90	70.33	32.37	22.83	9.532
100	84.18	40.49	28.27	12.22
110	98.09	49.17	33.99	15.18
120	111.8	58.29	39.91	18.39
130	125.3	67.78	45.96	21.82
140	138.4	77.55	52.10	25.45
150	151.1	87.53	58.28	29.26
160	163.5	97.69	64.47	33.21
170	175.5	108.0	70.65	37.31
180	187.0	118.3	76.80	41.52
190	198.1	128.7	82.89	45.84
200	208.7	139.2	88.92	50.24
210	218.8	149.6	94.87	54.72
220	228.6	160.0	100.7	59.27
230	238.1	170.4	106.5	63.88
240	247.2	180.7	112.2	68.53
250	256.0	191.0	117.7	73.22
260	264.4	201.2	123.2	77.95
270	272.5	211.3	128.6	82.70
280	280.3	221.4	133.9	87.47
290	287.8	231.3	139.1	92.26
300	295.0	241.2	144.1	97.06
310	301.9	251.0	149.1	101.9
320	308.6	260.7	154.0	106.7
330	315.0	270.3	158.8	111.5
340	321.2	279.8	163.5	116.3
350	327.0	289.2	168.1	121.1
360	332.5	298.5	172.6	125.9
370	338.1	307.6	176.9	130.7
273.15	275.0	214.5	130.3	84.20
298.15	293.7	239.4	143.2	96.17

capacities for deviations of the calorimetric sample from the ideal formula, and we have accordingly included estimates of this source of error in the uncertainties associated with the entropy values for these phases.

Our value for the entropy of copper at 298.15 K is 33.12±0.06 J/(mol·K) and may be compared with the values 33.15±0.17 J/(mol·K) given by Martin (1960) and 33.15 J/(mol·K) given by Furukawa and others (1968).

Weller and King (1963) gave 288.7±2.9 J/mol·K) for the entropy of muscovite, on the basis of their heat-capacity measurements between 52.6 and 296.6 K and an empirical extrapolation of C_p° to 0 K. Their value for $S_{298}^\circ - S_0^\circ$ includes a contribution of 18.2 J/(mol·K) caused by the extrapolation of C_p° between 52.6 and 0 K. The present result of 287.7±0.6 J/(mol·K) includes only 0.3 J/(mol·K) resulting from the extrapolation of C_p° below 15 K.

On the basis of their refinement of the crystal structure of a $2M_1$-muscovite from a pegmatite, Burnham and Radoslovich (1964) and Guven (1968) have shown that the Al/Si distribution in the two crystallographically distinct tetrahedra is random. Openshaw, Hemingway, Robie, Waldbaum, and Krupka (1975) have shown that, for the analogous case of tetrahedral Al/Si disorder in the alkali feldspars, the difference in the heat capacities below 300 K between low albite and analbite and between high sanidine and microcline is at most 0.5 percent and that the difference in $S_{298}^\circ - S_0^\circ$ for these two polymorphic pairs is only 0.1 percent. That is to say the Al/Si distribution has only a small

TABLE 10.—*Molar thermodynamic properties of illite,* $K_3(Al_7Mg)(Si_{14}Al_2)O_{40}(OH)_8$

[Formula weight = 1553.671 g·mol^{-1}]

Temperature, T, in kelvins	Heat capacity, C_p°, in J/(mol·K)	Entropy $(S_T^\circ - S_0^\circ)$, in J/(mol·K)	Enthalpy function $(H_T^\circ - H_0^\circ)/T$, in J/(mol·K)	Gibbs energy function $-(G_T^\circ - H_0^\circ)/T$, in J/(mol·K)
5	0.1872	0.0594	0.0450	0.0144
10	1.596	0.5098	0.3849	0.1249
15	5.868	1.813	1.373	0.4399
20	15.72	4.720	3.614	1.106
25	27.79	9.523	7.239	2.283
30	41.68	15.77	11.77	3.992
35	57.82	23.37	17.17	6.202
40	76.63	32.29	23.40	8.893
45	98.06	42.53	30.48	12.05
50	121.8	54.08	38.41	15.66
60	172.0	80.61	56.39	24.22
70	226.2	111.2	76.75	34.42
80	282.1	145.0	98.91	46.09
90	339.1	181.5	122.4	59.09
100	396.4	220.2	147.0	73.25
110	453.5	260.7	172.2	88.44
120	509.9	302.6	198.0	104.5
130	565.0	345.6	224.1	121.4
140	619.1	389.4	250.4	139.0
150	672.0	433.9	276.8	157.2
160	723.9	479.0	303.1	175.9
170	774.8	524.4	329.4	195.0
180	824.5	570.1	355.5	214.6
190	873.0	616.0	381.5	234.5
200	920.1	661.9	407.2	254.7
210	965.8	708.0	432.7	275.2
220	1009.8	753.9	458.0	295.9
230	1051.9	799.7	482.9	316.8
240	1092.2	845.4	507.4	337.9
250	1130.7	890.7	531.6	359.1
260	1167.5	935.8	555.4	380.4
270	1202.6	980.5	578.7	401.8
280	1236.0	1024.9	601.6	423.3
290	1267.3	1068.8	624.0	444.8
300	1296.4	1112.3	645.9	466.3
310	1323.6	1155.2	667.4	487.8
320	1349.9	1197.6	688.3	509.4
330	1376.4	1239.6	708.7	530.9
340	1403.1	1281.1	728.8	552.3
350	1428.0	1322.1	748.4	573.7
360	1449.7	1362.7	767.6	595.1
370	1472.1	1402.7	786.3	616.4
273.15	1213.3	994.5	585.9	408.6
298.15	1291.2	1104.2	641.9	462.3

effect upon C_p° and an even smaller effect upon $S_{298}^\circ - S_0^\circ$. We have therefore assumed that our value for $S_{298}^\circ - S_0^\circ$ corresponds to muscovite, in which the aluminum and three silicon atoms are randomly distributed in the tetrahedral positions, and that $S_{298}^\circ - S_0^\circ$ has approximately this same value for a hypothetical muscovite in which the tetrahedral aluminum and three silicon atoms are completely ordered.

Ulbrich and Waldbaum (1975) have pointed out that because of the randomness of the Al/3Si in the tetrahedral position, a configurational term of 18.70 J/(mol·K) should be added to the measured value of $S_{298}^\circ - S_0^\circ$ of the disordered (real) muscovite to obtain the correct entropy for use in thermodynamic calculations. Thus, for the hypothetical Al/Si ordered muscovite, $S_{298}^\circ = 287.7 \pm 0.6$ J/(mol·K), whereas for Al/Si disordered muscovite, $S_{298}^\circ = 287.7 + 18.70 = 306.4 \pm 0.6$ J/(mol·K). Using the S_{298}° values for the elements tabulated by Robie and Waldbaum (1968), we calculate $-1{,}279.1 \pm 1.0$ J/(mol·K) and $-1{,}260.9 \pm 1.0$ J/(mol·K) for the entropies of formation at 298.15 K for the hypothetical Al/3Si ordered and disordered muscovite, respectively.

From our heat capacity data for pyrophyllite, we obtain 239.4 ± 0.5 J/(mol·K) for $S_{298}^\circ - S_0^\circ$, of which 0.2 J/(mol·K) is the extrapolated part below 13 K. King and Weller (1970) obtained 236.8 ± 2.1 J/(mol·K) for $S_{298}^\circ - S_0^\circ$ for pyrophyllite, which included 7.2 J/(mol·K) because of the extrapolation of their measurements below 52 K. In the pyrophyllite structure there is no Al/Si disorder; therefore S_0° is zero and 239.4 ± 0.5 J/(mol·K) is the correct value for S_{298}° for use in thermodynamic calculations. The entropy change for the formation of pyrophyllite from the elements is $-1{,}253.1 \pm 0.7$ J/(mol·K) at 298.15 K.

From our heat-capacity measurements on illite, we derived $S_{298}^\circ - S_0^\circ = 1{,}104.2 \pm 6.0$ J/(mol·K), for $K_3(Al_7Mg)(Si_{14}Al_2)O_{40}(OH)_8$, of which 1.8 J/(mol·K) is due to the extrapolation below 15 K. The detailed structure of illite is unknown, and because the possibility of cation disorder in both the tetrahedral and octahedral positions exists, the zero-point entropy, S_0°, is probably not zero. Thus, we report only the value for $S_{298}^\circ - S_0^\circ$. If we assume, however, that the illite structure is ordered, then the absolute entropy is $1{,}104.2 \pm 6.0$ J/(mol·K) at 298.15 K.

Muscovite and illite are closely related structurally and chemically, and their mean atomic weights differ by only 2.5 percent. In comparing the entropy change $S_{298}^\circ - S_0^\circ$ for illite and muscovite, we must multiply the value for muscovite listed in table 8 by four. The difference in $S_{298}^\circ - S_0^\circ$ between illite and muscovite is 4.2 percent. The entropy change for the formation of ideal ordered illite from the elements is $-5{,}083.6 \pm 6.5$ J/(mol·K).

REFERENCES CITED

Burnham, C. W., and Radoslovich, E. W., 1964, Crystal structures of coexisting muscovite and paragonite: Carnegie Inst. Washington Year Book 63, 1963–1964, p. 232–236.

Comité International des Poids et Mesures, 1969, The International Practical Temperature Scale of 1968: Metrologia, v. 5, no. 2, p. 35–44.

Commission on Atomic Weights, 1972, Atomic weights of the elements, 1971: Pure and Appl. Chemistry, v. 30, p. 637–649.

Deer, W. A., Howie, R. A., Zussman, J., 1962, Rock-forming minerals—v. 3, Sheet silicates: New York, John Wiley and Sons, 270 p.

Ernst, W. G., 1963, Significance of phengitic micas from low-grade schists: Am. Mineralogist, v. 48, nos. 11–12, p. 1357–1373.

Eugster, H. P., Albee, A. L., Bence, A. E., Thompson, J. B., Jr., and Waldbaum, D. R., 1972 The two-phase region and excess mixing properties of paragonite-muscovite crystalline solutions: Jour. Petrology, v. 13, no. 1, p. 147–179.

Furukawa, G. T., and Saba, W. G., 1965, Heat capacity and thermodynamic properties of beryllium aluminate (chrysoberyl), $BeO \cdot Al_2O_3$ from 16 to 380°K: U.S. Natl. Bur. Standards Jour. Research, v. 69A, p. 13–18.

Furukawa, G. T., Saba, W. G., and Reilly, M. L., 1968, Critical analysis of the heat-capacity data of the literature and evaluation of thermodynamic properties of copper, silver, and gold from 0 to 300°K: U.S. Natl. Bur. Standards, Natl. Standard Ref. Data Ser. 18, 49 p.

Gaudette, H. E., 1965, Illite from Fond du Lac County, Wisconsin: Am. Mineralogist, v. 50, nos. 3–4, p. 411–417.

Gaudette, H. E., Eades, J. L., and Grim, R. E., 1966, The nature of illite, *in* Bradley, W. F., and Bailey, S. W. eds., Clays and clay minerals—Proceedings of the Thirteenth National Conference on Clays and Clay Minerals, 1964: New York, Pergamon Press, p. 33–48.

Giauque, W. F., and Stout, J. W., 1936, The entropy of water and the third law of thermodynamics: Am. Chem. Soc. Jour., v. 58, pt. 1, p. 1144–1150.

Guven, N., 1968, The crystal structure of $2M_1$ phengite and $2M_1$ muscovite: Carnegie Inst. Washington Yearbook 66, 1966–1967, p. 487–492.

——— 1970, Compositional and structural relationships between phengites and illites: Clays and Clay Minerals, v. 18, no. 4, p. 233–235.

——— 1972, Electron optical observations on Marblehead illite: Clays and Clay Minerals, v. 20, no. 2, p. 83–88.

Holste, J. C., Cetas, T. C., and Swenson, C. A., 1972, Effects of temperature scale differences on the analysis of heat capacity data: The specific heat of copper from 1 to 30 K: Rev. Sci. Instruments, v. 43, no. 4, p. 670–676.

Hurlbut, C. S., Jr., 1956, Muscovite from Methuen Township, Ontario: Am. Mineralogist, v. 41, no. 11–12, p. 892–898.

Hurley, M. and Gerstein, B. C., 1974, The low-temperature heat capacity of 1965-Calorimetry-Conference copper: a comparison with previous results: Jour. Chem. Thermodynamics, v. 6, no. 8, p. 787–793.

King, E. G., and Weller, W. W., 1970, Low-temperature heat capacities and entropies at 298.15°K of goethite and pyrophyllite: U.S. Bur. Mines Rept. Inv. 7369, 6 p.

Kittel, Charles, 1957, Introduction to solid state physics [2d ed.]: New York, John Wiley and Sons, 617 p.

Martin, D. L., 1960, The specific heat of copper from 20 to 300°K: Canadian Jour. Physics, v. 38, p. 17–24.

——— 1973, Specific heat of copper, silver, and gold below 30°K: Canadian Jour. Physics, v. 38, p. 17–24.

Openshaw, R. E., Hemingway, B. S., Robie, R. A., Waldbaum, D. R., and Krupka, K. M., 1976, The heat capacities at low temperatures and entropies at 298.15 K of low albite, analbite, microcline, and high sanidine: U.S. Geol. Survey Jour. Research, v. 4, no. 2, p. 195–204.

Osborne, D. W., Flotow, H. E., and Schreiner, Felix, 1967, Calibration and use of germanium resistance thermometers for precise heat capacity measurements from 1 to 25°K. High purity copper for interlaboratory heat capacity comparisons: Rev. Sci. Instruments, v. 38, no. 2, p. 159–168.

Osborne, N. S., Stimson, H. F., and Ginnings, D. C., 1939, Measurements of heat capacity and heat of vaporization of water in the range 0° to 100°C: U.S. Natl. Bur. Standards Jour. Research, v. 23, p. 197–260.

Pankratz, L. B., 1964, High-temperature heat contents and entropies of muscovite and dehydrated muscovite: U.S. Bur. Mines Rept. Inv. 6371, 6 p.

Rayner, J. H., and Brown, G., 1964, Structure of pyrophyllite: Clays and Clay Minerals, v. 13, p. 73–84.

Reesman, A. L., 1974, Aqueous dissolution studies of illite under ambient conditions: Clays and Clay Minerals, v. 22, no. 5–6, p. 443–454.

Robie, R. A., 1957, Thermodynamic properties of $CaMg(CO_3)_2$, $Mg_3Si_4O_{10}(OH)_2$ and $Ca_2Mg_5Si_8O_{22}(OH)_2$ between 12 and 300 degrees Kelvin: Univ. Chicago, Ph. D. thesis, 107 p.

Robie, R. A., and Hemingway, B. S., 1972, Calorimeters for heat of solution and low-temperature heat capacity measurements: U.S. Geol. Survey Prof. Paper 755, 32 p.

Robie, R. A., and Waldbaum, D. R., 1968, Thermodynamic properties of minerals and related substances at 298.15°K(25.0°C) and one atmosphere (1.013 bars) pressure and at higher temperatures: U.S. Geol. Survey Bull. 1259, 256 p.

Rosenbaum, R. L., 1968, Some properties of gold-iron thermocouple wire: Rev. Sci. Instruments, v. 39, no. 6, p. 890–899.

Sandenaw, T. A., 1959, Heat capacity of copper below 300°K, a test of two calorimeter designs: California Univ., Los Alamos Sci. Lab. [Rept.] LA–2307 Instruments, 19 p.

Shapiro, Leonard, 1967, Rapid analysis of rocks and minerals by a single solution method: U.S. Geol. Survey Prof. Paper 575–B, p. 187–191.

Sparks, L. L., and Powell, R. L., 1972, Low temperature thermocouples: KP, "normal" silver, and copper versus Au-0.02 at% Fe and Au-0.07 at% Fe: U.S. Natl. Bur. Standards Jour. Research, v. 76A, no. 3, p. 263–283.

Taylor, L. A., and Bell, P. M., 1971, Thermal expansion of pyrophyllite: Carnegie Inst. Washington Yearbook 69, 1969–1970, p. 193–194.

Ulbrich, H. H., and Waldbaum, D. R., 1975, Structural and other contributions to the third-law entropies of silicates: Geochim. et Cosmochim. Acta. v. 40, no. 1, p. 1–24.

Weller, W. W., and King, E. G., 1963. Low-temperature heat capacity and entropy at 298.15°K of muscovite: U.S. Bur. Mines Rept. Inv. 6281, 4 p.

Zen, E-an, 1961, Mineralogy and petrology of the system Al_2O_3—SiO_2—H_2O in some pyrophyllite deposits of North Carolina: Am. Mineralogist, v. 46, nos. 1–2, p. 52–66.

Jour. Research U.S. Geol. Survey
Vol. 4, No. 6, Nov.-Dec. 1976, p. 645–659

GEOTHERMAL FLUX THROUGH PALAGONITIZED TEPHRA, SURTSEY, ICELAND—THE SURTSEY TEMPERATURE-DATA-RELAY EXPERIMENT VIA LANDSAT-1

By JULES D. FRIEDMAN, DUANE M. PREBLE, and SVEINN JAKOBSSON,
Denver, Colo., Bay Saint Louis, Miss., and Reykjavík, Iceland

Work done in cooperation with the Icelandic Museum of Natural History and the U.S. National Aeronautics and Space Administration

Abstract.—The net geothermal flux through palagonitized basaltic tephra rims of the Surtur I and Surtur II craters at Surtsey, Iceland, in 1972, is estimated at 780±325 μcal $cm^{-2}s^{-1}$, indicating a decline since 1969 when a flux of 1,500 μcal $cm^{-2}s^{-1}$ was estimated. Heat flux in this range characterizes the postvolcanic environment on Surtsey in which the subaerial palagonitization of basaltic tephra is associated with mass transfer of hydrothermal vapor, either of meteoric or sea-water origin, only a few years after cessation of eruptive activity. The flux estimation is the result of the Surtsey data-relay experiment via Landsat-1 which was carried out in several phases. Successful field installation and test transmissions demonstrated the feasibility of repetitive long-distance (that is, 4,800-km) data transmission and reception from a volcanic environment in Iceland via the Landsat Data Collection System. Temperature data were transmitted for a 38-day period in November and December 1972. A near-surface vertical gradient of 69.4°C/m was obtained, suggesting a mixed mechanism of heat transfer, partitioned between conduction and convection. Comparison of four methods for estimating fluxes between 500 and 1,500 μcal $cm^{-2}s^{-1}$, using temperature data derived from the Data Collection Platform, suggests that, where the only temperature available are from the surface and a depth of 1 m, methods of estimating the net geothermal flux from examination of spectral radiance are superior to methods that assume dominant convection or conduction. A computerized thermal-modeling technique to construct parametric diurnal surface-temperature curves is particularly applicable. Flux-estimation methods that assume dominant convection or conduction are limited by the lack of temperature data at greater depths and lack of knowledge of the exact energy partition.

The Surtsey temperature-data-relay experiment was carried out under the auspices of the Icelandic Museum of Natural History (Náttúrufrædistofnun Íslands), the U.S. Geological Survey, and the National Aeronautics and Space Administration (NASA), as part of Landsat-1 (formerly ERTS-1) experiment SR 251, the thermal surveillance of volcanoes using the Landsat Data Collection System (DCS). The object of the Surtsey experiment was to test the Landsat-1 DCS in a thermally anomalous volcanic area, difficult of access, where continuously relayed surface and near-surface temperatures would be of scientific interest.

This component of the DCS experiment was designed to contribute data on the thermal environment in which the palagonitization process is taking place on Surtesy. The present report is a contribution to a larger study of the palagonitization process by Sveinn P. Jakobsson of the Icelandic Museum of Natural History.

The Surtsey DCS experiment had several phases: (1) design and construction of a thermistor-array network suitable for obtaining surface and near-surface temperatures in an environment of volcanic fume and vapor emission and compatible with the DCS, (2) field installation and testing of the Data Collection Platform (DCP) instrument station on Surtsey (including transmission tests via the Landsat–1 satellite), (3) development of a computer program for conversion of the binary-coded data to geophysical units (4) application of statistical procedures to the resulting temperature data, and (5) selection, testing, and evaluation of several methods to determine heat flux from the existing data.

An area in a topographic saddle between Surtur I and Surtur II tephra rims on Surtesy (figs. 1 and 2) was selected for instrumentation because there anomalous volcanogenic heat flow is associated with palagonitization of previously unconsolidated basaltic tephra. In Iceland, the end product of the palagonitization process, palagonite of the Móberg formation, is usually the result of leaching and hydration of sideromelane glass, which is formed by rapid subaque-

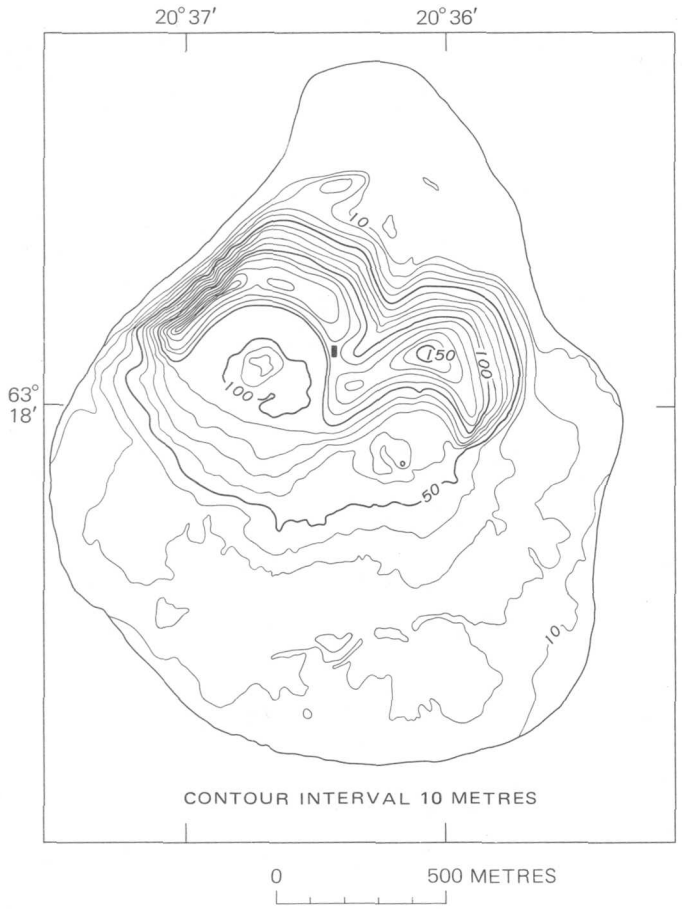

FIGURE 1.—Location of Data Collection Platform 6056, November 15 to December 25, 1972, shown by small rectangle. Map of Surtsey modified from Norrman (1970).

ous or subglacial quenching of basaltic magma. On Surtsey, the palagonitization process is taking place at the present time through the action of postvolcanic hydrothermal vapor on unconsolidated tephra deposited between November 1963 and February 1964 (Jakobsson, 1972). No previous data on temporal variations in surface and near-surface temperatures and on near-surface heat flow had been collected at this particular locality, although earlier aerial infrared scanner surveys (Friedman and others, 1969; Friedman and Williams, 1970, p. D121) and in situ measurements in August 1970 (Jakobsson, 1972) had delineated thermally anomalous areas.

The Surtsey experiment served two objectives: (1) to collect data on heat-flux levels in the area of continuing hydrothermal alteration which are of value in defining the process of palagonitization as well as in charting the declining postvolcanic energy yield from the Surtsey volcanic system, and (2) to test the feasibility of data transmission from a point as distant as Surtsey via the Landsat–1 DCS to the NASA Goddard Space Flight Center.

Moveover, the daily repetition of surface and 1-metre-depth temperature measurements under controlled conditions (provided by the DCS) could be of particular value in estimating the fluctuations or natural variations in the geothermal flux in the Surtesy anomalous area.

Acknowledgments.—The authors thank Jón Sveinsson for his assistance in installing DCP station 6056 on Surtsey, J. Earle Painter of the Goddard Space

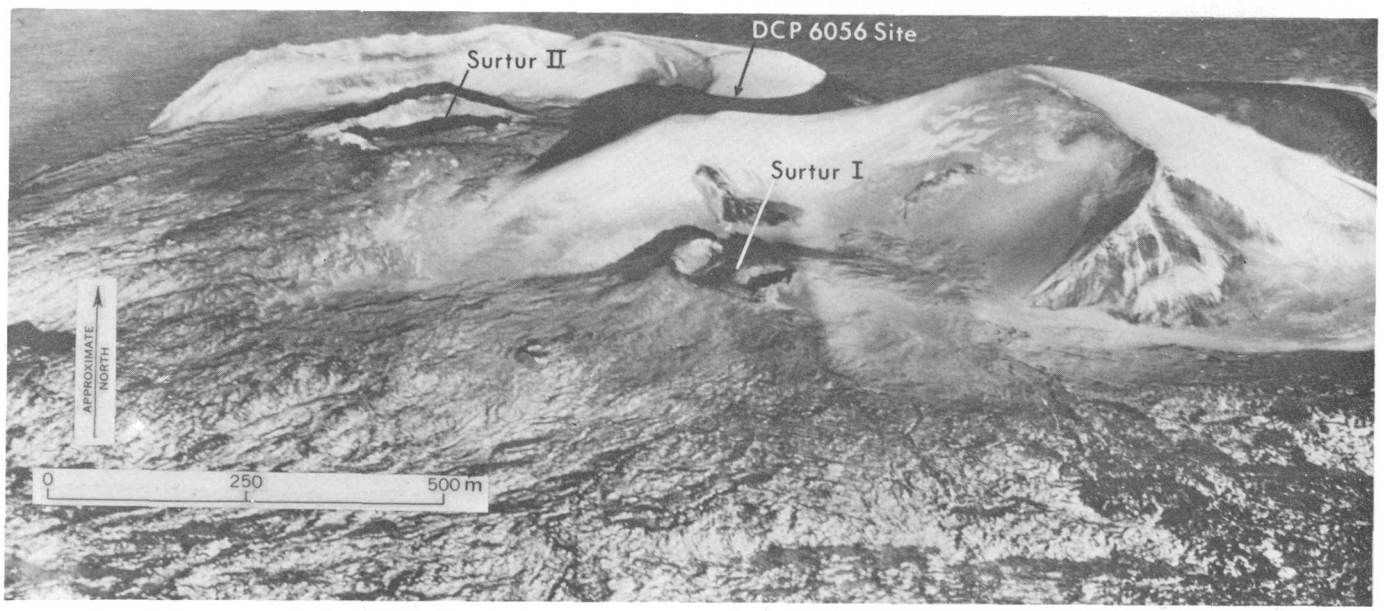

FIGURE 2.—Helicopter view of Surtsey, November 15, 1972, at the time of installation of Data Collection Platform 6056. Surtur I and Surtur II vent areas appear in middle ground, and tephra rims show in background. The DCP is in the topographic saddle between the rims of Surtur I and Surtur II.

Flight Center for his help in using the DCS Receiving Station Facilities, Don Sawatzky, U.S. Geological Survey, for conversion of an earlier IBM 370 computer program for reduction of DCP binary-coded temperature data for experiment SR 251 to a newer DEC–10 computer system, and Gary Raines, U.S. Geological Survey, for his assistance with statistical procedures and computer programs for analyzing correlation coefficients of temperature data. The authors are especially indebted to Kenneth Watson, U.S. Geological Survey, for application of his computerized thermal-modeling technique for derivation of geothermal heat fluxes from surface temperature and thermal and geodetic parameters.

Landsat–1 experiment 251 was supported by NASA under Contract No. S–70243–AG with the U.S. Geological Survey and was carried out under Task No. 434–641–14–03–40. The authors are indebted to Steingrímur Hermannsson, Director of the National Research Council of Iceland, for official permission to conduct the data relay experiment in Iceland, and Gudmundur Pálmason and Sigurdur Thórarinsson for suggesting the Surtsey site for the DCP experiment.

DATA ANALYSIS

Temperature data

Under Landsat–1 experiment SR 251 (Friedman and others, 1973), the U.S. Geological Survey received from the Goddard Space Flight Center binary-coded punched cards, each card corresponding to a Landsat-relayed message, giving the Surtsey DCP number, day of year, time of message reception, and voltage levels for as many as eight channels (corresponding to thermistor-probe resistances) of the Surtsey thermistor array. A U.S. Geological Survey DEC–10 computer program converted the voltages to equivalent temperature values for the five thermistor probes that functioned throughout the experiment.

Originally, an eight-probe thermistor-array set was designed; data from this array are given in table 1 (engineering specifications for this system are given in the section "Instrumentation and System Technology"), and temperature data from channels 1, 2, 4, 5, and 7 are plotted as a function of time in figure 3. Air-temperature (channel 1), ground-surface temperature (channel 2), and two 1-m-probe subsurface-temperature thermistors (channels 4 and 7) yielded good-quality data of high confidence over a 38-day period. One-metre-probe data of channel 5 are essentially nonvarying and show too low a linear correlation (table 2) with the other two 1-m-probe curves to be regarded as reliable and are not analyzed in this report; channel-5 sensor malfunction is presumed to have generated spurious data.

Sample mean temperature (w), sample variance (S^2), and sample standard deviation (S), as well as coefficients of variation (C), are given in table 1. In the thermally anomalous area, air temperature and ground-surface temperature during this period showed a 78-percent linear correlation (table 2), using the method of Koch and Link (1970, p. 15–18). Comparison of correlation coefficients between channels 1 and 2 (air and surface temperatures) as a function of time gave maximum correlation on the same day (table 2). Air temperature showed only a 1-percent correlation with curves for 1-m depth (channels 4 and 7). Correlation of surface temperature (channel 2) with temperature curves for 1-m depth (channels 4 and 7) was 25–29 percent on the same day; calculation of thermal time-lag correlations for this sample set did not yield conclusive results when an attempt was made to correlate temperatures for one day with those for other days.

In assessing the comparative influence of 1-m depth and air temperatures on surface temperature, the dominant correlation on the same day was between air and surface temperature (78-percent linear correlation, table 2). On the other hand, 1-m depth temperatures seem to be 99 percent free of influence (that same day) from air-temperature fluctuations but show a 27-percent linear correlation with surface temperature. If free or open convective venting were the completely dominant mode of heat transfer to the surface, in view

TABLE 1.—*Air, surface, and 1-m-depth temperature, in degrees Celsius, recorded by Surtsey Data Collection Platform Station thermistor array, November 15 to December 25, 1972 (at approx 1400 hours local G.m.t.)*

[Constant voltage levels were recorded for channels 3, 6, and 8; see table 4]

Data Collection Platform channel	Temperature variable measured	Sample mean temperature (w)	Sample variance (S^2)	Sample standard deviation (S)	Coefficient of variance (C)
1	Air (1 m above ground)	2.45	10.61	3.26	1.33
2	Ground surface in anomalously warm area (T_0)	8.58	13.56	3.68	.43
4	1-m depth near instrument station (T_{100})	77.99	24.87	4.98	.06
5	1-m depth downslope from station (T_{100})	29.16	−0.51	.72	.02
7	1-m depth upslope from station (T_{100})	78.96	13.45	3.67	.05

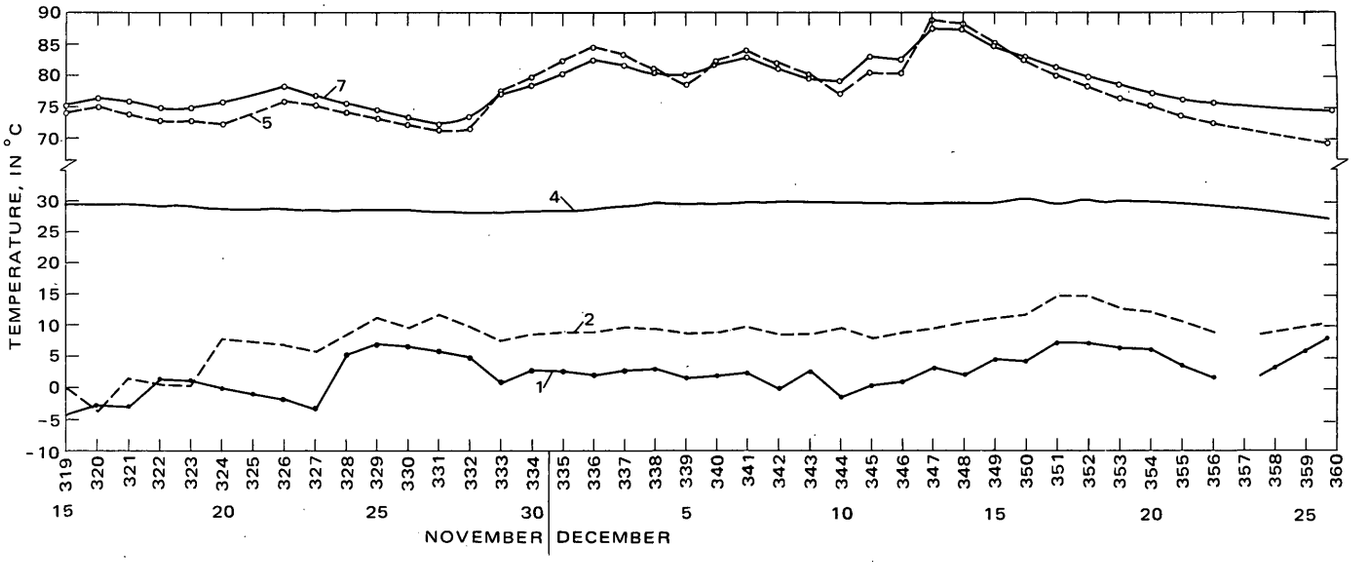

FIGURE 3.—Daily temperatures (°C) at approximately 1400 hours local Greenwich mean time from November 15 to December 25, 1972, as transmitted by Data Collection Platform 6056 from thermistor array in palagonitized tephra on Surtsey, Iceland, relayed by Landsat-1 and received by Data Collection System receiving station at Goddard Space Flight Center, Md. Channel 1, air temperature 1 m above the ground surface; channel 2, temperature of surface of palagonitized tephra; channel 4, temperature at 1-m depth at instrument station; channel 5, temperature at 1-m depth downslope from instrument station; channel 7, temperature at 1-m depth upslope from instrument station.

TABLE 2.—*Statistical correlation of temperature variations*

Data Collection Platform channels correlated	Temperatures correlated	Linear correlation coefficient (r) (1.00=100-percent correlation)	Confidence [2] (percent)
1 versus 2	Air T versus surface T (T_0)	0.779	>99
4	Air T versus 1-m depth (T_{100}) near station	.015	([3])
7	Air T versus 1-m depth (T_{100}) upslope	.009	([3])
2 versus 4	Surface T (T_0) versus 1-m depth (T_{100}) near station	.250	≈90
7	Surface T (T_0) versus 1-m depth (T_{100}) upslope	.292	93
4 versus 7	1-m depth (T_{100}) near station versus 1-m depth (T_{100}) upslope	.963	>99

[1] $r=\left[\frac{SS\,XY}{\sqrt{(SS\,X^2)\,(SS\,Y^2)}}\right]$ where $SS\,XY=\Sigma YX-\frac{\Sigma X\Sigma Y}{n}$; $SS\,X^2=\Sigma X^2-\frac{(\Sigma X)^2}{n}$; $SS\,Y^2=\Sigma Y^2-\frac{(\Sigma Y)^2}{n}$; and SS is the sum of squared deviations from the sample mean, n is the number of observations, X is the first variable (for example, air temperature), and Y is the second variable (for example, surface temperature).

[2] The linear correlation coefficient (r) can vary between the limits +1. Positive values of r indicate that the two variables are directly related; values approaching +1 indicate increasing linearity between the two variables; 0 implies no linear relationship whatsoever. To establish the confidence which may be put on the existence of a linear relationship indicated by the correlation coefficient, the probability that a relationship does not exist has been calculated. The inverse of the probability function is given as a percentage confidence that there is a linear relationship between the two data sets correlated and that it is not due to random chance. In analysis of geochemical data, confidence less than 90 percent has suggested that there is not a significant chance for a linear relationship; 90–95 percent is possibly significant; 95–99 percent is significant; over 99 percent there is a highly significant chance for existence of a linear relationship (Brooks, 1972, p. 140–141, 231).

[3] No confidence for this correlation; may be random.

of the known influence of barometric-pressure variations on vapor emission from geothermal surface manifestations, a greater degree of correlation might be expected between air and 1-m depth temperatures, due to fluctuations in barometric pressure. One-metre temperatures of channels 4 and 7 are 96 percent correlative with each other although channel 4 has a slightly greater amplitude of variation (0.06 coefficient of variation) than channel 7 (0.05 coefficient of variation). Note that the thermistor-probe types for channels 4 and 7 are very different; a nonlinear probe (that is, probe resistance is somewhat temperature dependent) having a rated accuracy of 0.5°C was used for channel 4; a linear probe of 1°C accuracy was used for channel 7.

The 0.69°C/cm vertical gradient in the first metre cannot be extrapolated accurately to greater depths, but the existence of this gradient suggests that there is a least a sizable conductive transfer component here. On the other hand, significant fluctuations in curves 4 and 7 (1 m), which indicate spasmodic increases or pulses in temperature, require convective venting as an explanation; this interpretation is discussed further in the next section. Both conduction

and convection appear to be important modes of transfer through the palagonitized tephra.

Interpretation of sample standard deviation of 1-m-depth temperature measurements based on repetitive measurements

Sample standard deviation (S) of 1-m depth temperatures (table 1) of 0.72 to 4.98 taken together with the high confidence (>99 percent) of correlation between curves for two 1-m-depth probes (table 2) suggest that the measured temperature variations of the order of 8–10°C at 1-m depth are true short-term temperature fluctuations. Such pulses can be accounted for by spasmodic emission of warm vapor through the tephra pile as a result of the driving-force effect of short-term variations in the geothermal flux or the pulling effect caused by fluctuations in barometric pressure and could not have been documented without repetitive temperature measurements.

GEOLOGIC AND GEOPHYSICAL INTERPRETATION

Convection through the tephra pile

Several lines of evidence suggest and virtually require a significant convective component of the total heat flow through the tephra pile.

1. Under suitable atmospheric conditions, vapor emission is visible from the Surtur II main vent and shield area about 200 m to the west and southwest. To the southeast and east (at a distance of 200–300 m) on the Surtur I tephra rim, lava-flow outcrops and hornitos (fig. 2) mark the position of extrusive outbreaks through the tephra along fractures that opened in 1967. Convection of hot vapors occurred and was recorded on infrared images as recently as 1968 (Friedman and Williams, 1970, p. D118) along linear and curvilinear zones in both of these areas. One might speculate that a similar subtephra dike-like intrusion (perhaps injected in 1969 when warming of the tephra rims was widely noted) is the heat source and accounts for the position of the local thermal anomaly monitored in this experiment. Extrapolating from these speculations, the upper surface of the subtephra heat source could be within 30 m of the surface.
2. Temperature fluctuations of the order of 10°–18°C at 1-m depth suggest convective pulses or spasmodic vapor emission through the tephra. The vapor emission may remove enough heat to spasmodically cool the tephra, thus accounting for the harmonic effect apparent in curves 5 and 7 (fig. 3).
3. The palagonitic alteration of the tephra involves (but is not limited to) hydration of the original glassy tephra pyroclasts which suggests hydrothermal alteration by moist warm or hot vapor, although palagonitization conceivably could occur through the action of warmed circulating meteoric waters.
4. The 69.4°C/m near-surface gradient, although requiring a large conductive flux, also suggests a significant convective flux. From an analysis of the variation of temperature according to depth in the Wairakei thermal area of New Zealand, Robertson and Dawson (1964) have shown that the change there from dominantly conductive to dominantly convective heat transport (that is, 50-percent energy partition) occurs where the mean annual temperature at a depth of 1 m is 25°C greater than the mean annual surface temperature. Although surface materials are more mafic at Surtsey than at Wairakei (and of greater density and higher thermal conductivity), permeabilities are high enough for free convection in both areas. Other conditions which affect the driving force of convection are no doubt different, but the high near-surface temperature gradient in itself suggests convection in addition to conduction.

Assessment of geothermal (volcanogenic) flux

Four methods were used to estimate the total heat flux in the thermally anomalous area where the DCP was emplaced. In all methods surface temperature (T_0) of the anomalously warm ground was determined statistically for November and December from analysis of temperature data derived by the DCP thermistor array. In methods 1 (assuming convection dominant) and 2 (assuming conduction dominant), DCP-derived 1-m-depth temperatures (T_{100}) were used. Methods 3 and 4, in which radiance from the surface is estimated, use DCP-derived surface temperature, statistical data found in the literature on Icelandic climatic factors, and estimates of thermal properties of the Surtsey surface materials based on comparison with similar materials for which thermal conductivity (k), thermal inertia (β), emissivity (ϵ), and albedo are known.

From least reliable (1) to most reliable (4), these methods (table 3) are as follows:

TABLE 3.—*Methods used to assess near-surface anomalous heat flux in palagonitized tephra, Surtsey, Iceland*
[DCP, Data Collection Platform]

Method	Description	Heat flux density, q, in microcalories per centimetre squared per second (=23.9·W m^{-2})
1. Assuming convection dominant.	On the basis of relation between T_0 and T_{100} mean values from DCP data, utilizing $q=1.24\ T_{15}^4\times10^{-6}$ cal m^{-2}s^{-1} and the relation between T_{100} and T_{15} established by Robertson and Dawson (1964) for dominantly convective areas.	*350
2. Assuming conduction dominant.	Conductive heat flow, based on Fourier equation $q=\frac{kA}{L}(t_1-t_2)$, minus that heat flow to surface on December 5, 1972, attributable to annual wave.	620–1,140
3. Anomalous radiance ----	Anomalous radiance, based on Stefan-Boltzmann function $W=\varepsilon 5.679\times10^{-12}(T_0^4-T_0{}^4)$ of warm surface minus radiance of cold surface, utilizing T_0 mean values from DCP data and statistical data on ground T_0 in Iceland.	850
4. Thermal modeling to determine net geothermal flux.	Thermal modeling to determine net geothermal emission, utilizing T_0 mean values from DCP data, statistical data on sea surface, T_0, sky radiance, and other parameters in geothermal model of Watson (1971).	780

*See section on "Evaluation of heat-flow methods for 1-m flux estimates on Surtsey" for a discussion of why this flux value is probably inapplicable.

1. Method 1 assumes convection is dominant and is based on the relation between mean values of T_0 and T_{100} (as defined above) for November and December, from DCP thermistor data, utilizing the empirical relationship $q=1.24\ T_{15}^4\times10^{-6}$ cal m^{-2}s^{-1}, where q is the total heat flux, and T_{15} is the temperature at 15 cm below surface (Dawson, 1964, p. 160), and the relation between T_{100} and T_{15} established by Robertson and Dawson (1964, p. 134–143) for areas of dominantly convective heat flow at Wairekei, New Zealand. The estimated flux at Surtsey by method 1 is 350 μcal cm^{-2}s^{-1}.
2. Method 2 assumes that conduction is dominant and is based on the Fourier equation for conductive heat flow (Gebhart, 1971), $q=\frac{kA}{L}(t_1-t_2)$, where k is the thermal conductivity in calories per square centimetre per second, A is the area in square centimetres, L is the length of section measured in centimetres, t_1 is the T_{100} temperature as derived from the DCP thermistor array, and t_2 is the T_0 temperature as derived from the DCP thermistor array. The excess heat flow to the surface attributable to the annual thermal wave in the November–December period is also taken into account. To model the annual wave, statistical data on T_0 and T_{100} temperatures throughout the year in Reykjavík, Iceland, were taken from Birkeland and Föyn (1932, p. 102). Thermal conductivity of the palagonitized tephra was estimated to range between 0.001 and 0.002 cal cm^{-1}s^{-1}, within the range of conductivities of typical volcanogenic soils, palagonitized tephra, and sintered tuff (Friedman, 1968, p. 80–81; Sukharev and others, 1975, p. 183). The estimated conductive flux by method 2 is 620–1,140 μcal m^{-2}s^{-1}, a range that thus indicates the uncertainty in thermal conductivity.
3. Method 3 assumes that excess or anomalous radiance from the surface is a rough measure of the heat flux if emissivity (ϵ) of the surface material is taken into account. The relationship for anomalous radiance,
$$\int_0^\infty W\mathrm{d}\lambda=5.679\times10^{-12}(T_0^4-T_0{}^4),$$
uses the Stefan-Boltzmann function (Reynolds and others, 1963, p. 6–153) for two surfaces: T_0, the warm surface derived from DCP thermistor data, and T_0, a hypothetical cold surface based on statistical ground-surface temperature data from Birkeland and Föyn (1932, p. 102), where $W\mathrm{d}\lambda$ is the power radiated per unit area. Integrated emissivity of the palagonitized tephra surface (ϵ) is estimated at 0.98 ± 0.02 by analogy with similar materials for which integrated emissivity is known.[2] The estimated anomalous radiant flux by method 3 is 850 μcal cm^{-2}s^{-1}.
4. Method 4, thermal modeling to construct parametric diurnal surface temperature curves to determine the net geothermal flux, is one of the more sophisticated methods available to the investigators in which DCP-derived T_0 values can be used. As developed by Watson (1971, 1975)

[2] That the apparent emissivity of surfaces of volcanic rock types approaches unity asymptotically with increased roughening was implied by the work of Gouffe (1945) who showed that the change in apparent emissivity of a surface is a function of cavity shape and integrated emissivity of cavity walls. More recent remote-sensing studies of volcanic rock surfaces (for example, Friedman, 1968) tend to confirm Gouffe's concept.

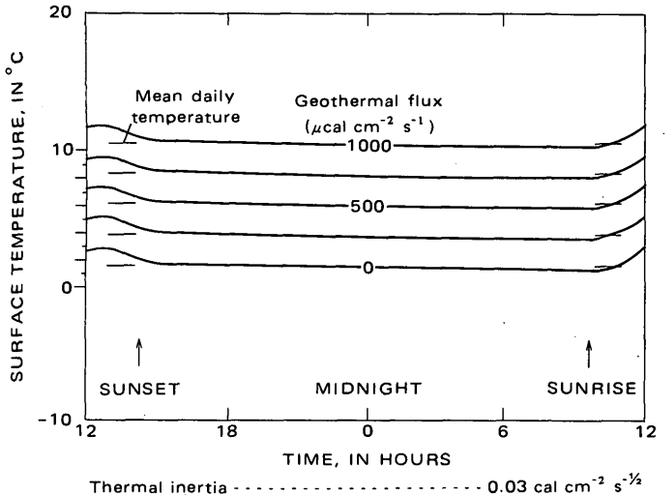

FIGURE 4.—Parametric diagram showing computed diurnal surface-temperature curves equivalent to specific geothermal-heat fluxes for December 5, 1972, at Data Collection Platform 6056 on palagonitized tephra. Surtsey, Iceland. Based on geothermal model of Watson (1971), for use with DCP thermistor-derived surface-temperature data.

for geothermal studies, the model used assumes one-dimensional periodic heating of a uniform half-space, conductive heat transfer in the ground, and radiative transfer in the atmosphere. The resulting diurnal temperature variation (fig. 4) is expressed as a function of geologic properties (albedo, thermal inertia,[3] emissivity, and geothermal flux); topographic properties (slope and azimuth); and solar-atmospheric properties (transmission, sky radiance, site latitude, solar declination, and cloud cover) (Watson, 1975, p. 136). The diurnal temperature variation is computed and plotted. The mean diurnal temperature, which is independent of the thermal inertia of the ground, can be used in conjunction with albedo measurements and topographic data to derive the geothermal flux (Watson, 1975, p. 136).

In applying the Watson thermal-modeling method, parametric diurnal surface temperature curves (fig. 4) equivalent to specific heat-flux levels were computed and plotted for the instrument station at Surtsey, December 5, 1972, the median date of the DCP measurements. Mean DCP surface-temperature data for 2400 hours local Greenwich mean time (G.m.t.) were used in conjunction with these curves because the curves are almost flat at that hour on December 5, that is, the diurnal temperature effect was then almost negligible. By comparison, simple nongeothermally influenced parametric diurnal temperature curves for the same locality on Surtsey are constructed as a function of solar declination in figure 5. The arrows indicate times of sunrise and sunset. These curves illustrate the overriding diurnal effect of solar radiation on surface temperatures of palagonitized tephra at Surtsey in the summer. It would have been more difficult to estimate the net geothermal flux at that time of year.

The computed net geothermal flux on December 5, 1972, by method 4 is 780 μcal cm^{-2}s^{-1}.

Evaluation of heat-flow methods for 1-m flux estimates on Surtsey

Method 1.—The use of the Robertson-Dawson empirical relationship for estimating convective flux where convection is the dominant mode of heat trans-

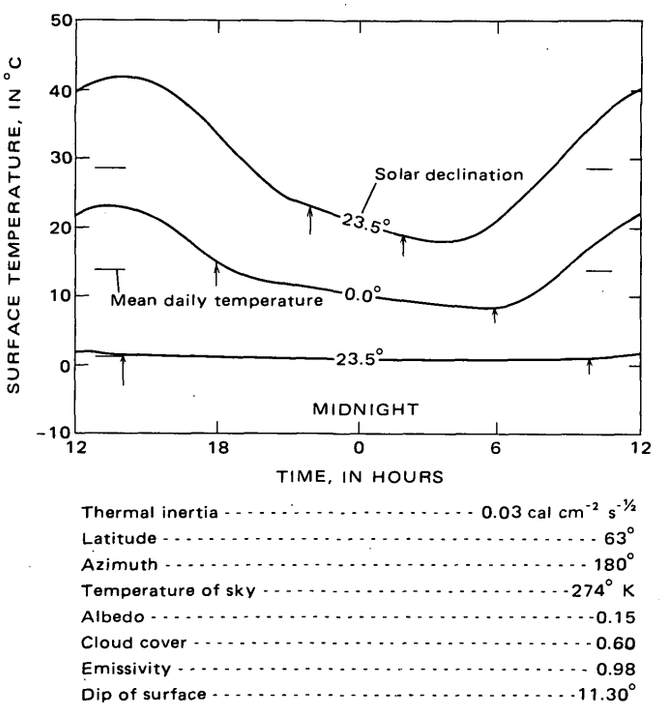

FIGURE 5.—Parametric diurnal surface-temperature curves as a function of solar declination, assuming thermal, physical, and geodetic parameters identical to those for Data Collection Platform 6056 instrument station, Surtsey, Iceland. Vertical arrows indicate time of sunset (left of O) and sunrise (right of O).

[3] Thermal inertia. β, a bulk property of materials, is a measure of the rate of heat transfer at the interface between two dissimilar media, that is, a measure of the resistance of a material to a change in temperature: β is equal to $(k\rho C)^{1/2}$, where k is thermal conductivity, ρ is mean density, and C is specific heat capacity. β is expressed in cal cm^{-2} s$^{-1/2}$ = 4.1868 × 10^4 J · m^{-2}s$^{-1/2}$.

fer is useful under conditions similar to those of Wairakei, New Zealand, that is, where the fracturing, porosity, permeability, and thermal properties of soils and silicic rocks, as well as heat-source strength, height and topography, are nearly the same. At Surtsey these variables are not fully analogous with their counterpart variables at Wairakei. The continuing process of palagonitization of originally unconsolidated basaltic tephra at Surtsey indicates the convective transfer of warm water vapor (of seawater or meteoric origin) through the tephra pile and suggests the applicability of the Robertson-Dawson method in which convection is assumed to be dominant. But the conductive-flux calculation of method 2 gives a flux three times as great, showing that this empirical convection-estimation method is inaccurate under the conditions prevailing at Surtsey.

Method 2.—In this experiment, the Fourier conduction estimate, though useful and probably accurate within a factor of two or three, is severly limited as an estimate of overall heat flux by at least the following four conditions: (1) Movement of water vapor through the tephra, as evidenced by the palagonitization process, indicates, as noted above, that heat transfer is not totally by conduction, but the exact energy partition is not known, (2) surface-temperature data for nongeothermal surfaces, required in application of the Fourier equation, were based on statistics for the period prior to 1932, (3) thermal conductivity of the palagonitized tephra is not precisely known, and (4) the vertical temperature gradient at depths below 1 m is not known.

Method 3.—The estimation of anomalous radiance is also limited by the use of data taken from the literature for the temperature of nongeothermal surfaces but does not depend on knowledge of the energy partition between conduction and convection. Moreover, method 3 has yielded a flux estimate close to that which resulted from use of the thermal-model method. This method of direct estimation of excess radiance is probably the best method available where access to a thermal-model computer program is not possible. It does not include heat lost to the atmosphere by evaporation.

Method 4.—Thermal modeling, judged the best heat-flux-estimation method available where only surface or near-surface temperature data are available and where a computer is accessible, adds several refinements to method 3. These include the effect of solar-atmospheric properties, thermal inertia of the ground surface, and topography on the diurnal temperature variation. Method 4 is limited by the significant error introduced by using several estimates or generalizations, including those for cloud cover, albedo of surface, and thermal conductivity of the palagonitized tephra. Like method 3, it does not include heat lost to the atmosphere by evaporation. The result is similar to that of method 3 but probably somewhat more accurate.

Interpretative results

Aside from technology development, transmission feasibility, and data-processing experiments inherent in this study and discussed in other sections, geologic and geophysical contributions were made in four general areas.

Process of palagonitization.—Palagonitic alteration of the basaltic tephra on Surtsey had been noted in 1969 by Jakobsson (1972). It was concluded that the palagonitization in Surtsey is a posteruptional process taking place at approximately 60°–100°C at the surface but at 100°C at depth, in the presence of abundant water. In 1971, only 3 years after the discovery of the thermal area, more than 12,000 m^2 of tephra had consolidated to tuff, and several hundred square metres had undergone palagonitic alteration. The alteration of the original sideromelane glass was found to have taken place by leaching of certain elements, mainly Na_2O, K_2O, CaO, and Al_2O_3; hydration of the glass; and oxidation of FeO. This is in good agreement with the results of Hay and Iijima (1968 p. 374) who studied palagonitic rocks from Hawaii and found that "a low-temperature, postvolcanic origin can be proven for some submarine palagonite and for the palagonite of tephra cones in Oahu, Oregon, and California."

Several workers have suggested for example, (Wentworth, 1938, p. 132) that palagonitization took place chiefly at the time of eruption. No such case, however, has been established for certain; on the contrary, all evidence seems to point to a posteruptional alteration. It is, however, clear that palagonitization can proceed under varying conditions and presumably with varying speed. Macdonald (1972, p. 194) states that palagonitization is largely the result of ordinary weathering. This statement can be substantiated by experience from Iceland. However, palagonitization probably proceeds very slowly under these circumstances because of very low temperatures. There is as yet no sign of alteration of the tephra outside the thermal area on Surtsey.

The thermal environment in which the palagonitization process is taking place on Surtsey is not that of ordinary weathering at ambient temperatures. The alteration is associated with mass transfer of hydrothermal vapor. Under these circumstances it is only a

matter of 1 to 2 years before dense palagonitic tuff is formed.

Geothermal flux variations.—The repetition of temperature measurements at 1-m depth over a 38-day period has identified a pattern of short-term vapor-emission pulses independent of diurnal or annual-wave variations on Surtsey and probably independent of surface-temperature influence. The vapor-emission pulses might be generated by the driving effect of deep-seated variations in the geothermal flux or might result from the "pulling" effect of reductions in barometric pressure, followed by the subsequent cooling of the tephra. Thus, in ascertaining near-surface temperatures of volcanogenic surface manifestations, the value of repetitive temperature measurements and statistical treatment of data is shown.

Postvolcanic decline in thermal emission.—The temperature data of 1972 provide a substantial basis for charting the magnitude of the postvolcanic decline in heat flow from the surface manifestations at Surtsey. An empirical comparison may be made between the 1972 near-surface heat-flow values reported here and the published estimate for 1969 (Friedman and Williams, 1970, p. D119). Nevertheless, it is not yet possible to construct comprehensive time-temperature-depth profiles for the thermally anomalous palagonitized tephra, because of the insufficient 1-m-depth temperature data prior to this study and the general lack of temperature data at greater depths. The construction of a comprehensive thermal model may be possible in the future after collection of additional temperature measurements at 1-m and greater depths.

Comparison of methods for assessment of near-surface thermal flux.—The results of the present study include a comparison of four methods for assessment of near-surface thermal flux where heat flows are of the order of 500–1,000 μcal $cm^{-2}s^{-1}$ and temperature data, albeit repetitive, are available for depths of only 1 m and the surface. The application to the same data set of the empirical Robertson-Dawson method for convection-dominanted systems, the Fourier conduction equation, the direct estimation of anomalous radiance, and the construction of parametric diurnal surface-temperature curves via thermal modeling has not been reported heretofore. The results suggest that thermal modeling is the most refined method available, and direct estimation of anomalous radiance is particularly useful where there is no access to a computer program for thermal modeling. All four methods are limited by the significant error introduced in approximating meteorologic conditions and thermal properties such as thermal conductivity.

INSTRUMENTATION AND SYSTEM TECHNOLOGY

The Landsat Data Collection System

The Landsat Data Collection System is designed to transmit samples of data from various types of sensors deployed on the Earth's surface to a central collection point by means of satellite radio relay (figs. 6 and 7). The system consists of a number of data formatter and transformer units called Data Collection Platforms (DCP), which accept and transmit sensor data to the satellite, a frequency translating reporter (that is, radio receiver and transmitter) on board the spacecraft, and two receiving stations at Goldstone, Calif., and Greenbelt, Md. The data are transmitted from the receiving stations by direct transmission to to the Goddard Space Flight Center where they are screened for quality, converted to a computer-compatible format, and distributed to the principal investigators in the Landsat experiment program.

Data are relayed through the system when the spacecraft is in mutual view of the DCP and the receiving station (figs. 7, 8). The DCP was designed to transmit one data sample every 3 minutes and mutual visibility theoretically must exist for at least 3 min to insure that one transmission is successfully relayed. The original system analysis and specifications prior to launch of Landsat–1 were conservative and predicted a coverage area of the conterminous United States, southern Canada, Mexico, and nearby Atlantic, Pacific, and Caribbean locations. Initial test transmissions from the Surtsey DCP installation verified that actual coverage could be considerably greater than the design specifications. Performance data from the Surtsey installation indicate that successful collection of data can occur from DCP's located as distant as 4,800 km from either NASA receiving station, provided appropriate steps are taken during installation of the DCP transmitter unit at the experiment site to increase the probability of transmission to the satellite.

The extended coverage (that is, increased probability of data relay) represented by the Surtsey DCP installation resulted from (1) decreasing the transmission repetition interval to 90 s, (2) lowering the antenna angle so that the radiation pattern would cover the horizon towards the southwest, and (3) increasing radio output power (10 watts instead of 5 watts) in the manufacture of DCP's over that used in the original system analysis.

Surtsey thermal instrumentation

In November 14, 1972, temperature measuring instruments (fig. 9) and a DCP (fig. 10) were installed on Surtsey by a team consisting of Sveinn Jakobsson,

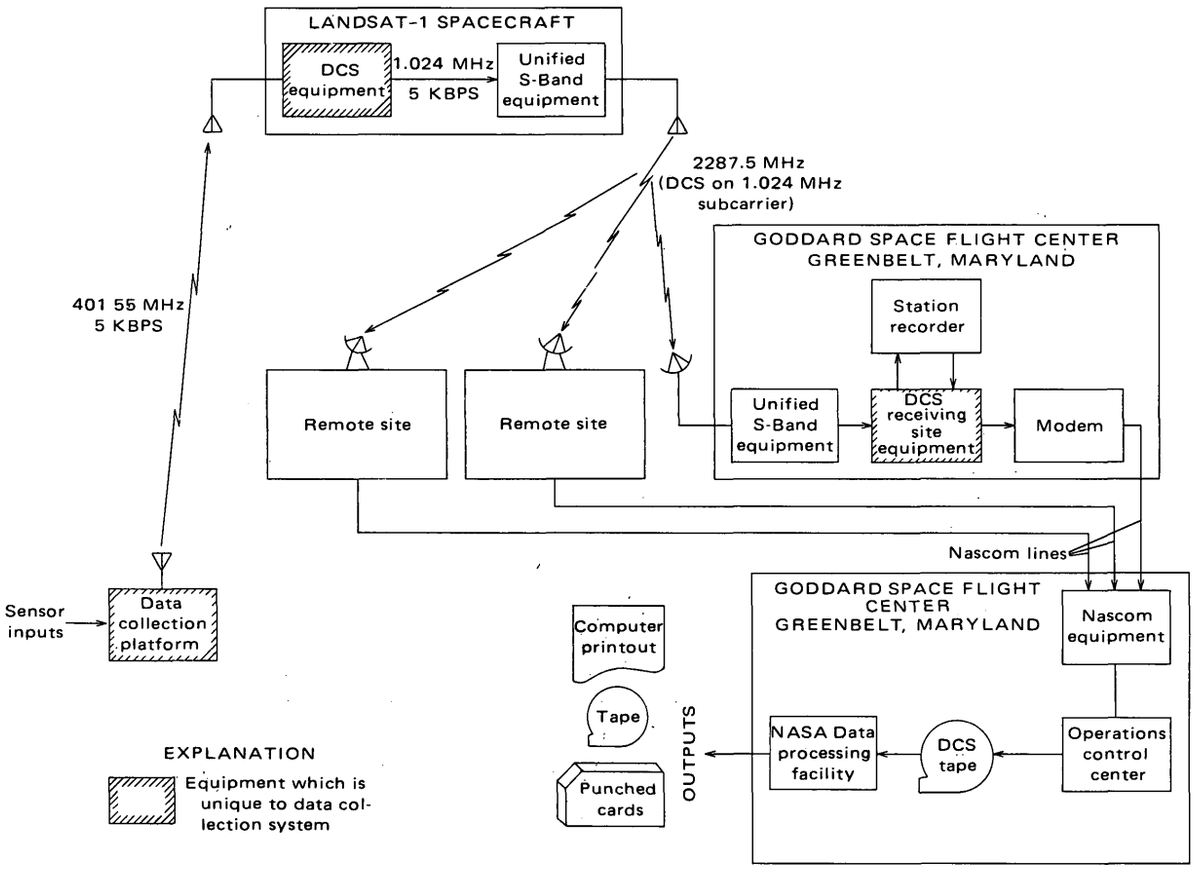

FIGURE 6.—Data Collection System (DCS) block diagram. Modified from National Aeronautics and Space Administration (1971). KBPS, kilobits per second; Mhz, megahertz; MODEM, modulator/demodulator; NASCOM, NASA Communications Network.

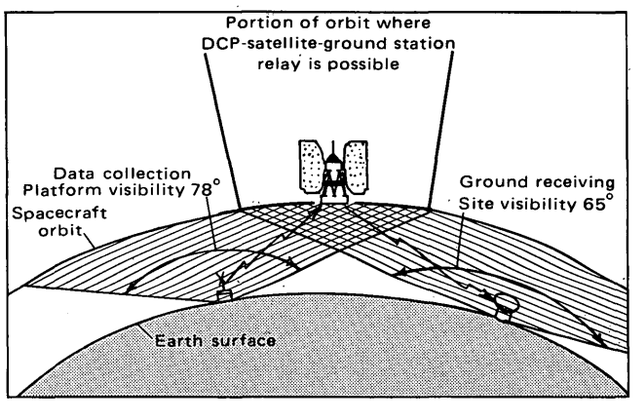

FIGURE 7.—Data Collection System data-relay geometry showing sector of mutual visibility. Modified from National Aeronautics and Space Administration (1971).

Jón Sveinsson, Duane Preble, Jules Friedman, and the helicopter pilot, Andri Heidberg (fig. 11). Original plans included transmission of eight temperature measurements twice daily over the Landsat–1 DCS and recording the measurement on paper tape every 32 hours. Figure 10 shows the basic system layout. This system transmitted data successfully and without interruption from November 14 until December 22, 1972, after which there was a hiatus until December 25 when transmission was resumed for 1 day, the last transmission from the Surtsey station received at Goddard Space Flight Center. At that time, North Atlantic gale-force winds destroyed the antenna and damaged the electronic circuit of the transmitting station. The station could not be repaired during the ordeal of the Icelandic winter of 1972–73. The only staging area in the Vestmannaeyjar archipelago, which the authors used when installing the DCP station on Surtsey by helicopter, the airstrip on the island of Heimaey, and all helicopter support, were subsequently unavailable during the Kirkjufell volcanic eruption at Heimaey that began in late January 1973.

The eight thermistor probes and their ranges are one air-temperature probe (−25°C to 25°C), two geothermal ground-surface probes (−25°C to 25°C), and five probes measuring temperature at 1-m depth at the geothermal site (0°C to 100°C). Table 4 gives

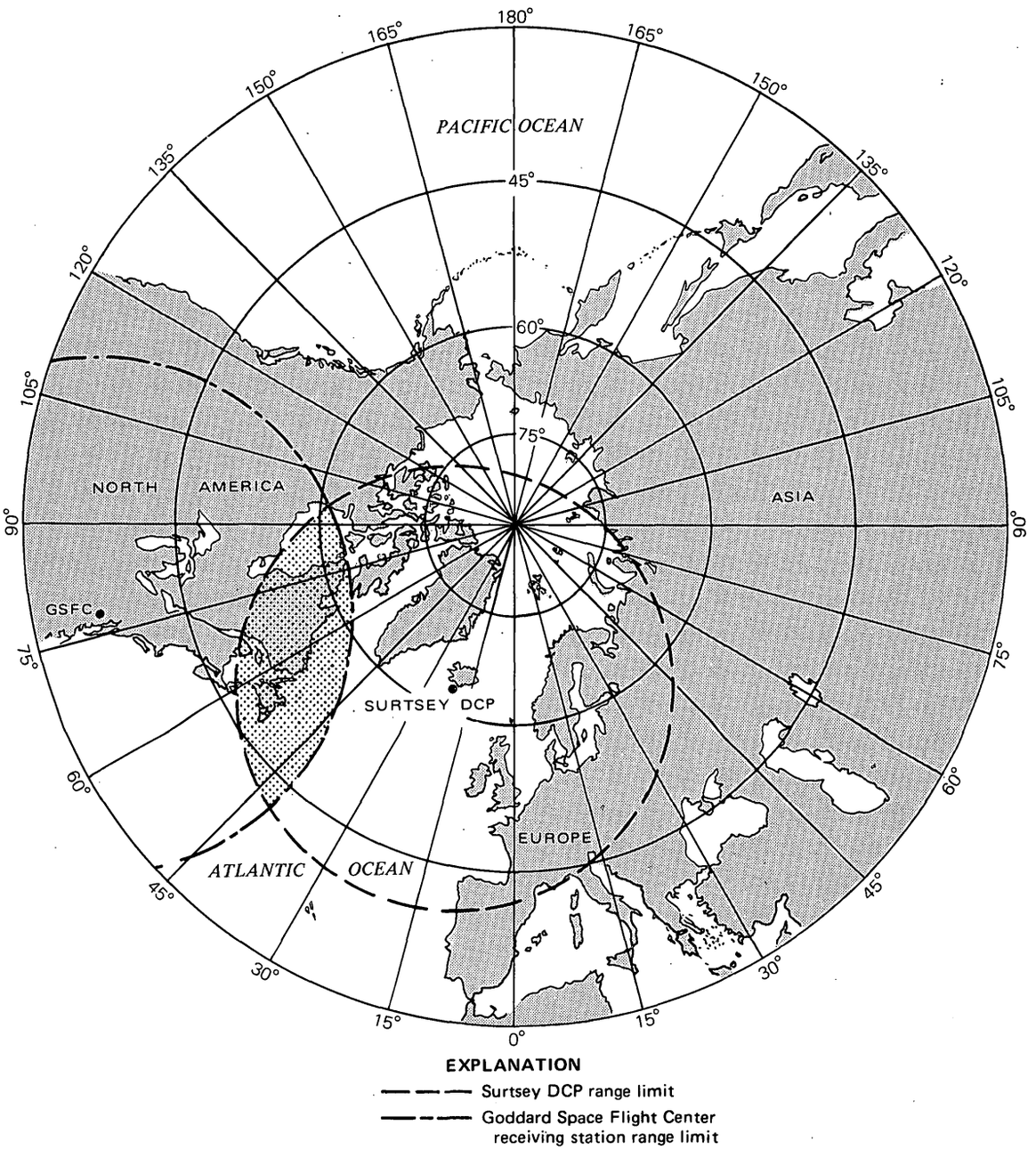

FIGURE 8.—Gnomonic projection of the northern hemisphere showing the zone of overlap of transmission range of Data Collection Platform 6056 from Surtsey, Iceland, and reception range of receiving station at Goddard Space Flight Center (GSFC), Md., at Landsat-1 orbital altitude of 926 km. Landsat-1 passes over shaded area at least twice daily, providing mutual visibility and successful data relay between Surtsey and GSFC.

the variables and their ranges during the field operation of the system. Linear thermistor networks (except for the thermistor for channel 4 whose relationship between voltage output and temperature is shown in fig. 12) encapsulated in stainless steel rods and prisms were used as the basic sensors. Stainless steel rods 1 m long were used for the geothermal depth probes; stainless steel prisms, 2.5 by 2.5 by 12 cm, were used for ground-surface sensing; and a stainless steel tube, 1 by 8 cm, sheltered from the wind and Sun, was used for the air-temperature thermistor mount. Each probe has a mating signal conditioner which, when power is applied, converts a full-scale probe-temperature change to a full-scale voltage range of 0 to 5.0 volts.

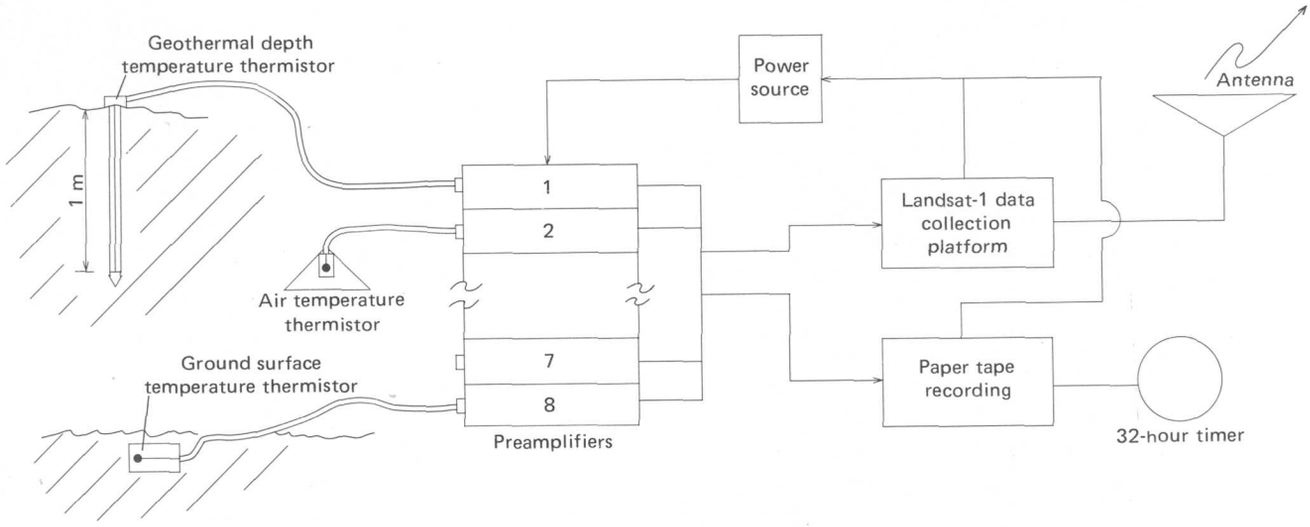

FIGURE 9.—Surtsey thermal instrumentation block diagram.

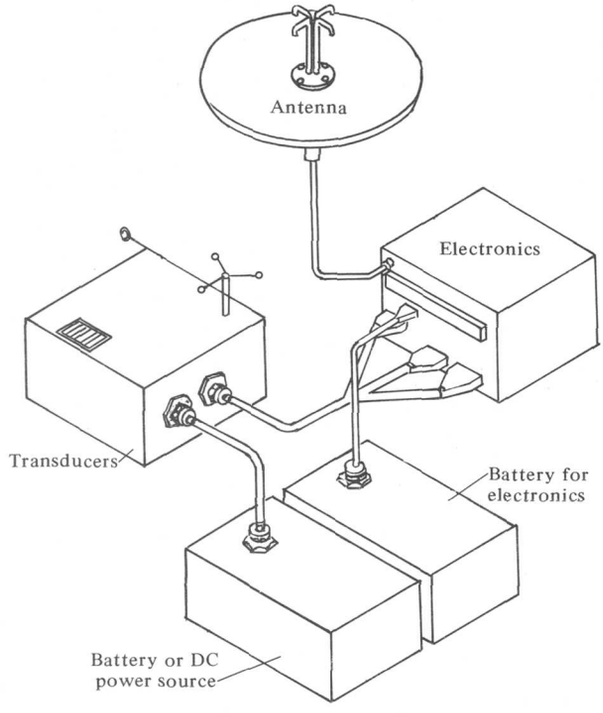

FIGURE 10.—Data Collection Platform block diagram. Modified from National Aeronautics and Space Administration (1971).

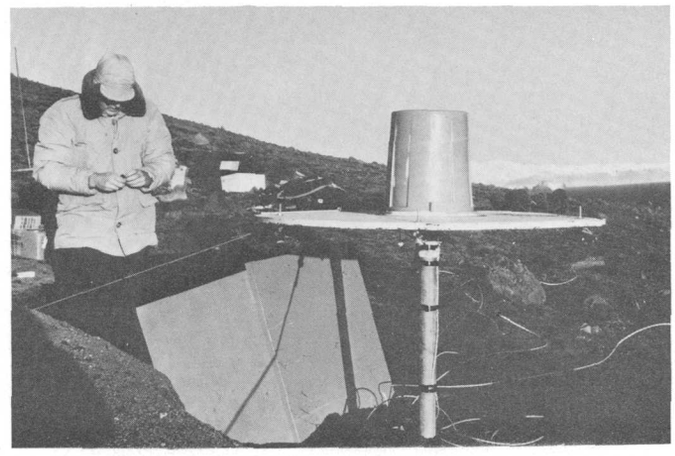

FIGURE 11.—Installation of Data Collection Platform and thermistor array on Surtsey, November 14, 1972.

The Landsat Data Collection Platform on Surtsey transmitted a 38-millisecond (ms) message every 90 s that included data from eight analog channels. Thirty-eight milliseconds prior to each transmission, the sensor preamplifiers were turned on by command from the DCP. Total operating time for the sensors was about 80 ms per transmission period. This low-duty cycle allowed a 5- to 8-month battery life using about 16 kg of alkaline batteries. Between November 15 and December 25, 1972, transmissions were regularly received twice daily. This station represented, at the time of its operation, the greatest spatial range over which the Landsat DCS had successfully communicated.

A 16-channel paper-tape recording system was operated as a backup to the DCP transmitter and yielded parallel data. The eight temperature parameters were recorded once every 32 h. A 32-h cycle gave three different daily recording times spaced 8 h apart, recurring on a 3-day cycle. Independent of the DCP and on command from the backup recording system timer, the sensor preamplifiers were turned on and the measurements sequentially punched on paper tape. After the last data point, which is a reference voltage level used for a system check, the recording system and

TABLE 4.—*Surtsey Data Collection Platform 6056 thermistor array*
[N.A., not applicable]

Data Collection Platform channel	Thermistor probe type [1]	Parameter measured	Relationship between voltage readout and temperature (V to T° C)	Temperature range (°C)	Accuracy (°C)
1	[1] YSI 44203	Ambient (air) temperature (T) 1 m above ground (protected from Sun)	T=−25+10(V)	−25 to 25	±1
2	YSI 44203	Ground-surface temperature (T_0)	T=−25+10(V)	−25 to 25	±1
3	YSI 44201	Blank (reads 3.43 V)	N.A.	N.A.	N.A.
4	YSI 30K44008	1-m depth T (T_{100}) near station	T=39.07+13.71(V)	45 to 110	±0.5
5	YSI 44201	1-m depth T (T_{100}) downslope	T=20(V)	0 to 100	±1
6	YSI 44201	Blank (reads 2.40 V)	N.A.	N.A.	N.A.
7	YSI 44201	1-m depth T (T_{100}) upslope	T=20(V)	0 to 100	±1
8	YSI 44201	Blank (reads 1.44 V)	N.A.	N.A.	N.A.

[1] Thermistor probe types (YSI) from Yellow Springs Instrument Co.

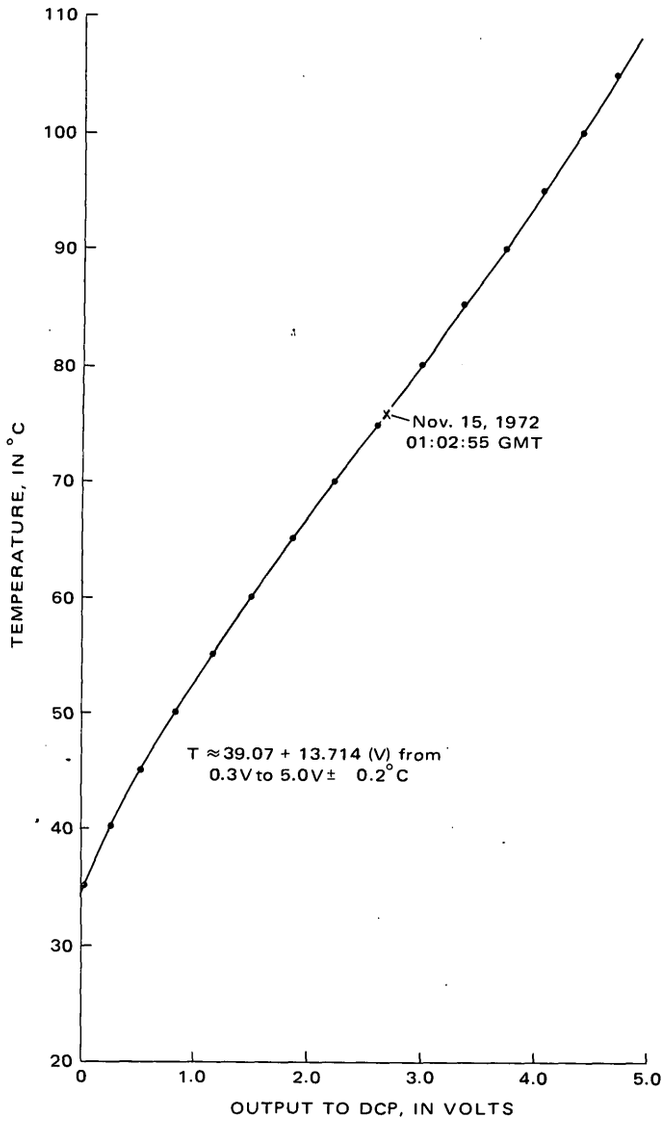

FIGURE 12.—Relationship between voltage output and temperature (T) for channel 4, Surtsey thermal monitoring instrument equipped with YSI thermistor network 44008 and electronic signal conditioner.

preamplifiers were shut off. Standby power consumption was about 2 milliwatts (70 microamperes at ≈13.4 volts).

The successful installation and message transmission demonstrated that heat-flow data may be collected in difficult and remote environments and reliably transmitted via a satellite relay system, such as the Landsat DCS, to a central receiving station.

COMMENTS ON USE OF DCP-TYPE STATIONS FOR SURFACE-TEMPERATURE MONITORING IN VOLCANIC AND GEOTHERMAL AREAS

In retrospect, several recommendations may be made based on the results of this experiment. If this experiment were to be repeated or a similar one carried out under the same conditions, the inclusion of a barograph-type sensor would help clear up the question of the atmospheric-pressure effect on the thermal-emission pulses.

A longer period of data accumulation would provide a better basis for linear correlation of data or regression analysis and might shed more light on the effect of the annual thermal wave. To accomplish this, a more rugged instrument station and antenna would be necessary in an environment as hostile as that of Surtsey.

To refine the comparison of the four thermal-flux determination methods, three steps could be taken:

1. The Fourier conduction estimate could be refined by (a) additional emplacement of a thermistor probe on a distinctly cool tephra surface, (b) emplacement of several thermistor probes at depths greater than 1 m, and (c) laboratory determinations of the thermal conductivity of the tephra.
2. The direct radiance and thermal-model flux determinations could also be refined by (a) emplacement of a thermistor (or, better yet, a recording radiometric sensor) on distinctly cool ground as

well as on warm ground surfaces, (b) use of a radiometric sensor to measure sea-surface temperature and concomitant sky radiance, and (c) installation of a memory or data-bunching and data-dumping system to permit a better spread of data during the diurnal cycle than is presently permitted by the semidiurnal overflight of the satellite. Such a system would permit the direct empirical construction of diurnal-temperature curves to check those deduced from the thermal model.

3. The spectral radiance and thermal-model flux estimation methods should be modified to include heat lost to the atmosphere by evaporation.

CONCLUSIONS

1. The feasibility of successful transmission of semidiurnal thermistor-derived temperature data from Iceland to the Goddard Space Flight Center, Md., via the Landsat Data Collection System for a distance of almost 5,000 km was demonstrated by this Surtsey experiment.
2. Temperature data for a 38-day period in November and December 1972 showed that in a thermally anomalous area in palagonitized tephra, surface-temperature fluctuations were 78 percent correlative with air-temperature variations and 27 percent correlative with temperatures at 1-m depth, whereas 1-m-depth temperatures were only 1.5 percent correlative with air-temperature variations. A near-surface vertical gradient of 69.4° C/m suggests a mixed mode of heat transport partitioned between conductive and convective mechanisms of transfer.
3. Anomalous-radiance methods of estimating the net geothermal flux, especially the computerized thermal-modeling technique of Watson (1971, 1975), using surface temperatures and concomitant thermal properties and geodetic data, are judged superior to methods assuming dominant convective or conductive transfer where only surface and 1-m temperatures are available. The net geothermal flux through palagonitized tephra in the vicinity of the DCP instrument station on Surtsey is estimated to be 780 ± 325 μcal $cm^{-2}s^{-1}$ excluding heat lost to the atmosphere by evaporation.
4. The heat flux through the Surtur I and Surtur II tephra piles, now in part palagonitized, has declined since 1969 when a heat-flux estimate of 1,500 μcal $cm^{-2}s^{-1}$ (Friedman and Williams, 1970, p. D119) was obtained. The present estimate of 780 ± 325 μcal $cm^{-2}s^{-1}$ may be useful as a reference level for evaluating the volcanogenic or geochemical significance of any future increase or decrease of heat flow in this area.
5. The limited accuracy of the heat flux obtained in the present experiment is largely the result of the necessity of using estimated or literature data for several parameters, that is, for nonthermally anomalous ground-surface temperature, thermal conductivity (k) of the palagonitized tephra, mean cloud cover, and sky radiance. The sample standard deviation of 325 μcal $cm^{-2}s^{-1}$ is perhaps equivalent to the accuracy of the heat flux obtained owing to these uncertainties. Heat lost to the atmosphere by evaporation should also be considered. Thermistor accuracy and DCS limitations would and an additional uncertainty of 240 μcal $cm^{-2}s^{-1}$.
6. Carrying out the experiment in the November–December period in Iceland in preference to seasons of greater diurnal change in surface temperature probably increased the accuracy of the result.
7. The thermal environment in which the palagonitization process is taking place on Surtsey is not that of ordinary weathering at ambient temperatures. Glassy tephra pyroclasts in the cones of Surtsey are presently undergoing palagonitization subaerially via mass transfer of hydrothermal vapor of seawater or meteoric origin associated with late-volcanic and postvolcanic thermal emission at the flux levels stated above.

REFERENCES CITED

Birkeland, B. J. and Foyn, N. J., 1932, Klima von Nordwesteuropa, *in* Handbuch der Klimatologie: v. 3, pt. L, 124 p.

Brooks, R. R., 1972, Geobotany and biogeochemistry in mineral exploration: New York, Harper and Row, 290 p.

Dawson, G. B., 1964, The nature and assessment of heat flow from hydrothermal areas: New Zealand Jour. Geology and Geophysics, v. 7, no. 1, p. 155–171.

Friedman, J. D., 1968, Thermal anomalies and geologic features of the Mono Lake area, California, as revealed by infrared imagery: U.S. Geol. Survey open-file rept., 84 p.

Friedman, J. D., Frank, D., Preble, D. and Painter, J. E., 1973, Thermal surveillance of Cascade Range volcanoes using ERTS 1 multispectral scanner, aircraft imaging systems, and ground-based Data Communications Platforms, *in* Symposium on significant results obtained from the Earth Resources Technology Satellite 1: NASA SP–327, v. 1, p. 1549–1560.

Friedman, J. D. and Williams, R. S., Jr., 1970, Changing patterns of thermal emission from Surtsey, Iceland, between 1966 and 1969, *in* Geological Survey research 1970: U.S. Geol. Survey Prof. Paper 700–D, p. D116–D124.

Friedman, J. D., Williams, R. S., Jr., Palmason, Gudmundur, and Miller, C. D., 1969, Infrared surveys in Iceland—

preliminary report, *in* Geological Survey research 1969: U.S. Geol. Survey Prof. Paper 650–C, p. C89–C105.

Gebhart, B. J., 1971, Heat transfer: New York, McGraw-Hill, 2d ed., 596 p.

Gouffe, Andre, 1945, Corrections d'ouverture des corps-noirs artificiels compte tenu des diffusions multiples internes: Rev. d'Optique Theorique et Instrumentale, v. 24, no. 1–3, p. 1–10.

Hay, R. L., and Iijima, A., 1968, Nature and origin of palagonite tuffs of the Honolulu Group on Oahu, Hawaii, *in* Coats, R. R., and others, eds., Studies in volcanology; a memoir in honor of Howell Williams: Geol. Soc. America Mem. 116, p. 331–376.

Jakobsson, S. P., 1972: On the consolidation and palagonitization of the tephra of the Surtsey volcanic island, Iceland: Surtsey Research Progress Rept. 6, p. 121–128.

Koch, G. S., Jr., and Link, R. F., 1970, Statistical analysis of geological data: New York and London, John Wiley and Sons, v. 1, 374 p.; v. 2, 438 p.

Macdonald, G. A., 1972, Volcanoes: Englewood Cliffs, N. J., Prentice-Hall, 492 p.

National Aeronautics and Space Administration, 1971, Earth Resources Technology Satellite data users handbook: NASA Goddard Space Flight Center, 218 p.

Norrman, J. O., 1970, Trends in postvolcanic development of Surtsey Island; progress report on geomorphological activities in 1968: Surtsey Research Prog. Rept. 5, p. 95–112.

Reynolds, M. M., Corruccini, R. J., Fulk, M. M., Burley, R. M., 1963, Radiometry, *in* Gray, D. E., coord. ed., American Institute of Physics Handbook: New York, McGraw-Hill Book Co., p. 6-153–6-156.

Robertson, E. I., and Dawson, G. B., 1964, Geothermal heat flow through the soil at Wairakei: New Zealand Jour. Geology and Geophysics, v. 7, no. 1, p. 134–143.

Sukarev, G. M., Taranukha, Y. u. K., and Zhitskii, P. Ya., 1975, Teplofizicheskiye svoystva spekshikhsya tufov rayona Vardziya, Yuzhnaya Gruziya (verkhov'ye reki Kury i lischel'ye reki Paravani) [Thermophysical properties of sintered tuff in the area near Vardziya, southern Georgia, along the upper reaches of the Kura River and in the gorge of the Paravani River]: Akad. Nauk. SSSR Doklady, v. 220, no. 1, p. 182–184.

Thorarinsson, Sigurdur, 1968, Sidustu thætir eyjælda [The last phases of the Surtsey eruption, with English summ.]: Náttúrufrædingurinn, v. 38, p. 113–135.

Watson, Kenneth, 1971, A computer program of thermal modeling for interpretation of infrared images: U.S. Geol. Survey Rept. USGS–GD–71–023, 33 p.; available from U.S. Dept. Commerce, Natl. Tech. Inf. Service, Springfield, Va., 22161, as Rept. PB–203–578.

——— 1975, Geologic applications of thermal infrared images: IEEE Proc., v. 63, no. 1, p. 128–137.

Wentworth, C. K., 1938, Ash formations of the Island Hawaii: Hawaiian Volcano Observatory, 3d Spec. Rept., 183 p.

Jour. Research U.S. Geol. Survey
Vol. 4, No. 6, Nov.-Dec. 1976, p. 661–665

A COMPARISON OF LANDSAT IMAGES AND NIMBUS THERMAL-INERTIA MAPPING OF OMAN

By HOWARD A. POHN, Denver, Colo.

Abstract.—Thermal-inertia maps can be used in conjunction with Landsat photographs to resolve ambiguous identification of lithologies in remote areas.

Thermal-inertia [1] mapping when used in conjunction with Landsat–1 provides an excellent supplement to geologic reconnaissance maps. Previously reported discrepancies (Pohn and others, 1974) between the U.S. Geological Survey reconnaissance geologic map of Oman and a thermal-inertia map (fig. 1) of the region based on data from Nimbus III and IV can now be largely resolved by comparing these maps with Landsat–1 images.

In the original study, Oman was selected as a test site because of large bare rock exposures having high thermal and reflectivity contrasts between individual lithologies. Very low annual precipitation and stable weather patterns added to the desirability of the site.

A thermal model constructed by Watson (1970a, b) was used to relate the reflectivity data from Nimbus III and the day and night temperature measurements from Nimbus IV (both having 8-km resolution) to a single parameter, thermal inertia. The thermal-inertia values corresponded closely to values from laboratory measurements of the various lithologies.

Several discrepancies were observed between the thermal-inertia map and the reconnaissance geologic map. Many of these differences were resolved when newer and more detailed maps were examined (fig. 2). The thermal inertias were consistent with the lithologies shown on these more detailed maps. Most of the discrepancies arose from the fact that the reconnaissance map had not included the presence of surficial materials (wadis, areas of eolian sedimentation versus deflation) or had portrayed units incorrectly.

A significant discrepancy, however, remained unresolved. The ophiolite belt (serpentinites, pillow lavas, gabbro, and diorite) which defines the axis of the Oman Mountains (from the northern boundary of the map to the area of the Jabal anticline at loc. 1, fig. 2, lat 23.4° N., long 57.4° E.) is shown on the reconnaissance map as a continuous zone of homogeneous material, whereas the thermal-inertia map shows the unit to be a heterogeneous series of highs and lows having a few very high anomalies.

Shortly after our previous paper went to press (Pohn and others, 1974), we received Landsat–1 images of the mapped area taken on October 5, 22, and 23, 1972. A mosaic of the images is shown in figure 3. It is immediately apparent, from this mosaic, that the ophiolite belt is, in fact, made up of discrete patches of low-albedo material within an area of intermediate-albedo material. The area of the latter material has an albedo, a texture, and a drainage pattern similar to the areas mapped as cherts and limestones. However, examination of the chert and limestone areas (intermediate-albedo material at localities A, B, and C on fig. 1) shows that the thermal inertia of the limestone (0.030–0.040 and, rarely, as much as 0.050 cal/cm^{-2}/s$^{-½}$) is generally lower than chert (0.040–0.060 cal/cm^{-2}s$^{-½}$). The thermal inertia of the material which surrounds the patches of ophiolitic rocks is clearly similar to the cherts and not the limestones. Thus, if the lithologies on the map are correct, the ophiolitic rocks almost certainly are erosional remnants on the widespread chert deposits.

The anomalies at localities D and E are of such high thermal inertia and low albedo that these areas are most probably unserpentinized dunite. The other materials having high thermal inertia and low albedo may represent varying degrees of either serpentinization in the ophiolitic rocks or mineralogic variation involving pyroxene and olivine.

The use of high-resolution albedo information from Landsat images in conjunction with lower resolution thermal-inertia data makes possible the definition of major lithologic boundaries. The step from discrimina-

[1] Thermal inertia is equal to $K\rho c$ (where K is the thermal conductivity, ρ is the density, and c is the specific heat) and is related more directly to the physical properties of surficial materials than are either reflectivity or temperature.

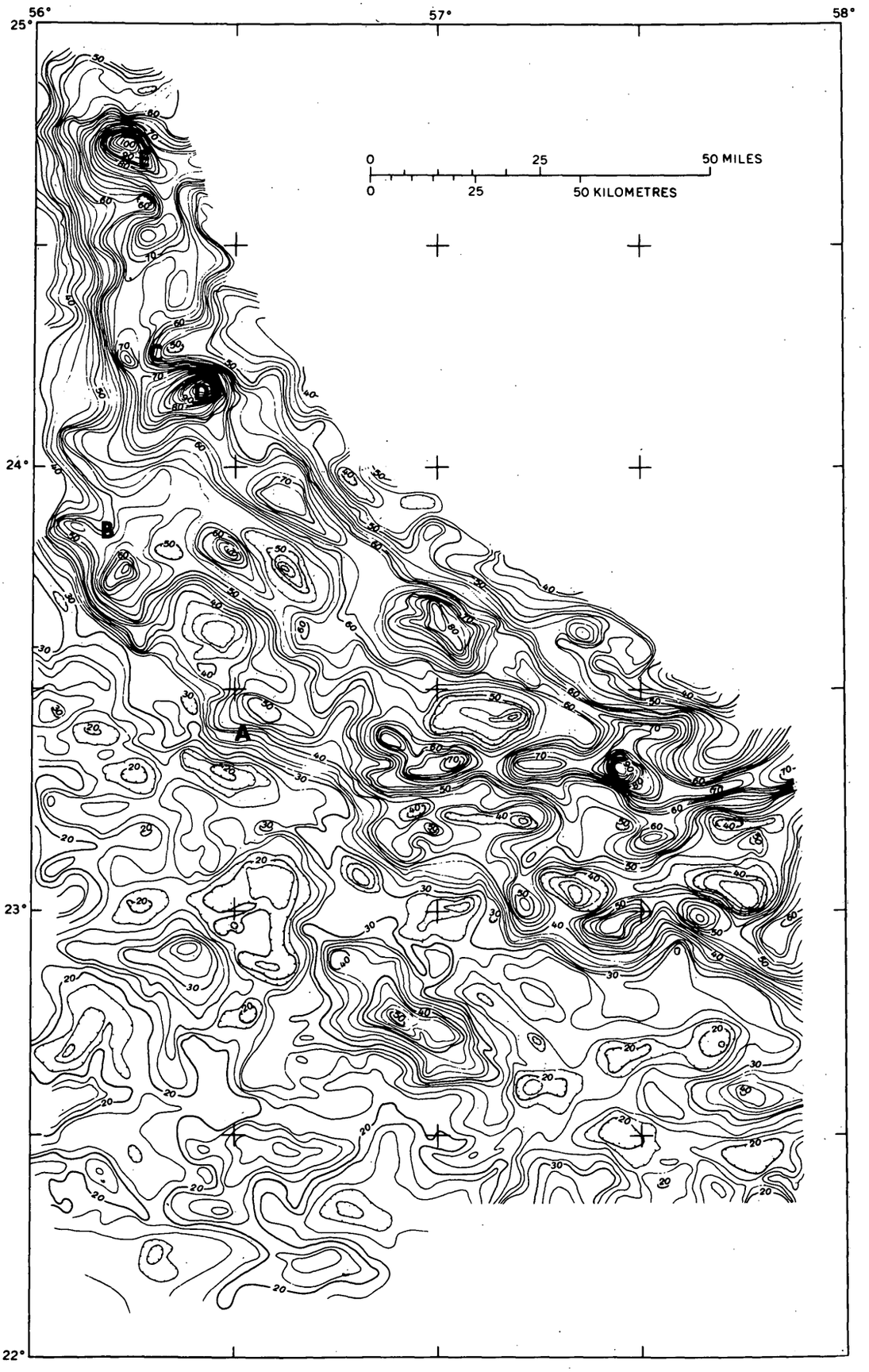

FIGURE 1.—Thermal-inertia map of a part of Oman. Contour interval 2×10^2 cal $cm^{-2}s^{-½}$. For true values multiply by 10^{-2}. (Reprinted from Pohn and others, 1974, fig. 5).

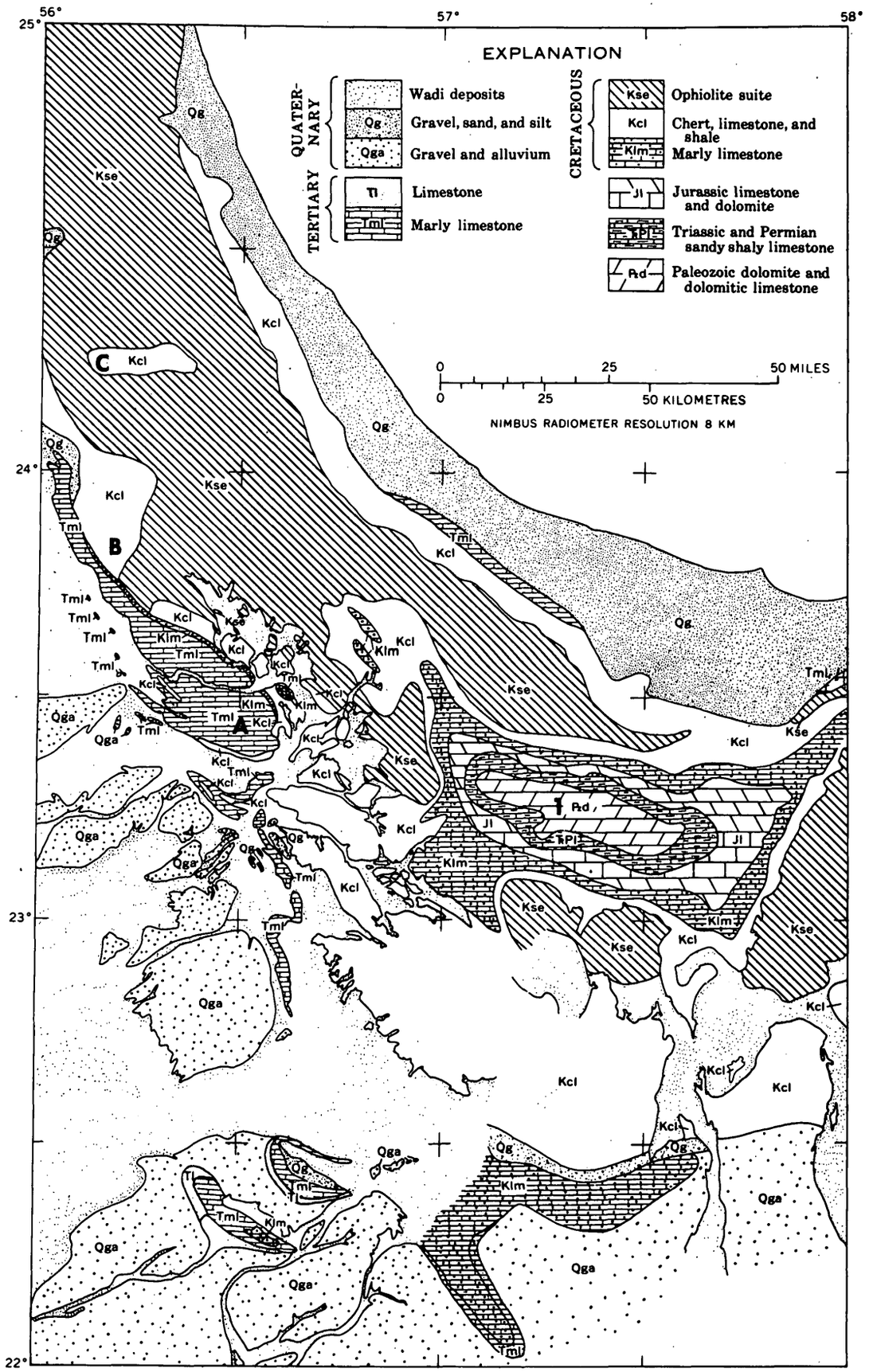

FIGURE 2.—Geologic map of a part of Oman. (Reprinted from Pohn and others, 1974, fig. 4.)

FIGURE 3.—Landsat–1 photomosaics of a part of Oman. The relative thermal inertias of the limestones and cherts can be seen by comparing the limestone at A with the cherts at B and C on figure 1. Photomosaic by Frank J. Sidlauskas, Jr.

tion to identification (a technique impossible when either type of data is taken separately) is of fundamental importance in the relatively unambiguous mapping of lithologies in remote or inaccessible areas.

REFERENCES CITED

Pohn, H. A., Offield, T. W., and Watson, Kenneth, 1974, Thermal inertia mapping from satellite—discrimination of geologic units in Oman: U.S. Geol. Survey Jour. Research, v. 2, no. 2, p. 147–158.

Watson, Kenneth, 1970a, Part A, Introduction and summary, and Part B, Data analysis techniques, *in* Remote sensor applications studies progress report, July 1, 1968 to June 30, 1969: U.S. Dept. Commerce, Natl. Tech. Inf. Service, PB–197 098, 62 p. [1971].

——— 1970b, A thermal model for analysis of infrared images: Natl. Aeronautics and Space Adm., 3d Ann. Earth Reources Aircraft Programs Rev., v. 1, sec. 13, 16 p.

Jour. Research U.S. Geol. Survey
Vol. 4, No. 6, Nov.-Dec. 1976, p. 667–682

GRAVITY STUDIES IN THE CAROLINA SLATE BELT NEAR THE HAILE AND BREWER MINES, NORTH-CENTRAL SOUTH CAROLINA

By HENRY BELL III and PETER POPENOE, Reston, Va.

Abstract.—The Bouguer gravity map of part of the Carolina slate belt near the Haile and Brewer mines in South Carolina shows anomalies related to rock units. The most conspicuous of the anomalies coincide with coarse-grained granitic plutons. Mathematically calculated models using an iterative three-dimensional solution of the gravity anomalies show that these plutons are steep-sided intrusive bodies that constrict at depth to small pipes or roots. The plutons are emplaced in and are probably largely confined to a unit of volcaniclastic rocks. The volcaniclastic rocks are probably 6,000 m to 10,000 m thick and similar in composition to those exposed in the vicinity of the plutons.

The Bouguer gravity anomaly map of the United States by G. P. Woollard and H. R. Joesting (American Geophysical Union, 1964) shows a broad gravity high trending northeast through the central Piedmont of North and South Carolina. The Haile-Brewer gold mining area in South Carolina is on this major Appalachian feature. Because this part of South Carolina has low topographic relief and because the rocks are poorly exposed, the geologic setting, and particularly the geologic structure, has been difficult to determine. Information about the structural setting of the mines, however, is important in aiding continued investigations of the mines and in the search for additional ore deposits. One source of significant information about the subsurface shapes of the coarse-grained upper Paleozoic granitic plutons and the other rocks in the Haile-Brewer area is the simple Bouguer gravity map of the part of the Carolina slate belt in this area (Popenoe and Bell, 1975). This map shows conspicuous gravity anomalies, most of which are clearly related to geologic rock units. Mathematically calculated models based on the contrast in density between rock units exposed at the surface can reconcile various geologic interpretations that would account for the shapes and distribution of masses revealed by the Bouguer gravity map. This approach, using the methods described by Cordell and Henderson (1968), has been applied to the granitic plutons in the Haile-Brewer area. Figure 1, part of the Bouguer anomaly map of the United States (American Geophysical Union, 1964), is an index map showing the location of the more detailed map of the Haile-Brewer area as well as the location of the nearby Lilesville area in southern North Carolina studied by Waskom and Butler (1971).

GEOPHYSICAL SETTING

Regional setting

A simple Bouguer gravity map of the Haile-Brewer area derived from the map of Popenoe and Bell (1975) and the Lilesville area in North Carolina studied by Waskom and Butler (1971) is shown in figure 2. Both areas are in the Carolina slate belt which trends northeast through the central Piedmont. The broad gravity high (fig. 1) on which these two areas are located is bounded on the west by a steep gradient near Charlotte, N.C., that becomes less pronounced in South Carolina. This gravity high may be offset about 20 miles (32 km) to the southeast, where a steep gradient is shown on the map of the Haile-Brewer area (fig. 2). The east side of the regional high-gravity anomaly is marked by a gradient of less relief extending from near Columbia, S.C., and Laurinburg, N.C. through Raleigh, N.C. (fig. 1). This gradient is shown in the southeast corner of the Haile-Brewer map (fig. 2).

Local setting

Most of the features revealed by the gravity data are clearly related to geologic rock units. Figure 3 is a geologic map compiled from Overstreet and Bell (1965) and Stuckey (1958) and modified from many more recent sources, particularly Randazzo, Swe, and Wheeler (1970), Waskom and Butler (1971), McSween (1972), Nystrom (1972), and the authors' present work. The anomalies shown on the Bouguer anomaly map (fig. 2) include two large gravity minima near the center of the map. The outcrop area of the quartz monzonite in the Liberty Hill pluton coincides closely

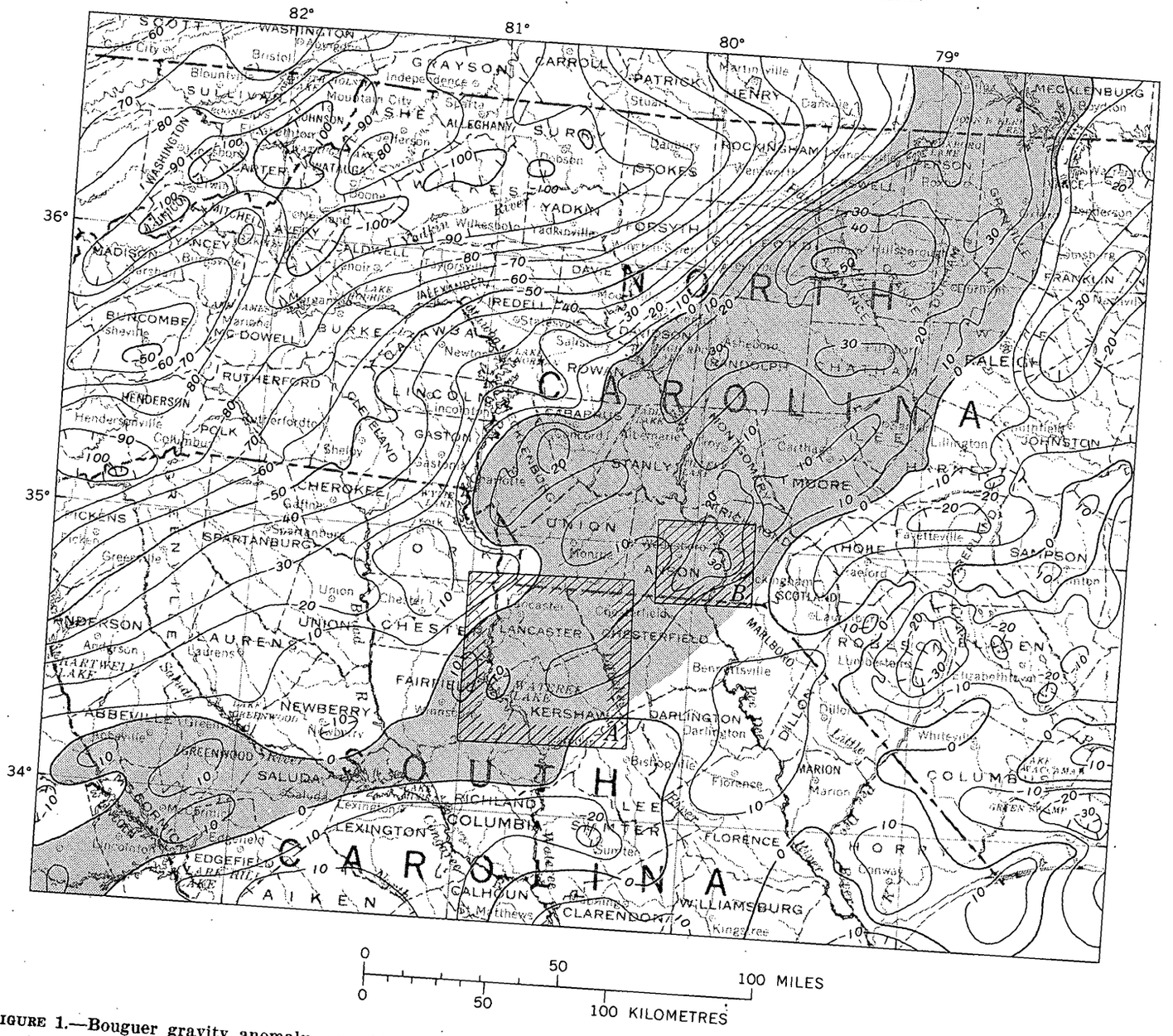

FIGURE 1.—Bouguer gravity anomaly map (American Geophysical Union, 1964) showing the central Piedmont gravity high (stippled) and the location of detailed gravity studies in South Carolina and North Carolina. *A*, Haile-Brewer area (this report); *B*, Lilesville area (Waskom and Butler, 1971). Contour interval, 10 milligals. Bouguer reduction density, 2.67 g/cm^3.

with the westernmost of the two anomalies, and the quartz monzonite in the Pageland pluton is clearly associated with the eastern anomaly. The outcrop area of the Pageland pluton, however, coincides with only a part of the area indicated by the gravity pattern to be underlain by low-density rock.

Near the western edge of the area, a gravity high shown on the Bouguer anomaly map (fig. 2) closely coincides with the outcrop pattern on the geologic map (fig. 3) of the Dutchmans Creek Gabbro of Mc-Sween (1972). Between the Liberty Hill pluton and the Pageland pluton, the Bouguer anomaly map shows a gravity high believed to be related to a poorly known and poorly outcropping gabbro. The gravity high may also be associated with a porphyritic mafic rock which has been seen only as stream cobbles near the gravity anomaly.

The steep gradient reaching a gravity minima of −30 milligals (mGals) shown in the northwest corner of figure 2 may be, in part, the gradient that marks

the west side of the Piedmont gravity high (fig. 1), where it is offset to the southeast in South Carolina. Granitic plutons nearby in South Carolina, but beyond the area shown in figures 2 and 3, may have locally modified the gradient. The depth to the source of the gradient in North Carolina, where it is well expressed northeast of Charlotte, has been discussed by Best, Geddes, and Watkins (1973). This gradient in South Carolina also seems to coincide with the transition from low-grade metamorphic rocks in the Carolina slate belt to higher grade metamorphic rocks in the Charlotte belt.

In the southern part of the Bouguer anomaly map (fig. 2) is a series of northeast-trending gravity lows in an area covered by sedimentary rocks of the Coastal Plain. The gravity gradient separating these lows from higher gravity to the north, where rocks of the Carolina slate belt crop out, is the southeast margin of the Piedmont gravity high (fig. 1). The gravity gradient also coincides with a similar gradient in both regional and detailed magnetic data (Taylor and others, 1968; U.S. Geological Survey, 1970). The gradient is believed to be a reflection of a major fault that crops out in the southwest corner of the map area (fig. 3) as a zone of mylonite and sheared rocks in the Carolina slate belt. Regional geophysical data indicate this to be an extension of a major fault that can be traced southwest across South Carolina into Georgia. The granitic plutons discussed in this report are emplaced into rocks of the Carolina slate belt.

GEOLOGIC SETTING

Carolina slate belt

In a broad sense the Carolina slate belt consists of a great thickness of volcanic and sedimentary rocks overlying and grading laterally into various granitoid gneisses, biotite-muscovite schists, and biotite-muscovite gneisses, often referred to as the Charlotte belt. Overstreet and Bell (1965a, b) inferred that all metamorphic rocks of the Piedmont in South Carolina could be divided into three great superimposed sequences of similar rocks, composed originally of sedimentary, pyroclastic, and extrusive materials, metamorphosed later to various degrees, and invaded many times by many varieties of plutonic and volcanic rocks. At the base of their middle sequence in the Carolina slate belt is a dark-green, gray, and black fine- to coarse-grained amphibolite, various mafic gneisses and schists, some diorite, metagabbro, and many basic dikes of several ages and relations. These mafic rocks probably represent a stratigraphic unit that helps to define the limbs of an anticline. The Liberty Hill and Pageland plutons are along the crest of this anticline. Overlying the mafic rocks are pyroclastic and volcaniclastic rocks (including agglomerate, breccia, tuff, and flows) that are predominantly felsic but that contain some mafic units. In the vicinity of Irmo and Winnsboro, southwest of the Haile-Brewer area (outside the area shown on fig. 3), these rocks have been described and divided into formations by Secor and Wagener (1968) who found them to be many thousands of feet thick.

In North Carolina, rocks of the Carolina slate belt are widely distributed. Stromquist (1966), Conley (1962a), Conley and Bain (1965), and Stromquist and Sundelius (1969) have mapped and described formations there that are also many thousands of feet thick. The lowest of these is a sequence of mostly felsic volcaniclastic rocks included in the Uwharrie Formation. The base of the Uwharrie Formation is not exposed in the area studied by Stromquist and Sundelius (1969), but they estimated the formation to be at least 20,000 feet (6,100 m) thick. In Randolph County, N.C., V. M. Seiders (oral commun., 1975) estimated a thickness for the formation of about 33,000 feet (10,000 m). The correlation of formations mapped in North and South Carolina is not established, but this great thickness of predominantly felsic volcaniclastic rocks in North Carolina seems likely to correspond in some way to the thick felsic volcaniclastic unit that overlies the mafic rocks at the base of the middle sequence of Overstreet and Bell (1965a, p. 10) in South Carolina.

In South Carolina, it is the felsic pyroclastic and volcaniclastic rocks that are gold bearing at the Haile and other nearby mines. These rocks are veined with quartz, hydrothermally altered, and contain massive sulfide deposits. Coarsely crystallized muscovite from hydrothermally altered areas dated by K-Ar methods as 415 and 358 million years (m.y.) old (Bell and others, 1972), indicates that this alteration and the associated mineralization preceded by a substantial length of time the emplacement of the nearby Carboniferous granitic plutons to which the mineralization had previously been tied (Pardee and Park, 1948). The alteration and mineralization, therefore, is more likely to be related to the volcanism that produced the pyroclstic and volcaniclastic rocks than to processes related to the emplacement of the granitic plutons.

The uppermost rocks of the Carolina slate belt in the Haile-Brewer area are gray and greenish-gray argillite or slates and graywacke. In hand specimen, some of these resemble the Tillery Formation, which is the lowest formation of the Albermarle Group in North Carolina and overlies the Uwharrie Formation. These thinly bedded rocks lend support to the inference that

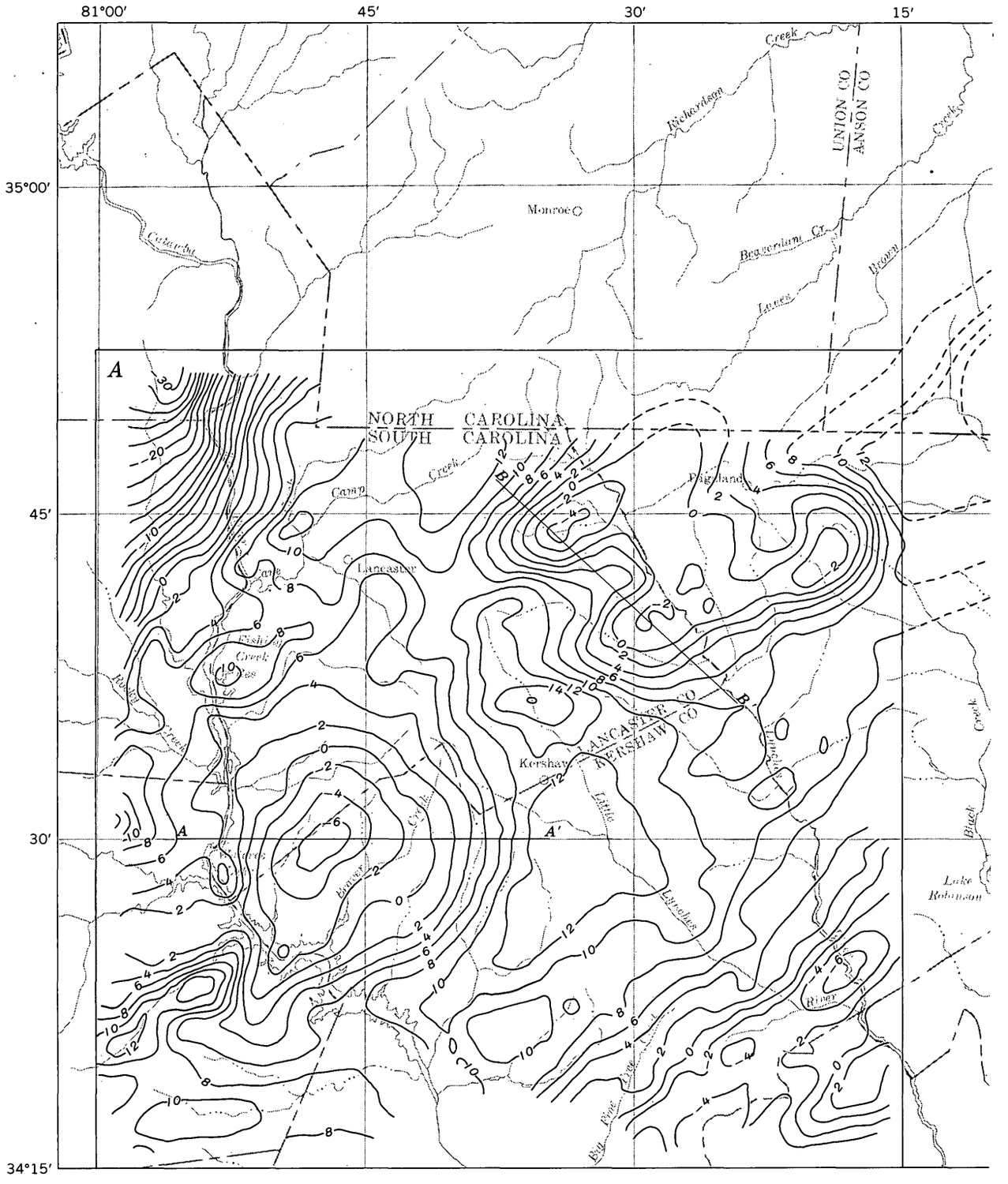

FIGURE 2.—Simple Bouguer gravity map of two areas in North and South Carolina. *A*, Haile-Brewer area, South Waskom and

the volcaniclastic rocks in the Haile-Brewer area correspond in some way to those of Uwharrie Formation in North Carolina.

Triassic basins

Sedimentary rocks of Triassic Newark age occur in the Wadesboro basin, the southernmost division of the

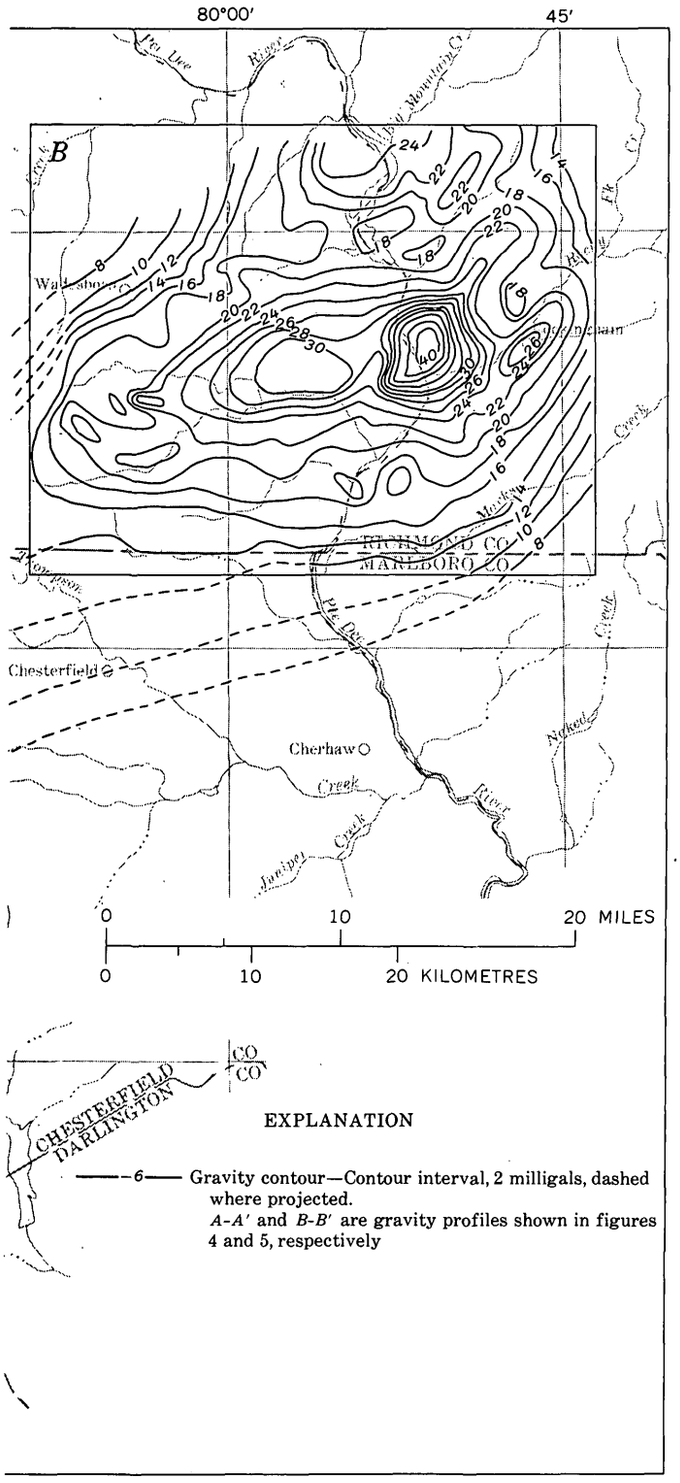

Carolina. *B*, Lilesville area, North Carolina (modified from Butler, 1971).

Deep River Triassic basin. The Wadesboro basin extends from southern North Carolina into South Carolina in the vicinity of the Pageland pluton. In addition, the small Crowburg basin and the Ellerbe basin are in the area shown in figure 3. Features of the sedimentary rocks and the tectonic settings of these basins have been described by Wheeler and his coworkers (Swe and Wheeler, 1964; Randazzo and Wheeler, 1965; and Randazzo and others, 1970). They described the rocks in the Wadesboro basin as arkosic and feldspathic wackes, siltstones, and lesser volumes of conglomerate, fanglomerate, and clay, largely derived from the adjacent bordering pre-Triassic rocks, including the coarse-grained granite in the Lilesville pluton. The Triassic rocks resemble those in other parts of the Deep River basin except that dark shales, coal beds, and fresh-water limestones have not been found.

Fanglomerates composed of rounded argillite fragments and some vein quartz are the major rock types exposed in the Crowburg basin (Bell and others, 1974). Maroon to red shale and siltstones are interbedded with the fanglomerates. No fragments of the Pageland pluton have been found in the fanglomerates or in other rocks in the Crowburg basin. This seems to indicate that the Pageland pluton, in contrast to the Lilesville pluton, was not unroofed at the time the basin was being filled. The close proximity of the pluton to the fault scrap along which the fanglomerates in the Crowburg basin were formed would seem to assure that some fragments of the granitic rock would be present if it had been exposed to erosion.

On the basis of a gravity-profile traverse across the Wadesboro basin, Mann and Zablocki (1961, p. 211) estimate that the thickness of sediments is 3,800 feet (1,160 m). The sedimentary rocks in the smaller Crowburg basin are probably much thinner.

The southwestern end of the Wadesboro basin is much faulted, and the Crowburg basin appears to be bounded by faults. Several narrow graben and horsts have been mapped by Randazzo, Swe, and Wheeler (1970) along the western border of the Wadesboro basin. The faults that bound these graben and horsts offset the contact of the Triassic and pre-Triassic rocks in a complicated fashion and extend some distance into the pre-Triassic rocks. The Crowburg basin in Chesterfield County is a graben partly bounded by faults which extend between the two lobes of the low-gravity anomaly associated with the Pageland pluton, perhaps as far as the Wateree River.

Three ages of faulting have generally been recognized in the Deep River basin (Reinemund, 1955; Conley, 1962b). The oldest faults are the eastern border faults, such as the Jonesboro fault, in the Sanford basin. Abundant cross faults trending from nearly north to west cut the Triassic rocks apparently mostly after sedimentation in the basin ceased. These faults cut

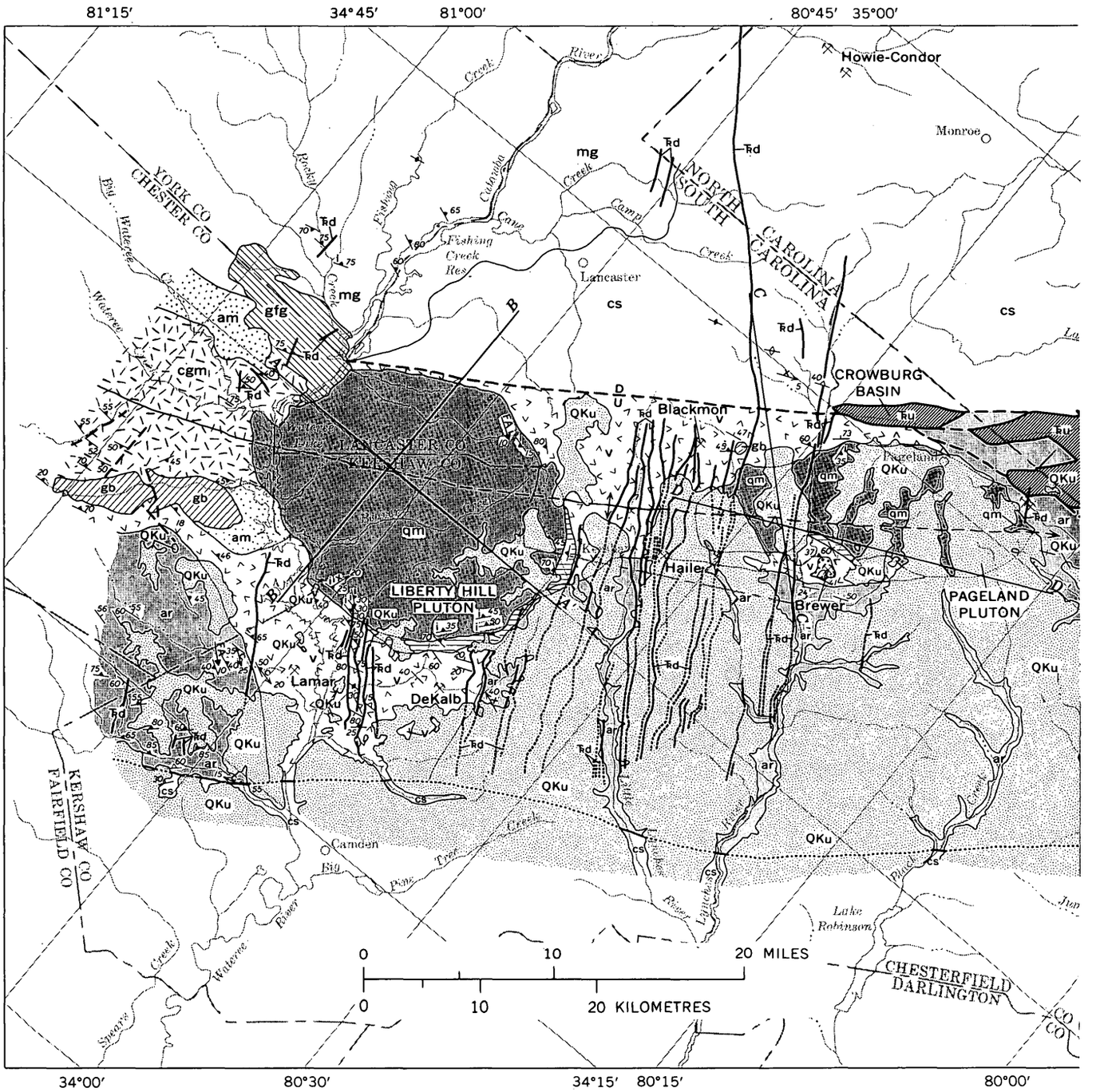

DESCRIPTION OF MAP UNITS

QKu — GRAVEL, SAND, CLAYEY SAND, AND CLAY (HOLOCENE TO CRETACEOUS)—Coastal Plain deposits with Middendorf Formation (Upper Cretaceous) at the base overlain by younger upland deposits; deeply weathered, and much redistributed by leaching, colluvial and aeolian processes. Middendorf Formation probably absent where less than 50 feet thick

Trd — DIABASE (TRIASSIC)—Black to dark-gray dikes from less than 1 foot to 1,000 feet thick; numerous dikes in Kershaw County projected on the basis of close-spaced airborne and ground geophysical data

TRu — CONGLOMERATE, SANDSTONE, SHALE, AND CLAYSTONE (TRIASSIC)—Various shades of red, brown, purple, and gray undifferentiated. Conglomerates in southernmost outcrops contain many fragments of argillite, phyllite, and schist derived from nearby sources in the Carolina slate belt

gb — GABBRO (UPPER PALEOZOIC)—Coarse-grained, dark, olivine-bearing, grades to diorite locally, noritic in part. Includes the Dutchmans Creek Gabbro of McSween (1972)

qm — QUARTZ MONZONITE (BIOTITE QUARTZ MONZONITE, GRANODIORITE, TONALITE, AND GRANITE) (CARBONIFEROUS)—Pink and gray porphyritic, coarse-grained, includes fine-grained and subporphyritic facies; commonly with abundant inclusions near contacts

gfg — GNEISSIC GRANITE (LOWER PALEOZOIC TO UPPER PRECAMBRIAN)—The Great Falls granitic pluton of Fullagar (1971)

cs — CAROLINA SLATE BELT UNDIFFERENTIATED (PALEOZOIC AND UPPER PRECAMBRIAN)—Argillite, tuffaceous argillite, and graywacke, includes felsic and mafic volcaniclastic rocks and volcanic flows. Metamorphic rocks, predominantly in greenschist or lower greenschist facies. North

FIGURE 3.—Geologic map of a part of the Piedmont in northeast South Carolina and adjacent North Carolina. Geology mainly McSween (1972); and

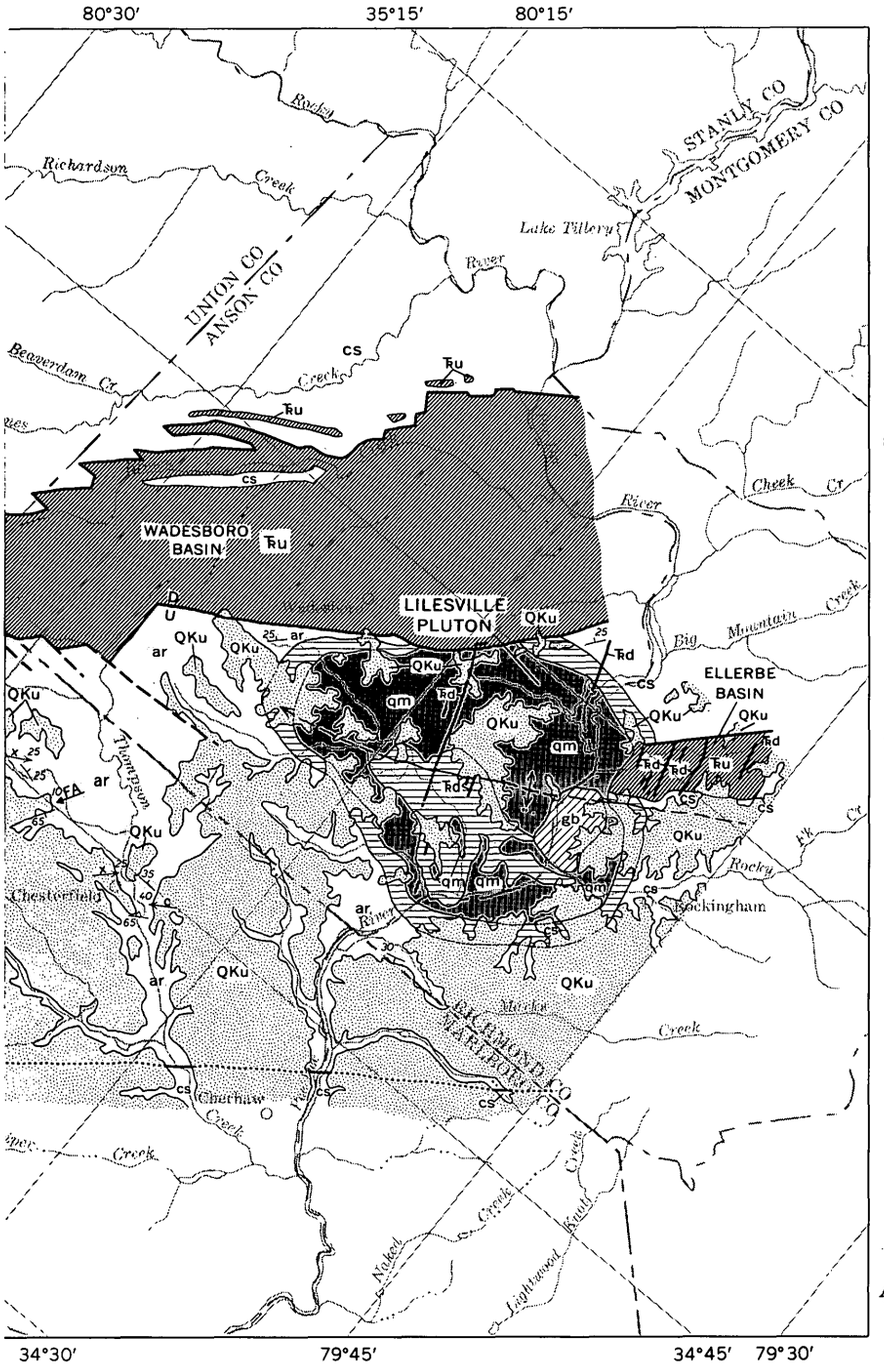

CORRELATION OF MAP UNITS

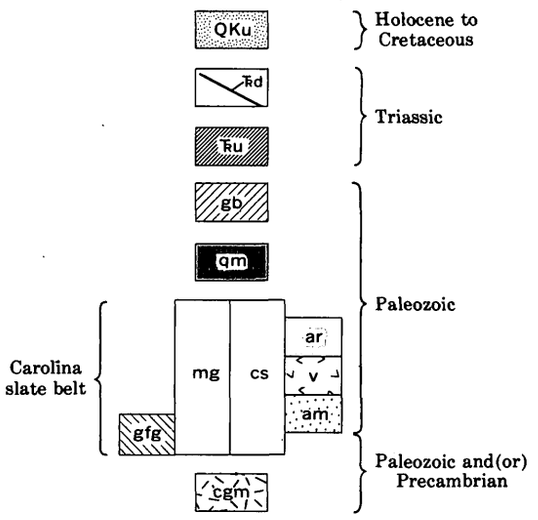

Contact—Dotted where concealed

D / U — Fault—Dashed where largely a shear zone; dotted where concealed or projected on geophysical data. U, upthrown side; D, downthrown side

Major anticline—Dashed where projected

FA 10 — Bearing and plunge of fold axes in tightly folded rocks

Strike and dip of beds—
25 — Inclined
— Vertical

Strike and dip of foliation—
37 — Inclined
— Vertical

35 i — Strike and dip of foliation—i, inclusion in igneous rock

Strike and dip of fracture cleavage—Little or no recrystallization in plane of cleavage
65 — Inclined
— Vertical

c 40 — Bearing and plunge of lineation—Variety of linear feature shown by letter; c, crinkles on bedding, foliation, or cleavage; x, intersection of bedding and cleavage

Mine, mining area, or prospect

A — A′ Line of section shown in figures 6 and 7

DESCRIPTION OF MAP UNITS

of the Jonesboro fault extended, includes the McManus Formation of Conley and Bain (1965)

mg — MICA GNEISS (PALEOZOIC AND UPPER PRECAMBRIAN)—Layered biotite gneiss and biotite schist, hornblende gneiss and hornblende schist with granitic layers common. Probably equivalent to large parts of the Carolina slate belt north of the Jonesboro fault extended except the metamorphic grade is almadine-amphibolite

ar — ARGILLITE AND SLATE (LOWER PALEOZOIC)—Gray and greenish-gray, thinly bedded and laminated argillite and slate

v — VOLCANICLASTIC ROCKS (LOWER PALEOZOIC)—Tuffs and flows are common near Kershaw. Muscovite, chlorite, phyllite, and muscovite-quartz schist, largely felsic but with some interbedded mafic units. Probably equivalent, at least in part, to the Wildhorse Branch and Persimmon Fork Formations of Secor and Wagener (1968)

am — AMPHIBOLITE (LOWER PALEOZOIC)—Dark-green, gray, and black amphibolite, includes some hornblende schist and hornblende gneiss, diorite, and metagabbro

cgm — GRANITOID GNEISS (LOWER PALEOZOIC AND UPPER PRECAMBRIAN)—Undivided granitoid gneisses, gneissic granites, and schists characteristic of the Charlotte belt

HORNFELS AND CONTACT METAMORPHIC ROCKS—Includes dark saccharoidal rocks at the contact of the Liberty Hill and Pageland plutons; biotite gneiss with some sericite schist adjacent to the Lilesville pluton. Around the Liberty Hill pluton mapped largely on the basis of geophysical data

INTENSELY SILICIFIED ROCKS—Vicinity of the Brewer mine; contains massive topaz locally

compiled from Overstreet and Bell (1965a, b); Stuckey (1958); Randazzo, Swe, and Wheeler (1970); Waskom and Butler (1971); Nystrom (1972).

both the eastern and western border faults of the Wadesboro basin, causing many of the conspicuous offsets in the contact between Triassic and pre-Triassic rocks. Diabase dikes have been intruded into many of these faults and parallel fractures. Some faulting and fracturing of pre-Triassic age in a northwest direction may have served as the locus of rejuvenated cross fracturing in Triassic times into which diabase of Triassic age was intruded. Faults produced during the third general age of faulting trend parallel to the length of the basins. These longitudinal faults have produced the narrow graben and horsts that have been mapped along the western border of the Wadesboro basin, and they offset many cross faults.

Diabase dikes

A striking feature of the Haile-Brewer area is the swarm of northwest-trending diabase dikes between the Liberty Hill and Pageland plutons. They closely resemble diabase dikes cutting the Newark-age rocks in the Triassic basins and probably are similar in age. These diabase dikes produce the strong magnetic anomalies recorded in airborne and ground magnetic surveys. Detailed aeromagnetic surveys. (U.S. Geological Survey, 1970) show the dikes to be more abundant and longer than was previously realized from geologic mapping. Many of these magnetic anomalies can be traced into the area where thick Coastal Plain sedimentary rocks occur. Some of the dikes cut the plutons but most do not. In composition, the dikes in North and South Carolina are quartz-normative and olivine-normative tholeiitic diabase (Wiegand and Ragland, 1970; Hermes, 1964; and Steele, 1971). They are younger and distinctly different from the metamorphosed andesitic and basaltic dikes that cut the volcaniclastic and volcanic rocks of the Carolina slate belt in this area.

Granitic plutons

The three granitic plutons shown in the geologic map (fig. 3) are the Liberty Hill pluton to the southwest, the Pageland pluton, and the Lilesville pluton to the northeast. The rocks of these three plutons are similar in appearance. They are coarse grained, they range in composition from quartz monzonite to granodiorite, their texture is porphyritic or subporphyritic, and they lack gneissic banding or strong foliation. The plutons were emplaced in rocks of the Carolina slate belt after the last regional metamorphic event. The plutons are, in general, uniform in grain size even up to their contacts with the country rocks. Although fine-grained marginal facies are not recognized, the Liberty Hill pluton has a centrally located mass of fine-grained rock which locally contains quartz phenocrysts. The fine-grained facies also occurs locally as dikes cutting the coarse-grained rocks of both the Liberty Hill (Wagener and Howell, 1973) and Pageland plutons. The plutons crosscut the foliation and bedding of the volcaniclastic rocks in which they occur, and have produced thermal aureoles reaching a maximum width of about 3 miles. All the plutons contain large septa and rotated inclusions of various sizes, particularly near their contacts. These are commonly recognizable as having been derived from the adjacent foliated country rocks and are good evidence for the intrusive nature of the granitic plutons. All three plutons are in contact with the argillites. In addition, the Liberty Hill pluton is in contact with amphibolite and granitic gneiss and schist on its southwest perimeter. The Lilesville pluton, as described by Waskom and Butler (1971), has features that set it apart from the other plutons to the southwest. It is in contact with rocks of the Wadesboro Triassic basin along a border fault and with those of the Ellerbe basin on the northeast. In the southern part of the pluton, an area of mica gneiss, which Waskom and Butler (1971) interpreted as a window through the granite, exposes thermally metamorphosed rocks that resemble the thermal aureole surrounding the pluton. A gabbro, clearly intrusive, as indicated by the contacts and inclusions of granite within the gabbro (Waskom and Butler, 1971, p. 2830), occurs in the eastern part of the pluton.

On the basis of their contacts and unmetamorphosed character, coarse-grained intrusive rocks such as these in the Piedmont of the Carolinas have been considered late Paleozoic or Carboniferous in age. Rubidium-strontium whole-rock isochron ages range from 299 to 332 m.y. (Fullagar, 1971; Butler and Fullagar, 1975). The initial Sr^{87}/Sr^{86} ratios, from the samples used in the whole-rock analyses, are shown in the following table from their data.

Pluton	*Number of samples*	*Initial strontium-isotope ratio*
Liberty Hill	5	0.7046±0.0010
Pageland	4	.7038± .0002
Lilesville	4	.7047± .0007

GRAVITY PATTERNS

Liberty Hill pluton

The gravity anomaly over the Liberty Hill pluton conforms closely with the outcrop area of the relatively low density quartz monzonite (figs. 2 and 3). The

gravity data substantiates geologic interpretations that the pluton has steep inward-dipping contacts except, perhaps, locally on the north and south perimeters. The gravity anomaly is nearly circular, the area of lowest gravity being on the crest of the regional anticline. In the northwest quadrant of the anomaly, the gravity gradient is slightly steeper than elsewhere. The pluton may there be in contact with an extension of the Triassic faults that bound the Crowburg basin. Figure 4 is an east-trending profile of the gravity anomaly. The profile shows that the magnitude of the anomaly at the contact between the pluton and the country rock is about 4 mGals on the west and 10 mGals on the east. The commonly apply half-amplitude method (in which values of less than half the anomaly amplitude at the contact indicate inward-dipping slopes) shows that the contacts of the Liberty Hill pluton dip inward.

Pageland pluton

The pattern of the gravity anomaly associated with the quartz monzonite in the Pageland pluton is very different from that of the quartz monzonite in the Liberty Hill (figs. 2 and 3). It is ameboid in shape; one lobe of the pattern is over the outcrop area, and a similar-shaped lobe is found to the northwest, where quartz monzonite is not known to crop out. Within the northwest lobe of the anomaly is an elongate area having a gravity value nearly as low as that at the center of the Liberty Hill pluton. The southeast lobe contains two embayments of low gravity. Figure 5 is

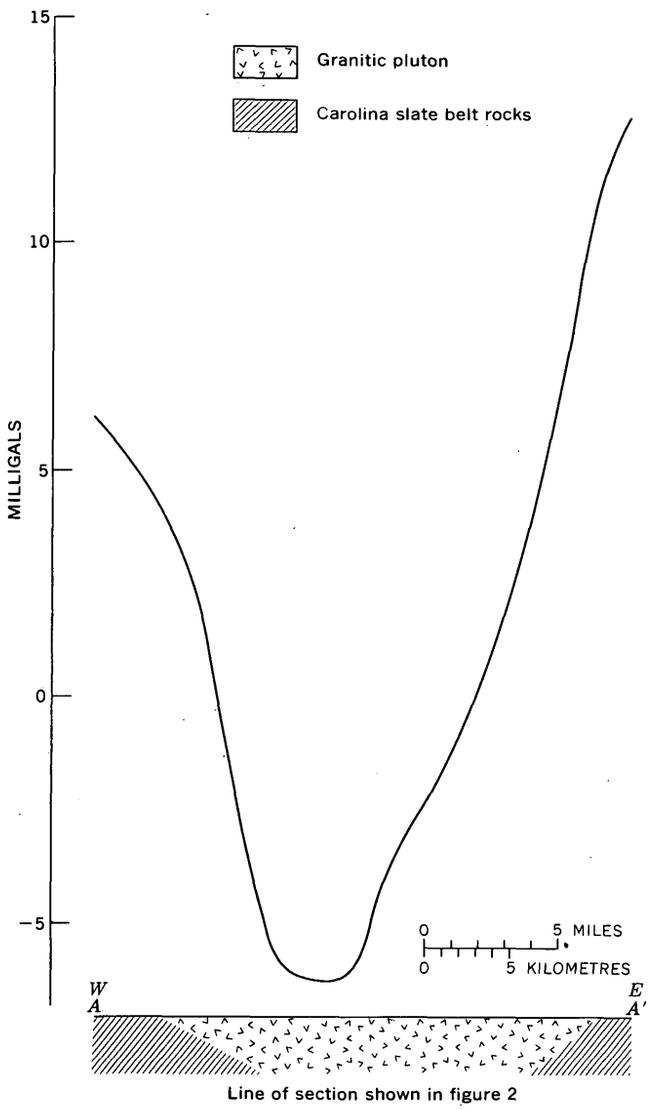

FIGURE 4.—Profile of the Bouguer gravity anomaly and diagrammatic geologic cross section of the quartz monzonite in the Liberty Hill pluton.

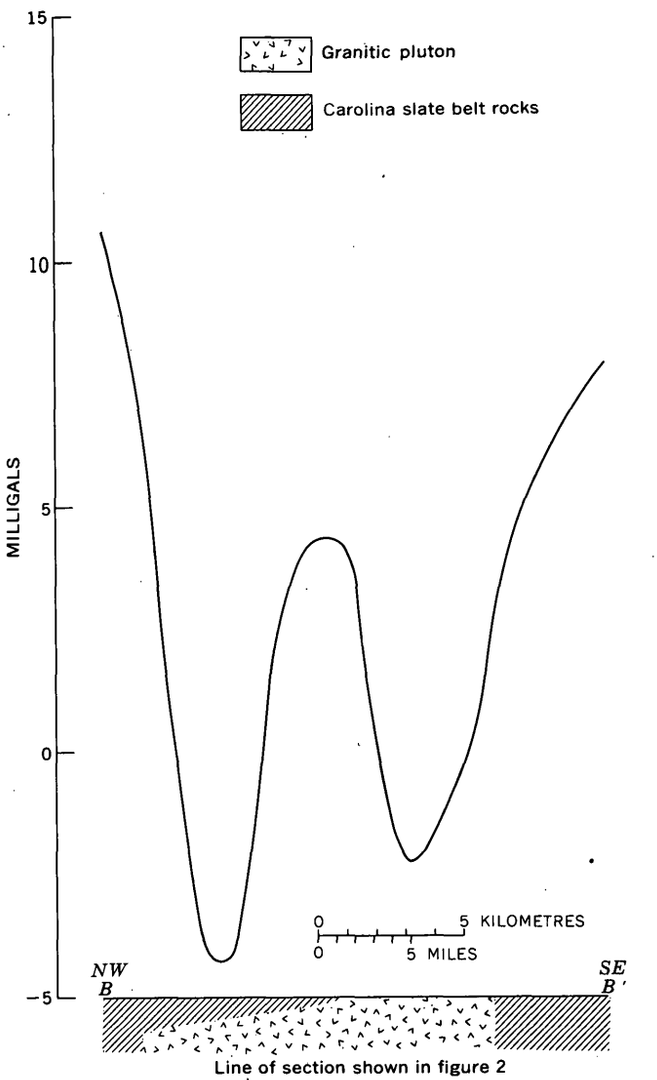

FIGURE 5.—Profile of the Bouguer gravity anomaly and diagrammatic geologic cross section of the quartz monzonite in the Pageland pluton.

a profile of the Bouguer anomaly through the two lobes of the pluton. The relation of the amplitude of the southeast lobe of the anomaly to the contacts of the quartz monzonite and its country rocks, indicates steep inward dips, except along the southeast side of the eastern low-gravity area. There, the inferred contact between quartz monzonite and slate-belt rocks beneath the covering sedimentary rocks of the Coastal Plain may be incorrectly located and perhaps should be moved to conform with the shape of the gravity anomaly. The northwest lobe of the anomaly would seem to be due to a steep-sided mass of low-density rock (probably also quartz monzonite) that approaches the surface but does not crop out.

No expression of the silicified rocks that surround the Brewer mine is apparent on the Bouguer anomaly map. No large mass of igneous or plutonic rock, closer than the quartz monzonite in the Pageland pluton, seems to be located at depth in the vicinity of the mine.

Lilesville pluton

The Bouguer gravity anomaly that coincides with the Lilesville pluton is distinctively different from the anomalies associated with the two plutons to the southwest. It is a positive Bouguer anomaly trending east and is slightly offset to the south from the outcrop area. A pronounced high-gravity area of 40 mGal is formed over the gabbro intrusion in the eastern part of the pluton. Waskom and Butler (1971, p. 2836) asserted that "The gabbro intrusion and the mica gneiss unit that underlie the batholith are * * * responsible for such a large gravity maximum over an otherwise felsic igneous intrusion." As a result of model studies, Waskom and Butler (1971) consider that the gabbro consists of a central mass and a tongue intruded northwestward toward the crest of an anticline. They consider the granite to be a thin sheet or tongue-like body, thickest to the northwest.

MODEL STUDIES

To test previous geologic interpretations and to derive new interpretations based on gravity data using methods suggested by Bott and Smithson (1967), the iterative three-dimensional method described by Cordell and Henderson (1968) has been applied to the gravity anomalies associated with the Liberty Hill and Pageland plutons.

Iterative methods, according to Cordell and Henderson (1968, p. 596), in general comprise there aspects: (1) a "starter" model, (2) calculation of the gravity effect of the tentative model, and (3) a modification of the model, based in some way on the disagreement between the previously calculated gravity anomaly and the observed anomaly. Steps two and three are iterated until a suitable fit is obtained. Because a computer is used to make the iterative calculation, it is, in effect, a computerized trial and error method. To use this method, the gravity data from 558 gravity stations were converted to a rectangular grid and the regional gravity gradient was removed. For the purposes of the computer program, the source of the gravity anomaly "is represented as an ensemble of vertical prism elements, each element having a cross-sectional area equal to one grid square, a uniform density, and a vertical position fixed with respect to a specified reference surface" (Cordell, 1970, p. 1). The reference surface can be either the upper or lower surface of the gravitating body. Because the gravitating body crops out at the surface and because topographic relief in the Haile-Brewer area is low, the ground surface was specified as this reference surface. The spacing between points on the grid to which the gravity is referred is 2 miles. The regional gravity gradient removed from the data was assumed to be a plane dipping southeast at about 0.3 mGals per mile.

The calculated models of the bodies show that a small regional gravity residual remained in the data. Figures 6 and 7 are geologic maps showing isopachs of the calculated low-density masses necessary to produce the Liberty Hill and Pageland anomalies when the density contrast is -0.15 between the quartz monzonite and the volcaniclastic rocks of the Carolina slate belt in which the plutons are emplaced. Geologic cross sections derived from the gravity-model isopach maps show the unremoved regional gravity residual as the distance between the model reference surface and the ground surface of the geologic cross sections.

The critical parameter involved in these gravity calculations is the bulk density of the rocks. Table 1 lists the bulk densities of rock specimens collected in the Haile-Brewer area and from nearby areas in North and South Carolina. These data are too sparse and too poorly distributed to give an adequate sample of the density of the rocks at the surface. Densities of rocks at depth are largely unknown and can only be inferred from surface samples or by other indirect methods. In addition, the density of many surface samples reflects the effects of weathering even in samples that in hand specimen seem to be only slightly altered. The effects of weathering seem to be particularly evident in the coarse volcaniclastic samples of the Carolina slate belt and are, perhaps, least evident in the granitic rocks. The densities listed in table 1, however, can be tested in the iterative modeling procedure. Be-

TABLE 1.—*Mean bulk densities of rock specimens in the Haile-Brewer area*

Lithologic unit	Number of samples	Mean bulk density (g/cm³)	Range of density
Intrusive rocks			
Granite	8	2.69	2.62–2.82
Do[1]	10	2.65	2.62–2.69
Do[2]	36	2.64	2.40–2.72
		[3]2.65	
Gabbro	5	2.93	2.84–3.05
Do[2]	7	2.98	2.91–3.03
		[3]2.96	
Diabase	55	2.97	2.79–3.08
Do[2]	13	2.91	2.86–2.98
		[3]2.96	
Felsic hypabyssal rocks	12	2.58	2.38–2.69
Mafic hypabyssal rocks	4	2.92	2.92–3.07
Carolina slate belt rocks			
Sedimentary rocks	8	2.64	2.42–2.77
Do[2]	5	2.61	2.40–2.81
Mica gneiss[2]	3	2.73	2.67–2.80
Volcaniclastic rocks	8	2.59	2.38–2.74
Do[4]	13	2.79	2.63–2.99
		(2.84)	(2.70–3.05)
		[3]2.69	

[1] Sloan (1908, p. 217–225).
[2] Waskom and Butler (1971, table 2, p. 2835).
[3] Weighted average mean.
[4] McCormick County, S.C., drill core samples as much as 300 feet below the collar elevation; figures in parentheses are powder-density values for the same samples and are not included in average.

cause the gravity anomalies associated with the granitic plutons show low gravity values in contrast to higher gravity surroundings, the bulk density of 2.59 grams per cubic centimeter (g/cm³) obtained from surface samples of volcaniclastic rocks is unrealistically low if applied to the mass of rock in which the granite is emplaced. Bulk density measurements on unweathered drill core of similar volcaniclastic rock from the Carolina slate belt in McCormick County, S.C., are more dense and give a contrast with average granite of 0.14. Densities obtained from pulverized samples have even higher density measurements and give a contrast with average granite of 0.19. If the setting in which the plutons are emplaced at depth includes both volcaniclastic rocks and sedimentary rocks having an average density similar to that in table 1, a density contrast of 0.04 (2.69−2.65) would be appropriate in the model calculations.

Figure 8 shows profiles of part of the Pageland pluton gravity anomaly; thicknesses have been calculated using density contrasts of −0.20, −0.15, −0.10 and −0.06 g/cm³. Figure 8 shows the effect that density contrast has on the thickness calculated for the pluton. The regional geologic setting as shown by Overstreet and Bell (1965a) indicates that the plutons are emplaced where the stratigraphic column consists of felsic volcaniclastic rocks estimated to be 5–10 km thick. These rocks are underlain by mafic lavas and other mafic rocks lying on granitic gneisses and overlain by thinly bedded or laminated mudstones which have been largely removed by erosion from the cover of the granite plutons. The best estimate of densities to use in model studies would seem to be the best estimate of the density contrast between average granite and the felsic volcaniclastic rocks in the Haile-Brewer area. The estimate used for figures 6 and 7 was a density contrast of −0.15 g/cm³. When this contrast is used, the thickness calculated for both plutons is close to the estimated thickness of the Uwharrie Formation in North Carolina and probably the volcaniclastic unit in eastern South Carolina. Other density contrasts, when used in the model computations, give results that imply unreasonable thicknesses and characteristics to the stratigraphic column in which the plutons are emplaced.

The density of the granite used in the model calculations was taken to be uniform throughout the pluton. Bott and Smithson (1967) pointed out that a lateral variation in density within the granite pluton from a less dense core to a higher density perimeter would produce a gravity profile similar to the profile over a pluton having uniform density and inward-dipping contacts. Although the Liberty Hill pluton has a centrally located fine-grained facies, it is similar in composition and density to the coarser grained rock.

CONCLUSION

Most of the anomalies revealed by the gravity data are related to rock units on the geologic map. The most conspicuous anomalies coincide with the outcrop area of three quartz monzonite plutons. The Bouguer anomaly map shows low gravity over two of the plutons and high gravity over the other.

Analyses of the gravity lows over the Liberty Hill and Pageland plutons confirm that these granitic plutons are steep-sided intrusive bodies emplaced in, and probably largely confined to, a thick unit of volcaniclastic rocks similar to those exposed in the vicinity and about the thickness estimated from geologic mapping. The gravity data, together with the geologic data, lead to the conclusion that these plutons constrict at depth to small pipes or roots and are not connected. The Liberty Hill pluton has a single root, whereas the Pageland pluton, including the unroofed part, has three such roots.

Waskom and Butler (1971, p. 2842), from their study of the gravity anomaly over the Lilesville pluton, come to the conclusion that "The positive Bouguer anomaly * * * can be explained by the presence of the gabbro unit and the mica gneiss unit which un-

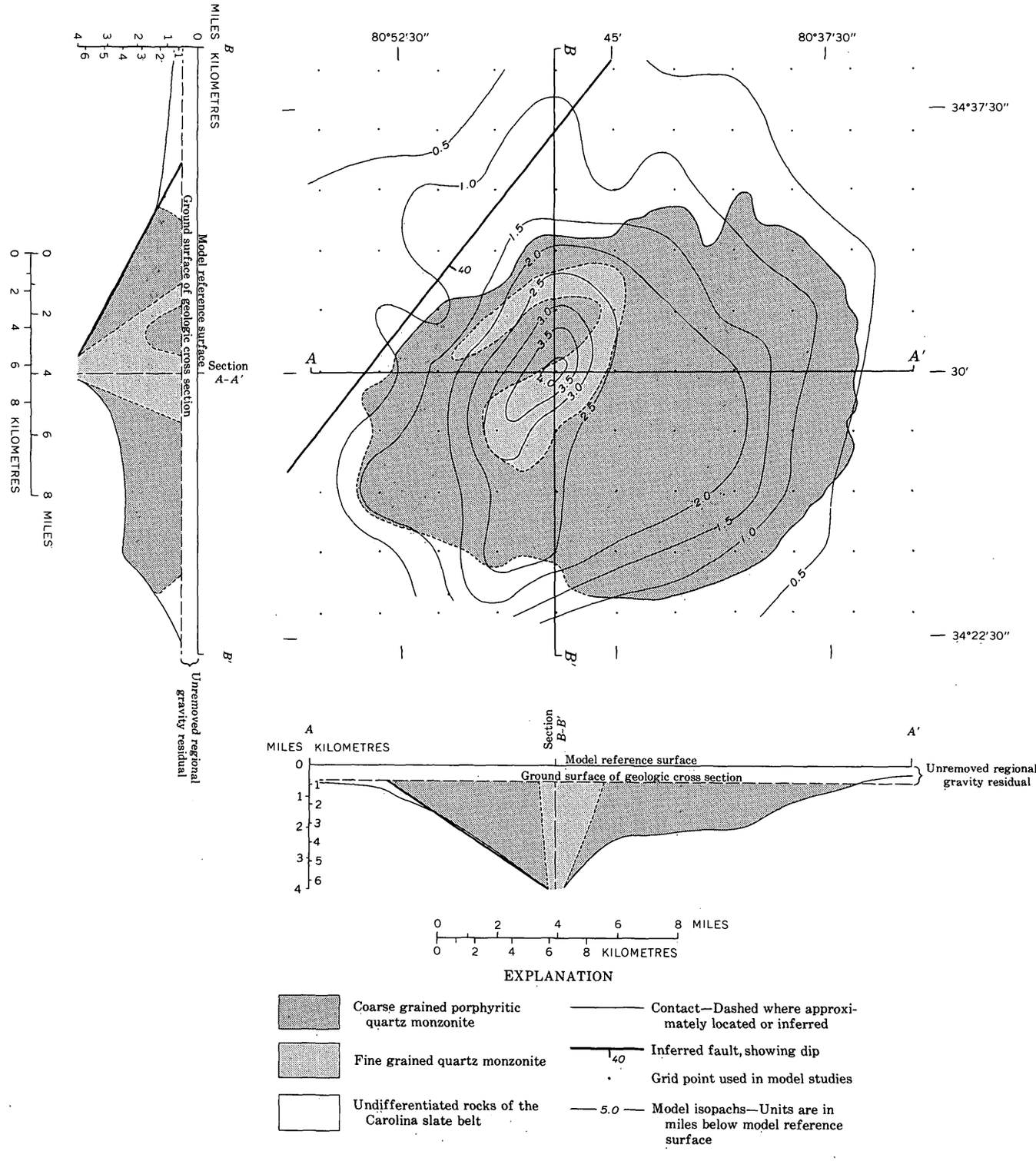

FIGURE 6.—Geologic map showing gravity-model isopachs and derived geologic cross sections of the quartz monzonite in the Liberty Hill pluton based on an iterative three-dimensional solution of its gravity anomaly.

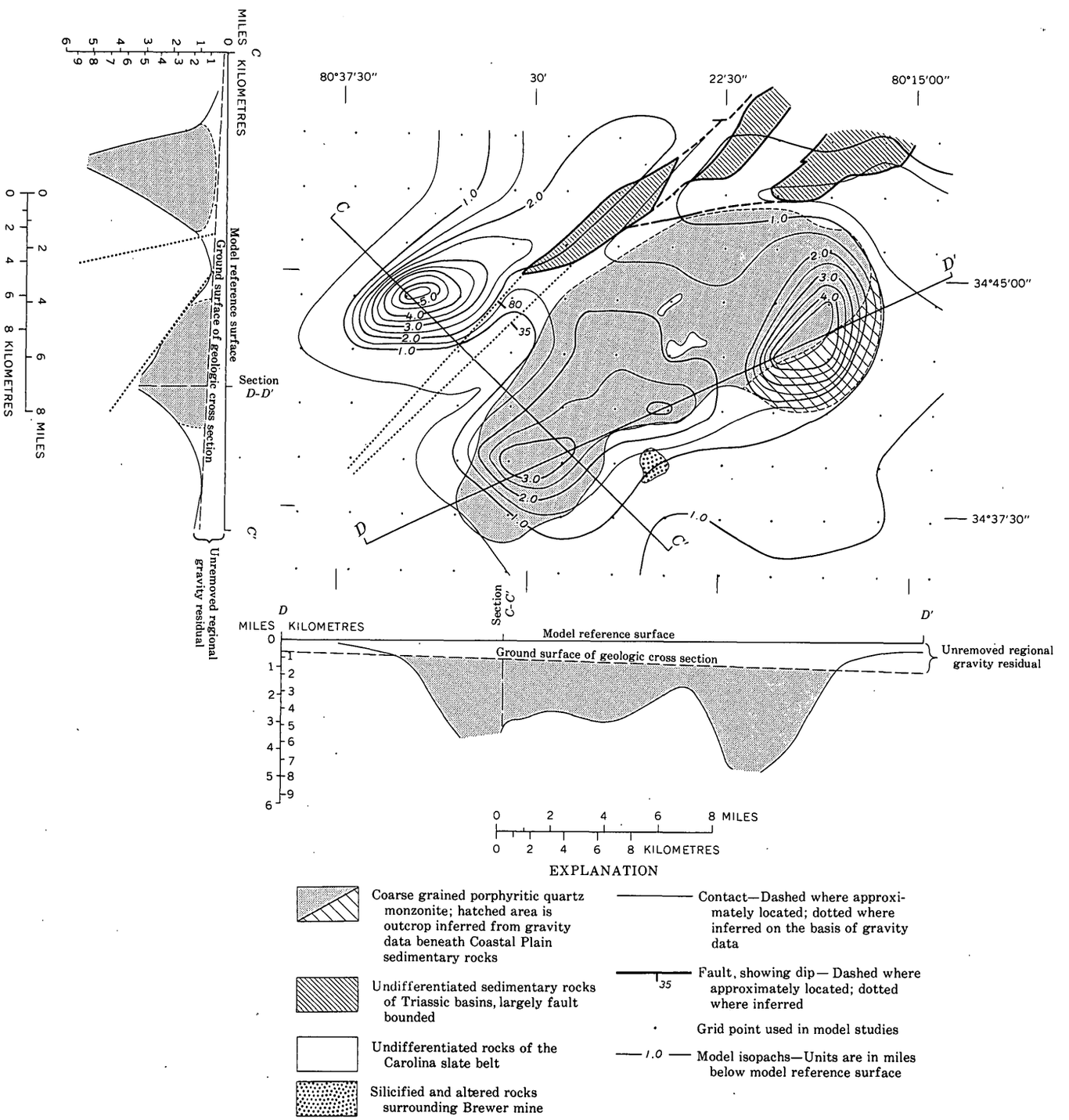

FIGURE 7.—Geologic map showing gravity-model isopachs and derived geologic cross sections of the quartz monzonite in the Pageland pluton based on an iterative three-dimensional solution of its gravity anomaly.

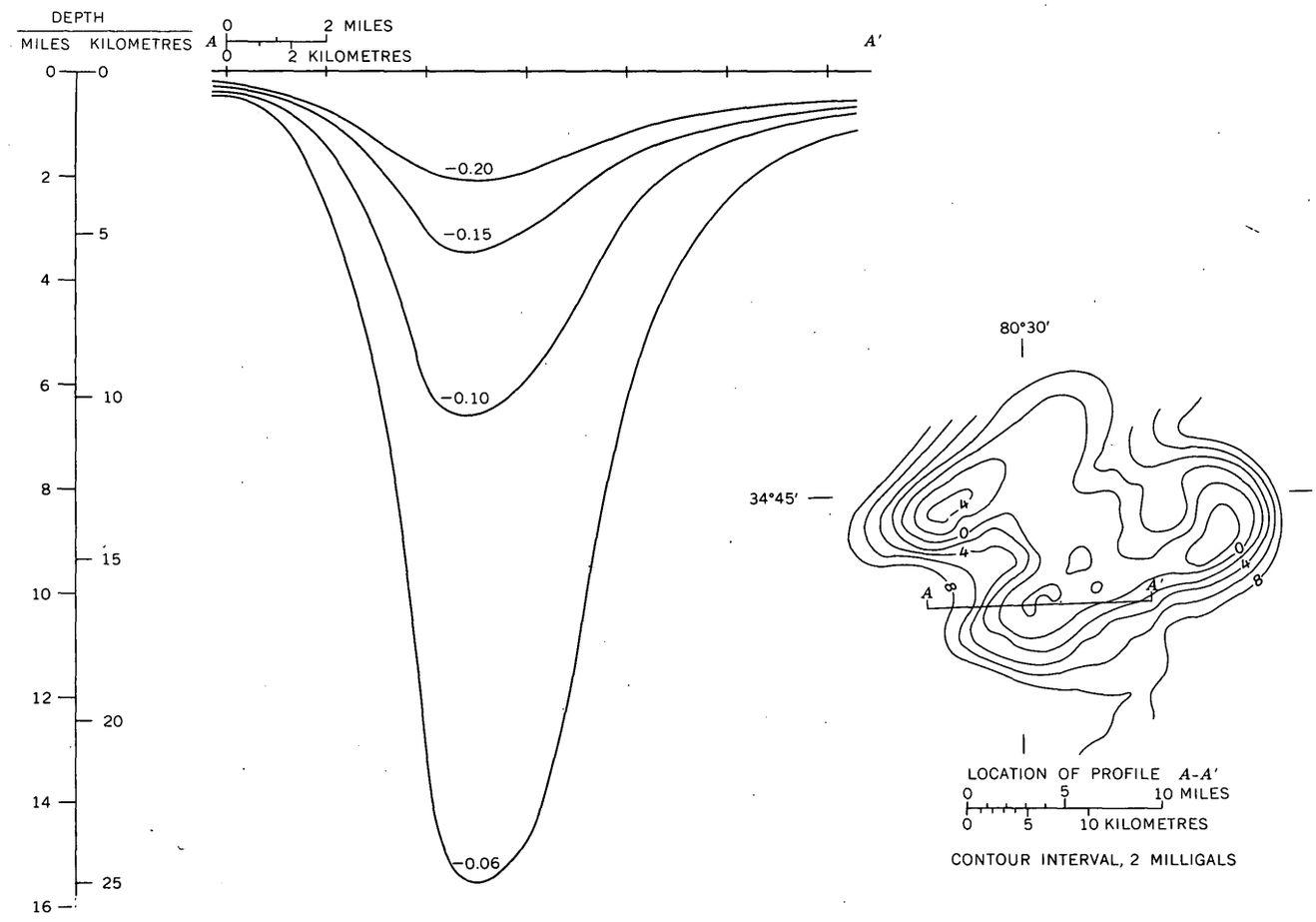

FIGURE 8.—Profiles of part of the Pageland pluton Bouguer gravity anomaly, showing thicknesses calculated with various density contrasts (given in grams per cubic centimetre).

derlies the central portion of the granite * * *." The Lilesville pluton in many geologic aspects is so similar to the plutons to the southwest that this is a convincing explanation for the high positive gravity over a type of pluton that characteristically has negative gravity anomalies.

Only the upper part of the Liberty Hill pluton is exposed; nevertheless, it is exposed to a deeper level than the Pageland pluton which is only partly unroofed.

The shapes of the granitic plutons at depth have been inferred from the gravity anomalies (figs. 6 and 7) and from model studies based on density contrasts between the granitic rock and the country rock in which it is emplaced. The commonly postulated processes by which such large bodies become emplaced—such as forcible intrusion of a magma with lateral shouldering aside and uplift of wall rocks, or granitization of rocks in place—have been discussed by Bott and Smithson (1967) in terms of the gravity profiles that would be expected to result. The problem of emplacement involves the location of the mass removed to make room for the granitic rock; it should be reflected in the gravity profiles but commonly is not. The gravity profiles over the plutons in the Haile-Brewer area resemble those over postkinematic plutons in other areas of the world. No unique evidence for a particular emplacement process has been recognized here. The plutons have characteristics such as rotated inclusions and blocks of country rocks that suggest forcible intrusion, but widespread structural evidence for forcible shouldering aside of country rocks to make room for the plutons is not very convincing. The explanation may be that the plutons were emplaced in a great thickness of volcaniclastic rocks such as tuffs and similar vesicular and porous rocks that might effectively have absorbed a large amount of compaction and shouldering aside without widespread deformation. In addition, the plutons are along the crest of a preexisting large-scale anticline where deformation caused by intrusion of the magma upward and outward may have been accommodated in large part by

the preexisting extentional structures in this part of the fold.

REFERENCES CITED

American Geophysical Union, Special Committee for the Geophysical Study of the Continents, 1964, Bouguer gravity anomaly map of the United States (exclusive of Alaska and Hawaii): Washington, D.C., U.S. Geol. Survey, 2 sheets, scale 1:2,500,000.

Bell, Henry, III, Butler, J. R., Howell, D. E., and Wheeler, W. H., 1974, Geology of the Piedmont and Coastal Plain near Pageland, South Carolina, and Wadesboro, North Carolina: South Carolina State Devel. Board, Div. Geology [Carolina Geol. Soc. Field Trip Guidebook], 23 p.

Bell, Henry, III, Marvin, R. F., and Mehnert, H. H., 1972, Potassium argon ages from areas of hydrothermal alteration in South Carolina: U.S. Geol. Survey Prof. Paper 800-D, p. D117-D121.

Best, D. M., Geddes, W. H., and Watkins, J. S., 1973, Gravity investigation of the depth of source of the Piedmont gravity gradient in Davidson County, North Carolina: Geol. Soc. America Bull., v. 84, no. 4, p. 1213-1216.

Bott, M. H. P. and Smithson, S. B., 1967, Gravity investigations of subsurface shape and mass distributions of granite batholiths: Geol. Soc. America Bull., v. 78, no. 7, p. 859-877.

Butler, J. R. and Fullagar, P. D., 1975, Lilesville and Pageland plutons and the associated metarhyolites, Eastern Carolina slate belt: Geol. Soc. America Abs. with Programs, v. 7, no. 4, p. 475.

Conley, J. F., 1962a, Geology of the Albemarle quadrangle, North Carolina: North Carolina Div. Mineral Resources Bull. 75, 26 p.

——— 1962b, Geology and mineral resources of Moore County, North Carolina: North Carolina Div. Mineral Resources Bull. 76, 40 p.

Conley, J. F., and Bain, G. L., 1965, Geology of the Carolina slate belt west of the Deep River-Wadesboro Triassic basin, North Carolina: Southeastern Geology, v. 6, no. 3, p. 117-138.

Cordell, Lindrith, 1970, Iterative three-dimensional solution of gravity anomaly data: U.S. Dept. Commerce Natl. Tech. Inf. Service, PB1-96979, 23 p.

Correll, Lindrith, and Henderson, R. G., 1968, Iterative three-dimensional solution of gravity anomaly data using a digital computer: Geophysics, v. 33, no. 4, p. 596-601.

Fullagar, P. D., 1971, Age and origin of plutonic intrusions in the Piedmont of the southeastern Appalachians: Geol. Soc. America Bull., v. 82, no. 10, p. 2845-2862.

Hermes, O. D., 1964, A quantitative petrographic study of dolerite in the Deep River Basin, North Carolina: Am. Mineralogist, v. 49, nos. 11-12, p. 1718-1729.

King, P. B., 1961, Systematic pattern of Triassic dikes in the Appalachian region: U.S. Geol. Survey Prof. Paper 424-B, p. B93-B95.

Mann, V. I., and Zablocki, F. S., 1961, Gravity features of the Deep River-Wadesboro Triassic basin of North Carolina: Southeastern Geology, v. 2, no. 4, p. 191-215.

McSween, H. Y., Jr., 1972, An investigation of the Dutchmans Creek Gabbro, Fairfield County, South Carolina: South Carolina Div. Geology Geol. Notes, v. 16, no. 2, p. 19-42.

Nystrom, P. G., Jr., 1972, Geology of the Catarrah NW (Jefferson) quadrangle: Univ. South Carolina, Columbia, S.C., M.S. dissert.

Overstreet, W. C., and Bell, Henry, III, 1965a, The crystalline rocks of South Carolina: U.S. Geol. Survey Bull. 1183, 126 p.

——— 1965b, Geologic map of the crystalline rocks of South Carolina: U.S. Geol. Survey Misc. Geol. Inv. Map I-413, scale 1:250,000.

Pardee, J. T., and Park, C. F., Jr., 1948, Gold deposits of the southern Piedmont: U.S. Geol. Survey Prof. Paper 213, 156 p.

Popenoe, Peter, and Bell, Henry, III, 1975, Simple Bouguer gravity map of part of Carolina slate belt including the Haile and Brewer mine areas, north-central South Carolina: U.S. Geol. Survey Geophys. Inv. Map GP-904.

Randazzo, A. F., and Wheeler, W. H., 1965, Stratigraphy and structure of the Wadesboro Triassic basin of North Carolina [abs.]: Geol. Soc. America Ann. Mtg., Kansas City, 1965, Program, p. 131.

Randazzo, A. F., Swe, Win, and Wheeler, W. H., 1970, A study of tectonic influence on Triassic sedimentation—the Wadesboro basin, central Piedmont: Jour. Sed. Petrology, v. 40, no. 3, p. 998-1006.

Reinemund, J. A., 1955, Geology of the Deep River coal field, North Carolina: U.S. Geol. Survey Prof. Paper 246, 159 p.

Secor, D. T., Jr., and Wagener, H. D., 1968, Stratigraphy, structure, and petrology of the Piedmont in central South Carolina—Carolina Geol. Soc. Field Trip. Oct. 18-20, 1968: South Carolina Div. Geology, Geol. Notes, v. 12, no. 4, p. 67-84.

Sloan, Earle, 1908, A catalogue of the mineral localities of South Caroilna: South Carolina Geol. Survey Bull., ser. 4, no. 2, 505 p. (Reprinted 1958 by South Carolina Div. Geology.)

Steele, K. F., Jr., 1971, Chemical variations parallel and perpendicular to strike in two Mesozoic dolerite dikes, North Carolina and South Carolina: Chapel Hill, N.C., Univ. North Carolina, Ph.D. thesis, 148 p.

Stromquist, A. A., 1966, Bedrock geologic map of the Denton quadrangle, North Carolina: U.S. Geol. Survey open-file map.

Stromquist, A. A., and Sundelius, H. W., 1969, Stratigraphy of the Albemarle Group of the Carolina slate belt in central North Carolina: U.S. Geol. Survey Bull. 1274-B, p. B1-B22.

Stuckey, J. L., 1958, Geologic map of North Carolina: North Carolina Div. Mineral Resources Map, scale 1:500,000.

Swe, Win, and Wheeler, W. H., 1964, Structural and stratigraphic relationships along the northwestern border of the Wadesboro Triassic basin of North Carolina [abs.]: Geol. Soc. America Spec. Paper 76, p. 259.

Taylor, P. T., Zietz, Isidore, and Dennis, L. S., 1968, Geologic implications of aeromagnetic data for the eastern continental margin of the United States: Geophysics, v. 33, no. 5, p. 755-780.

U.S. Geological Survey, 1970, Aeromagnetic map of the Camden-Kershaw area, north-central South Carolina: U.S. Geol. Survey open-file report.

Wagener, H. D., and Howell, D. E., 1973, Granitic plutons of the central and eastern Piedmont of South Carolina: Carolina Geol. Soc. Field Trip Guidebook, South Carolina State Devel. Board, Div. of Geology, 25 p.

Waskom, J. D. and Butler, J. R., 1971, Geology and gravity of the Lilesville Granite batholith, North Carolina: Geol. Soc. America Bull., v. 82, no. 10, p. 2827–2844.

Weigand, P. W., and Ragland, P. C., 1970, Geochemistry of Mesozoic dolerite dikes from eastern North America: Contr. Mineralogy and Petrology, v. 29, no. 3, p. 195–214.

Jour. Research U.S. Geol. Survey
Vol. 4, No. 6, Nov.-Dec. 1976, p. 683–696

METAGRAYWACKE IN THE SALINIAN BLOCK, CENTRAL COAST RANGES, CALIFORNIA–AND A POSSIBLE CORRELATIVE ACROSS THE SAN ANDREAS FAULT

By DONALD C. ROSS, Menlo Park, Calif.

Abstract.—The schist of Sierra de Salinas is a monotonously homogeneous biotite quartzofeldspathic schist with minor amounts of quartzite, amphibolite, and marble that forms a northwest-trending outcrop belt that strikes across parts of the Santa Lucia and Gabilan Ranges and is traceable further south in the subsurface to where it is presumably cut off by the San Andreas fault zone. Chemical composition of the schist is similar to that of "average" graywackes. This large and monotonous terrane of metagraywacke is anomalous in the Salinian block, where a great variety of metamorphic rocks is the general rule. The age of the schist is not known, but it has been intruded by granitic rocks of presumably mid-Cretaceous age. Although it contains somewhat greater amounts of admixed quartzite, amphibolite, and marble, the schist of Portal-Ritter Ridge (Pelona Schist?), on the east side of the San Andreas fault and west of Palmdale, is nevertheless modally and chemically similar to the schist (metagraywacke) of Sierra de Salinas, and I suggest that the two terranes are correlative and once were contiguous.

The Salinian block, that part of the California Coast Ranges between the San Andreas fault and the Sur-Nacimiento fault zone, is underlain by a basement of Mesozoic granitic rocks that includes large volumes of metamorphic rock of unknown age. Most of the metamorphic material is quartzofeldspathic gneiss, schist, and granofels with abundant local admixtures of carbonate rocks. The overall composition of these rocks suggests that they were originally shelf or miogeoclinal sediments, similar to much of the Paleozoic section in the Great Basin.

In this environment a large block (220 square kilometres) of monotonously homogeneous biotite quartzofeldspathic schist in the Sierra de Salinas (fig. 1) as well as 23 km² of similar schist in the Gabilan Range and similar rock in nine well cores in the Salinas Valley are anomalous. The composition and physical appearance of the schist of Sierra de Salinas (an informal formational name to encompass all the schist occurrences) suggest a thick pile of graywacke with shaly interbeds.

Acknowledgments.—I wish to thank F. G. Poole and J. H. Stewart for their helpful reviews of this paper and more particularly for their ideas and unpublished data that confirmed my suspicions that the schist of Sierra de Salinas really cannot be part of the Antler flysch. I also benefited greatly from discussions with John Dillon and Gordon Haxel, whose geologic analyses of the Chocolate and Orocopia Mountains of southern California finally made me realize that the Schist of Sierra de Salinas is probably part of the Pelona Schist controversy.

SCHIST OF SIERRA DE SALINAS

Main mass (Sierra de Salinas)

By far the largest body of schist underlies the Sierra de Salinas. The compositional uniformity of this mass is truly remarkable. The schist is gray on fresh surfaces but weathers to various red and brown shades. In outcrop the rock is well foliated, but in thin section the overall texture is granoblastic. Some roadcut exposures on the east side of the Sierra de Salinas show thick blocky layers from 1 to 10 m thick, subdivided by thinner, darker, more micaceous layers; the similarity to a sequence of graywacke beds with shaly partings is striking.

The schist is composed dominantly of andesine (in part twinned), quartz, and strongly pleochroic reddish-brown biotite (table 1). Minor amounts of K-feldspar and muscovite are common, and some specimens contain small amounts of pink garnet; rarely sillimanite is present. Small zircon and apatite crystals are commonly rounded, which suggests that they are detrital. Field observations and thin-section study suggest that the modes listed in table 1 are representative of the rocks on the Sierra de Salinas. One sample of a thin layer of calc-hornfels (DR–1612A of table 1) contained clinopyroxene and epidote in place of the

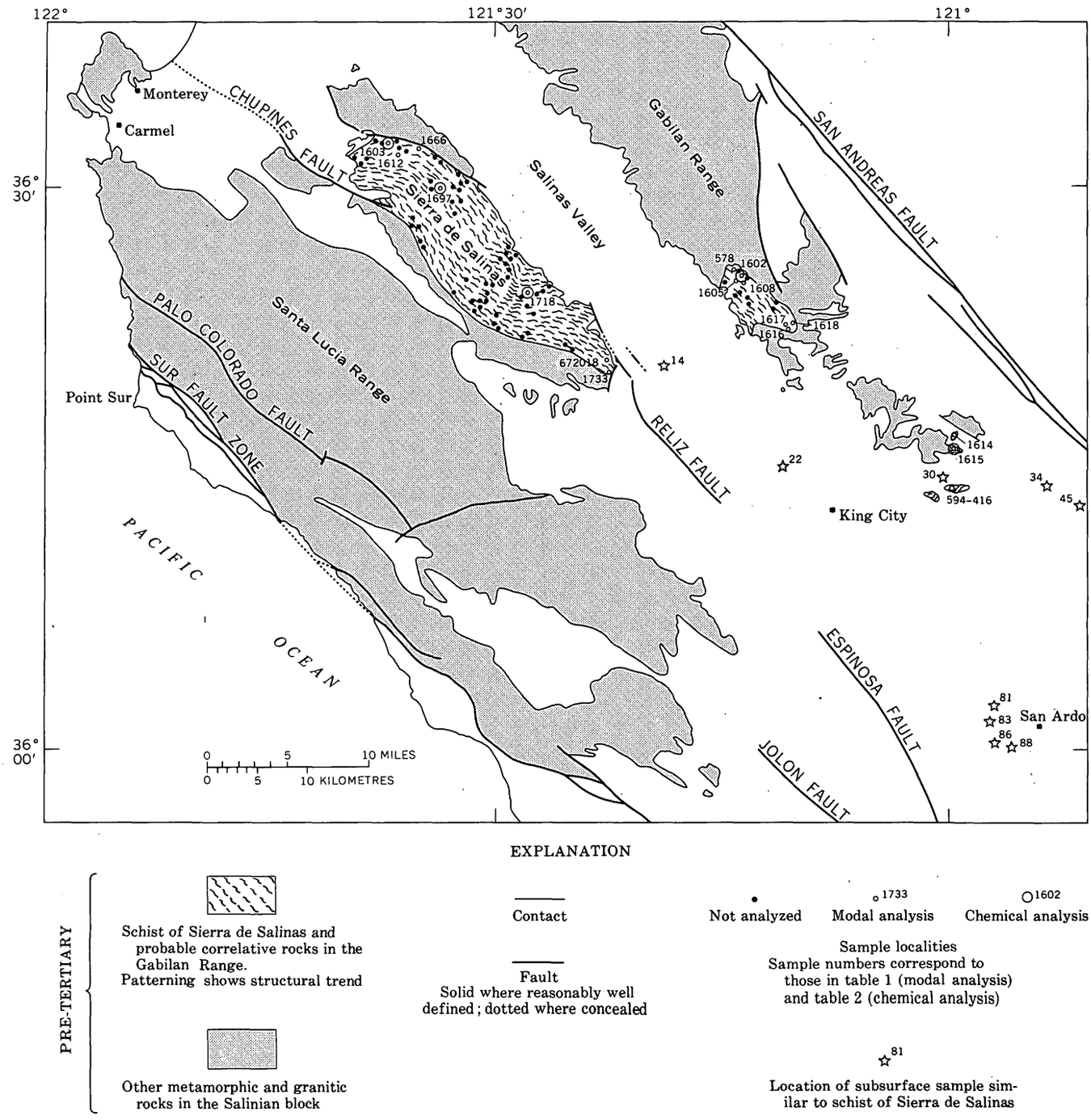

FIGURE 1.—Distribution of schist of Sierra de Salinas, central Coast Ranges, Calif.

biotite fraction of the schist. Some quartzite float was noted near the south end of the block, but it is not abundant.

Comparison of the three chemical analyses (table 2) from the Sierra de Salinas with their respective modes suggests that plagioclase was slightly overestimated and quartz slightly underestimated in the modes. The variation is only a few percent, which may only reflect the difference between my estimate of the chemical composition of the plagioclase and biotite and their true compositions because the individual minerals were not analyzed. Nevertheless, the variation is consistent for all three specimens, and 40 percent plagioclase and 35–38 percent quartz would better match the chemical analyses.

Vein quartz is common in the schist of the Sierra

TABLE 1.—*Modal data, in volume percent, for schist of Sierra de Salinas*

[Tr., trace; ------ not present]

Sample	Plagioclase[1]	K-feldspar	Quartz	Biotite	Other	
Sierra de Salinas						
672018(D)	40	<1	34	21	Muscovite, 5. Garnet, tr.	
DR-1603B	41(33)	<1	34.5	24.5		
DR-1666	45	1	34	19	Muscovite, 1.	
DR-1697	49(32)	5	29	14	Epidote, 2. Sphene, 1 Garnet, tr. Muscovite, tr.	
DR-1718B	44(30)	7	32	16	Muscovite, 1. Sphene, tr.	
DR-1733-1A-2.	53.5	---	31	15.5	Hornblende, tr.	
DR-1733-2B (float).	48.5	2	34	15.5	Muscovite, tr. Sphene, tr. Opaque minerals. tr.	
Average	46	2	33	18	1	
DR-1612A	45	3	30	---	Clinopyroxene, 18 Epidote, 3 Sphene, 1	Calc-hornfels.
Subsurface samples from well cores						
RS-22	42	<1	25	33		
RS-30	47	2	32	19	Magnetite, <1.	
RS-83B	53	9	25	13		
RS-86B	42	---	38	17	Muscovite, 3.	
Average	48	5	29	17	1	
Gabilan Range						
DR-578	45	---	32	22	Garnet, 1. Muscovite, tr.	
DR-1602	47(30)	---	33	20		
DR-1614	48	4	29	19	Muscovite, tr.	
DR-1615	41.5(31)	<1	40	16.5	Muscovite, 2.	
DR-1616	38	<1	31	24	Hornblende, 7	
DR-1617	43	---	37	20		
594-416	47	2	27	22	Muscovite, 2.	
Average	44	1	33	20.5	1.5	
DR-1608A	39	3	8	---	Hornblende, 48 Sphene, 2	Plagioclase amphibolite.
DR-1618	5	---	6	43	Hornblende, 46	Amphibolite.
DR-1605	------	---	85	---	Garnet, 12 Amphibole, 3	Garnetiferous quartzite.
Schist average.	45	2	32	19.5	1.5	

[1] Anorthite content of plagioclase (in parentheses) determined by X-ray diffraction.

de Salinas. The veins are commonly concordant and range in thickness from a few millimetres to more than a metre. The thickest extend for a few kilometres; Fiedler (1944, p. 190) noted veins as thick as 6 m that extended for 8 km along the southwest side of the crest of the Sierra de Salinas. The thinner ones probably were sweated out from the schist; they tend to be lenslike and to grade into the schist matrix. Most if not all of the vein quartz probably was locally derived from within the schist and in part was mobilized and squirted across the foliation.

Gabilan Range

One rather large mass of schist is present directly across the Salinas Valley from the south end of the Sierra de Salinas, and four smaller masses mark the southernmost exposures of the basement of the range. I examined the largest mass and the two northernmost small masses; the two southernmost outcrops were noted by Durham (1963, pl. 3; his specimen 594–416 is listed in table 1 of this report). The biotite quartzofeldspathic schist of these outcrops closely resembles the main schist mass of the Sierra de Salinas in both physical appearance and modal composition (table 1). The chemical analyses (table 2) are also strikingly similar. The schist in the Gabilan Range contains abundant quartz-rich lenses and thin layers that suggest material sweated out of the schist matrix. Prominent quartz veins, as thick as 3 m, extend for more than 1 km and are particularly abundant in the north part of the largest mass. The quartz veins generally parallel the structural trend, although some crosscut it.

The largest schist mass in the Gabilan Range is lithologically more variable than the schist in the Sierra de Salinas. Both amphibolite and garnetiferous quartzite (table 1) are locally abundant. A conspicuous lens of coarse-grained bright-green actinolite occurs in the center of the mass. One quartzite layer may contain quartzite pebbles. A brucite-bearing marble lens is present near the north end of the mass, and another marble lens is present near the south end. These occurrences, however, are only local variations from the predominant schist lithology.

The similarity of schist composition, rarity of metamorphic rock types other than schist, and abundance of vein quartz strongly suggest correlation between the Gabilan and Sierra de Salinas schist masses and also distinguish both of these masses from other metamorphic rocks in the two ranges.

Subsurface samples from well cores

Samples obtained from nine wells that penetrated the basement in the Salinas Valley area (fig. 1) are

TABLE 2.—*Chemical and semiquantitative spectrographic analyses of schists of Sierra de Salinas and Portal-Ritter Ridge*

	Schist of the Sierra de Salinas						Schist of Portal-Ritter Ridge			
	Sierra de Salinas			Gabilan Range (Miners Gulch)		Average				
	DR-1603[1,3]	DR-1697[1,3]	DR-1718[1,3]	DR-1602[2,3]	DR-1615[2,3]		DR-466[2,4]	DR-2417[2,4]	DR-2443[2,4]	Average
Chemical analyses, in weight percent										
SiO_2	70.3	72.1	70.3	70.50	70.22	70.5	69.83	67.49	69.73	69.02
Al_2O_3	14.1	14.1	14.5	14.26	14.92	14.4	15.01	15.67	15.30	15.33
Fe_2O_3	1.1	.80	.73	.95	.53	.8	.60	.96	.78	.78
FeO	2.9	2.0	2.7	2.79	2.74	2.6	2.14	2.59	1.98	2.24
MgO	1.9	1.1	1.5	1.35	1.39	1.5	1.52	1.85	1.36	1.58
CaO	2.9	3.0	2.8	2.80	2.54	2.8	3.67	3.43	2.59	3.23
Na_2O	2.8	2.8	3.0	3.67	3.19	3.1	3.31	3.52	3.46	3.43
K_2O	1.8	2.1	2.5	1.84	2.21	2.1	1.60	2.03	2.98	2.20
H_2O+	1.2	1.0	1.1	.90	1.08	1.1	1.15	1.16	1.21	1.17
H_2O-	.17	.13	.11	.09	.08	.1	<.02	<.02	.06	.02
TiO_2	.59	.42	.46	.54	.51	.5	.42	.50	.41	.44
P_2O_5	.13	.14	.12	.19	.11	.1	.14	.14	.10	.13
MnO	.07	.12	.12	.08	.05	.1	.06	.06	.04	.05
CO_2	<.05	<.05	<.05	<.05	<.05	<.05	.33	.26	.11	.23
Total	99.96	99.91	99.94	99.96	99.57	99.7	99.78	99.66	100.11	99.85
Semiquantitative spectrographic analyses, in parts per million										
Ba	500	500	500	300	300	-----	1,000	1,000	1,500	-----
Co	7	-----	5	10	7	-----	7	10	7	-----
Cr	50	20	30	50	70	-----	50	50	30	-----
Cu	7	-----	7	20	10	-----	10	15	7	-----
Ni	20	10	15	20	30	-----	20	15	15	-----
Pb	-----	-----	15	30	30	-----	10	15	20	-----
Sc	7	5	5	10	10	-----	10	10	7	-----
Sr	200	500	300	200	200	-----	500	700	1,000	-----
V	70	50	50	70	70	-----	70	100	70	-----
Y	-----	15	15	20	20	-----	15	15	10	-----
Zr	150	100	150	150	200	-----	100	100	100	-----
Ga	20	15	15	20	20	-----	20	20	20	-----
Yb	1	1	1	2	1.5	-----	3	3	1.5	-----
B	-----	-----	-----	-----	-----	-----	3	5	2	-----
Be	-----	-----	-----	-----	-----	-----	1.5	1.5	1.5	-----
La	-----	-----	-----	-----	-----	-----	20	50	30	-----
Nb	-----	-----	-----	-----	-----	-----	10	7	7	-----
Zn	-----	-----	-----	-----	-----	-----	100	100	70	-----
Ce	-----	-----	-----	-----	-----	-----	70	70	100	-----

[1] Chemical analyses determined by methods described by Shapiro and Brannock (1962), supplemented by atomic absorption. Analysts: P. Elmore, H. Smith, J. Kelsey, J. Glenn.
[2] Chemical analyses determined by X-ray fluorescence. I have arbitrarily added 0.5 percent SiO_2 to each analysis as SiO_2 tends to be incompletely determined with this method. Analysis: H. Elsheimer, L. Espos, J. Tillman.
[3] Semiquantitative spectrographic analyses by R. E. Mays.
[4] Semiquantitative spectrographic analyses by Chris Heropoulos.

similar to the schist outcrops in both the Sierra de Salinas and the Gabilan Range. Fresh core material was available for study from the four wells in the San Ardo area (81, 83, 86, 88) and from wells 22 and 30 near King City. Only small fragments from ditch samples were available from wells 14 and 34. The ditch samples contain not only schist chips but other rock types as well, and correlation is less certain for these wells. Well 45 penetrated schist of similar appearance, but the rock is brecciated and also contains chunks of other lithologies; the brecciation could be related to the nearby San Andreas fault. (For sources of the well-core data, see Ross, 1974.)

These subsurface schist samples are well-foliated gray rocks with abundant biotite that is strongly pleochroic in red-brown shades. Yet their overall appearance in thin section is granoblastic from abundant quartz and twinned plagioclase (oligoclase to andesine) and minor untwinned K-feldspar. Rounded zircons, which suggest a detrital origin, are found in most thin sections. Muscovite is minor but widespread. Some thin, quartz-rich lenses also resemble the presumably sweated out lenses that are common in the schist outcrops of the Sierra de Salinas and the Gabilan Range.

Very little can be said about the subsurface extent of the schist on the basis of so few samples, but a fair-sized body must be present just west of San Ardo. Basement wells that penetrate granitic rocks (Ross, 1974) provide limits for the schist near San Ardo to the east and south, but its extent west and north cannot be determined from the available subsurface data. Continuity of schist from well 22 to well 45 through wells 30 and 34 and the outcrops at the south end of the Gabilan Range is also possible but highly speculative. Extension of the schist basement northwest of well 22 to the two major outcrop areas is complicated

by the fact that a well midway between wells 22 and 14 reached granitic basement (Ross, 1974).

Some additional well information from M. B. Smith (written commun., 1974) shows not only that another well west of King City and south of well 22 (fig. 1) penetrated schist but that three nearby wells bottomed in "granite." The same communication notes schist in two wells just north of well 81, but "granite" was struck in wells east, west, and northwest of well 83. These data suggest that granitic terrane interrupts the area of schist between San Ardo and the Sierra de Salinas, but the size of this terrane and its contact relations are unknown.

COMPARISON OF SCHIST TO GRAYWACKE

The schist of Sierra de Salinas examined in some roadcuts resembles a pile of thick graywacke beds with shaly partings. The relatively close clustering of the modes, which represent samples collected over the rather extensive schist terrane (table 1, fig. 2), emphasizes a homogeneity that is compatible with a graywacke parent. These rocks, however, are thoroughly recrystallized and retain no original sedimentary texture.

Metamorphism of the schist, though fairly thorough, seems to have been largely isochemical but with local segregation of quartz and feldspar. Thus, a sample that is not near such segregations may approximate the chemical composition of the original sediment. Three schist samples have been chemically analyzed from the main mass as well as two from the Gabilan Range (table 2). The chemical analyses are remarkably similar, and it seems reasonable to presume that an average of these analyses represents the entire schist terrane, in view of the modal similarity of the schist outcrops and well cores.

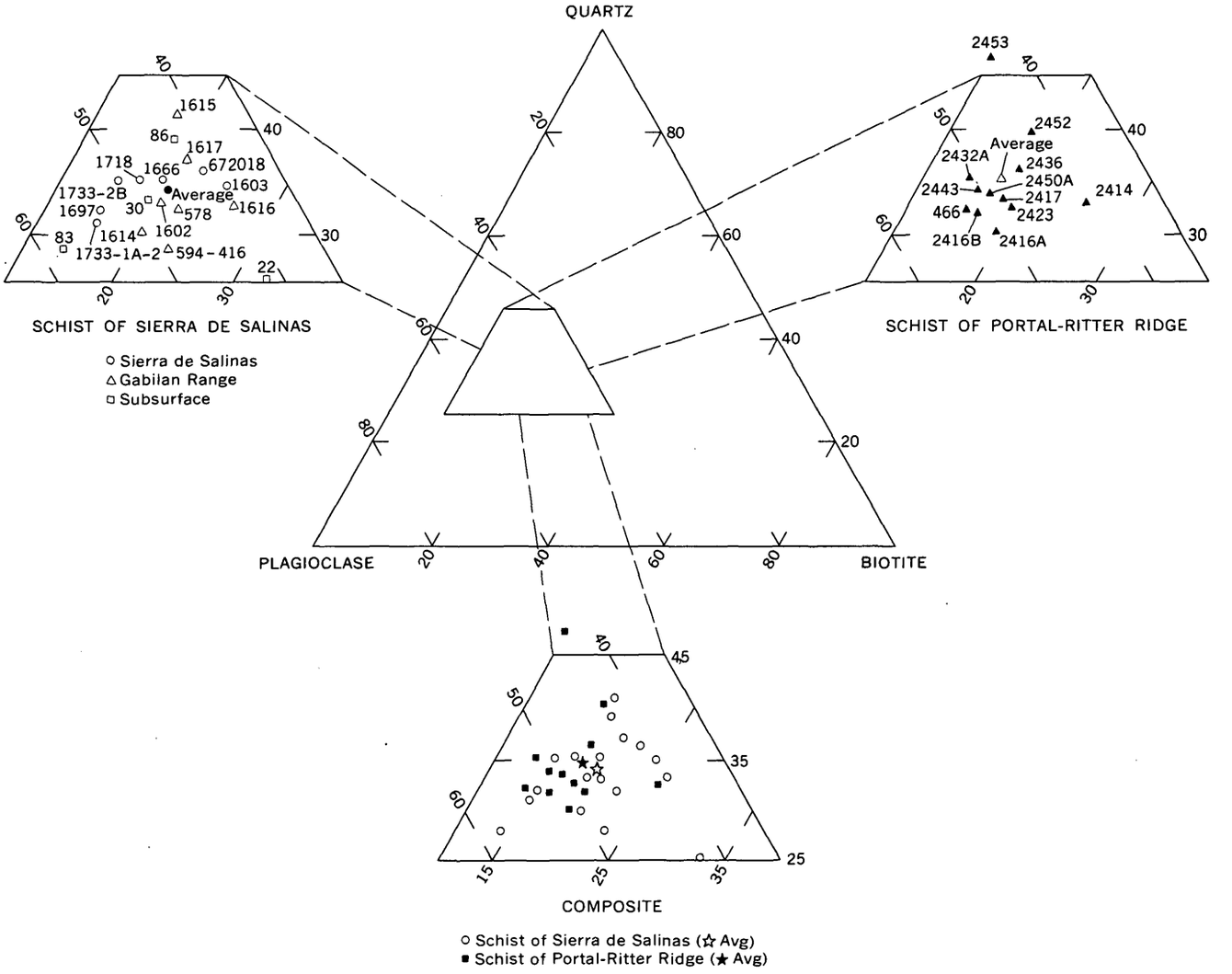

FIGURE 2.—Ternary diagrams of plagioclase, quartz, and biotite in schists of Sierra de Salinas and Portal-Ritter Ridge.

The general chemical similarity of the schist of Sierra de Salinas to graywacke is shown in table 3, which compares a number of graywacke averages with the average of the five schist analyses. Although the schist contains a little more SiO_2 and CaO and somewhat less total iron, the overall compositions are very similar. Pettijohn (1963) noted that graywackes characteristically have an excess of FeO over Fe_2O_3 and an excess of Na_2O and K_2O. The schist samples compare well with the average graywackes for both of these ratios (fig. 3). The plotted ratio of CaO to MgO (fig. 3) shows the somewhat higher CaO content of

TABLE 3.—*Average chemical analysis, in weight percent, for schist of Sierra de Salinas and schist of Portal-Ritter Ridge compared to some graywacke averages*

	(1)	("1A")	(2)	(3)	(4)	(5)	(6)	(7)
	Schist of Sierra de Salinas (average of 5 analyses)	Schist of Portal-Ritter Ridge (average of 3 analyses)	Pettijohn (1963, p. 57) (average of 61 graywackes)	Bailey and others (1964, p. 34) (average of 21 Franciscan graywackes)	Tyrell (1933, p. 26) (average of 30 graywackes)	Mattiat (1960) (average of 17 Harz Mtn. Paleozoic graywackes)	Reed (1957) (average of 14 New Zealand Mesozoic graywackes)	Reed (1957) (composite sample of 20 graywackes, Wellington, New Zealand)
SiO_2	70.5	69.02	66.8	67.5	68.1	69.7	69.7	71.1
Al_2O_3	14.4	15.33	13.5	13.5	15.4	14.3	14.3	13.9
Fe_2O_3	0.8	.78	1.6	1.2	1.0	1.9	1.0	Trace
FeO	2.6	2.24	3.5	3.0	3.4	2.4	2.5	2.7
MgO	1.5	1.58	2.1	2.2	1.8	1.8	1.2	1.3
CaO	2.8	3.23	2.5	2.4	2.3	1.3	1.9	1.8
Na_2O	3.1	3.43	2.9	3.6	2.6	3.1	3.5	3.7
K_2O	2.1	2.20	2.0	1.7	2.2	1.4	2.4	2.3
H_2O+	1.1	1.17	2.4	2.5	2.1	2.4	1.9	1.9
H_2O-	.1	.02	.6	.4		.4	.4	.3
TiO_2	.5	.44	.6	.5	.7	.5	.6	.5
P_2O_5	.1	.13	.2	.1	.2	.1	.2	.1
MnO	.1	.05	.1	.1	.2	.1	.1	---
CO_2	<.05	.23	1.2	.8	---	.9	.1	.1
Other	---	---	.5	---	---	---	.1	---
Total	99.7	99.85	100.5	99.5	100.0	100.3	99.9	99.7

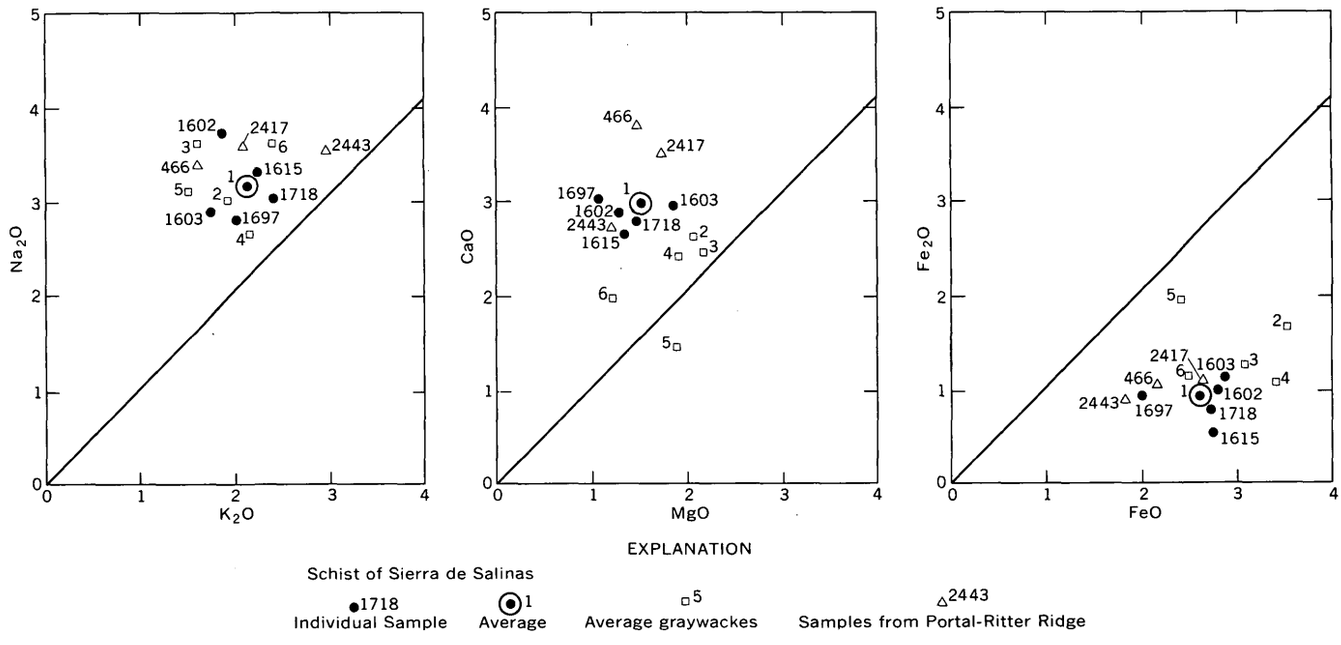

FIGURE 3.—Ratios of various oxides (weight percent) in schist of Sierra de Salinas compared to averages of graywacke (as listed in table 3) and samples from Portal-Ritter Ridge.

the schist compared to graywacke. Pettijohn (1963) further noted that, characteristically, arkose, argillite, shale, and slate have K_2O in excess of Na_2O. Thus, the chemical fingerprints of the schist eliminate these rock types and support the likelihood that the schist is a metamorphosed graywacke. A log plot of K_2O:Na_2O and Fe_2O_3:FeO (fig. 4) emphasizes further the close chemical affinity of the schist to graywacke. A comparison of trace elements with sandstone averages (table 4) shows a rather good correspondence with the exception of strontium, which is an order of magnitude higher in the schist.

The ternary diagram of total Fe as Fe_2O_3-MgO-TiO_2 (fig. 5) shows the average of the schist of Sierra de Salinas centered in the rather tightly clustered field of graywacke averages as listed in table 3. The ternary diagram of CaO-Na_2O-K_2O (fig. 5) shows that this schist is richer in CaO relative to the plotted graywacke averages. The ratio CaO:Na_2O:K_2O seems to divide the rocks into two groups: (1) the schist of Sierra de Salinas plus graywacke averages 2–4 have the ratio 1:1.1–1.5:0.7–0.9, whereas (2) graywacke averages 5–7 have the ratio 1:1.8–2.4:1.1–1.3 with K_2O higher relative to CaO than in the first group. Nevertheless, the overall field is relatively restricted, and the differences are probably not significant. Both ternary diagrams show the comparability of the chemical composition of graywacke to granodiorite.

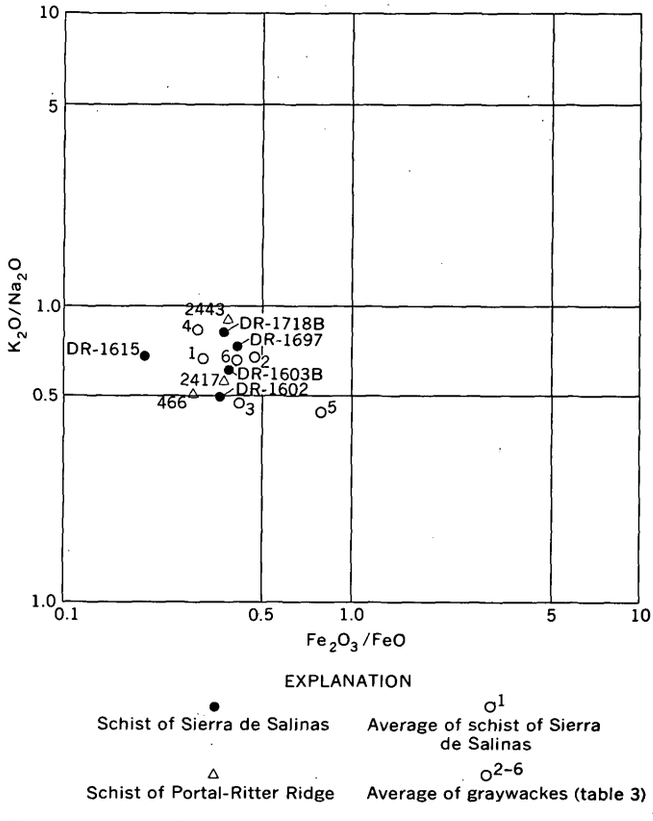

FIGURE 4.—Log plot of K_2O:Na_2O and Fe_2O_3:FeO for chemically analyzed specimens of schist of Sierra de Salinas, schist of Portal-Ritter Ridge, average of schist of Sierra de Salinas (1 of table 3), and various average graywackes (2–6 in table 3).

TABLE 4.—*Trace-element content, in parts per million, of schist of Sierra de Salinas compared to sandstones*

Element	Schist of Sierra de Salinas	Sandstone averages		
		Green (1959)	Turekian and Wedepohl (1961)	Pettijohn (1963)
Ba	500	170	300	*450
Cr	20–50	10–100	10–20	10–100
Cu	7	10–40	10–20	10–20
Ga	15–20	5(?)	5–10	5–10
Ni	10–20	2–10(?)	2	2–8
Pb	<7–15	9	9	7–8
Sc	5–7	1	1	1–4
Sr	200–500	26	35	26–45
V	50–70	10–60	10–20	10–60
Y	<10–15	2	4	4
Yb	1	-------	4	4
Zr	100–150	148	200–250	*220–370

*Graywacke.

These data on the chemical and modal character of the schist, combined with the vast area underlain by this schist, strongly suggest that the schist of Sierra de Salinas is a metagraywacke. No other sedimentary rock type, or combination of rock types, seems a likely alternative.

CONTACT RELATIONS WITH SURROUNDING GRANITIC TERRANES

The two largest schist masses (fig. 1) are definitely roof pendants in the granitic terrane; the smaller outcrops and subsurface occurrences also are assumed to be parts of pendants. Prior to writing this report, I was strongly impressed by the lithologic contrast between the main schist mass on the Sierra de Salinas and the surrounding mixed granitic and metamorphic terrane, the nearly parallel linear contacts along the two sides of that schist body (particularly along the west side), and the absence of granitic intrusive rocks within the body of schist. This led me to report (Ross and Brabb, 1973; Ross, 1974) that the schist was separated from the adjacent terranes by major Cenozoic faults. The following discussion refutes that supposition.

Near the south end of the Sierra de Salinas (loc. 1733, fig. 1), the contact of the schist with granitic rocks is marked by coarsened schist, granitic admixture, and the contact-metamorphic development of distinctive hornblende-rich layers in the schist. Similar hornblende-rich layers are found in the schist in the contact zone (west of sample loc. 1603, fig. 1).

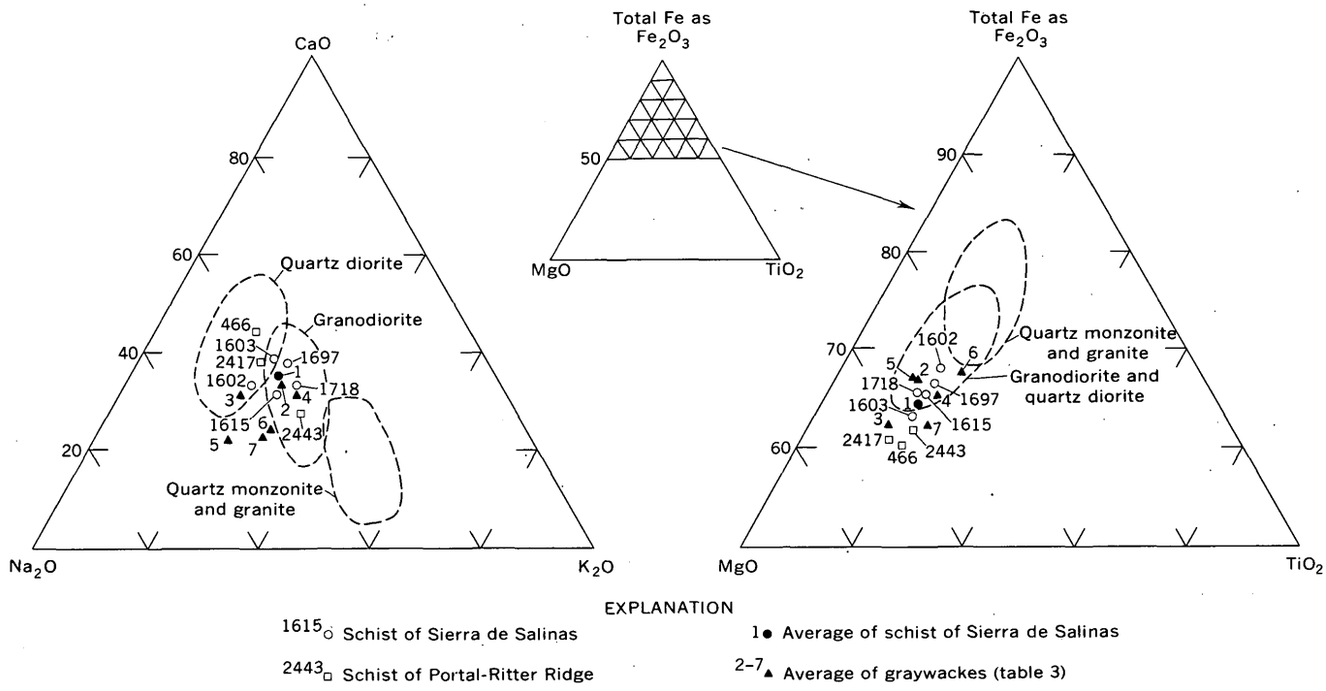

FIGURE 5.—Ternary diagrams showing relations CaO-Na_2O-K_2O and total Fe as Fe_2O_3-MgO-TiO_2 for chemically analyzed specimens of schist of Sierra de Salinas, schist of Portal-Ritter Ridge, average of schist of Sierra de Salinas (1 on table 3), and various average graywackes (2–7 in table 3). Dashed line fields from Condie (1967).

Here a body of dark-colored diorite and quartz diorite with as much as 30 percent each of biotite and hornblende and associated coarse-grained hornblende pegmatite has a gradational contact with the schist. The contact zone is more than 100 m wide and comprises coarsened schist studded with hornblende crystals grading into strongly foliated granitic material with wisps of schist and abundant dark, ellipsoidal inclusions. Dark granitic dikes are also associated with the gradational contact zone. Although exposures of the contact zone are rare, they strongly suggest abundant assimilation, if not extensive granitization. Similar hornblende-bearing layers were noted in the schist along the west contact midway between these two localities. The development of hornblende in these schist localities along the contact zone is almost certainly a contact metamorphic effect.

Although shearing was observed at one point along the west contact, the contact is unsheared a few kilometres away. Therefore, my original hypothesis that the Chupines fault continued along the west side of the schist of Sierra de Salinas and marked a major fault zone has been destroyed by the inescapable data that indicate this is an intrusive contact which has undergone minor postintrusive movement. Dibblee (1972a) showed the Chupines fault splaying out in the schist nearly parallel to the contact. The sharp lithologic contrast of metamorphic types across the western contact of the schist of Sierra de Salinas does suggest, however, a possible pregranitic stratigraphic and (or) structural break.

The northeastern contact of the schist of Sierra de Salinas is most likely a fault but could perhaps be an intrusive contact. The southernmost part of this contact is marked by a linear canyon with the blocky monotonous schist of Sierra de Salinas on the southwest side and felsic granitic rocks migmatitically mixed with metamorphic rocks, which contain abundant marble on the northeast side. Near modal specimen locality 1666 (fig. 1), a roadcut exposes about 1 m of gouge between the schist and mixed granitic and metamorphic rocks. The trend of the gouge zone lines up with the linear canyon to the southeast. To the northwest a fault has been mapped between the felsic granitic rocks and Cenozoic deposits (Dibblee, 1973), also on line with the other suggested fault segments. These three alined postulated fault segments and the abrupt change in lithology across the line suggest that this is a fault; the magnitude of displacement is unknown. By analogy with the relations along the southwestern contact, however, the feature could instead be an intrusive contact that has been somewhat sheared. Granitic rock is present about 400 m west of the presumed fault line (east of loc. 1697, fig.

1), but poor exposure precludes knowing if this is a fault slice or an intrusive body in the margin of the schist mass.

Along the northeast side of the largest schist mass in the Gabilan Range a gradational mixed contact zone about 100 m wide is exposed midway between modal sample localities 1602 and 1618 (fig. 1), and the same relations are also seen, but much more poorly exposed, near the north end of the mass (near sample loc. 578, fig. 1), which contains euhedral tourmaline crystals. Within the contaminated contact zone, aplite, pegmatite, and felsic granitic rock are abundant, and some migmatitic mixing of schist suggests schist assimilation (or granitization). This pendant contains several dikes of biotite-bearing granitic rock and an unusual hornblende leuco-diorite near the center of the mass, in addition to scattered pegmatite dikes. In contrast, the schist mass that underlies the Sierra de Salinas contains some pegmatite but no other granitic intrusive rocks in the interior of the pendant.[1] The greater abundance of intrusive material in the Gabilan Range mass may reflect its smaller size and the possibility that it may be a rather thin skin on the present surface (a gently dipping dip-slope slab). It seems characteristic that this schist is not intruded beyond the contact zone (and rarely even there) by the granitic plutons of the region. I suspect that most if not all of the quartz veins and pegmatite are locally sweated out of the schist and do not constitute true granitic intrusions.

Having been originally and erroneously convinced that these linear, abrupt contacts indicated post-granitic faults, largely on the basis of the absence of granitic apophyses in the schist, I have perhaps belabored the evidence for intrusion. Nevertheless, it seems important to document this evidence and to note that for some unknown reason, granitic intrusive rocks had difficulty in penetrating these schist masses, particularly in the Sierra de Salinas.[2]

SPECULATIONS ON CORRELATION

As previously noted, the schist of Sierra de Salinas contrasts markedly with most of the metamorphic terrane in the Salinian block, where compositionally variable rocks that probably represent a shelf or miogeosynclinal environment are the rule. The bulk of the evidence points to a graywacke source for the schist of Sierra de Salinas. If we look for graywacke-rich sedimentary sections with some admixtures of volcanic material (because of the amphibolites) from which such a mass of schist could be derived, the nearest sources are the Great Valley and the Franciscan assemblages, both of Mesozoic age (Bailey and others, 1964). Neither of these assemblages is known from the Salinian block, and neither is known to have reached the amphibolite grade of metamorphism. Thus, these two assemblages seem unlikely correlatives for the schist. However, in southern California a widespread terrane of schistose rocks is present that is largely derived from graywacke, siltstone, and shale and is now thought most likely to be Mesozoic in age (Muehlberger and Hill, 1958; Ehlig, 1968). These schistose rocks, collectively called the Pelona Schist, and their probable correlatives, the Rand and Orocopia Schists (fig. 6), at first glance seem a poor correlative for the schist of Sierra de Salinas. Most of the Pelona Schist and its correlatives have been metamorphosed to the greenschist facies and are rich in muscovite, albite, and chlorite in addition to quartz. One fault-bounded schist mass on the east side of the San Andreas fault is somewhat different from much of the Pelona Schist, but nevertheless most workers include it in the Pelona.

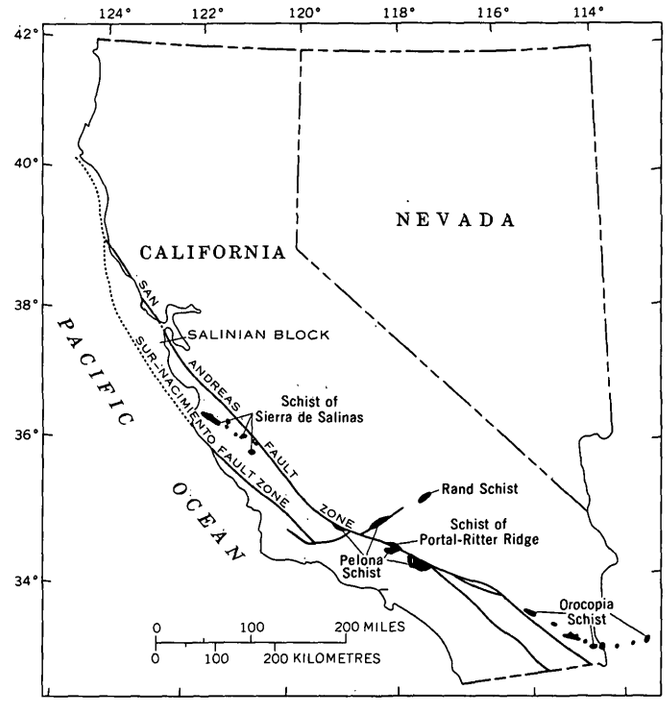

FIGURE 6.—Distribution of schist of Sierra de Salinas and Pelona Schist and its possible correlatives.

[1] John T. Dillon (written commun., 1975) found a granitic dike about 10 cm thick in the schist about 2 to 3 km west of locality 1718. He has shown me a colored slide of the dike, but no specimen was collected.

[2] I have been very impressed in the field by the almost total lack of crosscutting granitic material in this schist mass that covers more than 200 km². In contrast, granitic diking and magmatitic mixing are virtually ubiquitous in other metamorphic rocks in the Santa Lucia Range. If the Sierra de Salinas mass were transported and its margins with their intrusive evidence were consequently sheared away and the body were then examined in a typical poorly exposed setting, one would justly conclude it had not been intruded by granitic material. In this light, some of the now structurally isolated Pelona Schist masses might be analogous to the schist of Sierra de Salinas.

These rocks, exposed on Portal-Ritter Ridge, west of Lancaster (fig. 7), have been metamorphosed to the amphibolite facies but were derived largely from a graywacke protolith and represent the same depositional environment as the Pelona-Orocopia assemblages. Gordon Haxel (oral commun., 1975) has told me that part of the Orocopia Schist is in the amphibolite facies. Thus, though the Pelona and Orocopia

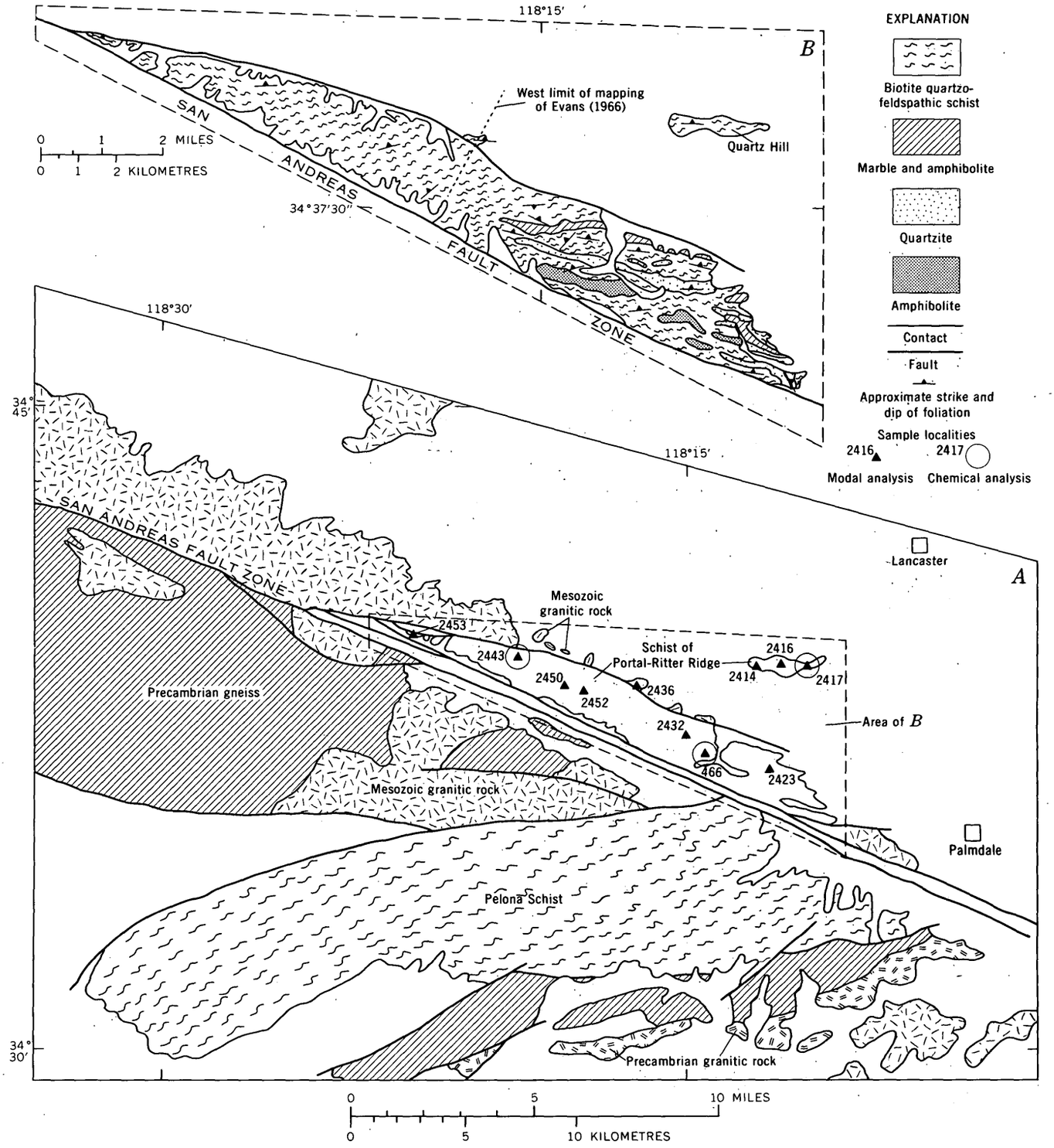

FIGURE 7.—Generalized geologic maps showing location of modally and chemically analyzed samples of schist of Portal-Ritter Ridge. *A*, Regional geologic map. *B*, Map of Portal-Ritter Ridge area.

Schists are dominantly greenschist, they do reach amphibolite grade locally, and it is fair to assume that the schist and associated rocks of Portal-Ritter Ridge are part of the Pelona-Orocopia terrane.

The metamorphic rocks of Portal-Ritter Ridge are dominantly biotite quartzofeldspathic schist whose eastern outcrops have been studied in detail by Evans (1966). Evans stressed the structural analysis of these rocks adjacent to the San Andreas fault, but he also presented abundant petrographic data on the schists and associated rocks. The following description draws heavily on Evans' data but is supplemented by petrographic studies I made after a reconnaissance study of Portal-Ritter Ridge in 1974.

The micaceous quartzofeldspathic schist of Portal-Ritter Ridge is very similar, in appearance and modal composition, to the schist of Sierra de Salinas (compare tables 1, 5). Plagioclase is well twinned and, in part, zoned. Evans (1966) noted cores as calcic as An_{65} with andesine to albite rims. In 10 samples of schist that I collected throughout the ridge area, X-ray diffraction patterns show that the plagioclase ranges from An_{28} to An_{34}. These values are comparable to the anorthite values obtained from plagioclase of the schist of Sierra de Salinas. Biotite is brownish to reddish brown, and pale garnet is scattered but widespread. The modes (table 5) show the general homogeneity of the schist. Chemical analyses of three specimens of the schist of Portal-Ritter Ridge (table 2) compare very closely with the Sierra de Salinas analyses (figs. 3–5). SiO_2 averages about 0.5 percent lower and Al_2O_3 about 1 percent higher in the Portal-Ritter Ridge specimens (tables 2, 3), but this does not appear to be a significant difference. The trace elements of the two terranes are also comparable, but both barium and strontium are somewhat higher in the Portal-Ritter Ridge rocks. Six elements were detected in the Portal-Ritter Ridge rocks (table 2) that were not noted in the Sierra de Salinas rocks. All six are near or at the lower level of detectibility, however, so the difference between the terranes on this basis is slight.

TABLE 5.—*Modal data for schist of Portal-Ritter Ridge*

Sample	Plagioclase [1]	K-feldspar	Quartz	Biotite	Muscovite	Garnet	Other
DR-466	51(28)	<1	31	15	3	0	<1
DR-2414	41	0	32	25	0	1	1
DR-2416A	49(30)	0	29	18	3	0.5	0.5
DR-2416B	50	1	30	15	1	1	2
DR-2417	46(28)	0	31	17	4	0	2
DR-2423	47(31)	3	30	18	1	<1	1
DR-2432A	50(34)	0	34	14	2	0	<1
DR-2436	45(32)	1	35	17	1	<1	1
DR-2443	42(28)	16	28	13	0	<1	1
DR-2450A	47	4	32	15	0	<1	1
DR-2452	40(31)	7	37	16	0	0	<1
DR-2453	42(31)	1	46	10	1	0	<1
Average	46	3	33	16	1	<1	1

[1] Anorthite content of plagioclase (in parentheses) determined by X-ray diffraction.

Evans (1966) noted that muscovite and chlorite were more abundant than biotite in the schist on the southern flank of Portal-Ritter Ridge. In my less detailed studies, I have found the biotite schist abundant throughout the area. Abundant muscovite and chlorite seem to be restricted to the southeast part of the ridge area, and, here, quartzite, amphibolite, and marble are commonly interbedded in the schist sequence (fig. 7). Brownish garnet is present and locally abundant in the quartzite. Red-violet piemondite is also a local but spectacularly vivid accessory mineral in the quartzite. The amphibolite occurs as two types: (1) fine-grained amphibolite composed of hornblende, andesine, and lesser epidote and associated with mica schist layers, and (2) coarser-grained layers associated with calc-hornfels and marble layers.

This area of mixed lithologies is similar to parts of the Gabilan Range where amphibolite, marble, and quartzite are associated with the biotite schist. Coarse bright-green lenses of actinolite are local but striking occurrences both in Miners Gulch (Gabilan Range) and on Portal-Ritter Ridge. In macroscopic appearance, petrographic character, and modal and chemical composition, the schist of Portal-Ritter Ridge strongly resembles the schist of Sierra de Salinas, and the correlation of these two schist terranes is strongly suggested.

White vein quartz is common, occurs as sill-like bodies, and, in part, appears to be sweated out of the schist and associated with simple pegmatite, much like in the outcrops of the schist of Sierra de Salinas. One contrast between the two terranes is the widespread occurrence of dark diabasic dikes composed of labradorite, hornblende, clinopyroxene, and minor quartz in the schist of Portal-Ritter Ridge. Such dikes have not been found in the schist of Sierra de Salinas. The age of the dikes is unknown, and it is possible that they postdate the postulated structural dislocation required if the schist of Portal-Ritter Ridge and Sierra de Salinas are correlative.

Another sequence that should be considered as a possible correlative to the schist of Sierra de Salinas is a belt of fine- to coarse-grained flysch of Late Devonian and Mississippian age (fig. 8) that strikes southward across Nevada and California and is truncated by the San Andreas fault in southern California. This sequence, called Antler flysch by Poole (1974), is composed of shale, siltstone, impure sandstone, conglomerate (rich in chert clasts), limestone, and local vol-

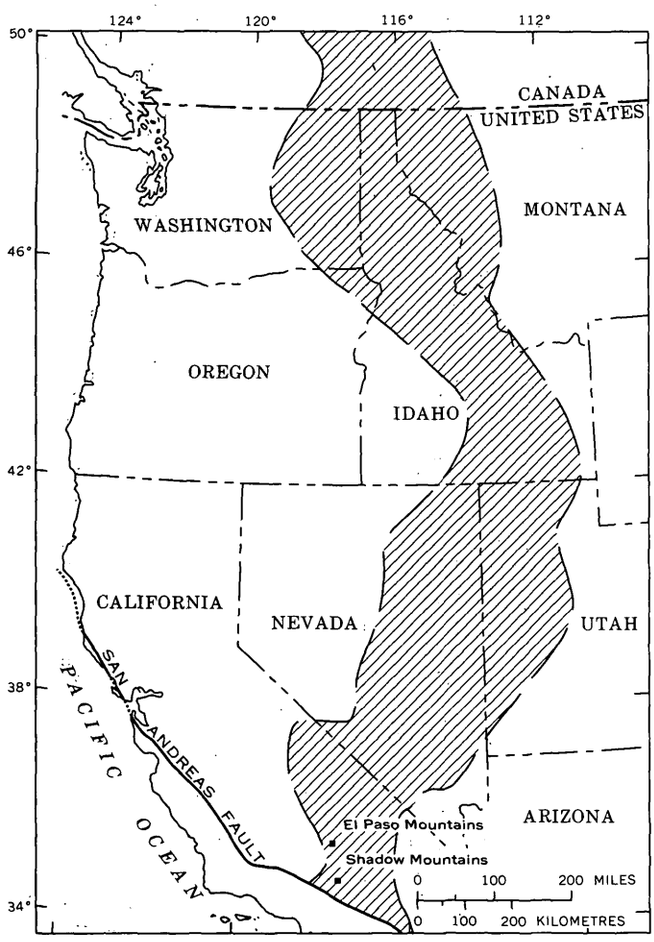

FIGURE 8.—Area of deposition of Antler flysch of Poole (1974) of Late Devonian and Mississippian age (diagonal lined pattern). Southernmost exposures of these rocks are in the Shadow Mountains.

canic layers. The lithologic variety of the Antler flysch and particularly the abundance of coarse clastic material are in rather sharp contrast to the monotonous and fine-grained protolith of the bulk of the schist of Sierra de Salinas. Poole (written commun., 1975) noted that the sandstone and quartzite of the Antler flysch belt are at best subgraywacke with more than 80 percent SiO_2 and less than 2 percent Na_2O plus K_2O, which seems to make an unlikely correlative for the metagraywacke of the Sierra de Salinas. My observations of the nearest Antler flysch deposits to the Portal-Ritter Ridge area, in the Shadow and El Paso Mountains (fig. 8), left me unconvinced of the correlation.

The only reason to cling to the perhaps remote possibility of the correlation of the Antler flysch and the schist of Sierra de Salinas is that the structure would be simpler if the schist were Paleozoic (the most probable age of the other metamorphic rocks in the Santa Lucia and Gabilan Ranges) rather than Mesozoic (the probable age of the Pelona and Orocopia Schists). All this notwithstanding, the physical character of the schist of Sierra de Salinas and its modal and chemical character support much more strongly the thesis that it is related to the Pelona and Orocopia schists, that it is more probably therefore Mesozoic, and that important pregranitic structural events took place to put the schist in its present anomalous position.

DISCUSSION

The schist of Sierra de Salinas furnishes the first real stratigraphic tie between the Santa Lucia and Gabilan Ranges (fig. 1). This relation almost rules out my earlier speculations about a major structural dislocation between the two ranges (Ross, 1972, p. 33). Compton (1966, p. 285) previously suggested that the structural sequence in the northern Gabilan Range was similar to that in the metamorphosed rocks in the Junipero Serra area of the Santa Lucia Range. This previous suggestion of a similar structural history for the two ranges, coupled with the schist correlation between the ranges, argues that the ranges are in the same structural block. If this is true, then the Salinas Valley is not a good candidate for major postgranitic (Cenozoic) strike-slip faulting along the King City fault as suggested previously by Ross and Brabb (1973). The Rinconada fault zone of Dibblee (1972b), which continues into this area as the Espinosa and Reliz faults (fig. 1), might have about 20 km of right-lateral offset at this latitude, but the general configuration of the schist belt does not allow for much more.

Johnson and Normark (1974) and Howell (1975), in recently proposed plate tectonic models that attempt to explain the anomalous position of the Salinian block, have suggested that the block has been stretched and segmented by internal strike-slip movements. Possibly they were influenced in part by my erroneous interpretation that the Salinas Valley marked a major strike-slip dislocation (Ross, 1972, p. 34). The schist correlation across the Salinas Valley, together with the intrusive relations along the west side of the schist belt and the continuity of metamorphic and granitic units further west in the Santa Lucia Range, mean that the Salinian block is probably a coherent basement block from the San Andreas fault west as far as the Palo Colorado fault (fig. 1). Any major segmenting of the Salinian block at the latitude of the Santa Lucia and Gabilan Ranges seems unlikely, but if it occurred, it must be west of the Palo Colorado fault, or pregranitic. Furthermore, the probable correlation of granitic units from the Gabilan Range

south through the subsurface to the La Panza Range (Ross, 1974) puts even more severe limits on the amount of stretching and segmentation that the Salinian block could have undergone.

The schist of Sierra de Salinas, a lithologically distinctive marker, appears to extend for about 100 km in a belt 10–15 km wide (fig. 6). It is thus a regionally important unit whose faulted counterpart should be readily recognizable in a similarly metamorphosed terrane. The only suitable terrane found so far is the schist of Portal-Ritter Ridge (figs. 6, 7). The lithologic similarity, metamorphic grade, and structural setting on the east side of the San Andreas fault make this a likely correlative. The previously discussed evidence that the Portal-Ritter Ridge schist is part of the Pelona-Orocopia terrane thus implicates the schist of Sierra de Salinas in this long-time and major controversy. If the correlation is valid, a minimum right-lateral offset of 300 km is called for along the San Andreas fault. But even beyond this is the difficulty in explaining the presence of a belt of Mesozoic schist nestled in the Salinian block among the other metamorphic rocks of probable Paleozoic age. All of the metamorphic rocks, including the schist of Sierra de Salinas, are intruded by Mesozoic (at least in part mid-Cretaceous) granitic rocks. Some major pregranitic structural contortions are required in order to insert the schist of Sierra de Salinas into the older metamorphic terrane.

One of the enigmatic problems connected with the schist of Sierra de Salinas is that it is intruded by Mesozoic granitic rocks, whereas its supposed correlatives and analogues, the Pelona and Orocopia Schists, are not. A model proposed by Dillon and Haxel (1975) suggests that the protoliths of the Orocopia and Pelona Schists were deposited in a back-arc basin on the continent side and well removed from the intrusive rocks of the magmatic arc.

To cope with this dilemma, John Dillon (oral commun., 1974) suggested to me the attractive possibility that the Cretaceous magmatic arc may have intersected the back-arc basin to the north. This would accommodate in the total Pelona-Orocopia picture the seemingly anomalous intrusive rocks in the Sierra de Salinas terrane. Despite the fact that there is as yet no direct evidence that Mesozoic intrusive rocks cut the Portal-Ritter Ridge schist terrane, the map pattern (fig. 7) suggests that granitic rocks interrupt the schist between the main mass and Quartz Hill, somewhat analogous to the pattern in the south part of the belt of schist of Sierra de Salinas (fig. 1). Therefore the lack of visible intrusive relations at Portal-Ritter Ridge should not rule out the correlation.

REFERENCES CITED

Bailey, E. H., Irwin, W. P., and Jones, D. L., 1964, Franciscan and related rocks, and their significance in the geology of western California: Calif. Div. Mines and Geol. Bull. 183, 177 p.

Compton, R. R., 1966, Granitic and metamorphic rocks of the Salinian block, California Coast Ranges: Calif. Div. Mines and Geology Bull. 190, p. 277–287.

Condie, K. C., 1967, Geochemistry of early Precambrian graywacke from Wyoming: Geochim. et Cosmochim. Acta, v. 31, no. 11, p. 2135–2149.

Dibblee, T. W., Jr., 1972a, Geologic map of the Jamesburg quadrangle, California: U.S. Geol. Survey open-file map.

Dibblee, T. W., Jr., 1972b, The Rinconada fault in the southern Coast Ranges, California, and its significance: Geol. Soc. America Abs. with Programs, v. 4, no. 3, p. 145–146.

Dibblee, T. W., Jr., 1973, Geologic map of the Salinas quadrangle, California: U.S. Geol. Survey open-file map.

Dillon, John, and Haxel, Gordon, 1975, The Chocolate Mountain-Orocopia-Vincent thrust system as a tectonic element of Late Mesozoic California: Geol. Soc. America Abs. with Programs, v. 7, no. 3, p. 311–312.

Durham, D. L., 1963, Geology of the Reliz Canyon, Thompson Canyon, and San Lucas quadrangles, Monterey County, California: U.S. Geol. Survey Bull. 1141–Q, 41 p.

Ehlig, P. L., 1968, Causes of distribution of Pelona, Rand, and Orocopia Schists along the San Andreas and Garlock faults, *in* Proceedings of Conference on geologic problems of San Andreas fault system: Stanford Univ. Pubs., Geol. Science, v. 11, p. 294–306.

Evans, J. G., 1966, Structural analysis and movements of the San Andreas fault zone near Palmdale, California: California Univ., Los Angeles, Ph.D. thesis, 186 p.

Fiedler, W. M., 1944, Geology of the Jamesburg quadrangle, Monterey County, California, *in* 40th report of the State Mineralogist: Calif. Jour. Mines and Geology, v. 40, no. 2, p. 177–250.

Green, Jack, 1959, Geochemical table of the elements for 1959: Geol. Soc. America Bull., v. 70, no. 9, p. 1127–1183.

Howell, D. G., 1975, Hypothesis suggesting 700 km of right slip in California along northwest-oriented faults: Geology, v. 3, no. 2, p. 81–84.

Johnson, J. D., and Normark, W. R., 1974, Neogene tectonic evolution of the Salinian block, west-central California: Geology, v. 2, no. 1, p. 11–14.

Mattiat, Bernhard, 1960, Beitrag zur Petrographie der Oberharzer Kulmgrauwacke: Beitr. Mineralogie u. Petrographie, v. 7, p. 242–280.

Muehlberger, W. R., and Hill, H. S., 1958, Geology of the central Sierra Pelona, Los Angeles County, California: Am. Jour. Sci., v. 256, no. 9, p. 630–643.

Pettijohn, F. J., 1963, Chemical composition of sandstones—excluding carbonate and volcanic sands: U.S. Geol. Survey Prof. Paper 440–S, p. S1–S21.

Poole, F. G., 1974, Flysch deposits of Antler foreland basin, western United States, *in* Dickinson, W. R., ed., Tectonics and sedimentation: Soc. Econ. Paleontologists and Mineralogists Spec. Pub. No. 22, p. 58–82.

Reed, J. J., 1957, Petrology of the lower Mesozoic rocks of the Wellington district: New Zealand Geol. Survey Bull., n.s., v. 57, p. 60.

Ross, D. C., 1972, Petrographic and chemical reconnaissance study of some granitic and gneissic rocks near the San Andreas fault from Bodega Head to Cajon Pass, California: U.S. Geol. Survey Prof. Paper 698, 92 p.

Ross, D. C., 1974, Map showing basement geology and locations of wells drilled to basement, Salinian block, central and southern Coast Ranges, California: U.S. Geol. Survey Misc. Field Studies Map MF–588, scale 1:500,000.

Ross, D. C., and Brabb, E. E., 1973. Petrography and structural relations of granitic basement rocks in the Monterey Bay area, California: U.S. Geol. Survey Jour. Research, v. 1, no. 3, p. 273–282.

Shapiro, Leonard, and Brannock, W. W., 1962, Rapid analysis of silicate, carbonate, and phosphate rocks: U.S. Geol. Survey Bull. 1144–A, 56 p.

Turekian, K. K., and Wedepohl, K. H., 1961, Distribution of the elements in some major units of the Earth's crust: Geol. Soc. America. Bull., v. 72, no. 2, p. 175–191.

Tyrell, G. W., 1933, Greenstones and graywackes: Comptes rendus reunion internat. pour l'étude du Precambrian (for 1931), p. 24–26.

Jour. Research U.S. Geol. Survey
Vol. 4, No. 6, Nov.-Dec. 1976, p. 697–702

DEEP EVAPORITIC STRATA OFF NEW YORK AND NEW JERSEY—EVIDENCE FROM INTERSTITIAL WATER CHEMISTRY OF DRILL CORES

By FRANK T. MANHEIM[1] and RAYMOND E. HALL,
Woods Hole, Mass.

Abstract.—Analyses of interstitial waters of cores from shallow core drillings on the Continental Slope off New York and New Jersey show consistent increases in salinity with depth. Similar increases of salinity have been observed in the course of the Deep Sea Drilling Project and in other offshore drill holes and are normally associated with diffusion of salt from buried evaporitic strata. Drill-hole data on evaporitic occurrences off the Maritime Provinces of Canada and in wells south of Delaware Bay suggest that the salt is Jurassic in age.

In 1967, a consortium of four oil companies (Humble, Chevron, Gulf, and Atlantic Richfield) drilled a series of shallow coreholes along the Atlantic Continental Slope of the Northeastern United States. The drilling was performed by the dynamically positioned drilling vessel, *Caldrill*. Beginning with site 15, U.S. Geological Survey personnel were allowed to sample cores for lithological, paleontological, and interstitial water data.

The senior author did analyses on board for site 15; for site 17, E. C. Rhodehamel and R. N. Oldale packaged samples for later onshore analyses. In addition, Esso Production Research Co. personnel kindly forwarded core splits at a later date from Houston, Tex., but the nature of the pore fluid and visible indications of drying showed that the sediments had evaporated significantly before packaging; hence they were not usable for pore-fluid study. A variety of unusual phenomena in addition to evaporation were noted: For example, extensive gypsum precipitation and anomalous sulfate concentrations attested to oxidation of iron sulfide in the presence of calcium carbonate.

Acknowledgments.—The authors wish to thank the crew of the *Caldrill* and personnel of Esso Production Research Co. for their cooperation, especially P. H. Monaghan, H. F. Belding, and Donald Perry, and managements of the four cooperating oil companies for releasing the data for publication. Particular thanks go to F. A. Kohout, U. S. Geological Survey, Woods Hole, Mass., without whose efforts the observations would not have been possible. The shipboard sampling by E. C. Rhodehamel, U. S. Geological Survey, Reston, Va., and R. N. Oldale, U.S. Geological Survey, Woods Hole, are acknowledged, and thanks are due to W. A. Berggren and Ann Boersma, Woods Hole Oceanographic Institution (WHOI) and to Duane Mellor, Yale University, New Haven, Conn., for assistance in paleontological dating for the cores.

METHODS

At site 15, samples from the inner parts of cores were immediately removed and were squeezed for pore fluid by using a syringe-press (Manheim, 1968). Other samples were packaged in tightly sealed jars at this site and at site 17 and were kept for squeezing in a stainless-steel squeezer (Manheim, 1966) at WHOI laboratories. Salinities were determined on a few drops of pore fluid by means of a Goldberg refractometer (American Optical Co., Keene, N.H.). Precautions taken and detailed techniques used have been more fully described in the above references and in the shipboard manual for the Deep Sea Drilling Project (DSDP) (Waterman, 1973) and in Manheim and Sayles (1974). The laboratory analyses included some additional chloride and sulfate analyses. Evidence for substantial freedom from contamination by drilling fluid and other aspects of pore-fluid technique have been discussed in a series of interlaboratory studies on materials from Leg 15 of the DSDP (Waterman, 1973).

PALEONTOLOGY

Paleontological dating was first attempted by analyses of planktonic foraminifers alone. However, radiolarians were used when foraminifers were absent or were so poorly preserved that they could not be

[1] Current address is Department of Marine Science, University of South Florida, St. Petersburg, Fla.

confidently identified. In all samples from the five sites examined in this study (tables 1 and 2), the foraminifers and radiolarians were sparse, so that dating should be considered tentative.

TABLE 1.—*Geologic ages of analyzed core samples from selected depths on the Continental Slope off New York and New Jersey*

Site	Depth (m)	Age
13–5	760	
13–12–C	865–870	Probably Pleistocene.
13–16–D	926–931	Not identifiable.
13–20–C	996–1,000	Do.
14	1,433	Late Miocene, transitional to Pliocene.
14–23–B	1,495	Early Miocene.
15	1,560	Reworked.
15	1,562	Late Eocene.
15	1,622	Middle Eocene.
15	1,720	Do.
17B–17A	1,501	Late Cretaceous.
17C–4 base	1,515	Reworked.
17C–17A	1,549	Late Cretaceous.
18–2–B	1,081	Pliocene or Pleistocene.
18–8–B	1,181	Late Cretaceous.
18–15–A	1,311	Do.
18–20–D	1,373	Do.

TABLE 2.—*Species of Radiolaria and Foraminifera found in core samples from the Continental Slope off New York and New Jersey*

Site	Depth (m)	Species
13		No foraminifers or radiolarians present.
14	1,495	Radiolaria:
		Dorcadospyris sp.
		Tholospyris authopora
		Theocorys spongoconus
		Calocycletta virginis
		Connartus prismaticus
		Cyrtocapsella cornuta
		Stichocorys armata
		Lychnocanium lupes
		Cyrtocapsella tetrapora
		Stichocorys delmontenis.
15	1,720	Radiolaria:
		Theocorys anaclasta
		Podocyrtis amorpha
		Lithochytris vespertilio
		Theocotyle venezuelenis
		Thysocyrtis hirsuta
		Podocyrtis papalis.
17	1,549	Foraminifera:
		Various species of *Globotruncana.*
18	1,311	Do.
	1,373	Do.

Sedimentary samples from site 13 contained insufficient microfossils for age determination. The sandy intervals are dominated by subangular to subrounded quartz grains and contain only occasional fragments of foraminifers. Although no foraminifers or radiolarians were identified from four samples, the proximity of site 13 to sites 14 and 15 seems to indicate that at site 13 the section between 865 and 870 metres in depth is Pleistocene in age.

Of two samples analyzed from site 14, the one at 1,433 m contained foraminifers that suggest an age of late Miocene transitional to Pliocene. Abundant radiolarians at 1,495 m indicate an early Miocene age.

At site 15 (1,720 m) the foraminifers were poorly preserved and could not be identified with certainty. Radiolarians here suggest a middle Eocene age.

At site 17C–17A (1,549 m) preservation of foraminifers was poor to fair. Fragments of two species of Late Cretaceous forms were seen, though their state of preservation precluded positive identification of species. Site 17B–17A (1,500 m) can also be labeled Late Cretaceous on the basis of several unidentified species of *Globotruncana.*

Three of the four samples from site 18 are Late Cretaceous in age, on the basis of *Globotruncana* forms that are better preserved than those at site 17.

LITHOLOGY AND INTERSTITIAL SALINITY

Locations of drill holes are shown in figure 1. The drill holes penetrated seaward-dipping Tertiary sedimentary rocks belonging to the coastal-plain wedge that is either slumped or truncated on the Continental Slope. Dredgings in submarine canyons and other areas in the vicinity have revealed outcrops ranging in age from Late Cretaceous to Miocene (Uchupi, 1970).

The uppermost strata sampled at sites 15 and 17 are gray silty clays. These sediments retain their high percentage of clastic-detrital grains and become increasingly consolidated as depth increases, reaching about 35 percent porosity (16 percent water content) at 150 m below the sea floor. At site 15, light-green slightly glauconitic foraminiferal-coccolith oozes dominate at 1,585 m (about 100 m below sea floor). These sediments still retain more than 50 percent porosity (30 percent water content) 230 m below the sea floor.

At site 15 (fig. 2), a continuous section yielded an interstitial salinity gradient smoothly increasing with depth. The slope of the gradient is approximately 6.7 g/kg (grams per kilogram) per 100 m of depth; the slope decreases below 1,700 m. The several core drilling restarts in different stratigraphic positions at site 17 complicate the plot (fig. 3); however, an increase in interstitial salt content with depth is evident.

The chloride values ran roughly parallel with salinity as expected, whereas sulfate was depleted with respect to seawater Cl/SO_4 ratios, as has been widely noted in interstitial waters from terrigenous sediments recovered in ocean-drilling operations.

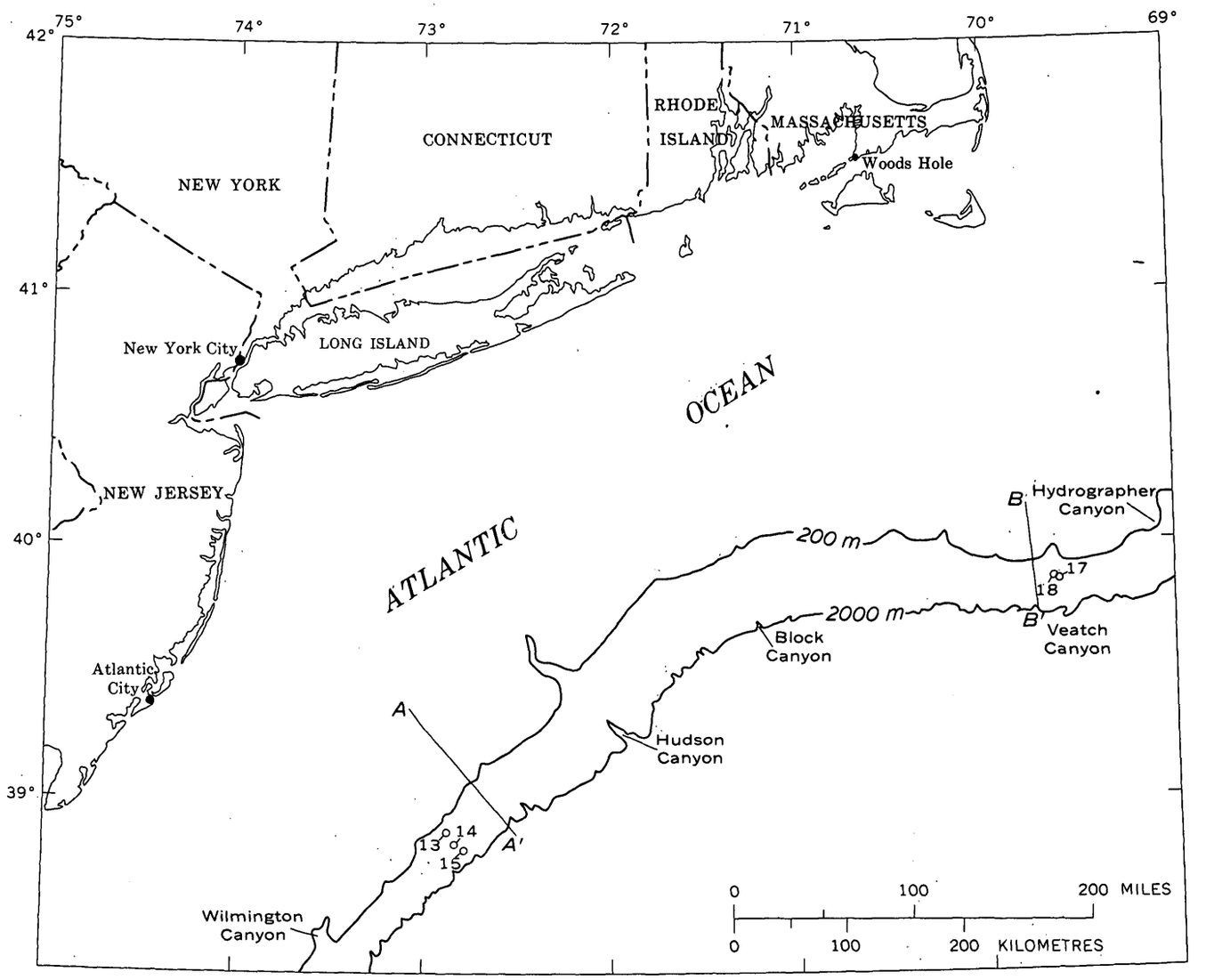

FIGURE 1.—Location map of investigated sites. *A–A'* and *B–B'* refer to seismic-profile lines 113 and 56, respectively (Uchupi, 1970, figs. 22 and 3).

DISCUSSION

Interstitial water data from many coring sites in the world ocean (Manheim and Sayles, 1974, and references therein) show increases in interstitial salinity of the kind seen here in the study area; they have been associated almost invariably with diffusion of salt from buried evaporites (rock salt). For example, significant salinity increases are found where salt diapirs are reached by the drill bit, whereas these increases are absent where basement rocks are basalts or metamorphic rocks. In time, the salt may diffuse through as much as 4 kilometres of sediment above evaporitic strata to yield salinity concentration gradients of the kind seen here. Except under special circumstances, the indications are distinct and consistent in strata that have been covered by the ocean throughout Pleistocene and Holocene time. This is true because of the lack of artesian movements that greatly complicate subsurface fluid patterns and compositions in sedimentary basins on land.

If interstitial salinity profiles are extrapolated to saturation concentrations for NaCl (approximately 260 g/kg, ignoring contributions of other ions) the depth of the buried salt deposits can be estimated. However, the estimate is only an approximate depth range when used for appreciable thicknesses of rocks, owing to variable diffusional properties of the rocks. Although the increase in temperature with depth partly compensates for decreasing diffusive permeability in consolidated or cemented rocks, other factors can cause departure of gradients from a straight line as depth increases. Particularly large departures from

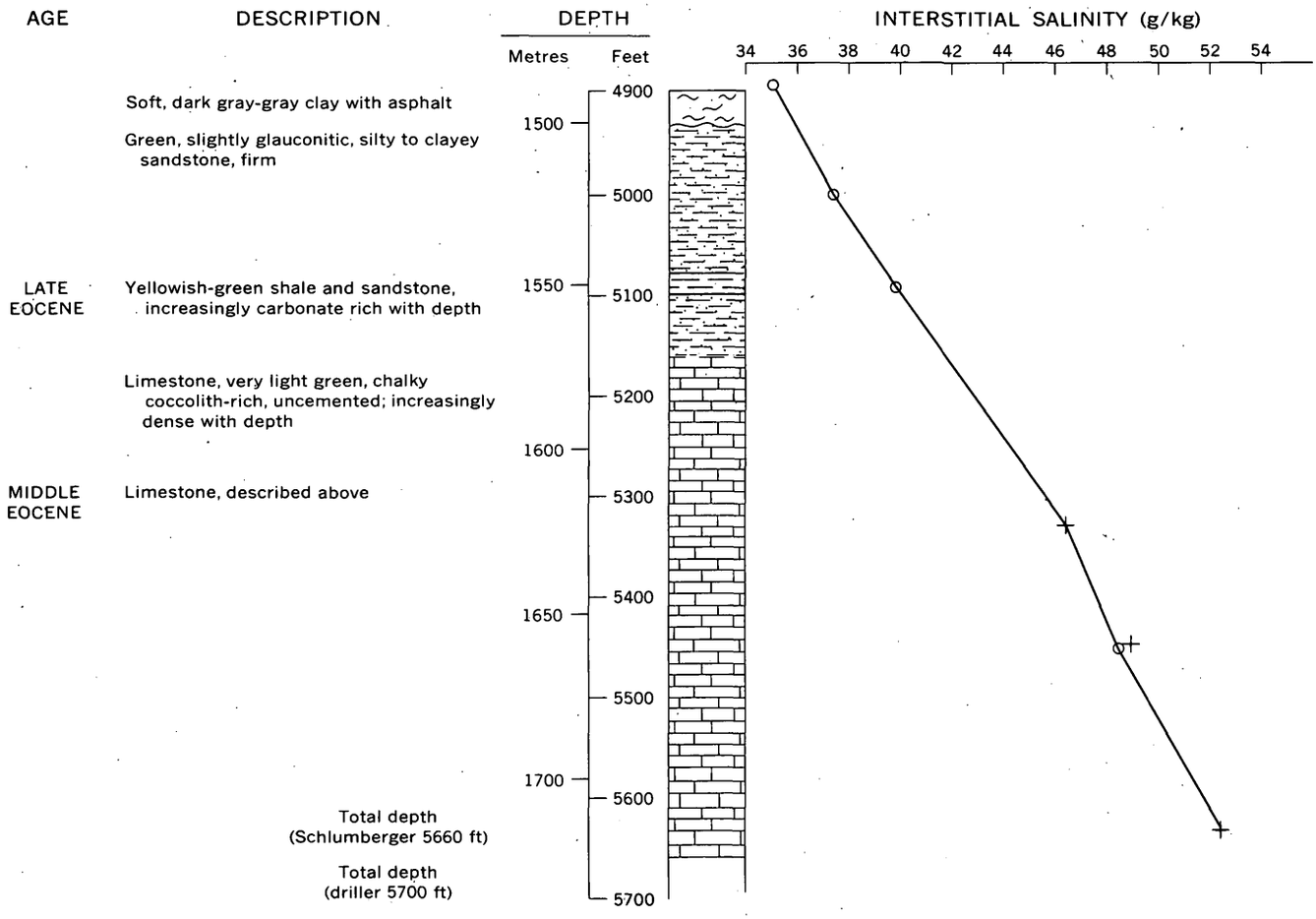

FIGURE 2.—Lithology and interstitial salinity at site 15. Circles refer to salinity by refractometer calibrated with seawater, on samples extracted on board ship. Crosses refer to total dissolved solids determined by evaporating to dryness at 170°C, on samples carefully preserved on board ship and later extracted in the shore laboratory.

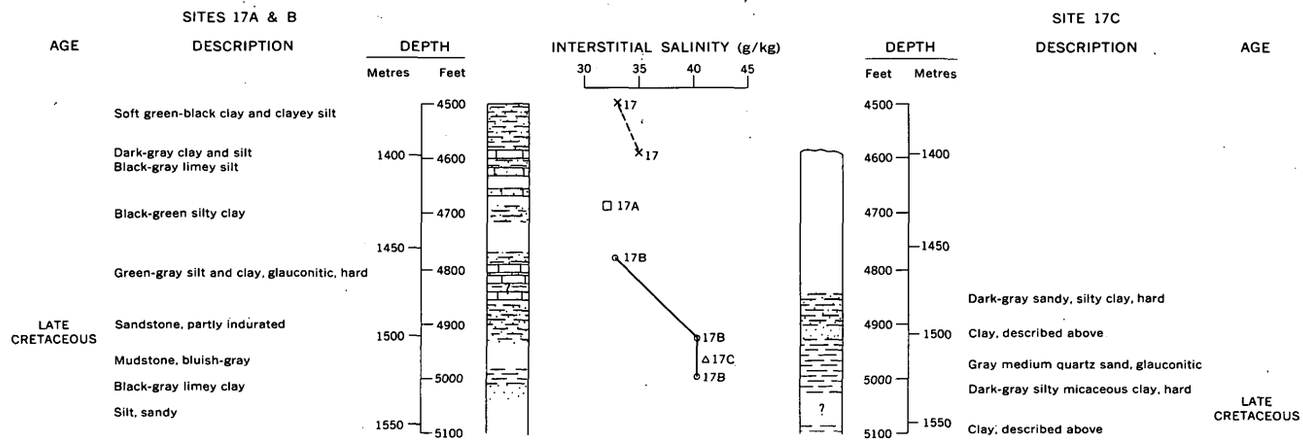

FIGURE 3.—Lithology and interstitial salinity at site 17. Different symbols refer to restarts of hole at slightly different locations within the coordinates lat 39°52.2′ N., long 69°35.5′ W.

straight-line gradients may be obtained where salt beds are overlain by poorly permeable deposits such as dense anhydrites.

If the approximately straight-line (presumably steady-state) gradient (about 6.7 g/kg salinity per 100 m) is extrapolated to 260 g/kg, one arrives at an estimated maximum sediment column of about 3,400 m overlying the salt beds.

Salt deposits are documented or indicated in Mesozoic strata both north and south of the sites studied here. McIver (1972) has summarized data from the many drill holes penetrating salt beneath the Continental Shelf off Nova Scotia. The Argo Salt of Early Jurassic age is found at variable depths greater than 2,000 m below the sea floor.

To the south, evaporitic beds occur in Jurassic-Lower Cretaceous strata penetrated by onshore drill holes along the Atlantic coast (Manheim and Horn, 1968, and publications cited therein). Wells in Delaware and eastern North Carolina (expecially Cape Hatteras) show a pronounced correlation between the high salinity of formation brines and the existence of evaporitic strata. Only anhydrites have been penetrated at these land sites, but rock salt has been postulated to occur farther seaward (P. M. Brown, oral commun., 1967; Manheim and Horn, 1968). Increase in interstitial chlorinity and salinity with depth in coreholes has been found in the central but not the outermost parts of the Blake Plateau (Manheim and Horn, 1968). This increase suggests that the buried evaporite beds terminate seaward beneath the shelf approximately under the 1,000-m isobath, hundreds of kilometres off the Florida-South Carolina coast.

Taking the stratigraphic sections and inferred occurrences of evaporites along the Atlantic continental margin into account, we may presume that the salinity gradients reported herein represent diffusion of salt from Jurassic evaporitic strata at depth on the New York-New Jersey Continental Slope. The stratigraphy as indicated in the seismic sections (fig. 4) provides no

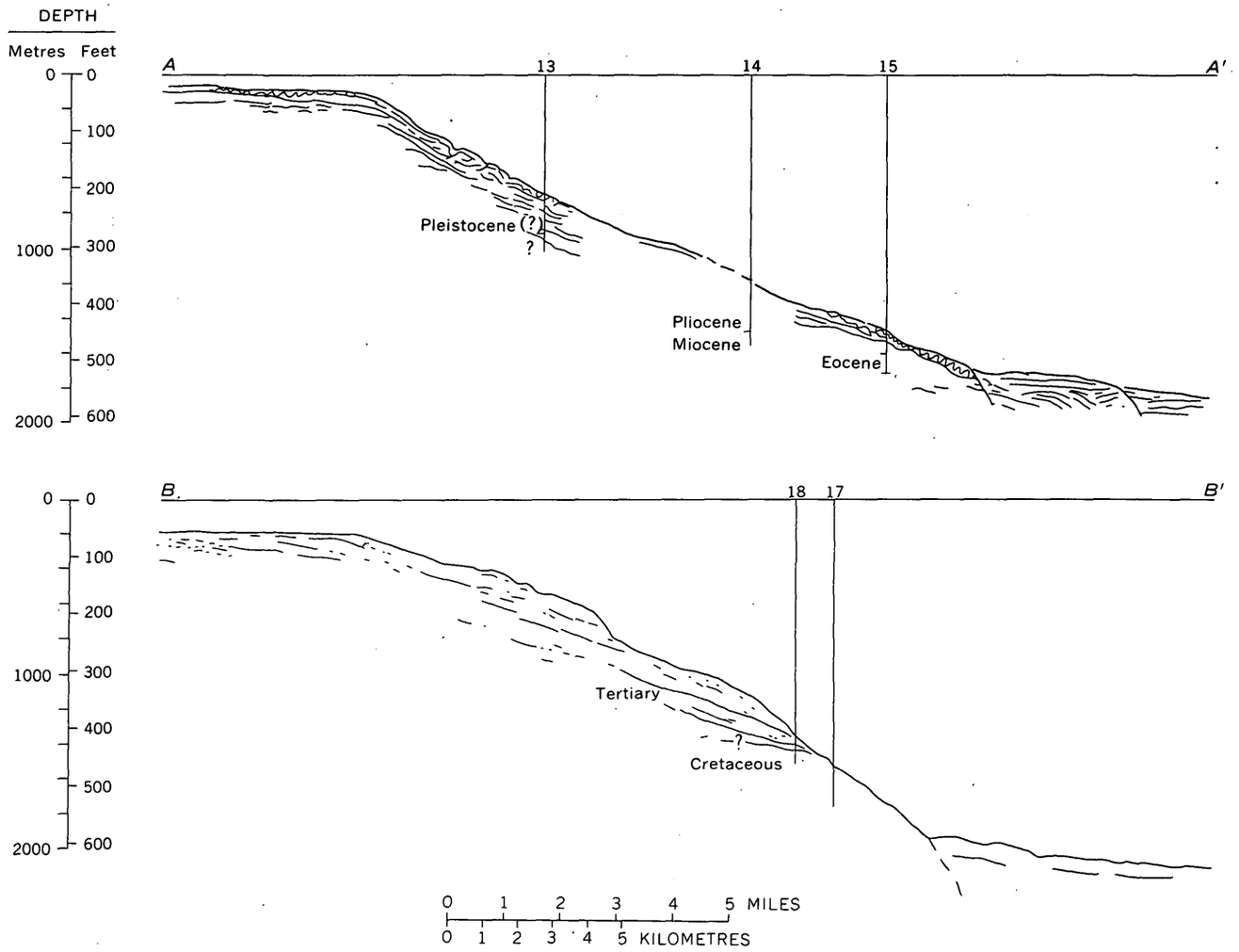

FIGURE 4.—Seismic sections in area of drill holes. Line *A–A'* (which refers to sites 13, 14, and 15) corresponds to track 113, and line *B–B'* (which refers to sites 17 and 18) corresponds to track 56 in Uchupi (1970). The sections here have been redrawn from original records. Vertical (depth) scale is based on a seismic velocity of 1,500 m/s. The positions of the core holes are approximate only, placed by applying the water depths to the sections, with adjustment for structure noted on the seismic profiles.

evidence of diapirism. Thus, we presume that salt diffusion is proceeding from conformable evaporitic strata at depth.

REFERENCES CITED

Manheim, F. T., 1966, A hydraulic squeezer for obtaining interstitial water from consolidated and unconsolidated sediments: U.S. Geol. Survey Prof. Paper 550–C, p. 256–261.

——— 1968, Disposable syringe techniques for obtaining small quantities of pore water from unconsolidated sediments: Jour. Sed. Petrology, v. 38, no. 2, p. 666–668.

Manheim, F. T., and Horn, M. K., 1968, Composition of deeper subsurface waters along the Atlantic continental margin: Southeastern Geology, v. 9, no. 4, p. 215–236.

Manheim, F. T., and Sayles, F. L., 1974, Composition and origin of interstitial waters of marine sediments, based on deep sea drill cores, *in* Goldberg, E. D., ed., The Sea, v. 5, Marine chemistry: New York, John Wiley & Sons, p. 527–568.

McIver, N. L., 1972, Cenozoic and Mesozoic stratigraphy of the Nova Scotia Shelf: Canadian Jour. Earth Sci., v. 9, p. 54–70.

Uchupi, Elazar, 1970, Atlantic Continental Shelf and Slope of the United States—Shallow structure: U.S. Geol. Survey Prof. Paper 529–I, p. I1–I44.

Waterman, L. S., 1973, Interstitial water program shipboard manual: La Jolla, Calif., Scripps Inst. Oceanography, Deep Sea Drilling Project, p. 1–141.

Jour. Research U.S. Geol. Survey
Vol. 4, No. 6, Nov.-Dec. 1976, p. 703–713

TEXTURAL DISTRIBUTION OF SEA-FLOOR SEDIMENTS, SOUTH TEXAS OUTER CONTINENTAL SHELF

By GERALD L. SHIDELER, Corpus Christi, Tex.

Abstract.—The general texture of sea-floor sediments along the south Texas Outer Continental Shelf was evaluated in terms of gravel, sand, silt, and clay components. The gravel component is quantitatively minor and is concentrated mainly in the southern sector; it consists, for the most part, of relict biogenic detritus dominated by molluscan shells. The sand component consists of terrigenous and biogenic detritus. Modern sand is localized along the shoreface sector, whereas palimpsest and relict sands characterize the northern and southern sectors, which are the respective locations of the ancestral Brazos-Colorado and Rio Grande deltas. The central sector contains an extensive modern mud blanket that appears to be migrating southward over relict deposits of the ancestral Rio Grande delta. The silt fraction is the highly dominant component of the mud blanket; silt appears to be hydraulically trapped within the shelf environment and constitutes the most abundant detrital component within the Outer Continental Shelf region. The subordinate clay component of the mud blanket is concentrated toward the shelf break and may be largely escaping into deeper water environments.

The south Texas Outer Continental Shelf (OCS) is a region of potential hydrocarbon resources within the northwest Gulf of Mexico. The region encompasses approximately 24,500 km² (square kilometres), extending southward from Matagorda Bay to the United States–Mexico international boundary (fig. 1). The general texture of surficial sea-floor sediments throughout the south Texas OCS was investigated as a part of the Federal OCS environmental studies program associated with the offshore petroleum lease sale. This program was funded by the U.S. Bureau of Land Management. In addition to sediment properties, the environmental assessment of the south Texas OCS included an evaluation of trace elements and hydrocarbon chemistry, benthonic and nektonic biology, and physical oceanography. Most previous knowledge regarding the sedimentology of the south Texas OCS was presented by Shepard and others (1960), who summarized the results of a regional study of the entire northwest Gulf of Mexico conducted during 1951–58. The objectives of the present study were to provide the necessary detailed sea-floor sediment data for an overall environmental appraisal and to provide further insight into regional sedimentary processes.

GENERAL HYDROGRAPHY

The south Texas OCS region extends from the seaward limit of Texas State waters (19 kilometres or 10.3 nautical miles offshore) to the approximate shelf break at the 180-metre isobath. The shelf topography can be generally characterized as a relatively smooth and gently sloping surface. The average width of the shelf is 94 km (51 nmi); the average gradient of the shelf surface is 1.9 m/km (3.5 m/nmi). Local areas of irregular topography are associated with relict carbonate banks, most of which are localized within the 45- to 90-m water-depth interval. The isobaths also denote two prominent seaward-facing salients at the northern and southern ends of the region; these salients reflect the locations of the Pleistocene–Holocene ancestral Brazos-Colorado delta and Rio Grande delta, respectively. Shoreward of the OCS region, the shoreface is generally smooth, except in the Rio Grande delta area where a system of shoreface-connected ridges has formed.

Seasonally variable winds are largely responsible for a complex circulation pattern of littoral and semipermanent shelf currents. Early general descriptions of the regional circulation system in the northwest gulf were presented by Lohse (1955) and Curray (1960). More recent studies based on additional drift data have further refined the understanding of shelf circulation within the OCS region (for example, Kimsey and Temple, 1963, 1964; Watson and Behrens, 1970; Hunter and others, 1974; Hill and others, 1976). A synopsis of these studies suggests a general OCS circulation model characterized by an annual cyclic pattern of coastwise surface and bottom currents controlled largely by seasonal winds. Littoral and coastwise offshore drift is predominantly south during winter months when winds have strong northerly com-

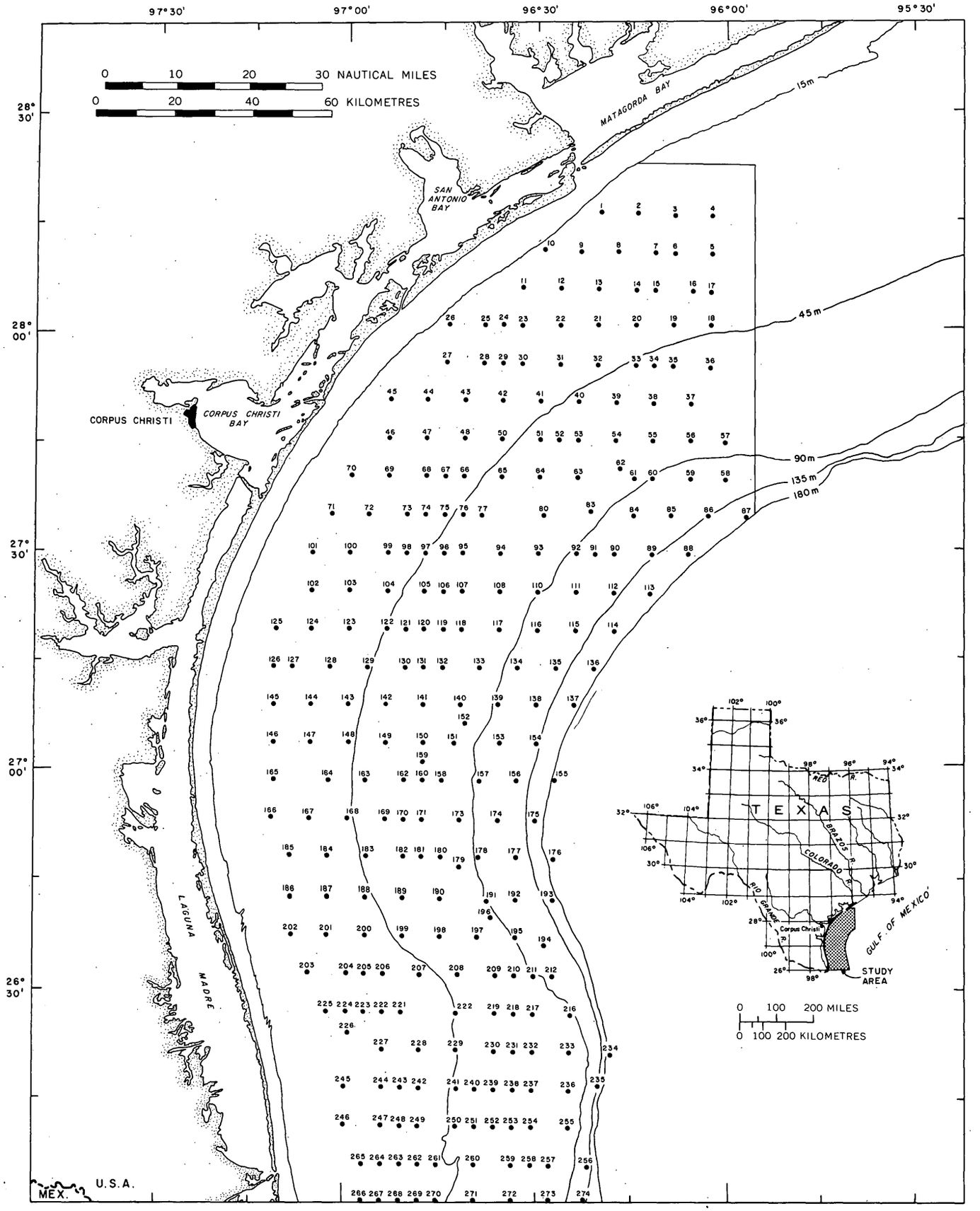

FIGURE 1.—Index map of south Texas Outer Continental Shelf area, showing sample station localities for study of the textural distribution of sea-floor sediments.

ponents, whereas predominantly northerly drift takes place during summer months when winds have strong southerly components. Transitional spring and fall seasons are characterized by variable drift directions, apparently resulting in the net development of migrating coastwise surface- and bottom-current convergence zones centered along the central Texas coast. Curray (1960) suggested that a semipermanent convergence zone results from the meeting of opposing westward- and southwestward-flowing currents across the Louisiana shelf with northward-flowing currents from the Rio Grande area. He described the position of convergence as being centered near lat 27°30′–28°00′ N. during the January–March period and shifting northeastward during the May–July period to approximately lat 28°00′–29°00′ N. During the fall months, the convergence zone again shifts southward to lat 27°00′–28°30′ N. Evidence supporting the presence of net longshore drift convergence in the vicinity of the lat 27°00′–27°15′ N. coastal sector has also been presented by Watson (1971). An annual cyclic pattern of the onshore-offshore drift component also appears to be induced by seasonal winds (Hunter and others, 1974). Hunter and others (1974) noted that onshore surface drift is most pronounced during the summer, as the result of predominantly onshore southeasterly winds, whereas the offshore surface drift component becomes more prominent during the winter when northerly winds are more common. The opposite relationship is shown by bottom-drift components.

The tidal range along the south Texas shelf during fair-weather conditions is relatively small, generally less than 0.3 m (Marmer, 1954). On the basis of wave data compiled by Bretschneider and Gaul (1956a, b) and by Wilson (1957), Curray (1960) noted that the probable frequency of fine sand movement by significant wave surge ranges from less than once in 20 years near the 180-m isobath to greater than 500 hours per year in depths of less than 18 m. The frequency zones are largely parallel or subparallel to the coast and isobaths, thus showing a generally increasing frequency as water depth decreases. In addition to fair-weather processes, the storm hydraulic regime must also have a major influence on sediment dispersal within the OCS region. This coastal sector is relatively vulnerable to "norther" storms during the winter season as well as to tropical storms and hurricanes during the summer and fall seasons.

METHODS OF STUDY

Field sampling of the south Texas OCS sea-floor sediments was conducted from late October to late December 1974. Grab samples were obtained at 263 stations, by means of a 0.015-m^3 Smith-MacIntyre sampler. A subsample was extracted for textural analysis by inserting a plastic tube (16-cm length by 3.5-cm diameter) vertically into the grab sample. Shipboard navigation was accomplished by a combination of systems consisting of precision Hi Fix, loran A, and satellite.

In the laboratory, the samples were analyzed texturally to determine the relative proportions of grain-size components in terms of gravel (>2 mm), sand (2 mm–63 μm), silt (63 μm–3.9 μm), and clay (<3.9 μm) fractions. A representative work sample of approximately 80 grams was used for the analyses. Carbonaceous organic matter was first removed by oxidation with a hydrogen peroxide solution (30 percent); the sample was then washed to remove soluble salts and dispersed in a standard sodium hexametaphosphate solution (5 g/l). Following dispersion, the samples were fractionated by wet-sieving into gravel, sand, and mud fractions; the mud fraction was subjected to further size analysis by Coulter Counter (Model TA) to determine relative proportions of silt and clay components. The weight percentage of each grain-size component was then determined, and sediment distribution maps were prepared. In addition to textural analyses, the gravel and sand components were analyzed microscopically to determine the general mineralogical composition. All gravel fractions were examined, whereas the examination of sand fractions was limited to the odd-numbered samples. Sand composition was determined by point counts of 100 grains within the fine-sand fraction (0.125–0.250 mm); the point-count data were utilized to establish a biogenic-terrigenous constituent ratio for each sample. Although sand composition is dependent upon the specific size fraction analyzed (for example, Shepard and Moore, 1954), the fine-sand fraction was selected as being representative because coarser sand grades are of minor quantitative significance within the OCS region.

RESULTS AND DISCUSSION

The general textural characteristics of sea-floor sediments within the south Texas OCS are illustrated by percentage isopleth maps of the individual grain-size components (figs. 2–5). In addition, efforts have been made to relate component variability to the general hydrographic framework in order to gain insight into the regional shelf processes of sediment transport and deposition.

Gravel component

The detritus constituting the gravel-size fraction (>2 mm) is essentially biogenic, consisting predomi-

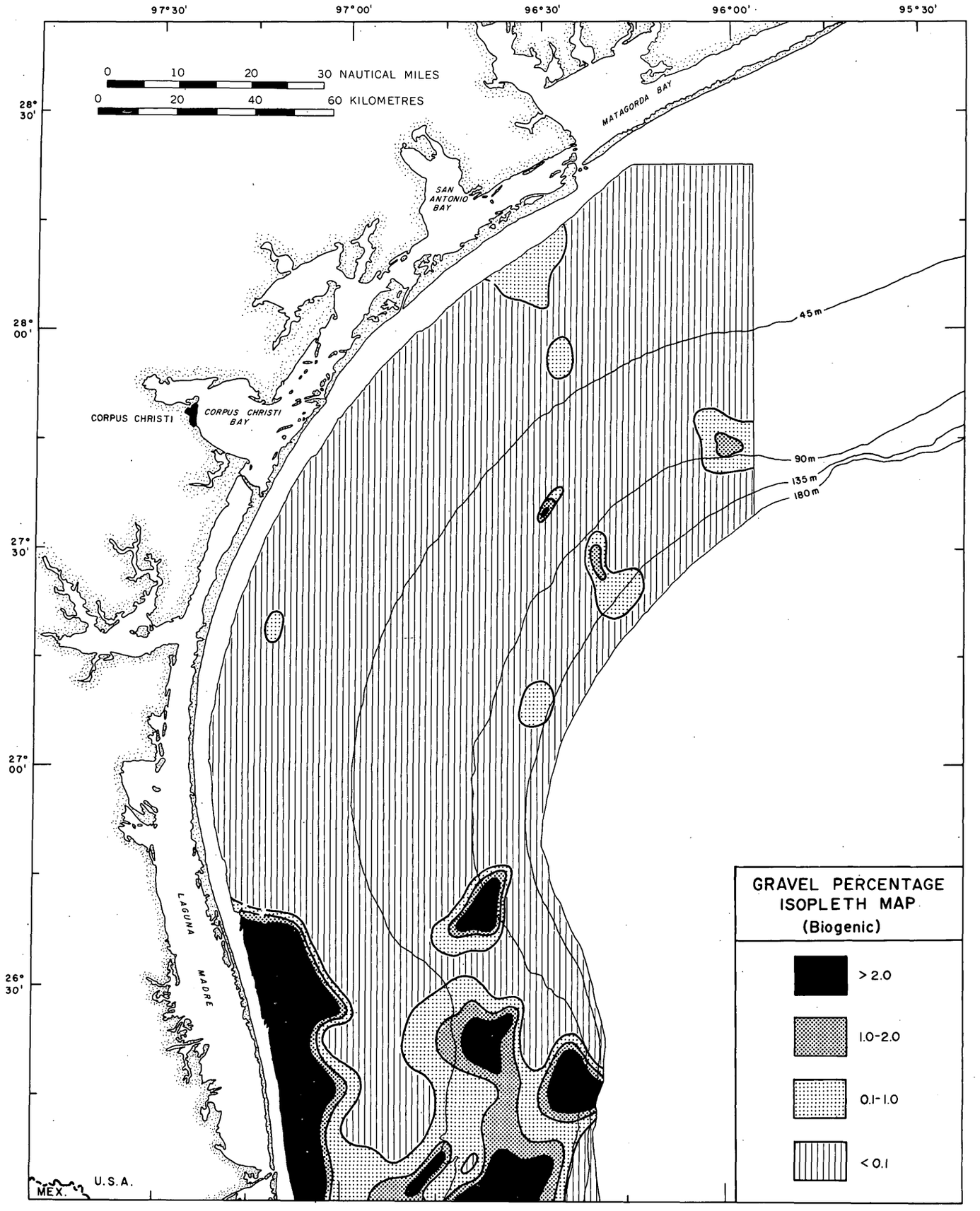

FIGURE 2.—Percentage isopleth map of gravel-size (>2 mm) biogenic detritus.

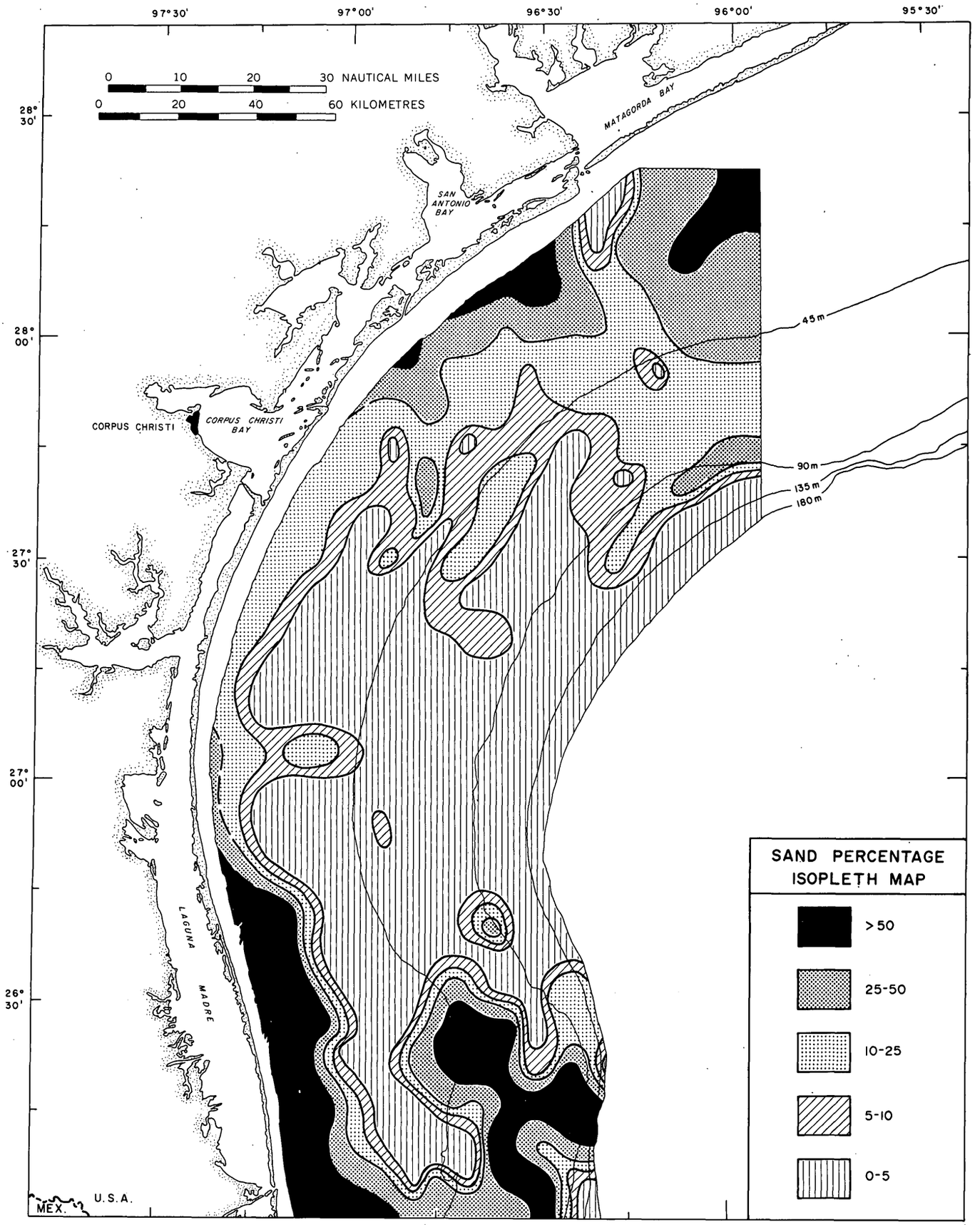

FIGURE 3.—Percentage isopleth map of sand-size (2 mm–63 μm) detritus.

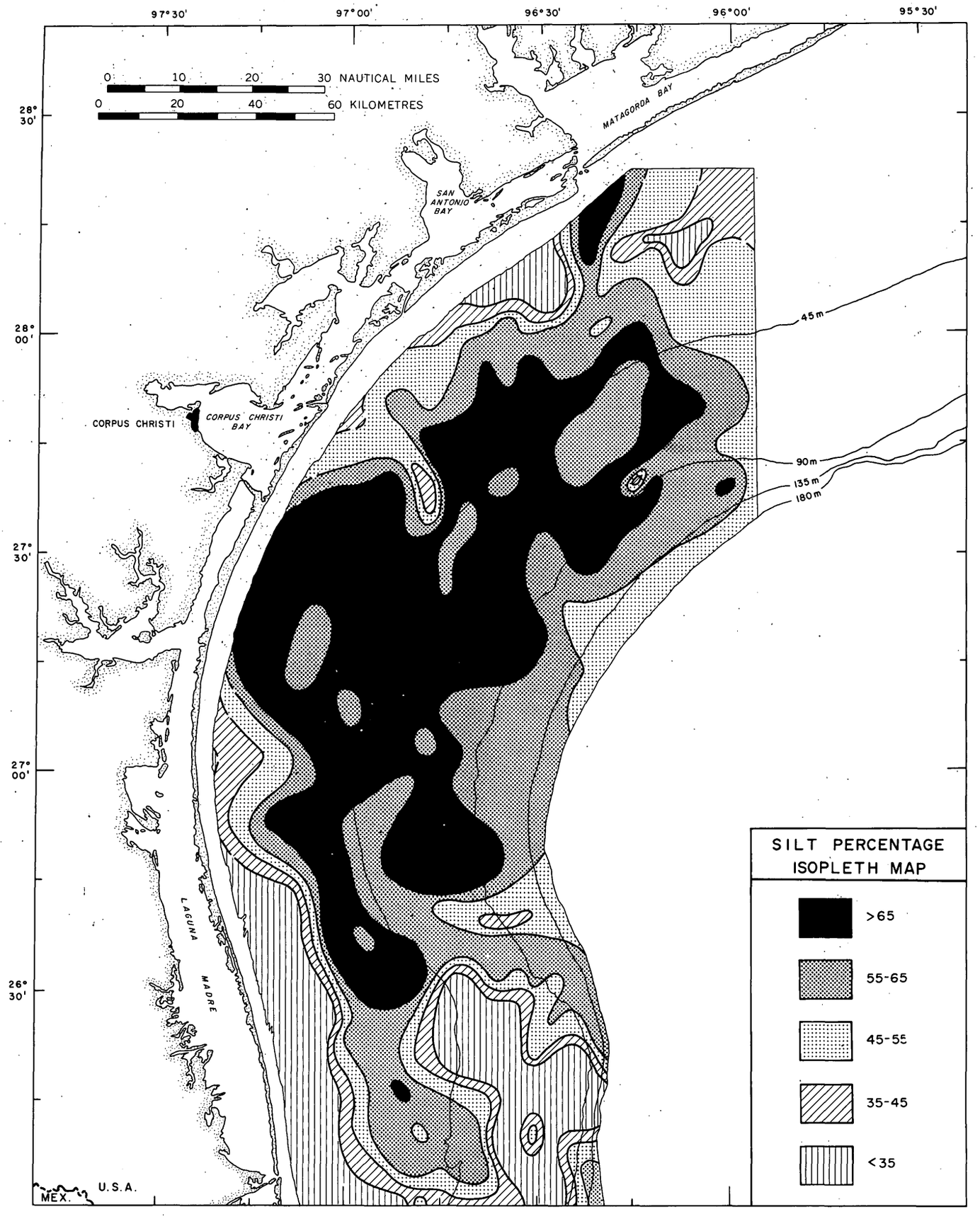

FIGURE 4.—Percentage isopleth map of silt-size (63–3.9 μm) detritus.

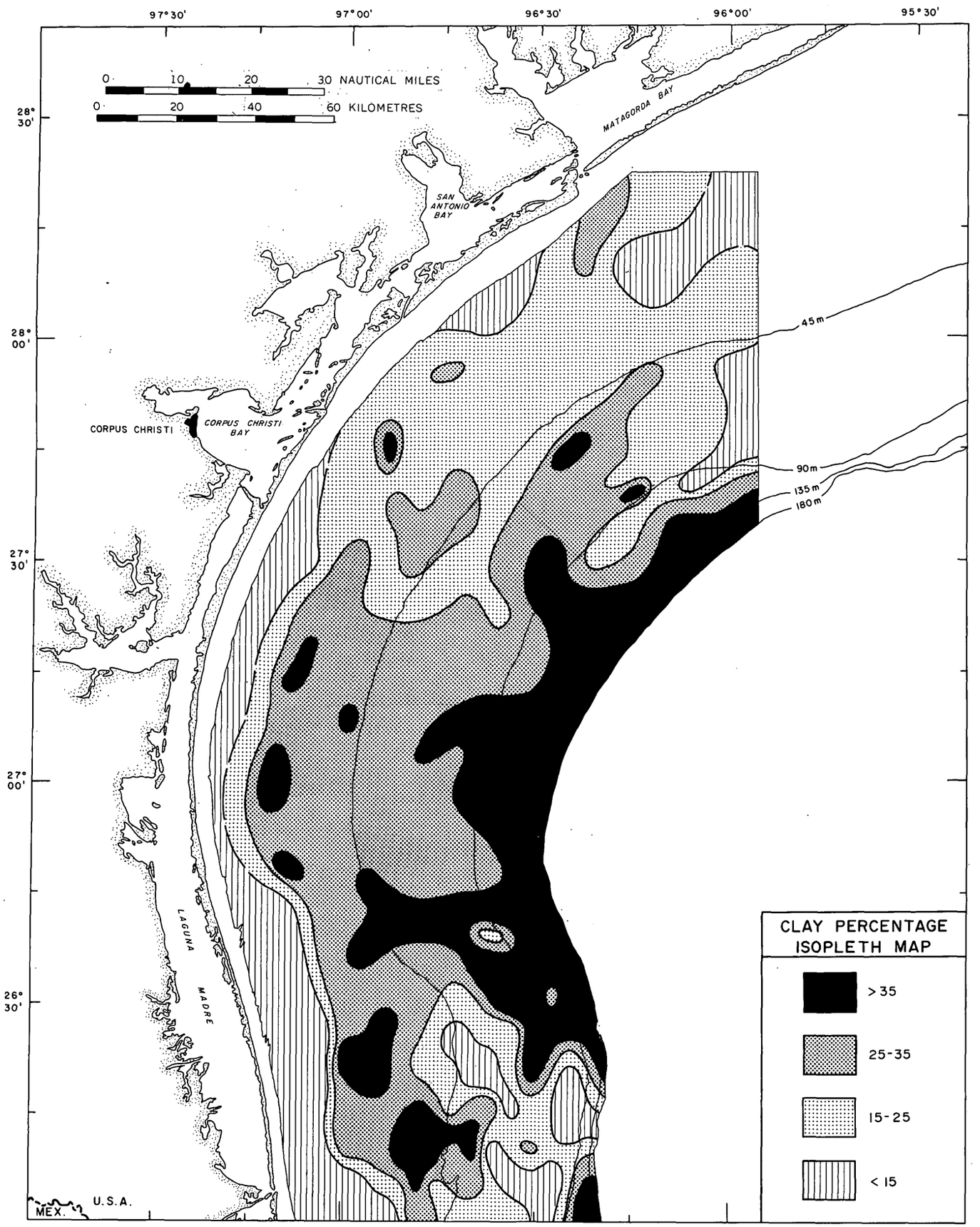

FIGURE 5.—Percentage isopleth map of clay-size (<3.9 μm) detritus.

nantly of molluscan shells. The shells are generally in a highly fragmented condition. Some of the more robust valves are highly etched and generally indicate a substantial degree of weathering. A more diverse bioclastic assemblage occasionally is found in the vicinity of carbonate banks, where mixtures of mollusks and coral-algal reef detritus are observed (for example, stations 80, 191, 196). Gravel-size material consisting of inorganic constituents is quantitatively insignificant. Other than shell detritus, the only other gravel-size constituents are occasional lithic clasts consisting of polygenetic limestone that were observed at a few stations (11, 80, 228, 265, 268, and 269).

The gravel percentages at individual stations mainly reflect the content of bioclastic detritus and range from near 0 to a maximum of 26.65 percent (station 80). The regional distribution pattern illustrated by the gravel isopleth map (fig. 2) shows that gravel-sized detritus is quantitatively minor, constituting less than 0.1 percent of the sea-floor sediment composition throughout most of the OCS region. Gravel concentrations in excess of 1.0 percent are primarily in the sector south of lat 27° N., within the area of the ancestral Rio Grande delta. North of lat 27° N., only small local concentrations exceeding 1.0 percent are present; they occur seaward of the 45-m isobath.

The gravel-distribution pattern does not show any systematic relationship to the present hydraulic regime, indicating largely relict shell concentrations rather than modern concentrations established by present ecological conditions. High shell concentrations are found most extensively over the ancestral Rio Grande delta, where they extend from the shoreface to the shelf break; these concentrations are interpreted as being largely lag concentrates derived from a partially reworked older Holocene substrate exposed on the present sea floor, but possibly containing some inclusions of modern shell admixtures. The shell concentrations in the ancestral Rio Grande delta area also have been noted by Curray (1960). The conspicuous tongue of low gravel percentages (<0.1 percent) extending southward into the delta slightly east of long 97°W. could indicate a net southward transport of modern sediments, resulting in a partial covering of the older shelly substrate. The small local concentration along the southern flank of the ancestral Brazos-Colorado delta at long 96° W. may be also largely a lag concentrate derived from a partially reworked older Holocene substrate. The local concentrations (>2 percent) centered at lat 26°40′ N., long 96°38′ W., and at 27°35′ N., long 96°28′ W., are associated with relict carbonate banks.

Sand component

The detritus constituting the sand-size component (2 mm–63 μm) consists of both terrigenous and biogenic constituents. The terrigenous part is composed mainly of quartz, feldspar, and heavy-mineral grains, whereas the biogenic fraction is composed mainly of foraminiferal tests (planktonic and benthonic) and echinoderm and molluscan shell fragments. An examination of the selected fine-sand fraction (0.125–0.250 mm) indicates a wide range in composition from nearly pure terrigenous to nearly pure biogenic among individual stations. The OCS region shows a general trend of increasing biogenic-terrigenous ratios seaward as well as toward the central interior sector. A biogenic-terrigenous ratio of less than 0.25 characterizes most of the northern and southern ancestral delta areas, as well as the intervening shoreface sector shallower than 25 m. Ratios exceeding 10.0 are generally restricted to depths exceeding 90 m and localized along the shelf break. This regional trend largely reflects the increasing contribution of planktonic foraminiferal tests as distance increases from the sources of terrigenous sand. Texturally, the OCS sands are predominantly fine and very fine grained (250–63 μm).

The areal variability of sand detritus in sea-floor sediments is illustrated by the sand isopleth map (fig. 3). Sand contents at individual stations range from near 0 to a maximum of 90.17 percent (station 267). Sand contents of less than 5 percent are most common. The sand distribution pattern denotes two distinct regional trends: a lateral gradient of increasing sand percentages shoreward and a longitudinal gradient of increasing sand percentages both north and south of the central sector. The isopleth spacing indicates that both trends have substantially higher gradients in the southern half of the OCS region. The areas of high sand concentrations (>25 percent) are generally localized along the shoreface, and in the areas of the ancestral Rio Grande and Brazos-Colorado deltas; the central sector between the two deltas is a conspicuous sand-deficient mud province. Noteworthy local areas of sand deficiency include the mud salient extending southward into the Rio Grande delta east of long 97° W. and the salient extending southward from near the Matagorda Bay inlet.

The sand-distribution pattern is interpreted as a composite response to various processes, reflecting both ancient and modern sediment-transport systems. The lateral regional trend of a shoreward-increasing sand content appears to indicate both a coastal source area for modern sand detritus and a progressive shoreward increase in significant wave-surge energy as water depth decreases. The trend suggests a net seaward

transport of modern sands. Transport of the fine and very fine grained OCS sands is probably largely associated with storms rather than with fair-weather hydraulic conditions. The seaward reflux of turbid coastal waters following storm surges can be an important sand-transport mechanism. As noted by Hayes (1967), storm-surge reflux along the Texas coast associated with Hurricane Carla (1961) resulted in the seaward deposition of sand over a previously muddy sea floor out to depths exceeding 18 m. Regarding the longitudinal coastwise trend, the high sand concentrations in the southern Rio Grande delta area extend to the shelf edge; this absence of depth control suggests that the sands are not in equilibrium with the modern hydraulic regime and probably are relict deposits of the ancestral delta. The sand concentrations in the southern sector largely coincide with the previously described areas of high shell-gravel concentrations; this relationship supports a relict origin for the sand. The conspicuous mud salient extending southward onto the delta east of long 97° W. may indicate southward transport and encroachment of modern mud onto the relict deposits of the delta platform. This interpretation is compatible with that of Curray (1960), who considered the Rio Grande sands to be relict shallow-water deposits of the basal Holocene transgressive series, with adjacent muds being modern shelf deposits.

The sand concentrations within the northern sector associated with the southwestern flank of the ancestral Brazos-Colorado delta show notable differences when compared with the southern sands. The northern sands are not as closely associated with high shell-gravel concentrations, and the percentage isopleths denote much lower gradients. These two factors suggest genetic differences between the northern and southern sand concentrations. The distribution pattern suggests that the northern sands are being derived from an ancestral Brazos-Colorado delta source and are being transported southward by modern coastwise currents, eventually grading into the mud facies of the central sector. In essence, the northern sands are interpreted as palimpsest deposits, which are in partial equilibrium with the modern hydraulic regime. As discussed by Swift and others (1971), the term "palimpsest" refers to Quaternary shelf sediments that have petrographic characteristics indicating an earlier depositional environment but that have been partially reworked during the Holocene transgression. In the context of hydraulic equilibrium, the term "palimpsest," as used in the present paper, refers to a textural adjustment stage intermediate between true relict deposits in total disequilibrium and true modern deposits in total equilibrium. Because a complete adjustment continuum probably exists, the distinction between the three sediment types is essentially an indication of their relative degrees of adjustment to present hydraulic conditions. The northern sands, which appear to have undergone some net transport southward, have apparently evolved to a higher state of hydraulic adjustment than have the southern sands. In contrast, the relict southern sands appear to be adjusting at a substantially slower rate; they seem to be undergoing only in situ winnowing with minimal mass dispersion.

The sand-deficient areas (<25 percent) are interpreted as being composed largely of mud deposits in equilibrium with the modern hydraulic regime. These modern muds cover most of the central region, which acts as a fine-sediment depocenter; mud salients appear to be encroaching southward onto the relict Rio Grande delta platform. Bathymetrically, the main south-trending mud salient east of long 97° W. is presently over a relatively low-gradient terrace area. However, seismic-reflection profiles indicate that the area immediately north of the ancestral Rio Grande delta was a major depocenter throughout the Holocene, receiving approximately 150 feet of deposits (H. L. Berryhill, Jr., oral commun., 1975). Consequently, the ancestral delta may have been topographically high throughout much of the Holocene, thus possibly serving as a barrier to the net southward sediment migration. The present south-trending mud salients could reflect the final stage of topographic infilling and the initial stage of delta submergence by modern sea-floor sediments. Southward dispersal of modern mud is supported by the conspicuous south-trending mud salient extending from the Matagorda Bay inlet (Pass Cavallo) area. The predominantly southward dispersal of suspended-sediment plumes from this area can be documented on ERTS–1 (now Landsat-1) imagery; the plumes may result from convergence of the inlet's tidal current regime with south-trending littoral and nearshore currents. Consequently, the mud salient could be the result of mixing and dispersal of south-flowing littoral drift and bay effluent. A more sandy salient appears to be associated with the San Antonio Bay inlet (Cedar Bayou) area. A minor east-trending sandy salient between lat 27°00′ and 27°15′ N. is also noteworthy, because it is in the general vicinity of a postulated longshore drift convergence zone (Watson, 1971). In general, the overall sand distribution pattern suggests a composite fabric of relict, palimpsest, and modern sediments. A modern regional dispersal system characterized by both net offshore and net southward transport of sediments is also suggested.

Silt component

The areal variability of silt-size (63–3.9 μm) detritus in sea-floor sediments is illustrated by the silt isopleth map (fig. 4). Silt percentages at individual sample stations range from approximately 6 percent to 79 percent (station 105). In contrast to the relatively limited distribution of sand-size detritus, silt detritus is a pervasive component throughout the OCS region; silt contents exceeding 55 percent are most common. The only conspicuous silt-deficient areas (<45 percent) are those of high sand concentrations along the southern ancestral Rio Grande delta and adjacent shoreface as well as in the northern ancestral Brazos-Colorado delta sector. The regional trend denoted by the silt isopleths is a general increase in silt content from peripheral areas toward the central interior. This trend is largely the inverse of the regional sand trend. In addition, the silt trend shows some seaward isopleth closure, indicating that the central interior of the OCS region is functioning as an effective silt depocenter. As delineated by the 55–65 percent isopleth interval, conspicuous local silt salients extend outward from the central interior. The most prominent local salients extend southward onto the Rio Grande delta (east of long 97° W.), northward to the Matagorda Bay inlet area, and westward near lat 27°30′ N., south of Corpus Christi Bay.

The silt distribution pattern largely appears to reflect the modern suspended-sediment dispersal system. The regional silt distribution pattern suggests that the central interior between lat 26°30′ N. and lat 28°00′ N. is hydraulically structured to function as a depocenter for silt-size detritus. The voluminous quantity of silt within the OCS region appears to have been derived from a combination of sources, including coastal erosion, suspended-sediment reflux from adjacent estuaries, southward littoral drift from north of Matagorda Bay, and possible in situ winnowing of relict and palimpsest sediments that compose most of the ancestral Rio Grande and Brazos-Colorado deltas. A significant contribution from the Matagordo Bay inlet area is indicated by the conspicuous silt salient extending southward from that locality. In contrast, the sediment influx associated with the Corpus Christi Bay inlet area appears to be silt deficient, as indicated by the conspicuous silt-deficient salient extending southeast from near the bay's inlet (Aransas Pass). The conspicuous west-trending silt embayment centered near lat 27°30′ N. is perplexing. It could be related to a postulated coastwise current-convergence zone, where seaward return flow may be occurring (for example, Curray, 1960). If this postulated convergence cell does indeed exist, voluminous quantities of silt could be derived from coastal erosion and transported alongshore by littoral and nearshore currents toward the convergence zone. Seaward return flow would then provide an escape route for the advective transport of silt into the central interior where dispersion and deposition could take place both north and south of the convergence node. Strong seaward-flowing currents have been noted by fishermen within this postulated convergence zone (Curray, 1960). In essence, the enigmatic silt embayment centered near lat 27°30′ N. could be explained by a major influx of silt-rich suspended sediment derived from the convergence of muddy coastal waters. However, the existence of this postulated convergence zone would require verification by future physical oceanographic studies.

Clay component

The areal variability of clay-size (<3.9 μm) detritus is illustrated by the clay isopleth map (fig. 5). Clay percentages in bottom sediments at individual stations range from 3.5 percent to a maximum of 53.6 percent (station 210). The distribution pattern illustrates that clay is quantatitively subordinate to silt as a constituent of the extensive modern mud blanket. The regional trend denoted by the clay isopleths is a general increase in clay content both seaward and toward the central interior. This regional clay distribution pattern is inversely related to the regional sand distribution pattern; the most conspicuous clay-deficient areas are those of high sand concentrations on the two ancestral delta platforms and along the shoreface sector. Local areas of relatively high clay content (>25 percent) form a pattern similar to that of silty areas; they occur as south-trending salients from the Matagorda Bay inlet area and east of long 97° W. on the Rio Grande delta platform. However, a west-trending clay embayment centered near lat 27°30′ N. is notably absent. Another notable contrast is that the clay isopleths do not denote the seaward closure illustrated by the silt pattern.

The clay distribution pattern appears mainly to reflect the modern suspended-sediment dispersal system. The general shoreward reduction in clay content is logically attributed to a progressive shoreward increase in significant wave-surge energy, which would tend to maintain clay particles in suspension. In contrast to the silt distribution pattern, the absence of seaward closure on the clay pattern indicates that the clay dispersal system is substantially different. Most silt appears to be hydraulically trapped within the OCS region, indicating a relatively closed dispersal system. In contrast, the clay pattern denotes a more

open dispersal system, whereby most clay detritus appears to be escaping from the OCS onto the adjacent Continental Slope and deeper Gulf regions. The sources of clay detritus are probably the same as for the silt fraction, namely, coastal erosion, suspended-sediment reflux from adjacent estuaries and possible in situ winnowing of relict and palimpsest sediments. Although increasing clay deposition normally takes place in a seaward direction, strong storm waves and tides might redistribute bottom shelf-edge clays en masse, possibly resulting in some net shoreward storm displacement. Some of the crenulations shown by the clay isopleths in the central sector could conceivably reflect varying dispersal directions under alternate fair-weather and storm hydraulic conditions.

CONCLUDING STATEMENT

The foregoing description of the general textural characteristics of sea-floor sediments represents an initial investigative phase of a broader sedimentological study of the south Texas OCS region. Additional ongoing and planned future studies of sea-floor sediments, suspended-sediment dispersal, and sedimentation rates will provide further knowledge of the OCS sedimentological regime. In turn, this knowledge should provide further insight into the complex sedimentary processes indigenous to continental shelves, thus establishing a credible basis for environmental assessment.

REFERENCES CITED

Bretschneider, C. L., and Gaul, R. D., 1956a, Wave statistics for the Gulf of Mexico off Brownsville, Texas: U.S. Beach Erosion Board Tech. Mem. 85, [37] p.

——— 1956b, Wave statistics for the Gulf of Mexico off Caplen, Texas: U.S. Beach Erosion Board Tech. Mem. 86, [51] p.

Curray, J. R., 1960, Sediments and history of Holocene transgression, continental shelf, northwest Gulf of Mexico, *in* Shepard, F. P., Phleger, F. B., and van Andel, Tj. H., eds., Recent sediments, northwest Gulf of Mexico: Tulsa, Okla., Am. Assoc. Petroleum Geologists, p. 221–226.

Hayes, M. O., 1967, Hurricanes as geologic agents—Case studies of hurricanes Carla, 1961, and Cindy, 1963: Texas Univ. Bur. Econ. Geology, Rept. Inv. 61, 56 p.

Hill, G. W., Garrison, L. E., and Hunter, R. E., 1976, Maps showing drift patterns along the north-central Texas coast, 1973–1974: U.S. Geol. Survey Misc. Field Studies Map MF–714.

Hunter, R. E., Hill., G. W., and Garrison, L. E., 1974, Maps showing drift patterns along the south Texas coast, 1970–1973: U.S. Geol. Survey Misc. Field Studies Map MF–623, 2 sheets.

Kimsey, J. B., and Temple, R. F., 1963, Currents on the Continental Shelf of the northwestern Gulf of Mexico: U.S. Bur. Commercial Fisheries Circ. 161, p. 23–27.

——— 1964, Currents on the Continental Shelf of the northwestern Gulf of Mexico: U.S. Bur. Commercial Fisheries Circ. 183, p. 25–27.

Lohse, E. A., 1955, Dynamic geology of the modern coastal region, northwest Gulf of Mexico, *in* Hough, J. L., and Menard, H. W., Jr., eds., Finding ancient shorelines—A symposium: Soc. Econ. Paleontologists and Mineralogists Spec. Pub. 3, p. 99–105.

Marmer, H. A., 1954, Tides and sea level in the Gulf of Mexico. *in* Gulf of Mexico, its origin, waters, and marine life: U.S. Fish and Wildlife Service Bull. 89, p. 101–118.

Shepard, F. P., and Moore, D. G., 1954, Sedimentary environments differentiated by coarse-fraction studies: Am. Assoc. Petroleum Geologists Bull., v. 38, no. 8, p. 1792–1802.

Shepard, F. P., Phleger, F. B., and van Andel, Tj. H., eds., 1960, Recent sediments, northwest Gulf of Mexico: Tulsa, Okla., Am. Assoc. Petroleum Geologists, 394 p.

Swift, D. J. P., Stanley, D. J., and Curray, J. R., 1971, Relict sediments on continental shelves—A reconsideration: Jour. Geology, v. 79, no. 3, p. 322–346.

Watson, R. L., 1971, Origin of shell beaches, Padre Island, Texas: Jour. Sed. Petrology, v. 41, no. 4, p. 1105–1111.

Watson, R. L., and Behrens, E. W., 1970, Nearshore surface currents, southeastern Texas Gulf Coast: Contr. Marine Sci., v. 15, p. 133–143.

Wilson, B. W., 1957, Hurricane wave statistics for the Gulf of Mexico: U.S. Beach Erosion Board Tech. Mem. 98, [103] p.

Jour. Research U.S. Geol. Survey
Vol. 4, No. 6, Nov.-Dec. 1976, p. 715–716

BRANNERITE FROM THE PENN HAVEN JUNCTION URANIUM OCCURRENCE, CARBON COUNTY, PENNSYLVANIA

By R. B. FINKELMAN and HARRY KLEMIC, Reston, Va.

Abstract.—Thorium-free brannerite has been identified in Upper Devonian uraniferous sandstone from Penn Haven Junction, Carbon County, Pa. The brannerite was located by a variation of the "Lexan" technique and is associated with galena, uraninite, and clausthalite. The angular thorium-free nature of the brannerite suggests that it formed by metamorphism of uranium-saturated leucoxene. As a result of the metamorphism some uranium may be in less soluble minerals than those found in the uranium deposits of the Western United States. For this reason, in-place leaching of the uranium may be impractical.

Reexamination of uraniferous sandstone of Late Devonian age from Penn Haven Junction, Carbon County, Pa., has shown the presence of thorium-free brannerite. Klemic, Warman, and Taylor (1963) had reported uraninite as a primary uranium-bearing mineral. However, the fine-grained nature of the uraniferous material in these sandstones made it difficult to determine the possible presence of other primary uranium minerals.

A knowledge of the nature of the primary uranium minerals is necessary to understand the genesis of the deposit and the processes required for extraction of uranium from ores in deposits of this type. Very fine grained uranium-bearing minerals have been found by means of fission tracks generated by neutron irradiation. This method has made it possible to obtain additional information on the minerals in this deposit.

The material used in this study consisted of previously studied samples of uraniferous rock and mineral separates, and uncovered thin sections of sandstone containing uranium minerals and clausthalite (PbSe).

Brannerite (ideally UTi_2O_6) and galena were identified for the first time in the uraniferous rock from the Penn Haven Junction uranium occurrence, and the presence of uraninite and associated clausthalite was confirmed. The possibility that some of the uranium may be in the form of coffinite, a hydrated uranium silicate, remains to be investigated.

EXPERIMENTAL PROCEDURE

The samples were prepared for analysis by using a variation of the "Lexan" technique of Fleischer, Price, Walker, and Hubbard (1964). Several grains of the uraniferous sandstone were ground to about 200 mesh. The powdered sample was then dispersed in a 1:1 collodian–amyl acetate solution and spread on several 1-by 2-inch strips of 10-mil (0.01-inch) Lexan. After irradiation in a flux of 10^{15} neutrons per square centimeter per second, the collodion film containing the sample was stripped from the Lexan. The Lexan was then etched in a $7N$ sodium hydroxide solution at 70°C to make the fission-track damage more visible. The Lexan slides were then washed, dried, and the collodion film replaced. The film can be repositioned to within a few micrometres of its original position by utilizing scratches or pits in the Lexan that have been replicated in the collodion film or by other registration marks made in the collodion and Lexan before stripping. Once the Lexan is properly repositioned, the particle from which the fission tracks were generated could be easily found, either by the similarity in shape of the particle and the area damaged by fission tracks (generally for grains greater than 20 micrometres in diameter) or by the proximity of tracks and the particle from which they were generated to the registration marks. This is done by measuring bearing and distance with a micrometre ocular.

This technique allowed the rapid location of microscopic uranium-bearing particles and the determination of some of their optical characteristics (index of refraction of collodion = 1.54). The grains were recovered for subsequent analysis by carefully scribing around the particle while it was in view under the microscope, removing the collodion chip containing the grain to a glass slide, and dissolving the collodion by means of amyl acetate from a micropipet, again keeping the particle in view under the microscope. Use of surgical scalpels and long-working-distance petrographic objectives facilitated this procedure.

RESULTS

Optical scan of the Lexan-collodion slides indicated that most of the fission-track clusters were generated by angular-to-subrounded opaque grains. About 10 percent of the fission-track clusters were associated with reddish-brown-to-yellow, weakly birefringent

granular particles. Many of the opaque and granular particles were still attached to or imbedded in the quartz-matrix material. Some areas of relatively diffuse fission tracks were associated with very finely dispersed brown inclusions in quartz.

Six opaque particles that caused extensive fission-track damage in the Lexan were isolated and examined by means of an energy-dispersive system on a scanning electron microscope. All the particles contained major uranium and titanium in constant proportions. Lead and selenium (presumably clausthalite) were concentrated in one area of one grain. Another particle showed characteristic peaks on the oscilloscope where both lead and sulfur peaks would be expected. Traces of silicon, aluminum and iron were observed on several grains. Four of these opaque particles were analyzed by the X-ray powder diffraction method. The only X-ray pattern obtained was that of galena from the grain containing lead and sulfur. These particles were then heated in air to 1000°C for 1¼ hours in a muffle furnace and analyzed again. All gave powder patterns similar to that of brannerite, which had been obtained after heating metamict material (Pabst, 1954).

The small size of the brannerite grains (<20 μm) precluded quantitative microprobe analysis. Compared with brannerite (kindly supplied by Adolf Pabst) from Mono County, Calif. (Pabst, 1954), counts for titanium, uranium, iron, and calcium were about 25 percent lower for the Pennsylvania brannerite. However, the Ti:U+Th ratio is well within the range of brannerites analyzed by Ferris and Ruud (1971). Thorium was looked for but not detected in these grains (limit of detection is less than 0.5 weight percent). Data on the rare-earth elements were not conclusive. However, no significant difference in concentration was apparent between the Pennsylvania and California brannerites. Energy-dispersive analyses did not indicate more than trace concentrations of any other elements.

Attempts were made to obtain X-ray powder patterns on several other opaque and granular uranium-bearing grains removed from the collodion. The only pattern obtained was that of uraninite from an opaque particle.

Several polished thin sections of the quartz sandstone were analyzed by means of an energy-dispersive system on an electron microprobe. The opaque phase in one slide is primarily clausthalite; in another, zircon and clausthalite are equally abundant. Galena is rare. Major concentrations of uranium were found in the interstices. In about half of the occurrences, uranium is associated with variable concentrations of titanium. In the rest of the occurrences, the uranium does not appear to be associated with any element other than silicon. However, as silicon is ubiquitous in the quartz sandstone, we could not determine whether the uranium is present as coffinite or uraninite.

CONCLUSION

The genesis of the brannerite in the Penn Haven Junction uranium occurrence requires explanation in the context of the genesis of the uranium deposit as a whole. Because the Penn Haven Junction uranium occurrence and others in Devonian rocks in Pennsylvania have characteristics similar to those of some Colorado Plateau-type uranium deposits (Klemic and others, 1963), uranium carried in solution was evidently deposited in the interstices of the detrital minerals of the sedimentary rocks. Some detrital brannerite may have been present in the sedimentary layers in which the uranium was precipitated. Another possibility is that uranium from solution may have impregnated porous leucoxene in the sedimentary layers in addition to that which was deposited as interstitial to clastic grains. Subsequent metamorphism (chlorite grade or anthracite grade) may have altered the uranium-saturated leucoxene to brannerite. We prefer the latter hypothesis because the general nature of the Penn Haven Junction uranium occurrnce is that of a Colorado Plateau-type uranium deposit rather than a detrital-type uranium-thorium deposit.

As a result of the low-grade metamorphism of the host rocks, some of the uranium may be in less soluble minerals than those found in many of the uranium deposits of the Western United States. Therefore, beneficiation tests of the uraniferous rock from the Penn Haven Junction deposit would be advisable in the early stages of evaluation of the deposit. Examination of the uraniferous rock exposed in a railroad cut at the discovery site indicates that the rock is relatively impermeable and that in-place leaching of the uranium would be impractical.

REFERENCES CITED

Ferris, C. S., and Rund, C. O., 1971, Brannerite: its occurrences and recognition by microprobe: Colorado School Mines Quart., v. 66, no. 4, 35 p.

Fleischer, R. L., Price, P. B., Walker, R. M., and Hubbard, E. L., 1964, Track registration in various solid-state nuclear track detectors: Phys. Rev., v. 133, no. 5A, p. 1443–1449.

Klemic, Harry, Warman, J. C., and Taylor, A. R., 1963, Geology and uranium occurrences of the northern half of the Lehighton, Pennsylvania, quadrangle and adjoining areas: U.S. Geol. Survey Bull. 1138, 97 p.

Pabst, Adolf, 1954, Brannerite from California: Am. Mineralogist, v. 39, p. 109–117.

Jour. Research U.S. Geol. Survey
Vol. 4, No. 6, Nov.-Dec. 1976, p. 717–725

MICROPROBE STUDY OF OLIVINE CHROMITITES OF THE GOODNEWS BAY ULTRAMAFIC COMPLEX, ALASKA, AND THE OCCURRENCE OF PLATINUM

By M. L. BIRD and A. L. CLARK, Reston, Va.

Abstract.—Electron-microprobe analyses of the dunite and olivine chromitite of the ultramafic complex at Goodnews Bay, Alaska, show that the chromite contains more ferrous and ferric iron than is found in chromite from alpine or stratiform complexes. The iron-magnesium distribution coefficients between chromite and olivine demonstrate that more ferrous iron is partitioned to the chromite in the Goodnews Bay complex than to the chromite in stratiform chromitite but that the distribution is similar to that for alpine chromitite. The high iron content of the chromite and olivine at Goodnews Bay and the general geology of the complex indicate that it is a concentric-type ultramafic complex similar to the platinum-bearing concentric complexes of southeastern Alaska. A platinum-alloy inclusion in the chromite found in the ultramafic section at Goodnews Bay demonstrates that the olivine chromitite is the source of at least some of the platinum.

The ultramafic complex at Goodnews Bay, Alaska (fig. 1) is composed largely of dunite intruded as a solid mass into metasedimentary and volcanic rocks of Paleozoic age (Mertie, 1940). The intrusion is tentatively dated as Late Cretaceous or early Tertiary (Mertie, 1968).

Chromite is present as an accessory mineral and as cumulate layers within the dunite. Peridotite and pyroxenite occur around the edges of the dunite and at the apex of the complex (Mertie, 1968). Drilling by mining companies has also revealed pyroxenite beneath the sedimentary cover on the flanks of the ultramafic body.

The economic interest in the Goodnews Bay complex is due to platinum placers, which have yielded more than half a million ounces of platinum. The placers are in fluvial gravels deposited by streams that have dissected the complex, and the platinum is thought to have been derived from the ultramafic rocks, although no particulate platinum had been found in place in the ultramafic section until this investigation. The gravels containing the platinum are all on the southeastern side of the complex (fig. 2).

In this investigation, petrographic and electron-microprobe analyses of the ultramafic rocks of the Goodnews Bay complex have been made to determine the chemical differences between the platinum-producing ultramafic complexes and other types of ultramafic complexes, such as the alpine type, which usually produce no platinum.

PREVIOUS WORK

The first study of the Goodnews Bay ultramafic complex was made by Mertie (1919) in his field studies

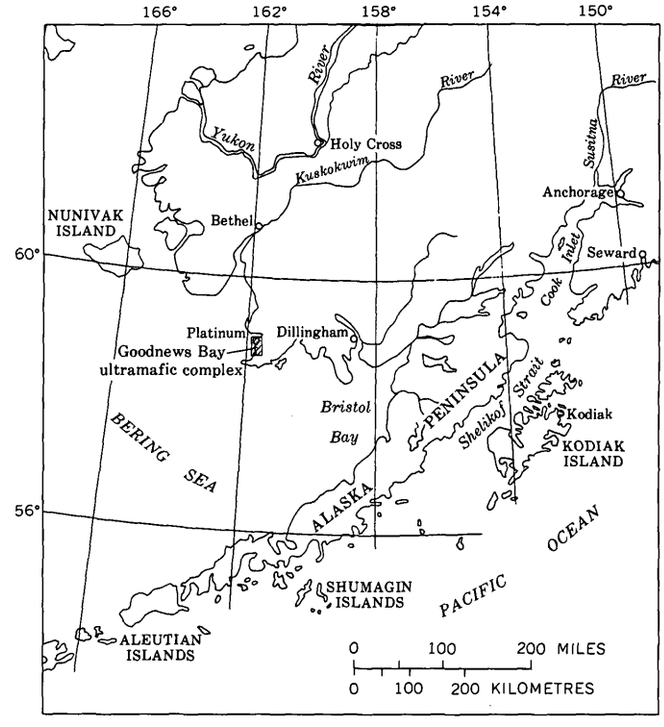

FIGURE 1.—Map showing location of Goodnews Bay ultramafic complex. The hatched area shows location of the map of figure 2.

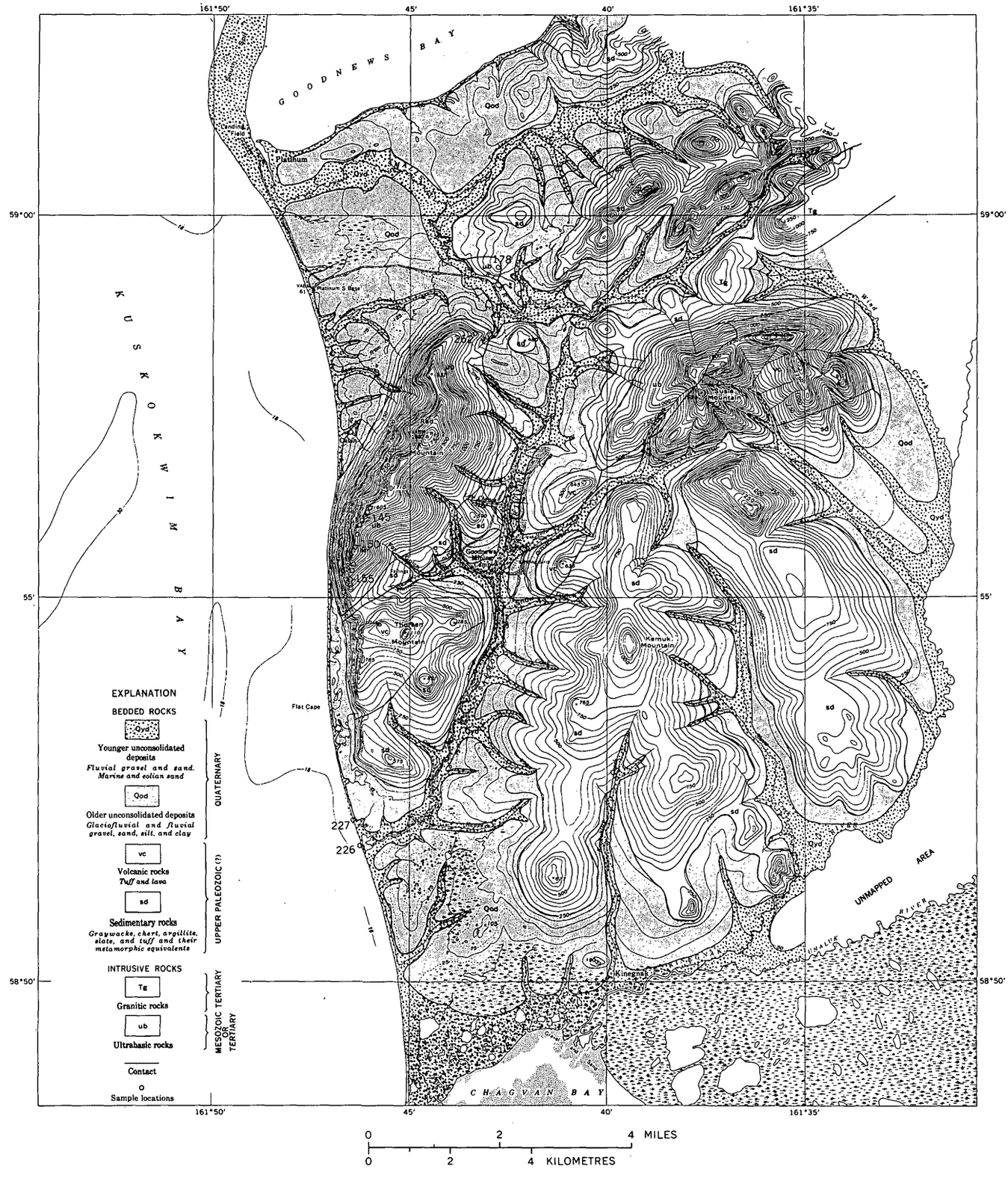

FIGURE 2.—Geologic map of the Goodnews platinum district, Alaska (from Mertie, 1969), showing locations of samples included in this study.

of the chromite deposits of Alaska. More detailed work on the complex was done by Mertie (1940) when he mapped the complex and related the distribution of the platinum metals to the ultramafic section. Mertie (1940) noted that several intergrowths of chromite and platinum had been found in placer nug-

gets, thus directly relating the occurrence of platinum to the olivine chromitites. Similarly, he noted that a small deposit of placer platinum had been found by a mining company in an amphitheater cut in the dunite high on the southwest slope of Red Mountain (Mertie, 1969, p. 81). Platinum has also been washed from the soil and grass on the mountain slopes. The occurrence of platinum in the ultramafic rocks is further indicated by the spectrochemical analyses of 40 rock samples collected by A. L. Clark on a traverse across Red Mountain. The analyses averaged 0.16 part per million Pt and 0.04 ppm Pd. These data are not included in this report. The samples with the higher values were from the central parts of the complex. Similar analytical results have been obtained by mining companies in the area (Mertie, 1940).

PRESENT STUDY

Method of study

Polished thin sections were prepared of 18 specimens collected from the Goodnews Bay complex by A. L. Clark. The thin sections were studied petrographically, and selected areas were analyzed using the electron microprobe.

Microprobe analysis

Electron-microprobe analyses of individual mineral grains in the specimens were made for the elements Ca, Cr, Al, Si, Fe, Mg, Ti, Ni, and Na, using an Applied Research Laboratories microprobe having three scanners with LiF, ADP, and RAP crystals.

The percentages of ferrous and ferric iron were determined from total iron by assuming that the total number of dipositive ions equals 1.000 and then recalculating the remaining iron as ferric iron. The Ti and Si are assumed to occupy trivalent sites, although some investigators put Ti into two divalent sites (see table 1).

Operating conditions for the microprobe included an accelerating potential of 15 kV (kilovolt) and a beam-current of 0.1 μA (microampere). X-ray counts on each element were integrated against 2.0 μA of beam-current for two consecutive counting periods. Corrections were made for background, absorption, fluorescence, and atomic number effect using the methods described by Sweatman and Long (1969).

Standards used for microprobe analysis were chromites from Union Bay, Alaska, and Stillwater, Mont., that have been chemically analyzed, and synthetic enstatite, anorthite, and diopside-jadeite ($di_{65}jd_{35}$) that had been prepared by J. F. Schairer at the Carnegie Geophysical Laboratory.

ANALYTICAL RESULTS

Petrography

Petrographic examination of the samples used in this study shows that they are olivine chromitites containing varying percentages of olivine and chromite. No pyroxene is present except for a few inclusions of diopside within the chromite. Observed for the first time in specimens from this locality were small round inclusions of a platinum alloy in the chromite.

The chromite occurs as an accessory and as a cumulate mineral in euhedral to anhedral grains. Much of the chromite is zoned; central cores are surrounded by rims of chromite, which are usually separated from the cores by concentric fractures (fig. 3).

The olivine crystals are large, show undulatory extinction, and, in general, poikilitically enclose accessory chromite grains. Where the chromite is more abundant, a net texture is evident. The olivine commonly contains abundant inclusions of several iron, calcium, magnesium, titanium, and chromium-bearing minerals which formed as platelets along preferred crystallographic directions. Figure 4 shows well-developed plates and skeletal crystals in olivine. In several samples the olivine is clouded by myriad minute inclusions which give a gray cast to the thin sections. Approximately 30–50 percent of the olivine is altered to serpentine which forms a reticulating network throughout the sample.

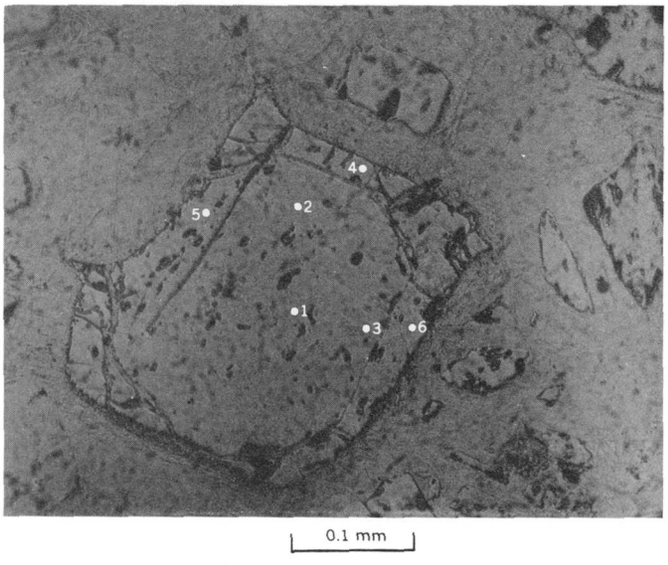

FIGURE 3.—Photomicrograph of chromite sample AGK–262 illustrating concentric zoning. The concentric fractures separate the more ferric rims from the central cores. Points on photomicrograph refer to microprobe analyses given in table 2.

TABLE 1.—*Electron-microprobe analysis of chromite and*

Sample Number	154B	155–1	155–2	178	143	154B	157–1	157–2	157–3	146	262–1
CHROMITE											
Oxide, in weight percent											
Cr_2O_3	31.82	32.77	26.86	39.01	37.97	42.53	28.92	36.66	43.70	44.62	33.97
Al_2O_3	8.50	12.53	2.00	10.01	10.51	12.32	2.49	10.66	12.40	12.02	14.74
Fe_2O_3	26.41	21.41	38.45	18.73	20.07	14.20	36.18	20.09	12.35	12.07	19.67
SiO_2	.24	.21	.21	.06	.11	.02	.21	.17	.09	.06	.21
TiO_2	.98	1.18	1.35	.58	1.30	.69	.86	.61	.64	.78	1.10
NiO	.20	.10	.23	.08	.11	.05	.19	.05	.06	.08	.09
Na_2O	.0	.0	.0	.0	.0	.0	.0	.0	.0	.0	.0
CaO	.0	.0	.0	.0	.0	.0	.0	.0	.0	.0	.0
FeO	27.07	26.50	28.18	27.28	23.83	22.14	28.16	27.15	23.49	21.58	23.73
MgO	3.58	4.59	2.21	3.90	6.32	7.51	2.26	4.01	6.63	7.76	6.88
Total	98.80	99.29	99.49	99.65	100.22	99.46	99.27	99.40	99.36	98.97	100.39
Number of cations/4 oxygens											
Cr	0.894	0.891	0.785	1.075	1.020	1.130	.845	1.009	1.168	1.189	0.890
Al	.356	.508	.087	.411	.421	.488	.109	.437	.494	.477	.576
Fe^{3+}	.706	.554	1.070	.491	.513	.359	1.006	.526	.314	.306	.491
Si	.008	.007	.008	.002	.004	.001	.008	.006	.003	.002	.007
Ti	.029	.033	.043	.016	.035	.018	.027	.017	.017	.021	.029
Ni	.006	.003	.007	.002	.003	.001	.006	.001	.002	.002	.002
Na	0.	.0	.0	.0	.0	.0	.0	.0	.0	.0	.0
Ca	.0	.0	.0	.0	.0	.0	.0	.0	.0	.0	.0
Fe^{2+}	.804	.762	.872	.795	.677	.622	.870	.790	.664	.608	.658
Mg	.190	.235	.122	.202	.320	.376	.124	.208	.334	.390	.340
OLIVINE											
Oxide, in weight percent											
Cr_2O_3	------	0.03	------	0.01	0.0	0.0	0.02	0.01	------	0.04	0.02
Al_2O_3	------	.0	------	.0	.0	.0	.0	.0	------	.0	.0
SiO_2	------	40.88	------	41.34	39.58	41.22	40.72	41.22	------	40.86	40.39
TiO_2	------	.0	------	.0	.02	.01	.02	.04	------	.0	.01
NiO	------	.15	------	.19	.31	.16	.18	.17	------	.20	.06
Na_2O	------	.0	------	.0	.0	.0	.0	.0	------	.04	.0
CaO	------	.0	------	.0	.08	.0	.0	.05	------	.03	.0
FeO*	------	10.89	------	8.52	10.71	8.59	9.51	8.54	------	9.52	11.07
MgO	------	50.05	------	52.02	50.70	52.12	50.90	51.68	------	51.06	49.47
Total	------	102.00	------	102.08	101.40	102.10	101.35	101.71	------	101.75	101.02
Number of cations/4 oxygens											
Cr	------	0.001	------	0.000	0.0	0.0	0.000	0.000	------	0.001	0.000
Al	------	.0	------	.0	.0	.0	.0	.0	------	.0	.0
Si	------	.987	------	.987	.065	.985	.984	.988	------	.984	.986
Ti	------	.0	------	.0	.000	.000	.000	.001	------	.0	.000
Ni	------	.003	------	.004	.006	.003	.004	.003	------	.004	.001
Na	------	.0	------	.0	.0	.0	.0	.0	------	.002	.0
Ca	------	.0	------	.0	.002	.0	.0	.001	------	.001	.0
Fe^{2+}	------	.220	------	.170	.218	.172	.192	.171	------	.192	.226
Mg	------	1.802	------	1.852	1.843	1.856	1.834	1.847	------	1.833	1.800

*Total iron as FeO.

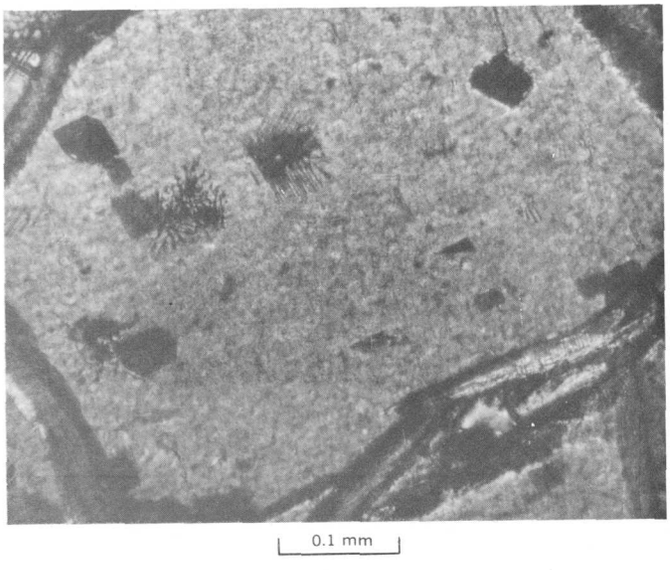

FIGURE 4.—Photomicrograph of inclusions in olivine in sample AGK–147. The inclusions are platelets of magnetite and ferrit-chromit.

Composition of Goodnews Bay chromite

Microprobe analyses of the chromite from Goodnews Bay are given in table 1. Characteristic of the chromite is the high content of ferrous and ferric iron and titanium and low percentages of magnesia, alumina, and nickel. The zoned chromite grains have peripheral zones significantly higher in ferrous and ferric iron and lower in chromium than the central zones (table 2).

Comparison of the chromite compositions with those of the Muskox stratiform complex of northern Canada shows some similarities, although titanium in the latter is significantly higher. Figures 5 to 7 include a chemical comparison of Goodnews Bay chromite with chromite of the Stillwater Complex. Chromite from both localities contains high percentages of ferrous and ferric iron and similar amounts of chromium. Significant differences in composition, however, are shown for chromite from alpine complexes. Chromite from alpine complexes contains much less ferric and

olivine of the Goodnews Bay ultramafic complex, Alaska

262–2	144	182A–1	182A–2	GK–226A	AGK–153	AGK–145–1	AGK–156A	AGK–147	GK–227A	AGK–150C	AGK–150–1	AGK–148
CHROMITE												
Oxide, in weight percent												
24.03	36.50	41.98	47.28	36.96	40.76	39.49	38.47	36.90	30.87	37.97	38.31	21.97
2.44	14.02	8.67	9.11	13.02	13.28	13.87	13.79	10.45	14.21	12.98	12.98	.0
41.05	17.41	17.69	13.90	21.72	18.00	18.20	19.13	22.73	22.86	18.21	18.21	45.65
.21	.17	.13	.17	.09	.04	.02	.04	.06	.06	.0	.11	.08
1.44	.20	.62	.58	.0	.0	.0	.0	.0	1.92	1.09	1.28	1.00
.15	.09	.09	.03	.0	.0	.0	.0	.0	.19	.18	.14	.14
.0	.0	.0	.0	.0	.0	.0	.0	.0	.0	.0	.0	.0
.0	.0	.0	.0	.01	.01	.01	.0	.0	.0	.01	.01	.0
28.92	24.31	27.36	26.59	24.03	21.29	21.06	20.74	25.24	25.08	21.64	21.50	30.00
1.94	6.38	3.88	4.97	6.98	8.67	8.74	8.87	5.52	6.04	7.89	8.19	.89
100.18	100.08	00.42	102.63	102.81	102.05	101.39	101.04	100.90	101.23	99.97	100.73	99.73
Number of cations/4 oxygens												
0.698	0.964	1.155	1.260	0.958	1.048	1.019	0.995	0.994	0.810	1.000	0.999	0.656
.106	.552	.356	.362	.503	.509	.533	.532	.420	.556	.510	.505	.0
1.136	.438	.463	.352	.536	.441	.447	.471	.583	.571	.456	.452	1.300
.008	.006	.004	.006	.003	.001	.001	.001	.002	.002	.0	.004	.003
.046	.032	.017	.015	.0	.0	.0	.0	.0	.053	.030	.035	.028
.005	.002	.002	.001	.0	.0	.0	.0	.0	.005	.005	.004	.004
.0	.0	.0	.0		.0	.0	.0	.0	.0	.0	.0	.0
.0	.0	.0	.0	.000	.000	.000	.0	.0	.0	.000	.000	.0
.889	.680	.796	.749	.658	.579	.575	.567	.719	.696	.603	.593	.948
.106	.318	.201	.250	.341	.420	.425	.433	.281	.299	.392	.403	.050
OLIVINE												
Oxide, in weight percent												
------	0.0	0.00	------	0.0	0.13	0.06	0.07	------	0.0	0.01	0.00	0.0
------	.0	.0	------	.0	.0	.0	.0	------	.0	.0	.0	.0
------	40.59	40.36	------	40.52	40.94	40.68	40.95	------	39.19	40.11	39.74	40.16
------	.0	.0	------	------	------	------	------	------	.02	.09	.0	.0
------	.08	.12	------	------	------	------	------	------	.09	.11	.25	.15
------	.0	.0	------	------	------	------	------	------	.0	.0	.0	.0
------	.0	.0	------	.06	.09	.09	.12	------	.05	.05	.17	.0
------	11.49	8.95	------	10.71	8.14	9.27	8.75	------	11.98	8.31	9.37	11.43
------	49.72	51.80	------	49.31	51.01	50.74	49.61	------	49.14	51.80	51.41	49.06
------	101.88	101.23	------	100.60	100.31	100.84	99.50	------	100.47	100.48	100.94	100.80
Number of cations/4 oxygens												
------	0.0	0.000	------	0.0	0.002	0.001	0.001	------	0.0	0.000	0.000	0.0
------	.0	.0	------	.0	.00	.0	.0	------	.0	.0	.0	.0
------	.984	.975	------	.991	.993	.987	1.003	------	.969	.974	.967	.985
------	.0	.0	------	------	------	------	------	------	.000	.002	.0	.0
------	.002	.002	------	------	------	------	------	------	.002	.002	.005	.003
------	.0	.0	------	------	------	------	------	------	.0	.0	.0	.0
------	.0	.0	------	.002	.002	.002	.003	------	.001	.001	.004	.0
------	.233	.181	------	.219	.165	.188	.179	------	.248	.169	.191	.234
------	1.797	1.866	------	1.798	1.844	1.835	1.810	------	1.811	1.875	1.865	1.793

TABLE 2.—*Microprobe analyses of chromite sample AGK–262*
[See figure 2 for location points]

Sample number	1	2	3	4	5	6
Oxide, in wt percent						
Cr_2O_3	33.97	32.24	32.26	24.57	24.03	23.01
Al_2O_3	14.74	15.10	14.83	3.10	2.44	2.97
Fe_2O_3	19.67	21.04	20.80	39.04	41.05	40.64
SiO_2	.21	.19	.19	.21	.21	.17
TiO_2	1.10	1.12	1.14	1.35	1.44	1.35
NiO	.09	.05	.09	.18	.15	.09
Na_2O	.0	.0	.0	.0	.0	.0
CaO	.0	.0	.0	.0	.0	.0
FeO	23.73	24.14	23.85	28.07	28.92	28.57
MgO	6.88	6.70	6.68	2.27	1.94	1.96
Total	100.39	100.58	99.84	98.79	100.18	98.76
Number of cations/4 oxygens						
Cr	0.890	0.844	0.851	0.719	0.698	0.677
Al	.576	.589	.583	.135	.106	.130
Fe	.491	.524	.522	1.088	1.136	1.138
Si	.007	.006	.006	.008	.008	.006
Ti	.029	.030	.031	.043	.046	.044
Ni	.002	.001	.002	.005	.005	.003
Na	.0	.0	.0	.0	.0	.0
Ca	.0	.0	.0	.0	.0	.0
Fe	.658	.668	.665	.869	.889	.889
Mg	.340	.330	.332	.125	.106	.109

ferrous iron and more magnesium. Still more significant are the larger amounts of aluminum in alpine chromite. Figure 6 also shows the trend of the graph of $Cr/(Cr+Al+Fe^{3+})$ plotted against $Mg/(Mg+Fe^{2+})$ for high- alumina alpine chromite. This trend is characteristic of alpine-type chromite and distinguishes it from either the stratiform or Alaskan (concentric)-type chromite.

Composition of olivine and pyroxene from Goodnews Bay

The microprobe analyses of olivine (table 1) indicate a variation of its fayalite content from 17 to 23 mole percent, assuming that all the iron is ferrous iron. As is indicated by figure 5, the iron-magnesium ratio for Goodnews Bay olivine is higher than that for the olivine of alpine complexes and is generally in the range of the iron-magnesium ratio for olivine of stratiform complexes.

The only pyroxene observed occurred as inclusions in chromite and olivine. The pyroxene included in

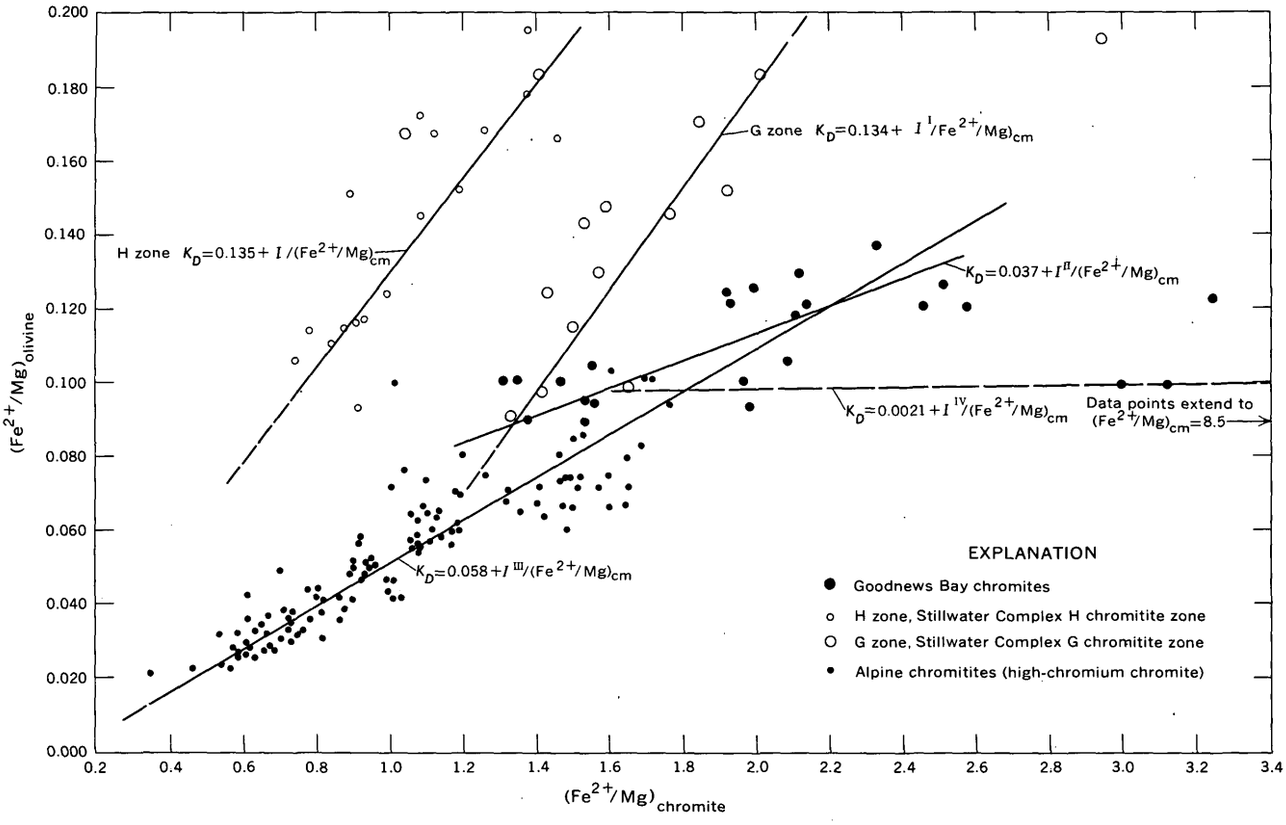

FIGURE 5.—Graph of $(Fe^{2+}/Mg)_{ol}$ versus $(Fe^{2+}/Mg)_{cm}$ for olivine-chromite associations in the Goodnews Bay, Stillwater, and alpine ultramafic complexes. The Stillwater data are from Jackson (1969) and the alpine data are from M. L. Bird (unpub. data, 1976). The values of I, I^{I}, I^{II}, I^{III}, and I^{IV} are intercepts on the ordinate.

chromite is diopside, and one enstatite inclusion was found in olivine.

Composition of inclusions in olivine

Table 3 gives the microprobe analyses of several of the larger inclusions occurring as platelets in the olivine. The analyses indicate that the inclusions are ferrit-chromit and magnetite. Smaller inclusions, for which unsatisfactory analyses were obtained, contained Ca and Ti in addition to Fe, Cr, and the elements of the olivine host, thus indicating the presence of additional mineral phases.

Distribution of Fe^{2+} and Mg between olivine and chromite

Figure 5 shows that the graph of $(Fe^{+2}/Mg)_{ol}$ plotted against $(Fe^{2+}/Mg)_{cm}$ for the rocks of the Goodnews Bay complex is essentially linear. The lines which were visually fit to the data suggest that two trends are required to describe the iron-magnesium relationships between olivine and chromite. The data along the line having a slope of 0.37 correspond to the central cores or zones of the chromite grains, whereas those points along the line for which the

TABLE 3.—*Microprobe analyses of olivine and of chromite inclusions in olivine, Goodnews Bay ultramafic complex, Alaska*
[N.d., not determined]

Sample number	AGK-147	AGK-156A	AGK-147	AGK-147	AGK-156A
	Olivine		Chromite inclusions		
Oxide, in wt percent					
Cr_2O_3	0.06	0.03	24.70	0.03	7.48
Al_2O_3	.0	.0	.30	.15	.06
Fe_2O_3	N.d.	N.d.	44.12	70.32	61.87
SiO_2	40.46	40.42	.17	.06	.34
CaO	.10	.09	.03	.22	.60
FeO*	10.76	11.37	29.36	30.66	29.17
MgO	49.56	48.69	1.39	.48	.98
Total	100.94	100.60	100.07	101.92	100.50
Number of cations/4 oxygens					
Cr	0.011	0.001	0.733	0.001	0.223
Al	.0	.0	.013	.007	.003
Fe^{3+}	N.d.	N.d.	1.245	1.989	1.757
Si	.987	.992	.006	.002	.013
Ca	.003	.002	.001	.009	.024
Fe^{2+}	.219	.233	.921	.964	.921
Mg	1.802	1.780	.078	.027	.055

*Total iron as FeO.

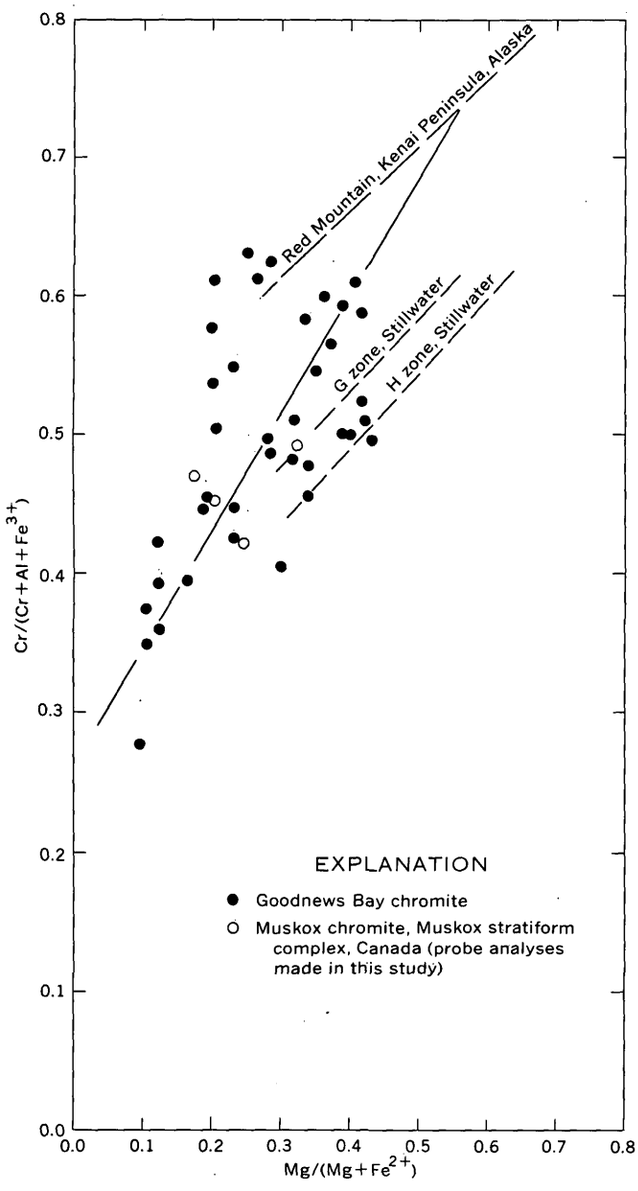

FIGURE 6.—Graph of $Cr/(Cr+Al+Fe^{3+})$ versus $Mg/(Mg+Fe^{2+})$ for chromite of the Goodnews Bay ultramafic complex. Data for the Stillwater Complex are from Jackson (1969). Data points for the Muskox intrusion shown for comparison. Red Mountain, Kenai Peninsula, Alaska, trend from M. L. Bird (unpub. data, 1976).

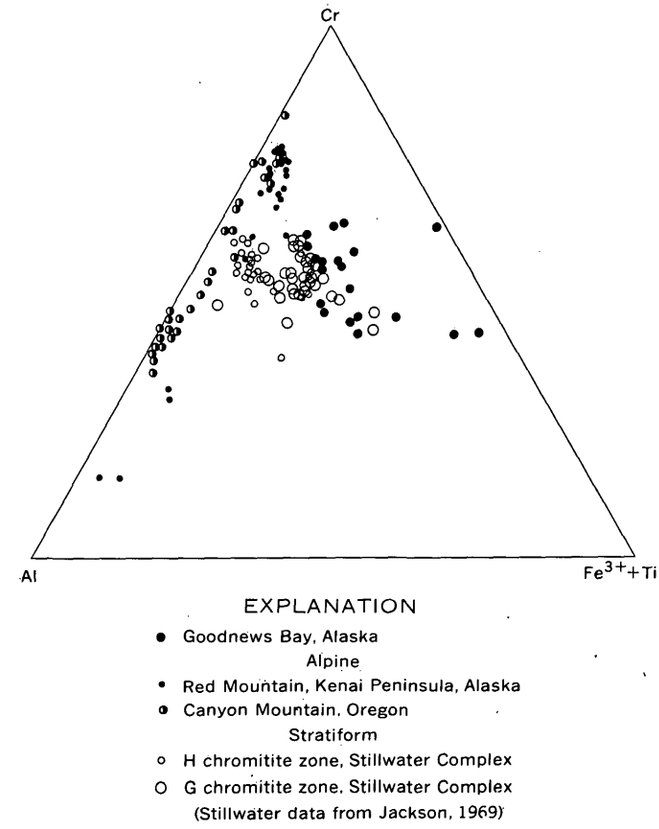

FIGURE 7.—Triangular plot of Cr, Al, and $Fe^{3+}+Ti$ components of chromite from the Goodnews Bay, alpine, and stratiform complexes. Stillwater data from Jackson (1969); all other data from M. L. Bird (unpub. data, 1976).

slope is 0.0021, correspond to analyses of the iron-rich peripheral zones. As is shown in figure 5, the iron-magnesium ratios for chromite extend to 8.5.

Comparison of these data with similar data for alpine and stratiform chromitites is also shown by graphs in figure 5. The data for Goodnews Bay chromitite appear to form an extension of the data for alpine chromitite, but a different slope or trend is discernible. Variation of the logarithm of the iron-magnesium distribution coefficient, ln K_D, with the chromium content of the Goodnews Bay chromite is similar to its variation for chromitite from alpine complexes, but is different from this variation in stratiform chromitite. The data for chromite from the Stillwater Complex show a significant difference in trend from that of data for chromite from Goodnews Bay or from alpine complexes. This difference suggests a possible difference in crystallization temperature or composition of the magma from which each type of ultramafic complex was derived.

A CONCENTRIC-TYPE ULTRAMAFIC COMPLEX AT GOODNEWS BAY

The large amounts of ferrous and ferric iron in the chromite and olivine of the Goodnews Bay complex, the concentric occurrence of pyroxenite rimming the dunite core, the intrusive nature of the complex, and the metamorphosed condition (although regional in character) of the surrounding country rock serve to classify the complex as an Alaskan or concentric-type of ultramafic complex (Jackson, 1971; Jackson and

Thayer, 1972). The Goodnews Bay complex, therefore, falls into the same class as the Blashke Islands, Union Bay, Duke Island, Salt Chuck, Mount Fairweather, and Klukwan complexes of southeastern Alaska (Ruckmick and Noble, 1959; Noble and Taylor, 1960; Taylor, 1967).

OCCURRENCE OF PLATINUM IN THE ULTRAMAFIC SECTION AT GOODNEWS BAY AND THE ULTRAMAFIC COMPLEXES OF SOUTHEASTERN ALASKA

The ultramafic complexes of southeastern Alaska are chemically similar to the Goodnews Bay complex, and all contain platinum. Comparison of platinum contents in the southeastern Alaska complexes with those from Goodnews Bay is made in tables 4 and 5. The comparison shows that each of these concentric-type complexes contains high concentrations of the platinum metals in the ultramafic rocks. Contrasting with the platinum-bearing concentric-type complex is the alpine-type complex at Seldovia, Alaska, which is also included in tables 4 and 5.

Foster and Keith (1974) have mapped many small ultramafic bodies in the Eagle quadrangle of east-central Alaska and classify the ultramafic bodies into groups I, II, and III, according to the mineralogy. The mineralogy of groups I and II is characteristic of the alpine-type ultramafic body; that of group III is characteristic of the Alaskan or concentric-type ultramafic body (Jackson, 1971; Jackson and Thayer, 1972).

Platinum analyses of rock samples from these ultramafic bodies show that rocks of groups I and II contain little or no platinum, whereas rocks of group III contain as much as 0.300 ppm Pt and 0.200 ppm Pd (Foster and Keith, 1974).

Analyses of chromitite and some of the other ultramafic rocks from platinum-bearing complexes show an absence of platinum metals (table 5), although an analysis of a sample from only a few feet away from the barren sample shows a high platinum concentration. This phenomenon and the particulate occurrence of platinum in the rocks suggest that the formation of the platinum mineral is limited in time and space and can easily be missed by routine sampling.

TABLE 4.—*Concentrations (in parts per million) of platinum, palladium, rhodium, and iridium (maximum values) in mafic-ultramafic complexes of Alaska*

[Data on complexes 1–7 from Clark and Greenwood (1972). Data on complexes at Goodnews Bay and Seldovia from samples collected by A. L. Clark and analyzed by the laboratory of the U.S. Geological Survey]

Complex	Platinum	Palladium	Rhodium	Iridium
1. Duke Island	0.200	0.140	0.010	----
2. Union Bay	1.600	.200	.062	0.215
3. Blashke Islands	.020	.020	----	----
4. Eklutna	.100	.140	----	----
5. Salt Chuck	.160	2.900	----	----
6. Mount Fairweather	.170	.184	----	----
7. Klukwan	.100	.100	----	----
8. Goodnews Bay	1.400	.020	.030	.300
9. Seldovia	.0	.0	.0	.0

TABLE 5.—*Distribution of samples containing platinum, palladium, rhodium, and iridium from the mafic-ultramafic complexes of Alaska*

[Data on complexes 1–7 from Clark and Greenwood (1972). Data on complexes at Goodnews Bay and Seldovia from samples collected by A. L. Clark and analyzed by the laboratory of the U.S. Geological Survey]

Complex	Platinum	Palladium	Rhodium	Iridium	Total number of samples
1. Duke Island	10	16	6	0	22
2. Union Bay	21	22	6	2	50
3. Blashke Islands	8	10	0	0	10
4. Eklutna	12	12	0	0	16
5. Salt Chuck	6	6	0	0	6
6. Mount Fairweather	6	6	3	0	7
7. Klukwan	7	7	0	0	10
8. Goodnews Bay	9	4	6	2	19
9. Seldovia	0	0	0	0	51

OCCURRENCE OF PLATINUM IN CHROMITE

Figure 8 shows an inclusion of native platinum alloy in the chromite of sample AGK–144. Several similar inclusions were found in this sample. Electron-microprobe analysis of the platinum mineral shows that it is a platinum-iridium-iron alloy which contains approximately 20 percent platinum, 40 percent iridium, 25 percent iron, and lesser amounts of rhodium, nickel, and chromium.

The relatively low-iron, high-magnesium, and high-aluminum content of the chromite enclosing the platinum alloy (table 1) indicates that this chromite is primary compared with the chromite of the iron-rich peripheral zone.

CONCLUSIONS

The chromite in the Goodnews Bay complex contains more ferric and ferrous iron than does the chromite of stratiform or alpine complexes and significantly less aluminum than chromite from alpine complexes. Figure 6 shows that the variation of MgO and Cr_2O_3 in the chromite of Goodnews Bay is distinctively different from the chromite from alpine or stratiform complexes.

The olivine of Goodnews Bay chromitite contains more ferrous iron than that of alpine chromitites but about the same amount as in the olivine of stratiform chromitites. The iron-magnesium distribution coefficient between olivine and chromite in Goodnews Bay chromitites is different from the coefficient between

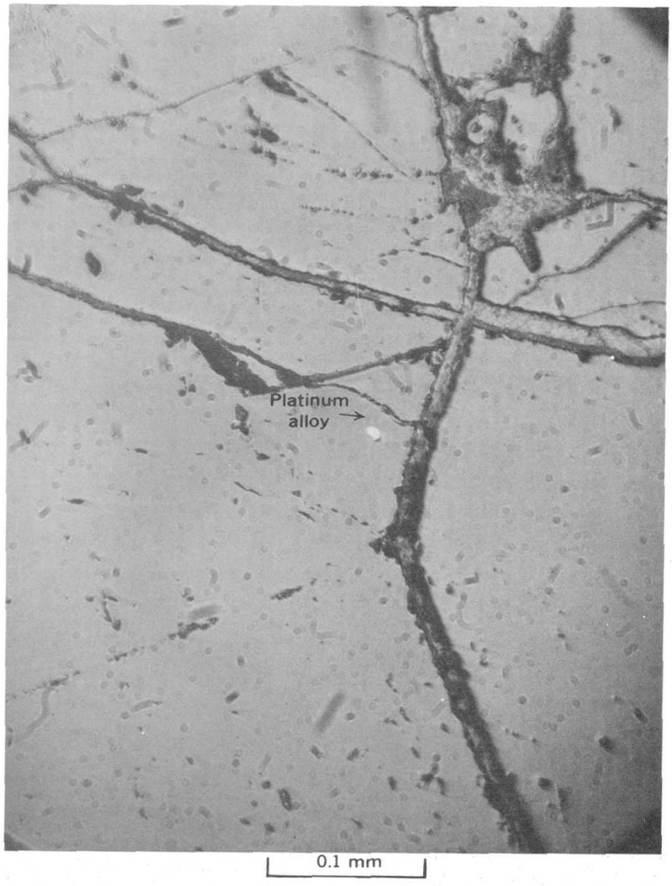

FIGURE 8.—Photomicrograph of platinum-alloy inclusion in chromite of sample AKG–144 of the Goodnews Bay complex.

these minerals in stratiform chromitites. The coefficient is similar to, although smaller than, that in chromitite from alpine complexes.

As seen in one specimen, platinum occurs in particulate form within the chromite of Goodnews Bay. The variation of the amount of platinum from zero to several parts per million in an ultramafic complex suggests that the platinum is not randomly distributed but occurs in local concentrations which are limited both stratigraphically and areally. Random sampling of the ultramafic section of different complexes may fail to find platinum although a complex is a host of the metal.

REFERENCES CITED

Clark, A. L., and Greenwood, W. R., 1972, Geochemistry and distribution of platinum-group metals in mafic to ultramafic complexes of southern and southeastern Alaska: U.S. Geol. Survey Prof. Paper 800–C, p. C157–C160.

Foster, H. L., and Keith, T. E. C., 1974, Ultramafic rocks of the Eagle quadrangle, east-central Alaska: U.S. Geol. Survey Jour. Research, v. 2, no. 6, p. 657–669.

Jackson, E. D., 1969, Chemical variation in coexisting chromite and olivine in chromite zones of the Stillwater complexes: Econ. Geology Mon. 4, p. 41–71.

Jackson, E. D., 1971, The origin of ultramafic rocks by cumulus processes: Fortschr. Mineralogie, v. 48, no. 1, p. 128–174.

Jackson, E. D., and Thayer, T. P., 1972, Some criteria for distinguishing between stratiform, concentric and alpine peridotite-gabbro complexes: Internat. Geol. Cong., 24th, Montreal, 1972, sec. 2, p. 289–296.

Mertie. J. B., Jr., 1919, Chromite deposits in Alaska: U.S. Geol. Survey Bull. 692, p. 265–267.

——— 1939, Platinum deposits of the Goodnews Bay district, Alaska: U.S. Geol. Survey Bull. 910–B, p. 115–145.

——— 1940, The Goodnews platinum deposits, Alaska: U.S. Geol. Survey Bull. 918, 97 p.

——— 1968, Platinum deposits of Alaska: U.S. Geol. Survey open-file report, 65 p.

——— 1969, Economic geology of the platinum metals: U.S. Geol. Survey Prof. Paper 630, 120 p.

Noble, J. A., and Taylor, H. P., Jr., 1960, Correlation of the ultramafic complexes of southeastern Alaska with those of other parts of North America and the world: Internat. Geol. Cong., 21st, Copenhagen, 1960, Rept., pt. 13, p. 188–197.

Ruckmick, J. C., and Noble, J. A., 1959, Origin of the ultramafic complex at Union Bay, southeastern Alaska: Geol. Soc. America Bull., v. 70, no. 8, p. 981–1017.

Sweatman, T. R., and Long, J. V. P., 1969, Quantitative electron-probe microanalysis of rock-forming minerals: Jour. Petrology, v. 10, p. 332–379.

Taylor, H. P., Jr., 1967, The zoned ultramafic complexes of southeastern Alaska, *in* Wyllie, P. J., editor, Ultramafic and related rocks: New York, John Wiley and Sons, p. 97–121.

Jour. Research U.S. Geol. Survey
Vol. 4, No. 6, Nov.-Dec. 1976, p. 727–732

USE OF THERMAL-INFRARED IMAGERY IN GROUND-WATER INVESTIGATIONS, NORTHWESTERN MONTANA

By A. J. BOETTCHER; R. M. HARALICK,[1] C. A. PAUL,[1] and NORMAN SMOTHERS,[1] Helena, Mont.; Lawrence, Kans.

Work done in cooperation with the Montana Bureau of Mines and Geology and the Bonneville Power Administration

Abstract.—Thermal-infrared imagery was used to locate ground-water inflow along a 50-mile (80-kilometre) reach of the Kootenai River and Lake Koocanusa and a 55-mi (88-km) reach of the Clark Fork of the Columbia River in northwestern Montana and northeastern Idaho. The imagery confirmed that measured streamflow gains below Noxon Rapids Dam, ranging from 1,000 to 2,500 cubic feet per second (28 to 71 cubic metres per second), resulted from inflow of ground water, which was about 2.5° Celsius warmer than surface water. The thermal scanner (8.5–11 micrometres) used in May 1972 and March 1973 was mounted in a twin-engined aircraft. On the March 1973 flight, the data were recorded in an analog format on magnetic tape in flight, later were converted to digital format, and then were computer processed using an assignment of patterns to indicate differences in water temperature. Thus, subtle temperature differences are much easier to identify than they are on conventional film-negative displays. The output data from the image-processing program can be converted to temperature maps having an isotherm spacing of 0.5°C.

Ground water flowing into stream channels affects the quantity and quality of many streams in Montana. Identification of the source of the inflow is useful for appraisal and management of water resources.

Infrared photography cannot measure water-surface temperature variations directly. Ground-water inflow may stimulate growth of certain plants. Thus, vigor of growth observed by infrared photography may indicate ground-water inflow. However, this method has no quantitative significance. In contrast, thermal-infrared sensors record an emitted electromagnetic radiation which, with help of computer techniques, can be quantified into spatial surface-temperature information if the following conditions are met: (1) differences in temperature exist between the surface water and ground water, (2) the quantity of surface water is not too large relative to the quantity of ground-water inflow, and (3) the density of the surface water is greater than the ground water, allowing detection of the ground water.

Thermal sensors enable the hydrologist to detect dispersion and circulation patterns and ground-water discharge in large bodies of water. This information is useful in such applications as locating areas having good fish-rearing characteristics and areas of potential water-quality changes, or in differentiating industrial effluent from natural patterns of a stream (Whipple, 1972; Pluhowski, 1972).

Extrapolation of temperature data over large areas from the film output obtained from a thermal scanner is difficult because the human eye cannot compare densities over a large area. Therefore, when thermal imagery has been obtained from a long reach of a river or lake, mechanical density-measuring devices are used to obtain standardization of the gray levels. A densitometer can be used for spot density measurements on the film output to assign temperatures based on ground-truth data. This method is time consuming, however, and cannot be done on the entire film output.

Another method of determining density is by use of a density slicer, which views the negative and portrays the varying densities by colors or binary patterns. Then each pattern or color can be identified by temperature values based on ground-truth data. Though useful, this method also does not work well with a large amount of imagery because of changes in film or developer.

The purpose of this investigation was threefold: (1) to determine if ground-water inflow into lakes and streams in northwestern Montana could be detected by the use of thermal-infrared imagery, (2) to determine the most useful data format on which to present the data, and (3) to test the capability of the digital

[1] University of Kansas.

computer for storage, retrieval, and processing of the data collected.

THE THERMAL-INFRARED SCANNER

An aircraft-mounted thermal-infrared scanner senses the distribution of energy radiated by a surface. The detected energy distribution is a function of the surface temperature and emmissivity and is modified by the intervening atmosphere. The thermal emmissivity of water is nearly uniform, which allows small changes in water-surface temperature to be measured. Solar-energy reflections from clouds and shadows complicate thermal scanning during daylight hours. Night and predawn flights are best for thermal scanning because the effects of solar-energy changes then are minimized and the air is calmer (Carr and Gross, 1972).

Temperature data were obtained by using a U.S. Forest Service thermal-infrared scanner mounted in a twin-engined aircraft capable of flying at 215 miles per hour (346 kilometres per hour). The scanner has two black-body calibration sources, which give it an accuracy of 0.2°C (Celsius). The total field of view is 120° and the imagery is processed in flight in near real time by a two-step rapid processor (Wilson and others, 1971). The flights discussed in this paper were flown between 2,000 and 2,500 ft (feet) or 610 and 762 m (metres) above the water surface during predawn hours. The scanner senses the 3- to 4.1- and 8.5- to 11-μm (micrometres) ranges of the electromagnetic spectrum. Only the 8.5- to 11-μm range was used to detect water temperatures in this investigation. The 3- to 4.1-μm range is used for detecting higher temperatures such as forest fires. The visible, infrared photography, and thermal-infrared imagery ranges of the electromagnetic spectrum are shown in figure 1.

THERMAL SCANNER IMAGERY EXPERIMENTS

On May 17, 1972, a flight was made along the Kootenai River and Lake Koocanusa from the United States–Canadian boundary to the confluence of the Fisher and Kootenai Rivers (fig. 2). The purpose of this flight was to determine (1) if ground-water inflow could be detected by using an airborne thermal scanner, (2) if ground-water plumes could be distinguished from the normal plumes in lakes, and (3) what range of temperature calibration would be necessary to obtain maximum contrast in the film output when flying over water.

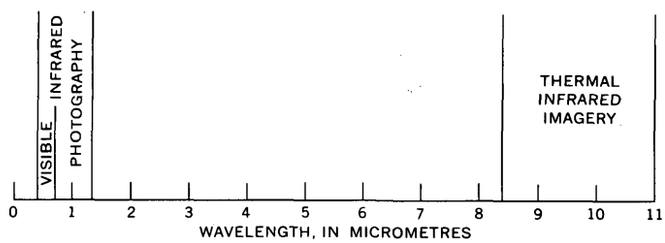

FIGURE 1.—Electromagnetic spectrum.

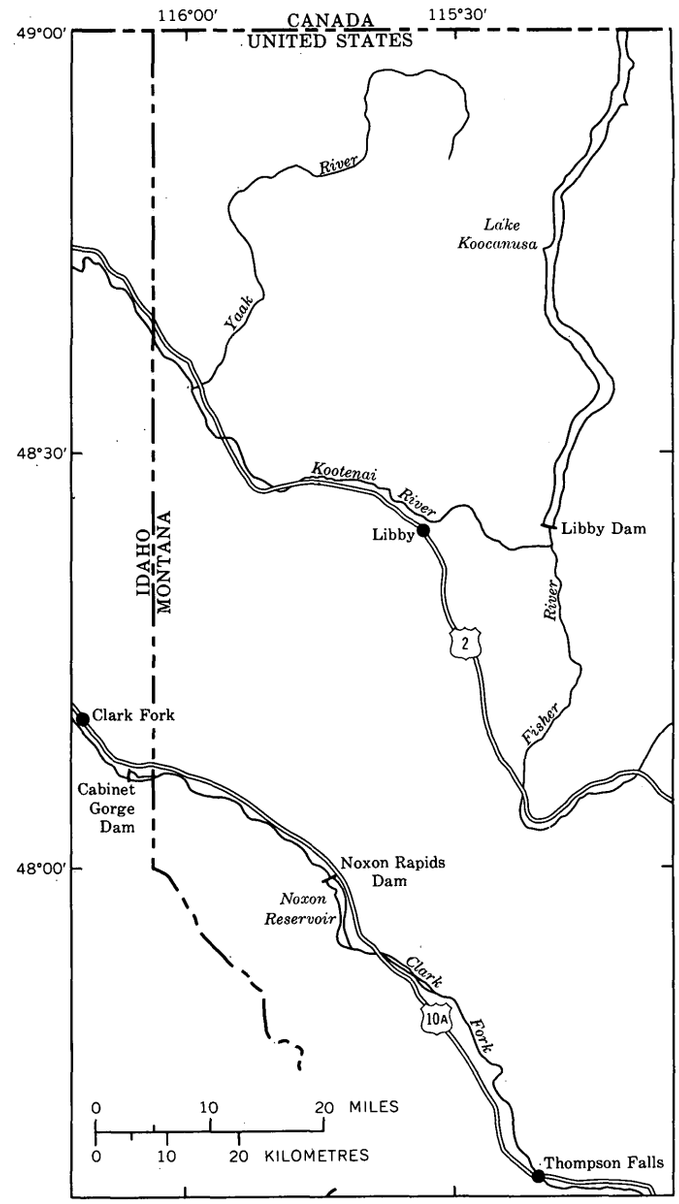

FIGURE 2.—Index map of the report area.

The flight was made when snowmelt was flowing in the tributaries of Lake Koocanusa and the Kootenai River with resulting temperatures of about 5° to 7°C. A 5°C temperature differential is apparent on figure 3*A*, where the measured temperature of the water in the forebay of Libby Dam was 12°C and the temperature of the water in the Fisher River was 7°C. Figure

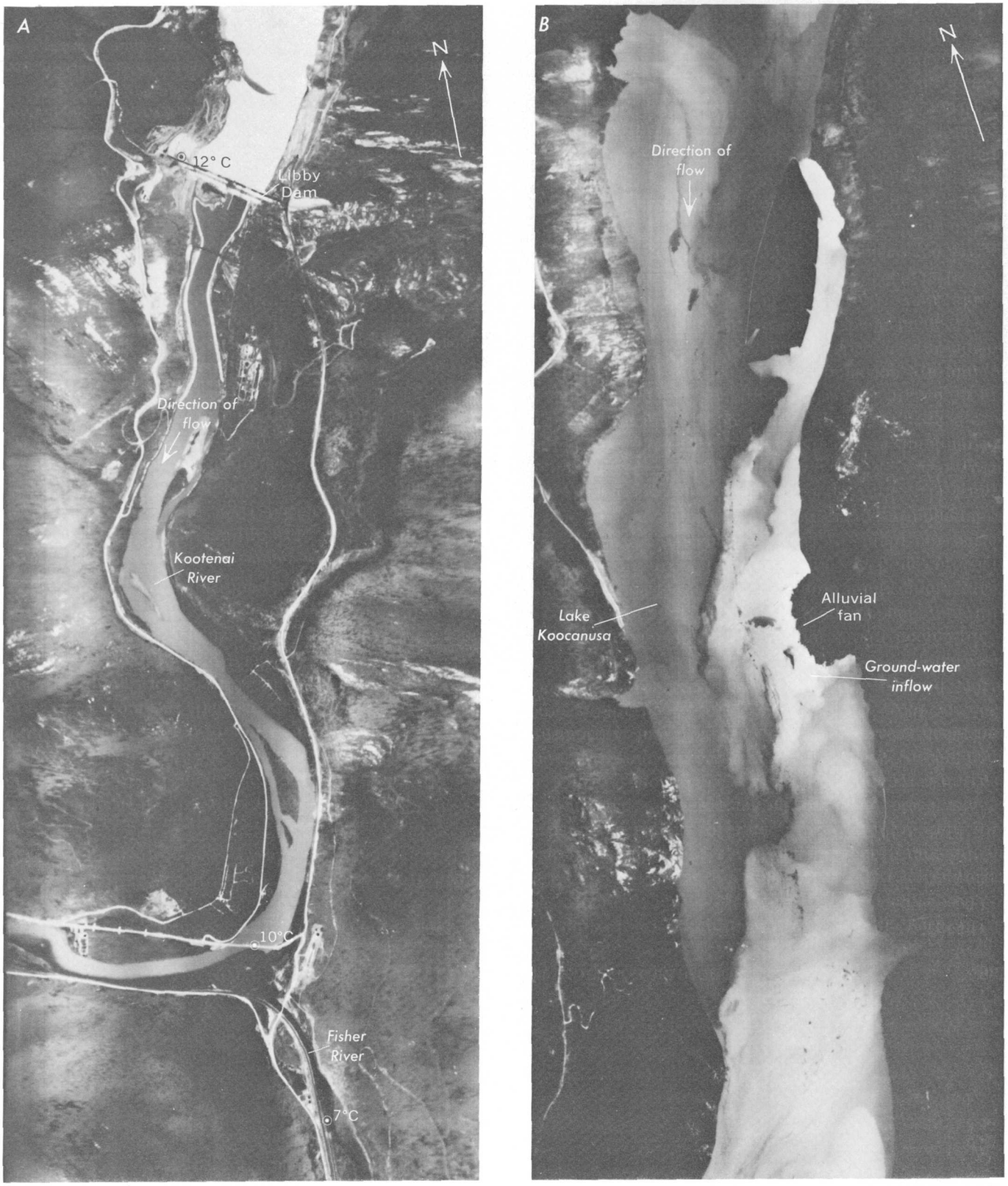

FIGURE 3.—Thermal-infrared imagery around Lake Koocanusa. *A*. Libby Dam and the confluence of the Fisher and the Kootenai Rivers. *B*. Ground-water inflow into Lake Koocanusa. Imagery by U.S. Forest Service

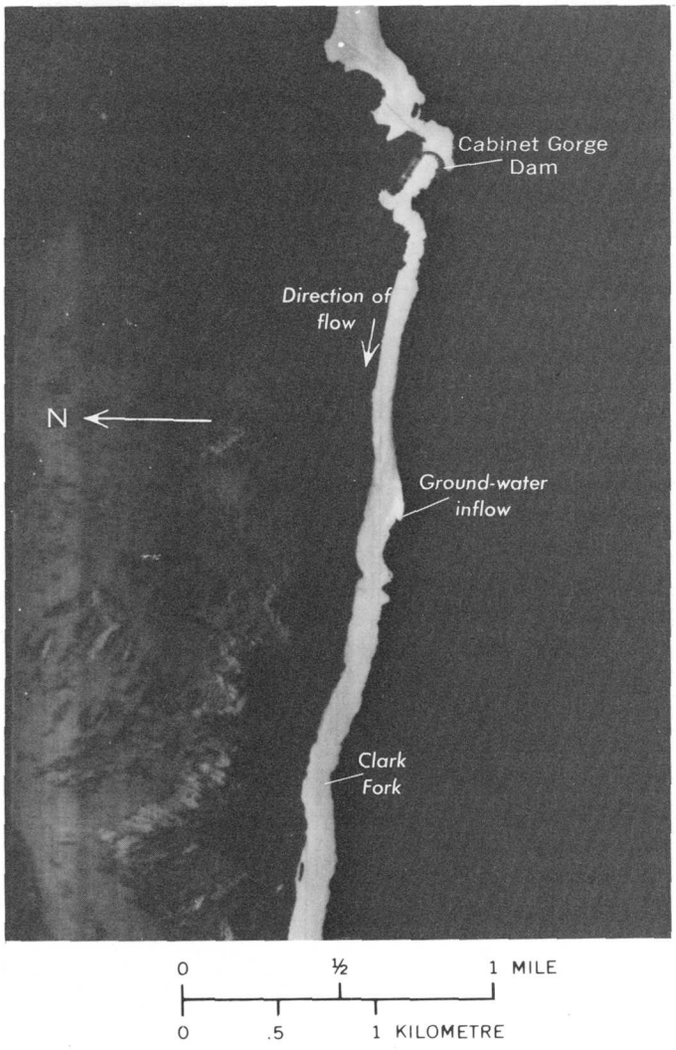

FIGURE 4.—Thermal-infrared imagery below Cabinet Gorge Dam. Imagery by U.S. Forest Service.

3*B* shows a plume of warmer ground water flowing into Lake Koocanusa from an alluvial fan. The temperature difference from black to white on the images is 7°C (from 5° to 12°C), as calibrated on the scanner.

On March 29, 1973 a flight was made over the Clark Fork of the Columbia River from Thompson Falls, Mont., to Clark Fork, Idaho (see fig. 2). The purpose of this flight was to determine if areas of ground-water inflow could be detected by thermal-infrared scanning techniques and if the data could be processed by computer to enhance the output. During the flight, scanner data were transferred to magnetic tape by a recorder attached to the scanner.

In this reach, the Clark Fork has eroded a deep narrow valley into rocks of the Belt Supergroup of Precambrian age. These rocks consist primarily of argillites and quartzites near Noxon Rapids and Cabinet Gorge Dams. The valley has been partly filled by semiconsolidated sand, gravel, and clay that form the Quaternary alluvium. Water flows from Noxon and Cabinet Gorge Reservoirs into the alluvium, then downvalley through the alluvium, and reenters the Clark Fork a short distance below the dams. From 1,000 to 2,500 ft^3/s (cubic feet per second) or 28 to 71 m^3/s (cubic metres per second) of water inflow from the alluvium has been measured below Noxon Rapids Dam.

The warmer ground-water inflow below Cabinet Gorge Dam can be seen along the left bank of the Clark Fork (fig. 4). Imagery of this area was used to test computer techniques because of a large temperature difference in a small area.

The five channels of the magnetic tape recorder recorded the various voltages of the scanner. The tape was later converted to a digital format for computer processing. Ground-truth and map-scaling factors were entered into the program to serve as a check on the computer.

After analog-to-digital conversion, the thermal-infrared imagery was a large matrix of numbers. This matrix is called a digital image. Each number represents the average temperature of a 5 by 5 ft (1.5 by 1.5 m) ground area. To draw lines of equal temperature, the first computer process consisted of a spatial averaging or defocusing of the data. The averaging, sometimes called convoluting, is done by generating a new digital image where the temperature of each resolution cell is computed to be the equally weighted average of the nearby temperatures of the resolution cells of a 8-node by 8-node window centered around it.

Because a 0.5°C-isotherm interval was needed, the second computer process consisted of an equal-interval quantizing of the smoothed digital display so that the smallest distinguishable difference between any two temperatures became 0.5°C. The final operation consisted of setting of blanks any resolution cell satisfying the condition that (1) its nearest vertical and horizontal neighbors have the same temperature it does or (2) its temperature is smaller than or equal to the temperatures of its nearest vertical and horizontal neighbors and one of these neighbors has a different temperature than it does.

The temperature of a mixture of ground-water inflow and river water was 8.5°C, whereas the river water was predominantly 6.0°C (fig. 5). Figure 5*A* is a computer version of the temperature changes caused by ground-water inflow. The isotherm interval is 0.5°C. The 5.5°C temperature is denoted by 0's and the 8.5°C temperature by 6's (fig. 5*A*). These data could be drawn on a plotter although figure 5*B* was drawn manually. The computer output described the sizes and locations of the anomalous plumes more distinctly

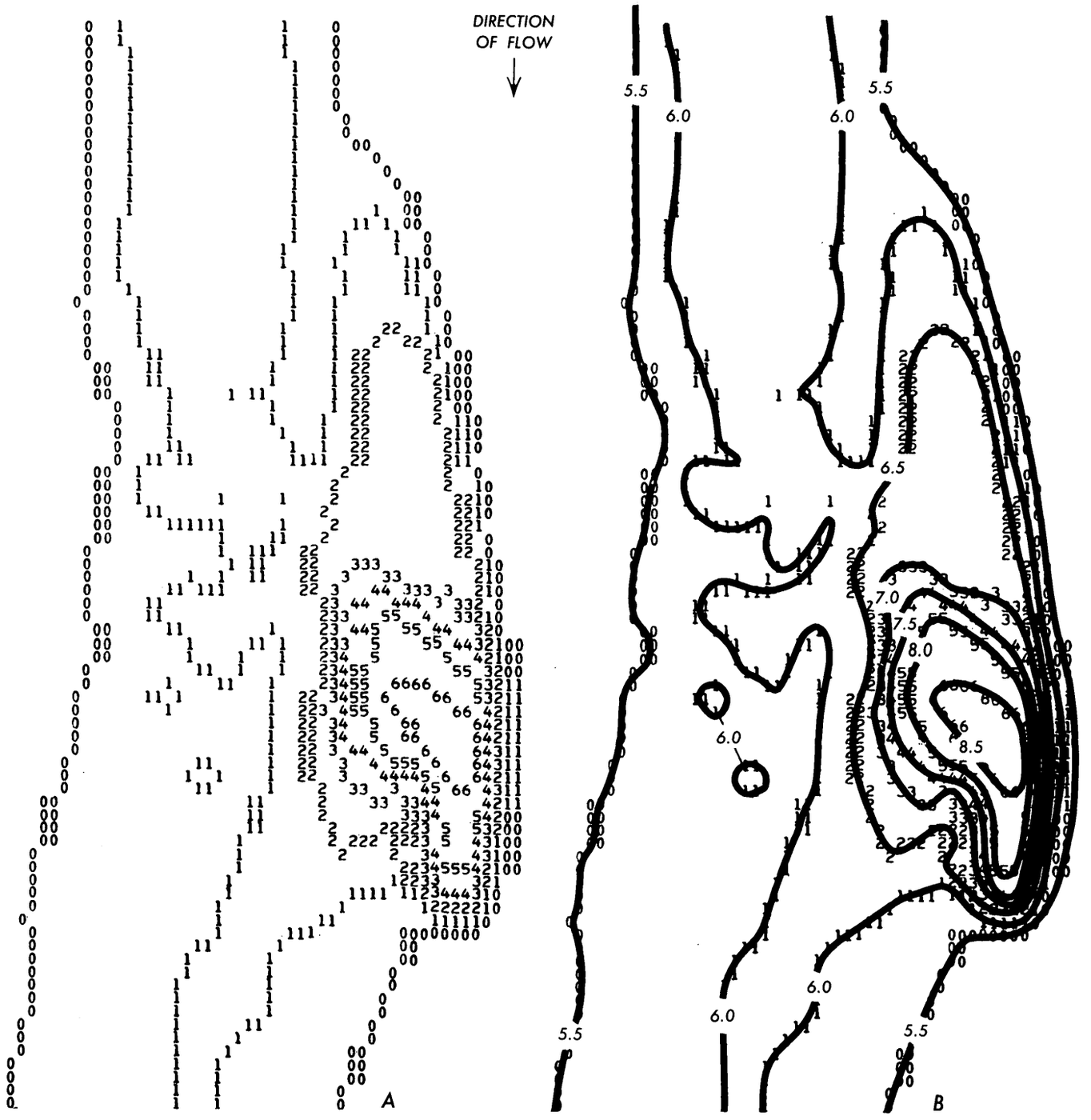

FIGURE 5.—Temperature data computerized. *A*. Computerized data showing numbers representing 0.5°C interval. *B*. Same as *A* except the isotherms have been manually drawn.

than the film output and can be reduced or enlarged much easier and more efficiently than the film output.

CONCLUSIONS

Ground-water inflow to streams and lakes was observed from an aircraft-mounted thermal-infrared scanner. Detection of small amounts of ground-water inflow to a sizeable river would be difficult because the large amount of river water would dilute the ground water rapidly. Computerization of the temperature data was found to be the most efficient way to manipulate the data because computer techniques are the most accurate. Large amounts of error-free temperature data can be stored and retrieved by a

computer. Additionally, items such as map-scaling factors and ground-truth data can be entered into the computer system to insure uniform temperature calibration. Two ground-truth data points were used in figure 5 and four points were used for a 20-mi (32-km) reach. The computer output can be made to overlay most map scales; therefore, the combination of obtaining data by the thermal scanner and processing it by the computer has furnished the hydrologist with a useful tool.

REFERENCES CITED

Carr, P. A., and Gross, H., 1972, Investigation of infrared anomalies in the Lac des Deux Montagnes area, Quebec: Canada Dept. Environment, Inland Waters Directorate, Water Resources Branch, Sci. Ser. 19, 16 p.

Pluhowski, E. J., 1972, Hydrologic interpretations based on infrared imagery of Long Island, New York: U.S. Geol. Survey Water-Supply Paper 2009–B, 20 p.

Whipple, J. M., 1972, Remote sensing of New York lakes: U.S. Geol. Survey Prof. Paper 800–C, p. 243–247.

Wilson, R. A., Hirsch, S. N., Madden, F. H., and Losensky, B. J., 1971, Airborne infrared forest fire detection system—final report: U.S. Dept. of Agriculture, Forest Service Research Paper INT–93, 99 p.

Jour. Research U.S. Geol. Survey
Vol. 4, No. 6, Nov.-Dec. 1976, p. 733–736

RELATIONS AMONG SURFICIAL MATERIALS, LIGHT INTENSITY, AND SYCAMORE-SEED GERMINATION ALONG THE POTOMAC RIVER NEAR WASHINGTON, D.C.

By ROBERT S. SIGAFOOS, Reston, Va.

Abstract.—Seed of sycamore, a common tree on river flood plains, germinate in mineral soil exposed to high light intensities. Germination rates are low on surfaces covered with leaf litter, and seedlings die when shaded by closely spaced herbaceous plants. All germination rates were higher when seed were kept moist. Surficial materials and light values in this study are similar to those on flood plains. Results were derived from counting seedlings after planting 1,000 seeds in each of several flats filled with different kinds of flood-plain and upland soils.

Species of trees that grow on flood plains are different from those that grow on uplands. In a larger study along 24 kilometres of the Potomac River, in which forest vegetation was mapped and species were recorded at many sites, sycamore was present at 61.2 percent of the flood-plain sites, whereas it was present only at 1.7 percent of the upland sites.

Other species have distribution along the Potomac River near Washington, D.C., (fig. 1) similar to that of sycamore. The percentage of sites where three other species are found are listed in table 1.

The objective of the study is to determine what environmental variations affect germination of sycamore seed and early seedling survival. This study showed that germination rates of sycamore are high on freshly exposed alluvium and low or nil in forest litter and under herbaceous plants.

The seed grow naturally in a ball, called a multiple fruit, and ripen in early autumn, but the balls generally remain on the tree until late winter or early spring. The ball either breaks up on the tree, releasing the seed, which falls gently to the ground, or the entire ball falls, according to the Division of Timber Management Research (U.S. Department of Agriculture, 1965, p. 491). They also reported that the seed are small, about 2×7 millimetres, and average about 90,000 per kilogram. A tuft of spreading hairs, about 3 mm long, grows from the base of the seed (U.S. Department

TABLE 1.—*The percentage of sites where four flood-plain trees are found along 24 kilometres of the Potomac River flood plain near Washington, D.C.*

	Upland sites	Flood-plain sites
Sycamore	1.7	61.2
River birch (*Betula nigra* L.)	0	35.4
Box elder (*Acer negundo* L.)	2.8	16.1
Silver maple (*Acer saccharinum* L.)	8.0	42.4

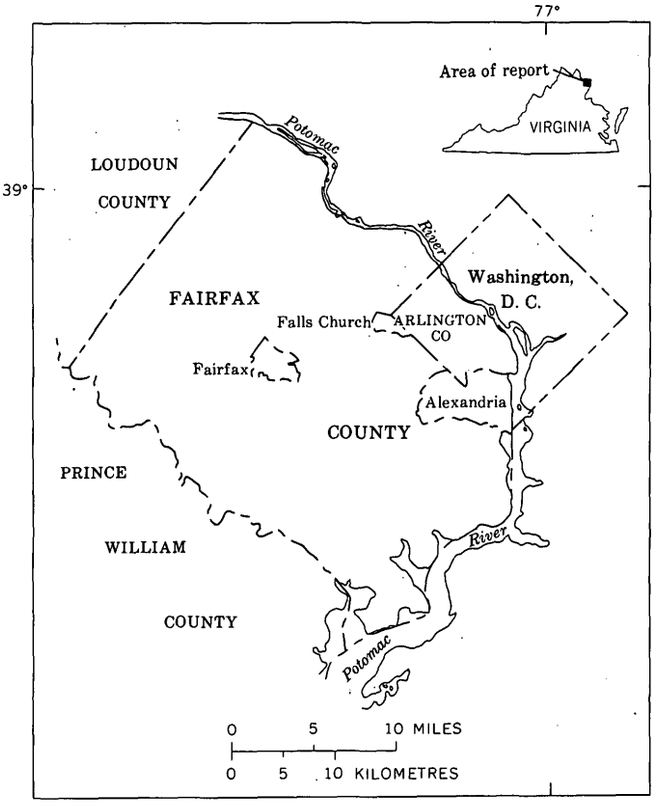

FIGURE 1.—Map of part of Potomac River near Washington, D.C. and Fairfax County, Va. Base from Maryland and Delaware and Virginia 1:500,000 maps.

Agriculture, 1974, p. 643). The hairs act as a parachute, and the seed are blown widely by wind. Seed that fall on water float and may come to rest on river bars.

Several wooden seed flats, approximately 90×60×15 centimetres were filled with different soil materials. The materials consisted of (1) sandy alluvium deposited by high water only 3 months before collecting; (2) silty-clay alluvium, also deposited by high water only 3 months before collecting; (3) a rectangular block of silty-clay alluvium containing rhizomes of perennial herbaceous plants; this alluvium was covered with leaf litter (called flood-plain litter in table 1) accumulated over several years and dug from a surface flooded less frequently than once in 2 years on the average (it had not been flooded for 10½ years); and (4) another block of litter, humus, and clay soil from an upland oak forest floor, called oak litter.

In each flat, 1,000 sycamore seeds were planted by broadcasting them evenly on the surface. They were not buried by raking, so that the seed dissemination simulated wild conditions.

In addition to the different materials, the flats received different treatment before and after seeding. The recently deposited sandy alluvium and silty alluvium were loose when collected and were placed in the flats without retaining soil structure. The infrequently flooded alluvium and the oak-forest, silty-clay soil were placed in flats as blocks. Blocks were cut to the size of the flats and carefully placed in flats to retain structure, herbaceous plants, and leaf litter. The first of a series of four flats was placed in mid-March in a greenhouse in Fairfax County, Va., approximately 16 km from the Potomac River. These were watered with a fine spray to keep them moist during the course of the study, and seedlings were counted every 1 to 3 days. These flats were moved outside to my backyard nearby in mid-May, and watering was continued. An additional series was prepared and planted in early May, consisting of two series similar to that placed in the greenhouse. One was watered; the other was not, and seeds and seedlings were dependent upon rain and dew for moisture. In addition, a flat of the oak litter and one of the flood-plain litter were mixed with a shovel to expose underlying soil. Only the humus and leaf litter were mixed with the upper layers of soil, and the herbaceous perennial plants present in the alluvium seed flat were not disturbed. These two flats were watered between rains to keep them moist.

Results of the counts are given in table 2. Data from the watered flats started outside are shown graphically in figure 2. All seedlings in the oak-litter flats were growing where soil was exposed next to the wooden sides; none was growing in the centers, which were covered with dead oak leaves.

TABLE 2.—*The maximum number of seedlings counted and the number growing at the end of the study*

	Greenhouse		Outside			
			Watered		Not watered	
	Maximum	End	Maximum	End	Maximum	End
Sandy alluvium	15	10	259	186	221	213
Silty-clay alluvium	71	31	254	178	165	116
Flood-plain litter	2	0	1	0	0	0
Disturbed flood-plain litter	--	--	6	2	---	---
Oak litter	5	4	67	66	40	34
Disturbed oak litter	--	--	277	230	---	---

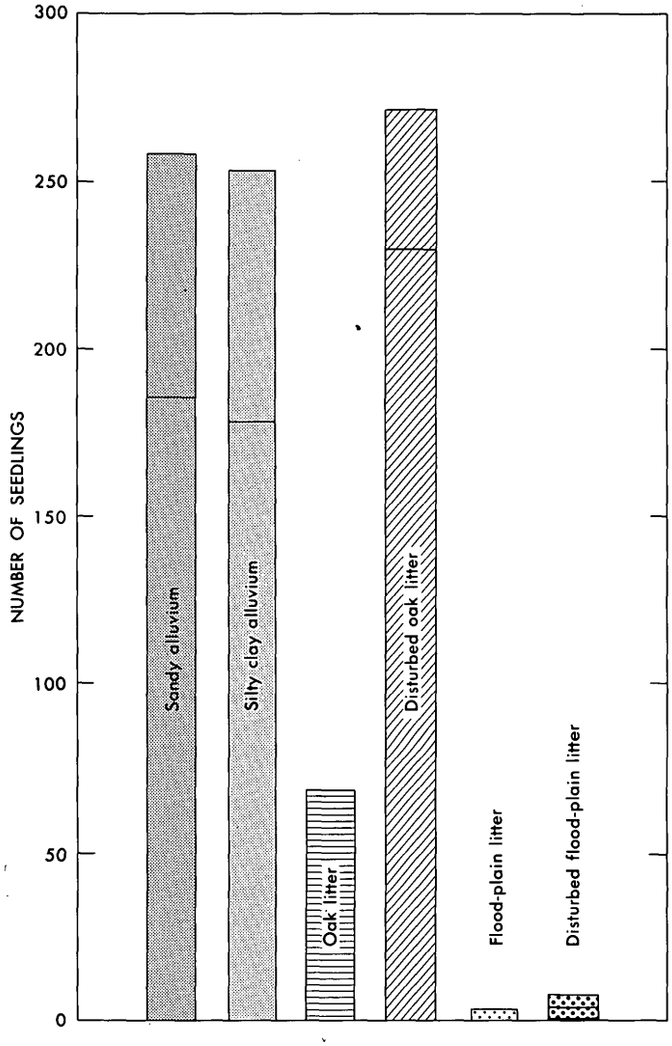

FIGURE 2.—Number of sycamore seedlings per 1,000 planted seeds counted in flats containing different kinds of soil placed outside and watered. Total height represents maximum number counted; line inside bar represents number when counts were discontinued.

The maximum number of seedlings listed in the table is approximately the same as germinative energy, and the number at the end of the study is nearly the same as germinative capacity (U.S. Department Agriculture, 1974, p. 865). Germinative energy is that number of seed that have germinated at the time of the peak germination rate. Capacity is the number germinated when germination has ceased. In U.S. Forest Service germination tests (U.S. Department Agriculture, 1974, p. 643), percentages for these values for sycamore seed are 34 and 35 percent, but are based on sound seed only. In my study, no attempt was made to select viable seed, so some probably were not sound, thus accounting for lower percentage of germination.

Comparison of the number of seedlings in both types of alluvium and oak litter, disturbed and undisturbed, shows that sycamore seed must come into contact with soil before they germinate. Hosner and Minckler (1960, p. 73–74) found that sycamore seed do not germinate in litter thicker than 10–15 mm. Leaf litter, in this study and in the woods, catches newly fallen seed because of the tuft of hairs and light weight. The seed then dries within hours after rain or watering. Seed, resting on leaf litter, would not germinate or tiny seedlings would die within a day because of a dry seed bed. Surface layers of litter and humus also would dry, and if seed did germinate, seedlings would not survive long enough for seedling roots to reach moist humus or soil.

When soil was collected for the outside study on April 2, leaves of waterleaf (*Hydrophyllum virginianum* L.), yellow addersmouth (*Erythronium* cf. *americanum* Ker.), mayapple (*Podophyllum peltatum* L.), and spring beauty (*Claytonia virginica* L.) were partly grown. Waterleaf and mayapple leaves formed a complete cover 150–300 mm high over the infrequently flooded alluvial soil flat by May 1.

Either none or an insignificant number of sycamore seedlings survived in the flood-plain litter flats. The texture of the soil in these flats was similar to that in silty-clay alluvium flats, where germination was high. Failure in germination seems to be the result of the presence of litter and the growth of herbaceous plants. Mixing of litter with mineral soil exposed the mineral soil in both the disturbed oak-litter and the disturbed flood-plain litter flats. As many seed germinated in the disturbed oak litter flat as in the bare silty alluvium and silty-clay alluvium flats.

Low light intensity under herbaceous plants and possible allelopathic agents produced by them or a combination of the two seem to inhibit sycamore seed germination. Allelopathic agents are substances secreted by roots of plants that inhibit or prevent germination and growth of the same or other species. The inhibition of growth of certain bacteria by penicillin produced by the fungus *Penicillium* is a well known example of allelopathy, as is inhibition of tomatoes by an alkaloid secreted by black walnut roots. Krebs (1972, p. 41–47) briefly reviewed the historical and recent allelopathic studies. McDermott (1953, p. 204) found that sycamore seed did germinate in the dark, but the percentage of germination was only 3.1 compared with 17.5 in the light. Intensity was lower in McDermott's lighted experiment than under the shade of herbaceous plants reported here. Light intensity, in foot candles, was measured with a photographic cadmium sulfide exposure meter on a clear day over the flats and in the open (table 3). Light measurements were made under the herbaceous plants in the flood-plain litter flats as close to the seedlings as possible.

Germination and survival of seedlings were high in seed flats that contained exposed mineral soil and received ample sunlight. Some attrition occurred in these seed flats, even if watered, and it was about equal to the attrition in flats that were not kept moist. Failure of seed germination in the flood-plain-litter flats apparently was the result of growth of herbaceous plants. The waterleaf and mayapple leaves had formed a dense cover just before heavy germination started. On May 12 only 9 seed had germinated in all 10 flats. On May 19 waterleaf and mayapple leaves were mature. No seedlings were growing under them in the undisturbed flood-plain-litter flat and only six in the disturbed flat.

TABLE 3.—*Light intensities in the open and over seedlings in flats*
[Values given in approximate foot candles (1 ft-c=10.76 lm/m²)]

Time (e.s.t.)	Sky condition	Light intensity						
			Over seedlings planted in indicated soil					
		In the open	Sandy alluvium	Silty-clay alluvium	Oak litter	Flood-plain litter	Disturbed oak litter	Disturbed flood-plain litter
10:00 a.m.	Clear	8,000	500	400	260	130	400	130–
Noon	High, thin cirrus clouds.	12,000	*500–6,000	*500–6,000	*500–6,000	175	500–6,000	260 400
5:00 p.m.	Clear	1,000	400	260	260	130	260	130

* Flats were in partial shade and sun flecks appeared on the surface in places.

In the other eight flats, 699 seedlings were growing.

These experimental data suggest that sycamore seed germination requires at least two concurrent environmental conditions and possibly a third. These are bare soil, high light intensity, and absence of allelopathic agents. Field observations suggest also that the seed bed must remain moist. These conditions are met on flood plains, where sycamore trees are most abundant and reach greatest size (U.S. Department Agriculture, 1965, p. 490). Flows that overtop flood plains erode litter, humus, and soil in places and deposit them elsewhere.

Most flood plains underlain by silty-clay and sandy alluvium flooded more frequently than once every 2 years along the Potomac River and tributaries near Washington, D.C., are kept nearly free of perennial herbaceous plants by frequent floods. Waterleaf, yellow addersmouth, spring beauty, bluebells (*Mertensia virginica* (L.) Pers.) violets (*Viola* sp.), mayapple, and many other spring flowering species are common on bottom lands at and above the 2-year flood level, but are rare below. The frequently flooded surfaces, then, that are underlain by recently eroded or deposited fine alluvium are not shaded by herbaceous plants, thus are adequate seed beds for the germination of seed. The less frequent floods do not destroy herbaceous perennial plants above the 2-year flood level. The flood which crested at 359,000 cubic feet per second (10,167 cubic metres per second) on June 24, 1972, and which occurs on the average of once every 30 years, did not remove herbaceous plants on higher bottom-land surfaces. A lesser flood (4,245 m^3/s) on March 21, 1975, also did not destroy plants above the 2-year level, although the recurrence interval of this floood is about 3 years.

Although 1,000 seeds planted in the 0.54-m^2 flats may seem high, natural sycamore seed-fall in some years is higher. Over a period of 4½ years, seed were caught in 1-m^2 traps. Traps consisted of a frame about 100 mm deep, covered on the bottom with window screen and on the top by 10 mm mesh hardware cloth. Seed fell through the coarse mesh and were trapped in the frame. Contents were removed, brought to the office, and seed were identified and counted. Numbers of sycamore seed in traps placed near sycamore trees ranged from a low of 3 to 129 per year to a high of 183 to 2,351 per year. Heavy seed crops occur every 2 to 3 years.

Seed were also caught in traps placed in upland forest at distances ranging from about 180 to 300 m from large sycamore trees. In these, the annual catch of sycamore seed ranged from a low of 1 to 8 to a maximum of 47 to 763. No seedlings or small sycamore trees have been found near these sites. Catches in the uplands are markedly lower than on flood plains; over a period as long as 100 years, however, sufficient numbers of sycamore seed would be present for a few to germinate and to grow if environmental conditions were favorable.

Observations were made to learn if experimental results reported here are duplicated in the field. These observations showed that river birch, boxelder, silver maple and sycamore seed (table 1) germinate only in soil or thin layers of comminuted organic debris that remains moist. Seed counted in many square-metre plots either did not germinate or were destroyed by floods. Seed that did not germinate and were not destroyed by floods were in plots whose surface layers appeared on occasion to be dry. Many seedlings were found outside the sample plots and were counted; all were destroyed by floods. No flood-plain trees have been observed to grow from seed to even small saplings.

REFERENCES CITED

Hosner, J. F., and Minckler, L. S., 1960, Hardwood reproduction in the river bottoms of southern Illinois: Forest Sci., v. 6, p. 67–77.

Krebs, C. J., 1972, Ecology: New York, Harper and Row, 694 p.

McDermott, R. E., 1953, Light as a factor in the germination of some bottomland hardwood seeds: Jour. Forestry, v. 51, p. 203–204.

U.S. Department Agriculture, 1965, Silvics of forest trees of the United States: U.S. Agriculture Handb. 271, 762 p.

——— 1974, Seeds of woody plants of the United States: U.S. Dept. Agriculture Handb. 450, 883 p.

Jour. Research U.S. Geol. Survey
Vol. 4, No. 6, Nov.-Dec. 1976, p. 737–751

CLASSIFICATION OF ORGANIC SOLUTES IN WATER BY USING MACRORETICULAR RESINS

By J. A. LEENHEER, and E. W. D. HUFFMAN, Jr.,[1]
Denver, Colo., Wheatridge, Colo.

Abstract.—A series of macroreticular resin adsorbents was evaluated for ability to extract and fractionate organic solutes found in natural waters. Studies with organic solute standards and natural water samples lead to the development of dissolved organic carbon (DOC) fractionation analysis whereby the DOC is concentrated and fractionated by macroreticular resins into acid, base, and neutral hydrophobic organic solute fractions and into acid, base, and neutral hydrophilic organic solute fractions. The hydrophobic solutes were sorbed and fractionated on nonionic, nonpolar macroreticular resins, and the hydrophilic solutes were sorbed and fractionated by macroreticular ion-exchange resins. Organic-inorganic complexes as well as organic solutes were isolated by resin sorption. DOC fractionation analysis was developed to serve as a compound classification that fills the gap in organic solute characterization between the organic solute concentration (DOC) and specific compound identification.

With the recent emphasis on development of the Nation's fossil fuel resources to meet the growing need for energy, individuals involved with water-quality studies have recognized the need for better characterization of organic solutes. Changes in water quality caused by organic residuals must be determined. Many schemes have been devised, advocated, and tested, but no perfect system has been developed, possibly for the following reasons: (1) Specific compound identification and measurement is a difficult analytical problem due to the numerous organic compounds possible, (2) organic solute concentrations are usually smaller than inorganic solute concentrations by several orders of magnitude, causing interference, (3) many organic solutes are unstable or volatile, making isolation difficult and leading to sampling and preservation problems, (4) available analytical instrumentation and techniques limit isolation schemes, and (5) most important, there has been no completely satisfactory comprehensive analytical scheme to isolate, identify, and measure all organic solutes in the aquatic environment. The purpose of this report is to present a simplified scheme of organic solute characterization which, although not ideal, fulfills the needs of many water-quality studies while minimizing some of the aforementioned problems.

[1] Huffman Laboratories, Inc.

LIMITATIONS OF CURRENT SCHEMES OF ORGANIC SOLUTE CHARACTERIZATIONS

The present state of organic solute characterization is described in a report by Christman and Hrutfiord (1973). They state that the development of organic water-quality standards has "occurred on a piece-meal basis in response to current crises. At one time or another, scientific teams have deliberated the significance of, and have established water quality standards for, specific compounds such as nitrilotriacetate (NTA) and phthalic acid; certain classes of compounds such as pesticides, phenols, polychlorinated biphenyls, phthalate esters, oil, and grease; and poorly defined groups of compounds known primarily by their properties or manner of isolation such as foaming agents, color, taste, and odor, as well as carbon adsorbable organics (O–CA)."

Characterization schemes based on these aforementioned standards are limiting for these reasons: (1) They are not capable of separating or recovering all organic solutes; they apply only to specific classes, and, therefore, many organic solutes are not measured, (2) a materials balance based on organic carbon is seldom used; thus, the relationship between specific compounds and compound classes to the total organic solute concentration is unknown, (3) characteristics such as color, taste, and odor and oils and grease are nonspecific, and (4) most analytical schemes are based on methodology that incorporates liquid-liquid extraction or carbon adsorption to extract and concentrate organic solutes prior to analysis. These analytical techniques, like most others, have their limitations and drawbacks.

Limitations of liquid-liquid extraction

Liquid-liquid extraction is an efficient method for extracting certain classes of organic solutes from water, particularly those nonpolar solutes that have low water solubility but high solubility in organic solvents immiscible with water. Multiple-stage (American Society for Testing and Materials, 1975) and continuous (Goldberg and others, 1971) liquid-liquid extraction schemes have been devised which reportedly approach quantitative recovery data for selected compounds. A basic assumption of the extraction technique is that the distribution or partition coefficient of an organic solute between two immiscible liquids is constant, but this does not always follow. Examination of organic solute distribution coefficients listed in the International Critical Tables (Forbes and Anderson, 1928) indicates that generally distribution coefficients vary with the concentration of the solute. For example, acetic acid at a concentration of 0.002 *M* (molar) partitions between water and chloroform to give a distribution coefficient of 36.2; whereas, at a concentration of 4.0 *M*, the distribution coefficient is 2.2. This means that chloroform becomes less efficient as an extraction solvent for acetic acid as the absolute concentration decreases. Most organic solutes in natural waters are present at concentrations in micrograms per litre where the distribution coefficients for extraction are less favorable and large volumes of extractant and pH adustments must be used to improve recoveries.

Liquid-liquid extraction is difficult for highly polar organic solutes. A major fraction of organic solutes found in natural waters is highly polar compounds. Another consideration in liquid-liquid extraction is solvent removal; losses of volatile solutes are frequently a problem.

Limitations of carbon adsorption

Adsorption of organic solutes from aqueous solution upon granular activated carbon is currently an accepted method of extracting and fractionating organic solutes (ASTM method D–2910 in American Society for Testing and Materials, 1975). Activated carbon is an efficient agent for removing organic solutes from water by adsorption; however, its use in quantitative analytical schemes is limited by the fact that many organic solutes are not desorbed and (or) altered by the activated carbon. These limitations are well documented in the literature (Baker and Malo, 1967; Burnham and others, 1973).

The problems arise from the heterogeneous nature of the surface of most activated carbons. The carbon surface that acts on organic solutes by physical adsorption mechanisms also has many oxygen-containing functional groups which tightly bind organic solutes by chemical adsorption mechanisms (Bartell and Lloyd, 1938; Ward and Getzen, 1970). Nonpolar desorbing solvents that disrupt physical adsorption tend to strengthen the solute-activated carbon bonds through chemical adsorption. Polar desorbing solvents that disrupt the chemical adsorption tend to strengthen the physical adsorption bonds. Therefore, organic solutes held by multiple-bonding mechanisms are irreversibly adsorbed and cannot be recovered for analysis. Another consideration is that once all available sorption sites are filled, selective organic sorption occurs and previously sorbed organic solutes are desorbed. Thus, the recovered organic fraction may not represent the original sample composition. Certain organic solutes, such as polysaccharides and amino acids, are not adsorbed on activated carbon. Because neither adsorption nor desorption are quantitative, activated carbon cannot be used to measure total organic solute concentrations in aqueous systems. Its use is based on its ease of handling and ready availability. Standardization of test procedure permits certain qualitative interpretation of the resulting data.

ADVANTAGES OF SYNTHETIC RESIN ADSORBENTS

In a comparison of processes that concentrate organic solutes found in natural waters, adsorption is often superior to liquid-liquid extraction, flash evaporation, freeze concentration, and freeze drying for the following reasons: (1) It is a low energy process which does not involve a phase transition; adsorption does not remove the organic solute from the aqueous environment as does liquid-liquid extraction and freeze drying, and it takes less energy for a solute to be adsorbed on a surface than to cross a liquid-liquid interface; solvent extraction can also alter the chemical nature of the solute, (2) the low temperature and high vapor pressure at which adsorption occurs prevents the losses of volatile solutes that frequently occur during flash evaporation or freeze drying, and (3) adsorption is selective; adsorbents can be selected such that organic solutes are separated from inorganic solutes, and organic solutes can be fractionated into different groups depending upon which adsorption mechanism is used. Flash evaporation, freeze concentration, and freeze drying indiscriminately concentrate both organic and inorganic solutes. This may lead to problems depending on the concentration range attempted and the properties of the system.

The ideal adsorbent for analytical purposes should have a homogeneous surface. Only one adsorption

mechanism should be operative so that solutes can be quantitatively sorbed and desorbed. The adsorbent should have a high surface area to give high capacity, good chemical and structural stability, and good hydraulic flow characteristics for column operation. These requirements are met by three-dimensional copolymers possessing a so-called macroporous or macroreticular structure (Kun and Kunin, 1968). Adsorption rather than absorption is the primary binding mechanism of organic solutes on the surface of this copolymer (Gustafson and others, 1968). Macroreticular adsorbent resins are available with nonpolar surfaces (Amberlite XAD–2 and XAD–4), intermediate polarity surfaces (Amberlite XAD–7 and XAD–8), highly polar surface (Amberlite XAD–12), cation-exchange surface (Bio-Rad AG MP–50) and anion-exchange surface (Bio-Rad AG MP–1). The properties and applications of the Amberlite XAD resins are described in a report by Simpson (1972), and the advantages of the use of macroreticular ion-exchange resins are discussed by Rieman and Walton (1970).

No one resin adsorbent by itself is capable of quantitatively extracting and fractionating all the diverse organic solutes found in natural waters; instead, a series of adsorbent resins must be used in a sequence that utilizes various adsorption mechanisms to extract and separate the organic solutes.

CLASSIFICATION SCHEME FOR ORGANIC SOLUTES

A proposed classification scheme for organic solute characterization is given in figure 1. It is designed to handle all organic solutes found in natural waters. Classification levels 1–3 are based on a methodology employing macroreticular resins to extract and fractionate organic solutes. Classification levels 4–6 are primarily based on gas and liquid chromatographic methods to further separate and analyze the organic solutes at specified levels. Because levels 1–3 are based on a new methodology and levels 4–6 are based on an existing methodology, this report confines itself only to a discussion of classification levels 1–3.

This scheme has a logical progression from one classification level to the next, and it uses a materials balance based on total DOC of the input water and the summation of the DOC in each fraction. The meaning and significance of the DOC parameter in water-quality investigations is discussed more extensively in a report by Malcolm and Leenheer (1973).

The first classification level divides organic solutes into hydrophobic and hydrophilic classes. Hydrophobicity and hydrophilicity are opposite properties, and organic solute analysis is greatly facilitated if the solutes are first divided into these two classes. This classification refers to mechanisms by which organic solutes interact with the solvent, with each other, and with sediment. Hydrophobic solutes are defined in the proposed fractionation procedure as those organic solutes that are adsorbed on macroreticular resin surfaces

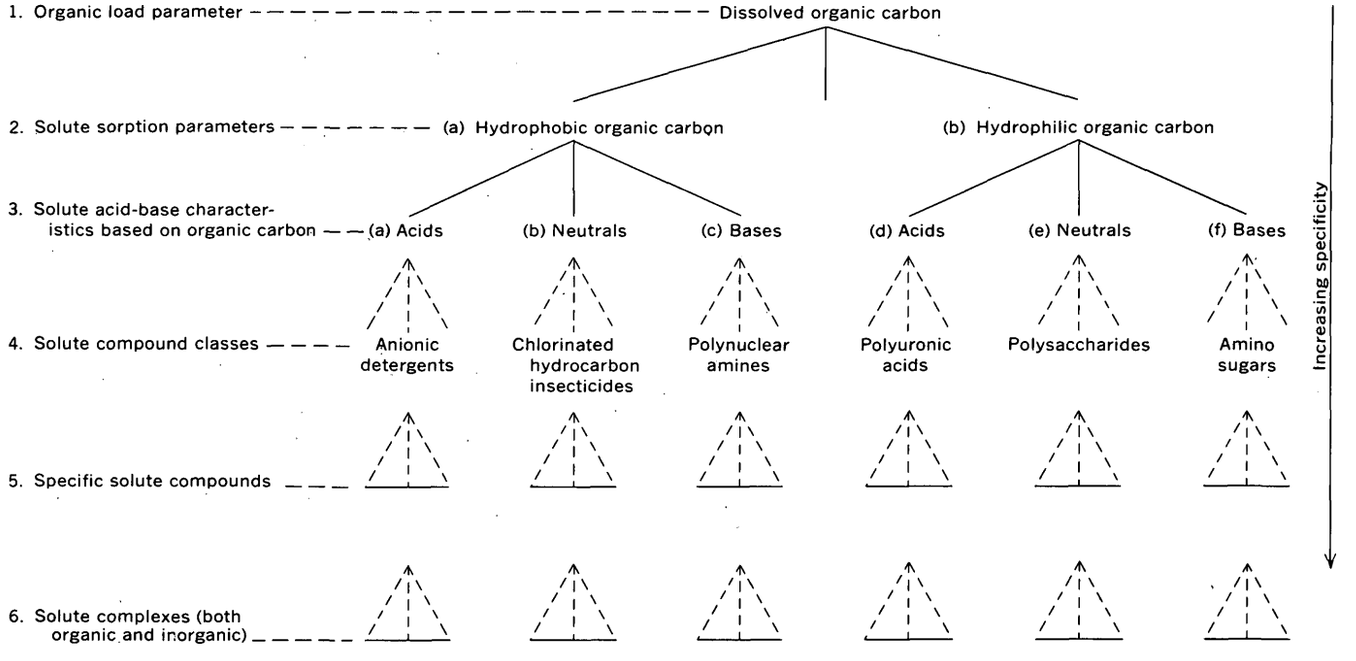

FIGURE 1.—Proposed classification scheme for organic solute characterization.

of low and intermediate polarity. The hydrophilic solutes are those that are not adsorbed on these resins. The hydrophobic-hydrophilic organic solute concept is defined and described in the report by Simpson (1972).

Hydrophobic organic solutes have hydrocarbon portions of their molecular structure that repel water and are attracted to hydrocarbon surfaces on sediment or to hydrocarbon portions of other solute molecules. The attraction mechanism involves physical adsorption, which is also referred to as van der Waals bonding. Hydrophilic organic solutes have water-attracting oxygen, nitrogen, or sulfur-containing functional groups distributed over the molecular structure such that the molecule cannot act in a hydrophobic manner. Hydrophilic solutes interact with water, with each other, and with sediments through hydrogen-bonding and ion-exchange mechanisms. Most hydrophobic organic solutes have hydrophilic portions of their molecular structure that render them water soluble. Organic detergents have a hydrophilic functional group for water solubility and a hydrophobic hydrocarbon portion to attract hydrocarbon oils and render them water soluble.

The third classification level refers to organic solute acid-base characteristics. Hydrophobic acids and bases are functionally defined as the hydrophobic DOC (dissolved organic carbon) concentrations that are desorbed from non- or low-polarity macroreticular resins by aqueous alkali and acid, respectively. Hydrophobic neutral solutes are defined as that portion of hydrophobic DOC that is not desorbed by aqueous alkali and acid. Hydrophilic acids and bases are determined as the DOC that is adsorbed on anion- and cation-exchange resins, respectively, after the hydrophobic solutes have been removed from solution. Hydrophilic neutral compounds are defined as the DOC that remains in solution after the entire resin-adsorption procedure. Organic solutes have thus been classified and separated into six groups that are very similar in their chemical reactivity.

Compound class analysis at the fourth level of classification is greatly facilitated by the previous solute separations which have simplified the organic mixture and removed most of the inorganic solutes. All the chlorinated hydrocarbon insecticides are found isolated in the neutral hydrophobic group. Certain compound classes will be found in multiple groups at the third level of classification. Most amino acids will fall into the hydrophilic base group, but the amino acid phenylalanine will fall into the hydrophobic neutral group because of the hydrophobic phenyl ring (Gustafson and others, 1968).

The last two classification levels, specific solute compounds and solute complexes, demand more in the way of analytical requirements. If a water-quality study requires additional detail, the proposed classification scheme lays a meaningful groundwork for quantitative organic solute analysis.

DISSOLVED ORGANIC CARBON FRACTIONATION ANALYSIS

The analytical fractionation scheme that concentrates and separates organic solutes up to the third level of classification by macroreticular resin adsorption and desorption is called DOC fractionation analysis. The research and development of this analytical fractionation scheme was performed by the authors at Huffman Laboratories, Inc., located in Wheatridge, Colo.

Fractionation of hydrophobic solutes

The analytical fractionation scheme was designed to extract hydrophobic organic solutes first because of the specificity that certain macroreticular resins were reported to have for hydrophobic solutes. Ion-exchange resins are used next to remove ionic hydrophilic compounds. Neutral, nonionic hydrophilic compounds are not adsorbed on either type resin. Most of the research concerning fractionation of hydrophobic solutes is based on the work of G. A. Junk and his colleagues of the Ames Laboratory at Iowa State University (Burnham and others, 1972; Junk and others, 1974).

The experimental procedure used to test the performance of the macroreticular resins for hydrophobic solutes was quite simple. Various hydrophobic and hydrophilic organic solute standards were dissolved in distilled and deionized "carbon free" reagent water at volumes and concentrations such that the adsorptive capacities of the resins, which varied from 5 to 20 milligrams organic carbon per gram of resin, would not be exceeded. The resins were prepared for use by slurring the resin beads in methanol, decanting fines, and sequential 24-hour Soxhlet extractions with ether, acetonitrile, and methanol to remove organic contaminants. From 5 to 20 grams of resin were packed in glass columns at a height-to-diameter ratio of about 10:1, and the methanol was washed from the resin with 8 to 10 litres of reagent water. Both standard and real water samples were allowed to flow through the resin column at a flow rate of about 10 millilitres per minute which was controlled by a syringe pump which pressurized the glass reservoir containing the sample solution with air. DOC was used to monitor the adsorption and desorption of the solutes. DOC can

be determined to a lower limit of 0.1 mg/l with a precision of ±10 percent (Malcolm and others, 1973).

In general, the standard solutions contained a mixture of hydrophobic acid, neutral, and base components. The standard solution was acidified to pH 2 with HCl to improve the adsorption by suppressing the ionization of the acids. The first pass through the resin column was intended to adsorb the acid and neutral hydrophobic solutes. The hydrophobic bases stay in solution at pH 2 as protonated cations which are ionized. The hydrophobic bases were adsorbed next after adjusting the pH to 10 with NaOH and passing the standard solution through a second resin column. Hydrophobic acids were removed from the column by desorption with 200 ml of 0.05 *M* NH_4OH. Hydrophobic neutral solutes were recovered by elution with 150 ml of ether followed by 100 ml of methanol. Hydrophobic bases were also recovered from the second column with these quantities of ether and methanol or with 200 ml of 0.1 *M* HCl. The solvents were removed from the eluates by Kuderna-Danish evaporative concentrations followed by drying in a desiccator. Recoveries of solutes were determined by summation of DOC in the recovered aqueous fractions or by weighing and organic carbon analysis of the solute after organic solvent removal.

A series of seven experiments were performed to determine the adsorption characteristics of the various types of XAD macroreticular resins. The results are summarized in table 1.

The purpose of experiment 1 was to determine if small amounts of low-molecular-weight hydrophobic solutes consisting of an organic acid, an organic neutral compound, and an organic base could be adsorbed as a mixture, fractionated by selective adsorption and desorption, and recovered in reasonable quantities. This experiment was essentially a duplication of the work reported by Burnham and others (1972), and comparable recoveries based on DOC analyses were obtained. Recoveries based on direct weighing of the solutes after evaporation of the solvent were considerably lower, which indicates that losses of volatile solutes occur during evaporation. Aniline, which had the highest volatility, was recovered in the lowest quantity.

Experiment 2 was run to determine whether a high-molecular-weight natural organic solute mixture, fulvic acid, which is frequently found in natural waters, could be adsorbed and recovered from the 1:1 mixed bed of XAD–2 and XAD–4 resins. The test fulvic acid was extracted from the spodic horizon of a soil of the Lakewood series, collected near Wilmington, N. C. Its characterization is described in a report by Leenheer and Malcolm (1973). The recovery based on DOC indicated that only 16 percent was adsorbed and only 11 percent was recovered after desorption with aqueous ammonia. It was postulated that this poor recovery was attributed to the lack of inorganic solutes in the reagent water. Inorganic solutes sometimes serve to "salt-out" organic solutes by decreasing their solubility. Therefore, experiment 3 was performed with 463 mg/l of NaCl dissolved with the fulvic acid. In this experiment, only 8.3 percent of the DOC was adsorbed; therefore, the addition of salt did not improve the recovery. In experiments 2 and 3, discoloration of the XAD resin adsorbents indicated that desorption with aqueous ammonia was not complete. These negative results indicated that the XAD–2 and XAD–4 resins were unsatisfactory for recovering high-molecular-weight natural hydrophobic organic solutes.

TABLE 1.—*Recovery efficiencies of hydrophobic organic solute standards after adsorption and fractionation on XAD macroreticular resins*

Experiment	Type and quantity of resin	Compounds tested	Solute DOC concentration (mg/l)	Recovery based on DOC (percent)	Recovery based on weighing (percent)
1	10 g of a 1:1 mixture of XAD–2 and XAD–4.	(a) Benzoic acid	(a) 7.8	(a) 89	(a) 54
		(b) *p*-Methylbenzyl alcohol	(b) 7.2	(b) 93	(b) 79
		(c) Aniline	(c) 8.4	(c) 65	(c) 3
2	----do	Fulvic acid	3.7	16, adsorbed; 11, recovered	----
3	----do	----do	6.0 with 463 mg/l of NaCl.	8.3, adsorbed	----
4	10 g of XAD–8	----do	4.5	60, absorbed; 51, recovered	----
5	----do	(a) Benzoic acid	(a) 6.5	(a) 69, adsorbed; 61, recovered	----
		(b) *p*-Methylbenzyl alcohol	(b) 9.7	(b) 47, adsorbed	(b) 48
6	Stratified column of 5 g of XAD–8 over 5 g of XAD–2.	(a) Fulvic acid	(a) 4.9	(a+b) 75	(a+b) 40
		(b) Benzoic acid	(b) 5.0		
		(c) *p*-Methylbenzyl alcohol	(c) 5.5	(c) 77	(c) 66
		(d) Aniline	(d) 7.6	(d) 59	(d) 19
7	----do	(a) Acetic acid	(a) 4.0	(a) 0	----
		(b) Sucrose	(b) 4.3	(b) 0	----
		(c) Ethylenediamine	(c) 3.8	(c) 0	----

The macroreticular resin adsorbent, XAD–8, was developed specifically to adsorb the lignosulfonic acids found in kraft pulpmill effluents. Lignosulfonic acids are chemically and structurally similar to fulvic acids. This resin has intermediate polarity which attracts both the hydrophobic and hydrophilic portions of the molecule. It has a large average pore diameter of 250 angstroms, which allows large molecules such as fulvic acid to enter into the interior of the resin bead. The results of experiment 4 show that the adsorption of fulvic acid was much greater (60 percent) and 85 percent of the adsorbed fulvic acid was desorbed with 0.1 *M* NaOH. The fulvic acid solution was entirely decolorized after passage through the XAD–8 resin. The DOC measurement on the eluate showed substances not sorbed and corresponded to possible hydrophilic polysaccharides and polyuronic acids, which comprise about 30 percent of the DOC of this fulvic acid preparation (Leenheer and Malcolm, 1973). Therefore, the colored hydrophobic fulvic acid constituents appear to be quantitatively adsorbed by the XAD–8 resin.

Experiment 5 was run to determine both the adsorptive capacity of the XAD–8 resin with respect to the low-molecular-weight standards and whether the adsorbed solutes could be quantitatively desorbed from the medium polarity XAD–8 surface, which might irreversibly adsorb solutes because of strong hydrogen bonding. The results indicated a lower adsorptive capacity of the XAD–8 resin compared to the 1:1 mixture of the XAD–2 and XAD–4 used in experiment 1, but the adsorbed solutes were almost quantitatively desorbed and recovered.

The results from the five experiments suggested experiment 6 in which a stratified column of 5 grams of XAD–8 over 5 grams of XAD–2 was used to recover the mixture of low- and high-molecular-weight hydrophobic organic solutes found in natural waters. High-molecular-weight solutes, such as fulvic acid, are first removed and do not contact the XAD–2 resin where irreversible adsorption has been shown to occur. The XAD–2 was included because of its higher adsorptive capacity for the low-molecular-weight hydrophobic solutes. The two resins were segregated in the column by a glass-wool plug.

The stratified XAD resin column was tested in experiment 6 with a mixture of low- and high-molecular-weight hydrophobic solutes. The recoveries based on DOC were higher than experiment 5, which indicates that inclusion of the XAD–2 resin did permit higher recoveries than were obtained with just the XAD–8 resin; but the recoveries were lower than experiment 1, which suggested that the sorptive capacity of the stratified column had been exceeded for the low-molecular-weight standards.

The last experiment was designed to test if three hydrophilic organic solutes—acetic acid, ethylenediamine, and sucrose—would be adsorbed on the stratified XAD resin column. The results of experiment 7 indicate no measurable adsorption of these hydrophilic solutes; therefore, the hydrophobic XAD resins are specific for hydrophobic solutes.

Table 2 presents certain organic elemental analyses obtained on the standards recovered from the XAD resin. Acids such as benzoic acid are recovered as ammonium salts because they are desorbed from the resin with ammonium hydroxide. The results indicate that ammonium benzoate is not stable when dry because additional drying of this fraction in a desiccator over P_2O_5 caused a change in the elemental analysis such that carbon increased and nitrogen decreased. This effect most likely is caused by ammonium benzoate reverting to benzoic acid with the loss of ammonia. The neutral fraction represented by *p*-methylbenzyl alcohol was recovered in pure form as indicated by the elemental analyses. This compound was stable with drying. Aniline presented severe recovery problems when dried. The high volatility of the aniline caused significant losses when the methanol and ether solvents were removed. The high value for hydrogen in the elemental analysis indicated that the analyzed aniline was still contaminated with solvent.

The elemental analyses of the various fractions are sufficient to indicate that the XAD resin adsorption and fractionation procedure does separate the acid-base-neutral mixture into the individual compounds; however, problems with compound volatility and in-

TABLE 2.—*Organic elemental analyses, in percent, of standards after fractionation and recovery from XAD resins*

Experiment and fraction [1]	Compound	Actual analysis				Theoretical analysis			
		C	H	O	N	C	H	O	N
1–a -----	Ammonium benzoate -----	[2]63.63(1)	5.86(1)	---	5.21(1)	60.43	6.47	23.02	10.07
		65.44(2)	5.34(2)	---	2.16(2)				
6–c ------	*p*-Methylbenzyl alcohol ---	78.33	8.32	---	0.04	78.48	8.13	13.01	0
6–d -----	Aniline ----------	63.81	15.78	---	5.21	77.38	7.58	----	15.04

[1] Experiment notation from table 1.
[2] (2) was dried twice as long as (1).

stability at the solvent-removal or drying step severely limit the usefulness of organic elemental analysis for characterization of the separated fractions. Relatively nonpolar organic solvents, such as ether, were found to be ineffective for desorbing natural polar organic solutes, such as the fulvic acids; therefore, polar solutes were best desorbed by polar solvents such as water and methanol. However, evaporation of these polar solvents prior to elemental analysis caused severe solute losses. Because of these limitations, organic elemental analysis was abandoned as a means to characterize the acid, base, and neutral fractions. Subsequent characterizations were mainly limited to the determination of DOC in each fraction, which did not necessitate removal of the aqueous acid or base used as the desorbing solvent.

Three natural water samples were run through the stratified XAD resin column under the conditions previously specified for experiment 6 as part of the evaluation of the XAD resin adsorbents. The DOC fractionations from these three samples are presented in table 3.

The Clear Creek sample was collected when the creek was receiving a large urban storm-sewer runoff during a period of snowmelt. Suspended sediment was removed from the sample by passing it through a continuous-flow centrifuge at a rate such that all particles less than 0.1 micrometre in diameter were removed, assuming the particles had a specific gravity and dimensions possessed by a clay mineral particle. About 60 percent of the DOC was adsorbed by the XAD resins, and this adsorbed DOC fractionated almost equally between the hydrophobic acid and hydrophobic neutral fractions. There were no problems encountered with the analytical procedure.

The Piceance Creek sample was taken during a period of low flow in midwinter. This sample can be considered typical of an uncontaminated surface-water sample from northwest Colorado in an area slated for development of oil-shale resources. The DOC was much lower than the Clear Creek sample, which was contaminated with organic solutes from the metropolitan Denver area. As with the Clear Creek sample, about 60 percent of the DOC was adsorbed by the XAD resins, but, in this instance, the major portion of the adsorbed DOC consisted of hydrophobic acids. When the sample pH was adjusted to 10 with sodium hydroxide for adsorption of the hydrophobic bases, a gelatinous white precipitate formed which may have coprecipitated a small amount of DOC and thus affected the results.

The trona water sample, also termed "black water" because of its appearance, is an alkaline ground water found in strata associated with oil shale in the general vicinity of Rock Springs, Wyo. Because of the very high DOC of 45,000 mg/l, only 2 ml of sample were applied to the XAD resin column. The initial acidification caused formation of a brown, organic precipitate, so the sample was first eluted through the stratified column with 200 ml of pH 10.5 Na_2CO_3 solution to adsorb the hydrophobic organic base and neutral constituents. The precipitate, which formed when the alkaline eluent from the XAD resin column was acidified, was applied in suspension to the second stratified XAD resin column. This precipitate did not plug the column, and it completely dissolved when the hydrophobic acids were eluted with aqueous ammonia. Almost 70 percent of the DOC fractionated into the hydrophobic acid fraction, 27 percent of the DOC was found in the hydrophobic neutral fraction, and only about 4 percent of the DOC consisted of hydrophilic solutes which did not sorb on the XAD resins.

In all three water samples, the majority of the DOC fractionated into the hydrophobic acid and neutral fractions. The hydrophobic organic base-solute concentrations were expected to be low because they are adsorbed on sediments as cations by cation exchange

TABLE 3.—*DOC fractionation of certain water samples by use of XAD macroreticular resins*

Sample site	Sample date	pH (units)	Specific conductances (μmhos/cm) at 25°C)	DOC (mg/l)	Hydrophobic acid DOC (mg/l)	Hydrophobic neutral DOC (mg/l)	Hydrophobic base DOC (mg/l)	Hydrophilic DOC (mg/l)
Clear Creek at Kipling Street Bridge, Wheatridge, Colo	2–11–75	6.7	1,750	29.0	8.3	8.3	0.7	11.7
Piceance Creek at mouth on White River, near Meeker, Colo	2–21–75	8.1	1,480	4.4	2.0	.6	.1	1.7
Trona water collected from well on Ed Tomish Ranch near Eden, Wyo	2–20–75	10.3	17,000	45,100	30,700	12,240	130	2,030

as well as by hydrophobic interactions. They may be utilized as a source of nitrogen for microbiological processes, and there simply are not as many natural organic sources for organic bases as there are for organic acid and neutral solutes. Where there was enough material isolated, the acid and neutral hydrophobic organic solute fractions were characterized by organic and inorganic elemental analysis. The results are presented in table 4.

Relatively high ash contents were found for most of the organic fractions isolated from these water samples. The ash is due to inorganic constituents isolated with the organic constituents possibly as metal organic complexes, metaloid organic complexes, clay-colloid organic complexes, amorphous silica and clay colloids physically entrapped by the macroreticular resins, and inorganic cations and anions adsorbed by the macroreticular resins. The inorganic elemental analysis was obtained by semiquantitative emission spectroscopy. Almost all of the acid and neutral fractions have high percentages of aluminum, silicon, and titanium which are indicative of aluminosilicate clay minerals.

In the Clear Creek sample, a dark band formed at the interface of the ammonium hydroxide eluent and the ether eluent. This band was isolated in a separatory funnel, and the solvents were removed. Surprisingly, the material contained in this band was almost entirely inorganic and consisted of sodium and sulfur. Some of the other fractions were also found to be relatively high in sulfur. Possibly the inorganic sulfur is sorbed by the bisulfite addition reaction, which could possibly occur on the acrylic-ester surface of the XAD–8 resin, or by physical adsorption of undissociated polysulfides and elemental sulfur. Adsorption of the bisulfite anion could explain the presence of sodium as the counter cation.

Lastly, the high percentage of boron found in the organic trona acids is significant. Many trona waters have high concentrations of boron, and it appears from these results that boron may possibly be complexed with the organic trona acids. Borates are known to form anionic complexes with organic solutes which have α-hydroxy groups (Gast and Thompson, 1958).

The final experiment in the evaluation of the XAD resin adsorbents was to determine the adsorptive capacities of a specified XAD resin column for certain organic solutes at a fixed flow rate. The column selected for use was a glass chromatographic column with Teflon end plates. The internal dimensions of the column were 0.9 cm × 30 cm. The column was packed with 2.5 grams of XAD–8 resin over 2.5 grams of XAD–2 resin. Glass-wool plugs were placed at both ends of column so the column could be eluted in either direction, and the two resins were separated by a glass-wool plug. Each resin bed had a height to diameter ratio of about 12:1. The influent stream to the column was passed downflow first through the XAD–8 resin, followed by the XAD–2 resin at a flow rate of 4 ml/min. This flow rate (calculated to be 0.25 millilitre per minute per cubic centimetre of resin) was considerably less than the recommended flow rate of 1.27 (ml/min)/cm^3 of resin (Simpson, 1972). Therefore, the solutes should have sufficient time to equilibrate with the XAD resins at this flow rate so that a true estimate of the adsorptive capacity is obtained. These column, resin, and flow rate specifications were followed in all subsequent experiments.

Four litres of 50 mg/l DOC solutions of fulvic acid, benzoic acid, *p*-methylbenzyl alcohol, and aniline dis-

TABLE 4.—*Organic and inorganic elemental analyses of organic fractions derived from certain water samples by use of XAD macroreticular resins*

[Analyses are given in percent]

Sample site	Fraction	Fraction weight (mg)	Ash	C	H	O	N	S	Al	B	Co	Cu	Fe	Mg	Na	Si	Ti
Clear Creek at Kipling Street Bridge, Wheatridge, Colo.	Acids desorbed with NH_4OH.	58.5	27.0	36.4	4.6	23.5	4.7	3.0	10	1	5	0.1	2	5	10	(1)	.5
	Neutrals desorbed with ether .	25.3	---	68.7	9.1	23.1	.1	---	---	---	---	-----	---	-----	---	---	-----
	Neutrals desorbed with methanol.	32.8	---	29.4	3.5	---	2.1	---	(1)	.5	1	.1	.1	10	10	10	10
	Interface between NH_4OH and ether.	262	97.5	1.4	.3	---	.1	21.2	.1	---	.01	.05	.01	.01	(1)	.1	.001
Piceance Creek at mouth on White River, near Meeker, Colo.	Acids desorbed with NH_4OH.	17.5	---	35.1	4.6	27.1	--	---	1	2	1	.1	.1	.1	1	10	.01
	Neutrals desorbed with methanol.	6.5	---	43.9	11.7	---	--	---	---	---	---	-----	---	-----	---	---	-----
Trona water collected from well on Ed Tomish Ranch, near Eden, Wyo.	Acids desorbed with NH_4OH.	76.6	15.1	63.9	8.0	12.1	3.5	1.9	.5	10	.5	.1	.05	.1	.1	5	.1
	Neutrals desorbed with ether.	12.4	15.0	53.9	7.4	29.3	.9	---	---	---	---	-----	---	-----	---	---	-----
	Neutrals desorbed with methanol.	38.8	---	2.2	.2	---	2.2	1.2	(1)	.01	1	.001	.1	1	---	10	(1)

[1] Major.

solved in an inorganic matrix solution of 2 milliequivalents per litre of $CaCl_2$, 2 meq/l of $NaHCO_3$, and 1 meq/l of $MgSO_4$ were passed through stratified XAD resin columns, and the DOC was determined on the column effluent at 250-ml intervals. The results are presented in the DOC-breakthrough curves of figure 2.

The adsorptive capacities were calculated by determining the milligrams of DOC of the solute sorbed per gram of resin at the point arbitrarily defined where there was 5-percent leakage of the solute through the stratified resin column. The adsorptive capacities are: Benzoic acid at pH 2=14 mg DOC/g resin, *p*-methylbenzyl alcohol at pH 7=10 mg DOC/g resin, aniline at pH 7=4 mg DOC/g resin, and aniline at pH 10=4 mg DOC/g resin. The fulvic acid, being a mixture of both hydrophobic and hydrophilic compounds, showed a continuously increasing leakage of DOC through the column and a meaningful adsorptive capacity could not be calculated. The lack of inflection points on the fulvic acid curve (fig. 2) indicates that there is no sharp distinction between the hydrophobic and hydrophilic solutes of this fulvic acid preparation. Most likely, there also is no discrete break between the hydrophobic and hydrophilic organic solutes in the complex mixtures found in natural waters.

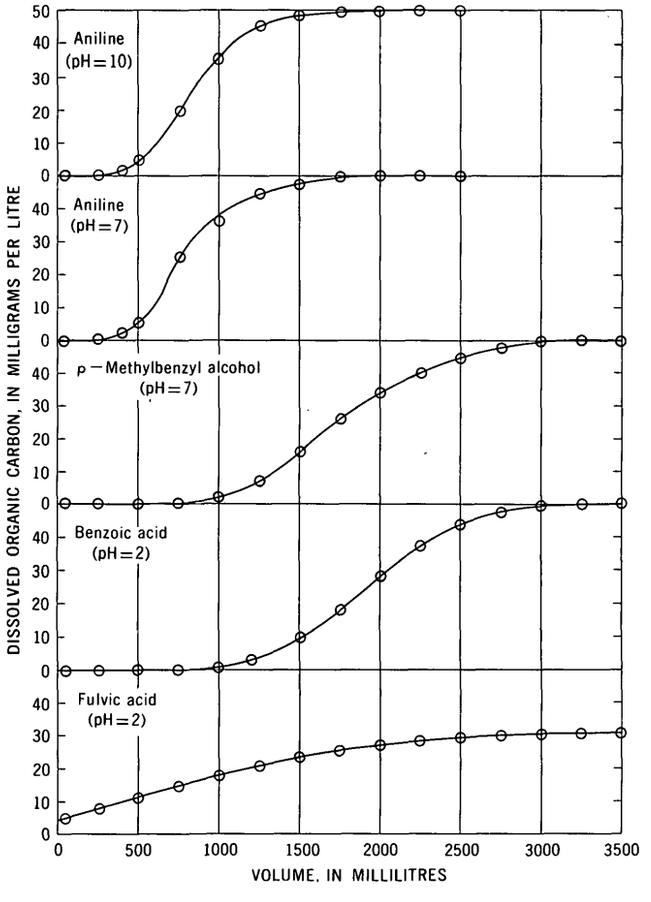

FIGURE 2.—DOC-breakthrough curves for various organic solutes passed through the stratified XAD resin column.

The adsorptive capacity selected as a reasonable value at which to make the hydrophobic-hydrophilic break was 4 mg DOC/g resin. At this value, quantitative recoveries of the most weakly adsorbed hydrophobic standard, aniline, can be obtained, and about 85 percent of the fulvic acid can be recovered. Based on the assumption that a maximum of 80 percent of the total DOC in natural waters is hydrophobic DOC (usually the percentage is much lower), the specified XAD resin column can quantitatively adsorb the hydrophobic DOC from a 1-litre water sample at a maximum DOC concentration of 25 mg/l. Smaller volumes of sample should be passed through the column if the initial DOC concentration is greater than 25 mg/l so that the specified adsorptive capacity of 4 mg DOC/g resin is not exceeded.

In summary, the XAD hydrophobic resins were found to efficiently adsorb and fractionate hydrophobic organic solutes when used in the manner described in this report. The fractionation is best determined by monitoring DOC changes in the sample and in the aqueous desorption solvents. Elemental analysis has limited utility in characterizing organic solutes because of loss and changes in the organic solutes when the solvents were removed, because of the high inorganic ash contents resulting from organic-inorganic complexes which sometimes interfered in the organic elemental analysis, and because of the small quantities of material obtained which sometimes prevented completed analysis. In the three water samples, different hydrophobic DOC fraction ratios were found. These fraction ratios can be used either in geochemical interpretations or as indicators to monitor changes in organic solute mixtures. Only slight modifications were needed in the experimental procedure when water samples with widely divergent organic and inorganic solute concentrations were fractionated on the XAD macroreticular resins. Lastly, the isolation of organic-inorganic associated solutes from the natural water samples is significant for those studies concerned with organic solute complexation.

Fractionation of hydrophilic solutes

The analytical scheme for dissolved organic carbon fractionation analysis was completed by fractionating the hydrophilic organic solutes into acid, base, and neutral fraction by use of macroreticular ion-exchange resins. All of the DOC that remains in solution after the water sample has passed through

the combination of XAD–8 and XAD–2 resins quantifies the hydrophilic DOC. This distinction between hydrophobic and hydrophilic DOC is admittedly method dependent. Therefore, the fractionation of the hydrophilic organic solutes that remain on the ion-exchange resins must necessarily follow the fractionation of the hydrophobic organic solutes on the XAD resins.

The ion-exchange resins selected for use possessed the same macroreticular structural characteristics and matrix composition as the XAD–2 resin. Therefore, the only variable between the XAD–2 resin and the ion-exchange resin is the surface chemistry determined by the ion-exchange group.

The cation-exchange column was placed ahead of the anion-exchange column in the analytical scheme because the eluent from the XAD resins is acidic, which protonates the hydrophilic base solutes such that they act as cations and are adsorbed on the cation-exchange resin. The cation-exchange resin selected for use was Bio-Rad AG MP–50, which was hydrogen saturated. It has an ion-exchange capacity of 1.6 to 1.8 meq/ml of packed bed. The matrix composition is a styrene-divinyl benzene copolymer, and the cation-exchange group is sulfonic acid. The resin was purified by Soxhlet extraction with methanol for 24 hours, followed by exhaustive leaching with deionized water. Approximately 5 grams of resin filled a glass chromatographic column identical to the column specified for use with the XAD resins. Aliquots for specific conductance and DOC analyses were taken after 200 to 300 ml of sample had passed through this column. Specific conductance was monitored before and after the sample passed through the column to determine if the resin capacity had been exceeded. Water samples with a specific conductance in excess of 2,000 micromhos per centimetre exceed the resin capacity if 300 ml are passed through; therefore, aliquots have to be taken after 150 ml.

The anion-exchange column was placed in series directly after the cation-exchange column. The anion-exchange resin selected for use was Bio-Rad AG MP–1 which was hydroxide saturated. Its physical characteristics and matrix composition were the same as the cation-exchange resin. Its anion-exchange functional group is a quaternary amine, and its anion-exchange capacity is about 1.0 meq/ml of packed bed. The column, resin quantities, and experimental procedure were identical to those specified for the cation-exchange resin.

Hydrophilic base DOC is determined by that portion of DOC adsorbed on the cation-exchange resin, hydrophilic acid DOC by that portion adsorbed on the anion-exchange resin, and hydrophilic neutral DOC by that portion remaining in solution after the entire procedure. Both hydrophilic base DOC and hydrophilic acid DOC are difference determinations as measured by the decrease in DOC when a sample is passed through the ion-exchange resins.

Numerous attempts were made to directly determine hydrophilic base DOC and hydrophilic acid DOC by their quantitative desorption from the cation- and anion-exchange resins, but most of these experiments gave DOC recoveries that were much too high, possibly from resin leaching. In theory, DOC analysis on desorbed fractions is much more accurate than determining adsorbed fractions by difference because DOC is concentrated in a small volume of the desorbing solvent and only one DOC measurement is needed. Reasonable DOC recoveries were obtained only after the ion-exchange resins were extensively purified by sequential leaching with aqueous acid, alkali, and deionized water.

The results of a successful desorption experiment are given in table 5. The cation-exchange column was purified by passing 1 litre of 1.0 *M* NaOH through the column to desorb the organic base contaminants, followed by 1 litre of 1.0 *M* HCl to resaturate the resin with hydrogen ions, followed by 1 litre of deionized water. The anion-exchange column was prepared in a similar manner except with acid and base rinses interchanged. The acid and base rinses used to resaturate the resin columns were first passed through "pre-columns" containing hydrogen-saturated cation-exchange resin and hydroxide-saturated anion-exchange resins, respectively, such that organic acid and base contaminants would be adsorbed on these "pre-columns" rather than on the analytical columns. The deionized water rinses were also passed through these "pre-columns."

Citric acid and ethylenediamine were selected as the acid and base solute standards because their mul-

TABLE 5.—*Desorption of citric acid and ethylenediamine from anion- and cation-exchange resins*

Fraction (ml)	Citric acid (μg C)	Ethylenediamine (μg C)
0–10	90	0
10–20	400	0
20–30	1,000	0
30–40	580	0
40–50	430	0
50–60	240	0
60–70	160	140
70–80	110	1,130
80–90	80	860
90–100	50	280
100–110	30	110
110–120	----	40
120–130	----	20
Total	3,170	2,580

tiple acid and base functional groups should make them difficult to desorb and, therefore, serve as a good test of the experimental procedure. These standards were prepared at DOC concentrations of 5.0 mg/l in an inorganic matrix solution consisting of $CaCl_2$ at 2.0 meq/l, $NaHCO_3$ at 2 meq/l, and $MgSO_4$ at 1.0 meq/l. The standard solutions were acidified to pH 2 with HCl so as to duplicate the standard procedure. The standards were adsorbed on the respective columns by passing 500 ml of the standard solutions through the columns at a flow rate of 4 ml/min. The ethylenediamine was desorbed from the cation-exchange resin with 1.0 M NaOH at a flow rate of 2.0 ml/min and the citric acid was desorbed from the anion-exchange resin with 1.0 M HCl at a flow rate of 2.0 ml/min. The direction of column flow was reversed for desorption. Sequential 10-ml fractions for DOC analysis were collected during desorption such that the rate of desorption could be determined.

The results given in table 5 indicate the ethylenediamine was quantitatively recovered at the theoretical quantity of 2,500 μg C within the limits of experimental error. The 3,170 μg C of citric acid was high by 670 μg C. This high result may be caused by impure resin or by inorganic carbon which was not completely purged from the samples prior to the DOC determinations. Citric acid was eluted almost immediately from the anion-exchange resin, indicating that the resin was almost exhausted. The cation-exchange resin still retained most of its hydrogen saturation after the adsorption run because it took more than 80 ml of 1.0 M NaOH to make the resin basic so that desorption occurred. This difference in column saturations is related to the acid pH of the standard samples and to the differences in adsorptive capacities of the two resins.

The results of this desorption experiment indicate that hydrophilic DOC compounds can be quantitatively desorbed from the ion-exchange resins; however, the extensive resin purification procedure and the large quantities of inorganic salts desorbed with the organic solutes, which cause difficulties with DOC determinations, are limiting factors for the direct determination of hydrophilic acids and bases on desorbed DOC fractions. Quantification of hydrophilic base and acid DOC by desorption of the concentrated fractions into a small volume of eluent should be attempted only in cases where hydrophilic DOC concentrations are below the lower limits of DOC analysis. In this case, adsorption DOC analysis, which is the difference of two low DOC concentrations, is meaningless as compared to the experimental error.

Two experiments were conducted whereby mixtures of hydrophobic and hydrophilic organic solute standards were prepared in solutions containing inorganic solutes of the type and concentrations found in natural waters, and these standard solutions were fractionated on the XAD and ion-exchange macroreticular resins to determine if the DOC fractionation procedure could separate the individual compounds of the organic solute mixture. The results are presented in table 6.

Standard sample 1 fractionated in the first experiment contained an organic solute representative for each of the six fractions. Theoretically, the mixture should have an initial DOC concentration of 18 mg/l, and each fraction should contain 3 mg/l DOC. All the fraction DOC values fell within 0.5 mg/l of the theoretical values except for the hydrophobic acid DOC value, which was 1.5 mg/l too low, and the hydrophilic base DOC, which was 1.1 mg/l too high. This experiment was repeated, and the same results were obtained. The deficit in hydrophobic acid DOC was made up by a surplus in hydrophilic base DOC. One possible explanation is that the hydrophobic acid representative, benzoic acid, reacted with the hydro-

TABLE 6.—*DOC fractionation analysis of hydrophobic and hydrophilic organic solute standards*

	Compound	DOC concentration (mg/l)	Concentration (mg/l)
Standard sample 1 [pH, 6.9; specific conductance, 1,700 μmhos/cm at 25°C]			
Organic solute standards:			
Hydrophobic acid	Benzoic acid	3	---
Hydrophobic neutral	p-Methylbenzyl alcohol	3	---
Hydrophobic base	Quinoline	3	---
Hydrophilic acid	Acetic acid	3	---
Hydrophilic neutral	Sucrose	3	---
Hydrophilic base	Ethylenediamine	3	---
Inorganic solutes	Na_2SO_4	-	502
	$CaCl_2 \cdot 2H_2O$	-	803
	$NaHCO_3$	-	134
Initial solution	Organic and inorganic compounds.	17.5	---
DOC fractions:			
Hydrophobic acid solutes		1.5	---
Hydrophobic neutral solutes		3.4	---
Hydrophobic base solutes		2.6	---
Hydrophilic acid solutes		3.5	---
Hydrophilic neutral solutes		2.4	---
Hydrophilic base solutes		4.1	---
Standard sample 2 [pH, 6.7; specific conductance, 1,700 μmhos/cm at 25°C]			
Organic solute standards:			
Hydrophobic amphoteric solute	Quinaldic acid	5	---
Hydrophilic amphoteric solute	Glycine	5	---
Inorganic solutes	Na_2SO_4	-	492
	$CaCl_2 \cdot 2H_2O$	-	787
	$NaHCO_3$	-	181
Initial solution	Organic and inorganic compounds.	9.8	---
DOC fractions:			
Hydrophobic acid solutes		0.7	---
Hydrophobic neutral solutes		.2	---
Hydrophobic base solutes		.1	---
Hydrophilic acid solutes		0	---
Hydrophilic neutral solutes		0	---
Hydrophilic base solutes		9.0	---

philic base representative, ethylenediamine to produce a solute complex which acts as a hydrophilic base.

The second experiment was conducted to determine the behavior of amphoteric organic solutes in DOC fractionation analysis. Quinaldic acid was selected as the hydrophobic amphoteric solute, and the amino acid, glycine, was selected as the hydrophilic amphoteric solute. The results given in table 6 show that almost all the DOC from these two compounds appear in the hydrophilic base DOC fraction. Apparently, the quinaldic acid does not adsorb on the hydrophobic XAD resins because the molecule retains an ionic charge either on the acid or base functional groups throughout the pH range used in this experiment. Both amphoteric compounds are determined as hydrophilic bases rather than hydrophilic acids simply because the cation-exchange resin is placed ahead of the anion-exchange resin in the DOC fractionation analytical scheme. Therefore, in natural waters, it is likely that amphoteric organic solutes and the bulk of organic nitrogen will be found in the hydrophilic base fraction.

Addition of the hydrophilic solute fractionation scheme completes the analytical development of DOC fractionation analysis. The previous two experiments indicated that reasonable recoveries and readily interpretable results can be obtained by applying DOC fractionation analysis to organic solutes in standard solutions. The presence of inorganic solutes has little apparent effect upon the results of DOC fractionation analysis.

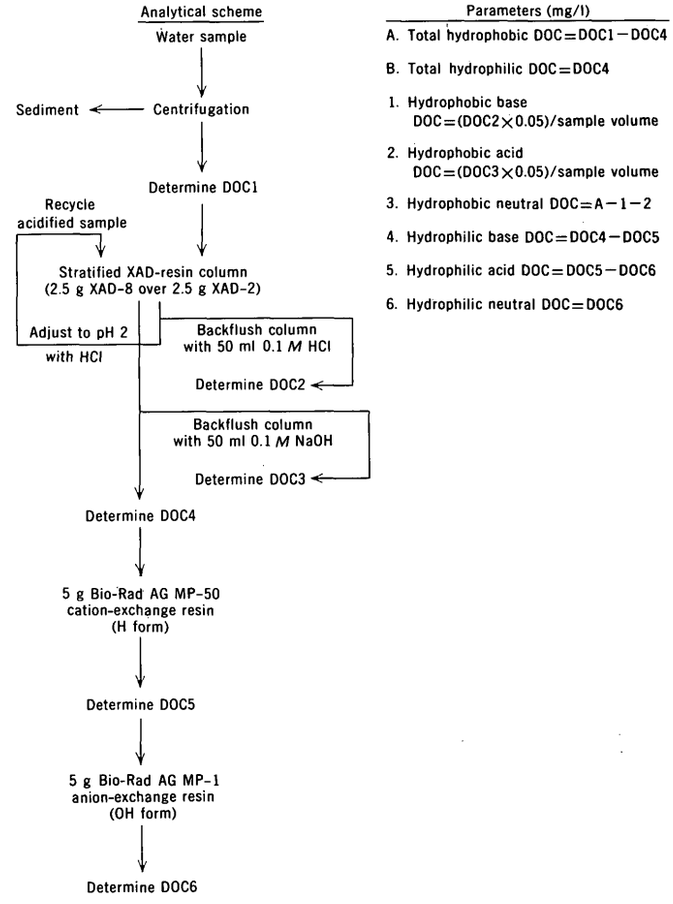

FIGURE 3.—Dissolved organic carbon (DOC) fractionation analysis.

Final analytical fractionation scheme

The final analytical fractionation scheme for dissolved organic carbon fractionation analysis is presented in flow-chart form in figure 3. Many modifications of this scheme were tried during the research described above, but the scheme presented in figure 2 has the widest range of applicability to natural water samples as judged by the experience obtained through running a wide range of natural water samples.

Two litres of water should be collected in organic-free glass containers to insure a sufficient sample for analysis. Samples should be preserved during the shipment from the field to the laboratory by chilling the samples on ice to 4°C. Immediately upon receipt of the samples in the laboratory, suspended sediment should be removed by centrifugation such that all particulate matter less than 0.1 μm in diameter is removed based upon the dimensions and density of clay mineral particles. A continuous-flow, air turbine-driven, super centrifuge was used at a centrifuge speed of 25,000 revolutions per minute which generated a force equal to 15,000 times the normal gravity at sea level. A flow rate of 100 ml/min removes sediment whose diameter is greater than 0.1 μm and whose specific gravity is greater than 1.65 grams per cubic centimetre (Jackson, 1956). All solutes remaining in the water sample after centrifugation are arbitrarily called dissolved despite the fact that there is no discrete break between the particulate and dissolved states of matter. About 0.1 gram of sodium azide should be added per litre of water after centrifugation to prevent bacterial growth.

DOC 1 quantifies the total concentration of organic solutes in the sample. If the sample is above pH 6.5, the sample is pumped through the stratified XAD resin column at a flow rate of 4.0 ml/min without pH adjustment. The hydrophobic bases and neutrals are adsorbed during this first pass through the column. If the pH is below 6.5, it is adjusted to pH 7 with NaOH before the sample is passed through the stratified column. Hydrophobic bases become protonated in acidic solutions and are not adsorbed on the XAD resins. Adjustment of the pH to 10 is not advocated with

natural water samples because of the carbonate and hydroxide precipitates which often result. Hydrophobic bases are desorbed after the entire sample has passed through by backflushing the column with 0.1 *M* HCl at a flow rate of 2 ml/min. Backflushing was found to be necessary for desorption of high-molecular-weight organic solutes which tended to foul the XAD–2 resin if forward elution was used.

Following the base desorption procedure, the XAD-resin column is connected in series with the cation- and anion-exchange resin columns. The pH of the sample is adjusted to pH 2 with HCl so that the hydrophobic acids would adsorb, and the sample is pumped through all three columns arranged in series. It is necessary to recycle the sample through the same stratified XAD resin column after pH adjustment because certain weak hydrophobic acids adsorb during the first pass through the column and should be included when the acids from the column are later desorbed. Aliquots for DOC and specific conductance are taken at the exits of the cation- and anion-exchange columns after 200 to 300 ml of sample has passed through the columns. If the specific conductance of the sample exceeds 2,000 μmho/cm at 25°C, aliquots should be taken sooner so that the ion-exchange capacities of these columns are not exceeded before the aliquots are taken. The ion-exchange columns are disconnected from the XAD resin column after the aliquots are taken, and the remainder of the acidified sample is pumped through the XAD resin column. After the sample has been completely recycled through the XAD resin column, the hydrophobic acids are desorbed by backflushing the column with 50 ml of 0.1 *M* NaOH. The calculations of the various DOC fractionation parameters are also presented in figure 3.

This analytical scheme for DOC fractionation analysis is directly applicable to natural water samples whose DOC concentrations range between 5 and 25 mg/l. Samples containing less than 5 mg/l DOC can be run through the analytical scheme, but the results will be subject to relatively high errors which arise primarily from the variance of the DOC determination at low DOC concentrations. Samples containing greater than 25 mg can be separated satisfactorily, but less than 1 litre of sample should be fractionated so that the adsorptive capacities of the resins are not exceeded.

APPLICATIONS

Selective adsorption of organic solutes upon macroreticular resins can be used for preparative purposes to extract and fractionate organic solute and organic-inorganic solute complexes from aqueous solution so that these solutes can be characterized (table 4). An equally important use is the application to characterize organic solutes with respect to their DOC fraction ratios. The following two examples will illustrate two applications of DOC fractionation analysis.

Two ground-water samples were collected near Hanna, Wyo., and were subjected to DOC fractionation analysis to determine changes in organic solute composition when a coal seam about 90 m below land surface was ignited in a U.S. Bureau of Mines in situ coal gasification experiment (Campbell and others, 1974). When the burn was extinguished, ground water flooded the burned zone and became contaminated with organic solute combustion products. The data are presented in table 7. Sample 1 is uncontaminated ground water withdrawn from the coal seam outside the burned area. Sample 2 is contaminated ground water withdrawn from a well in the center of the burned area. These two samples were only passed through the hydrophobic solute fractionation scheme because the hydrophilic solute fractionation scheme was not yet developed.

The data presented in table 7 could be interpreted in the following manner. The greater ratios of hydrophobic/hydrophilic acids in sample 1 most likely indicate that the DOC of the uncontaminated sample is more hydrocarbon (hydrophobic) in nature and is at a lower oxidation state as compared to the contaminated sample 2. Most likely, the combustion of the coal during gasification gave rise to organic solutes with a higher oxidation state (more acids) and a greater polar functional group content (more hydrophilic) as compared to the organic solutes in the uncontaminated ground water. The elemental carbon which resulted from the carbonization of coal during gasification may also have adsorbed a portion of the hy-

TABLE 7.—*DOC fractionation analysis of Wyoming groundwater samples*

	Sample 1 (uncontaminated)	Sample 2 (contaminated)
Specific conductance ---------- μmho/cm at 25°C	1,050	2,050
pH ---------- units	8.0	8.4
Initial DOC ---------- mg/l	42.0	22.0
Hydrophobic DOC ---------- mg/l	26.0	11.0
Hydrophilic DOC ---------- mg/l	16.0	11.0
Hydrophobic acid DOC ---------- mg/l	10.5	8.6
Hydrophobic neutral DOC ---------- mg/l	15.2	2.3
Hydrophobic base DOC ---------- mg/l	.3	.1
Hydrophobic DOC ---------- percent of initial DOC	61	50
Hydrophilic DOC ---------- do	39	50
Hydrophobic acid solutes ---------- percent of hydrophobic DOC	40	78
Hydrophobic neutral solutes ---------- do	59	21
Hydrophobic base solutes ---------- do	1	1

drophobic solutes in contaminated sample 2 such that the hydrophobic DOC concentration is reduced In this case, DOC fractionation analysis showed large fraction ratio changes which can be interpreted in terms of organic solute changes.

The second example illustrates an application to studies involving organic-inorganic complexes. Certain ground-water samples collected near Golden, Colo., were found to contain high concentrations of DOC and selenium (R. Moran, oral commun., 1975). An experimental procedure based on DOC fractionation analysis was designed to also observe selenium fractionation both in the natural ground water and in a synthesized water sample that contained similar concentrations of selenium and other inorganic solutes with no DOC. Comparison of the data for these two samples should allow certain conclusions about the association between DOC and selenium. These data are presented in table 8.

These data clearly show that only very minor amounts of selenium were associated with the hydrophobic organic solute fractions which compose 58 percent of the total DOC. Almost all of the selenium was adsorbed from both samples as an anion on the anion-exchange resin. It is possible that selenium is associated with the hydrophilic acid DOC, but because the fractionation of selenium in sample 2, which contained only inorganic solutes, is identical to the selenium fractionation of ground-water sample 2, it is most likely that selenium in the ground water is not directly associated with organic solutes. This is not a surprising conclusion because most organic acid solutes and selenium solutes have anionic natures, which tend to discourage complex formation.

TABLE 8.—*DOC fractionation analysis and selenium fractionation analysis of Colorado ground-water sample*

	Sample 1 (ground-water)	Sample 2 (Se standard)
Specific conductance ---------- μmho/cm at 25°C--	4,300	4,800
pH ---------- units--	7.1	7.5
Initial Se ---------- μg/l--	200	240
Initial DOC ---------- mg/l--	10.0	0
Hydrophobic DOC ---------- mg/l--	5.8	0
Hydrophilic DOC ---------- mg/l--	4.2	0
Hydrophobic acid DOC ------ mg/l--	3.4	0
Hydrophobic neutral DOC --- mg/l--	2.4	0
Hydrophobic base DOC ------ mg/l--	0	0
Hydrophilic acid DOC ------- mg/l--	3.7	0
Hydrophilic neutral DOC ---- mg/l--	0.5	0
Hydrophilic base DOC ------- mg/l--	0	0
Se after hydrophobic base and neutral DOC extraction---------- μg/l--	200	380
See after hydrophobic acid DOC extraction ---------- μg/l--	240	240
Se after hydrophilic base DOC extraction ---------- μg/l--	260	300
Se after hydrophilic acid DOC extraction ---------- μg/l--	6	12
Se found in hydrophobic acid DOC extract ---------- μg/l--	1.3	------
Se found in hydrophobic neutral DOC extract ---------- μg/l--	0	------

These studies have shown how organic solutes can be classified, fractionated, and analyzed by use of macroreticular resins to produce meaningful data without resorting to highly complex organic analyses. For certain purposes, highly complex analyses are necessary to identify the various organic compounds found in natural waters. However, many needs can be satisfied by DOC fractionation analysis, which characterizes organic solutes to the third level of the classification scheme of figure 1.

REFERENCES CITED

American Society for Testing and Materials, 1975, Annual Book of ASTM Standards—Water: Philadelphia, pt. 31, 922 p.

Baker, R. A., and Malo, B. A., 1967, Water quality characterization—Trace organics: Jour. Sanitary Engineering Div., ASCE, v. 93, no. 6, p. 41–54.

Bartell, F. S., and Lloyd, L. E., 1938, Alteration of adsorption properties of charcoal: Activation of charcoal in different gases at different temperatures: Am. Chem. Soc. Jour., v. 60, p. 2120–2125.

Burnham, A. W., Calder, G. V., Fritz, J. S., Junk, G. A., Svec, H. J., and Willis, R., 1972, Identification and estimation of neutral organic contaminants in potable water: Anal. Chemistry, v. 44, no. 1, p. 139–142.

Burnham, A. K., Calder, G. V., Fritz, J. S., Junk., G. A, Svec, H. J., and Vick, R., 1973, Trace organics in water—Their isolation and identification: Am. Water Works Assoc. Jour., v. 65, no. 11, p. 722–725.

Campbell, G. G., Brandenburg, C. F., and Boyd, R. M., 1974, Preliminary evaluation of underground coal gasification at Hanna, Wyo.: U.S. Bur. Mines Tech. Prog. Rept. 82, 14 p.

Christman, R. F., and Hrutfiord, B. F., 1973, Water-quality standards for organic contaminants: Analytical limitations and possibilities: Water Quality Conf., 15th Urbana, Ill., 1973, Proc., p. 63–72.

Forbes, G. S., and Anderson, G. W., 1928, Phase-equilibrium data for condensed systems containing two liquid phases with a third component in distribution equilibrium between them, the two liquid phases being practically nonmiscible; distribution coefficient: Internat. Critical Tables, v. 3, p. 418–435.

Gast, J. A., and Thompson, T. G., 1958, Determination of the alkalinity and borate concentration of sea water: Anal. Chemistry, v. 30, p. 1549–1551.

Goldberg, M. C., DeLong, Lewis, and Kahn, Lloyd. 1971, Continuous extraction of organic materials from water: Environmental Sci. and Tech., v. 5, no. 2, p. 161–162.

Gustafson, R. L., Albright, R. L., Heisler, J., Lirio, J. A., and Reid, O. T., Jr., 1968, Adsorption of organic species by high surface area styrene-divinylbenzene copolymers: Indus. Eng. Chemistry Prod. Res. Devel., v. 7, no. 2, p. 107–115.

Jackson, M. L., 1956, Soil chemical analysis—advanced course: Madison, Wisconsin Univ., Dept. of Soils, p. 152–160.

Junk, G. A., Richard, J. J., Grieser, M. D., Witiak, J. L., Arguello, M. D., Vick, R., Svec, H. J., Fritz, J. S., and Calder, G. V., 1974, Use of macroreticular resins in the analysis of water for trace organic contaminants: Jour. Chromatography, v. 99, p. 745–762.

Kun, K. A., and Kunin, Robert, 1968, Macroreticular resins—III, Formation of macroreticular styrene-divinylbenzene copolymers: Jour. Polymeric Sci., v. 6, pt. A–1, p. 2689–2701.

Leenheer, J. A., and Malcolm, R. L., 1973, Fractionation and characterization of natural organic matter from certain rivers and soils by free-flow electrophoresis: U.S. Geol. Survey Water-Supply Paper 1817–E, 14 p.

Malcolm, R. L., Leenheer, J. A., McKinley, P. W., and Eccles, L. A., 1973, Organic carbon, *in* Goerlitz, D. F., and Brown, Eugene, eds., Methods for analysis of organic substances in water—Supplement II: U.S. Geol. Survey Techniques Water Resources Inv., book 5, chap. A3, 34 p.

Malcolm, R. L., and Leenheer, J. A., 1973, The usefulness of organic carbon parameters in water-quality investigations: Anaheim, Calif., Inst. Environmental Sci. Proc., April 1973, p. 336–340.

Rieman, W., and Walton, H. F., 1970, Ion exchange in analytical chemistry: New York, Pergamon Press, p. 197–203.

Simpson, R. M., 1972, The separation of organic chemicals from water: Philadelphia, Rohm and Hass, 26 p.

Ward, T. M., and Getzen, F. W., 1970, Influence of pH on the adsorption of aromatic acids on activated carbon: Environmental Sci. and Technology, v. 4, no. 1, p. 64–67.

Jour. Research U.S. Geol. Survey
Vol. 4, No. 6, Nov.-Dec. 1976, p. 753–756

LIQUID SCINTILLATION COUNTING OF FILTERED ALGAE IN PRIMARY PRODUCTION STUDIES

By DOYLE W. STEPHENS, Bay Saint Louis, Miss.

Abstract.—A technique for preparing phytoplankton samples for liquid scintillation counting and standardization has been developed. It consists of digestion of the carbon-14 labeled algae on small, inert filters coupled with a filter standardization and channels ratio method of efficiency determination. The technique is an alternative to many currently used methods which result in two-phase systems whose counting efficiency cannot be easily determined. Although it does not produce a purely homogeneous solution, the proposed technique does allow for a more accurate determination of counting efficiency within the usual range of application in eutrophic or saline water.

Liquid scintillation has been recognized as a workable and accurate method of determining photosynthetically fixed carbon-14 in primary production studies (Ward and Nakanishi, 1971). However, several problems exist in the techniques of preparation of samples and of determination of counting efficiencies used by the U.S. Geological Survey (Slack and others, 1973) and earlier workers (Wolfe and Schelske, 1967; Lind and Campbell, 1969). Samples prepared according to these techniques exhibit considerable phase separation which makes it difficult to determine the counting efficiency accurately when the weight of the filtered material exceeds 1 milligram (Pugh, 1973). In addition, the use of carbon-14 toluene as an internal standard only estimates counting efficiency for a radioisotope that distributes itself homogeneously throughout the fluor. It does not indicate the counting efficiency for suspended or nondissolved material.

The method currently used by the Survey suggests filtering the sample containing carbon-14 labeled algae, unincorporated carbon-14 carbonate, and water through a 47-millimetre membrane filter having a porosity of 0.45 micrometre. The filter and residue are then washed with 0.1 *N* hydrochloric acid and rinsed with filtered lake water. The filter is removed from the holder and rolled algal side inward to form a cylinder which is then placed upright in a liquid scintillation vial containing 0.10 millilitre of NCS basic solubilizer (Amersham/Searle Corp., Arlington Heights, Ill.) to absorb any CO_2 evolved before the addition of the scintillation cocktail. Prior to counting, 18 ml of a standard scintillation cocktail (PPO and POPOP in Triton-X and para-xylene) are added. After counting, 100 microlitres of carbon-14 toluene standard are added to 20 percent of the samples, and the contents of the vials are recounted. The counting efficiency is then calculated from the average difference between the samples counted before and after the addition of the labeled standard.

The counting efficiency for nonhomogeneous samples is difficult if not impossible to determine accurately. Self-absorption by cells, filters, and fragments is not predictable, and most currently used standardization procedures are applicable only to homogeneous samples (Bush, 1968; Pugh, 1970). Pugh (1970) stated that the use of carbon-14 toluene as an internal standard to determine counting efficiencies for whole filters is erroneous because it only estimates the counting efficiency of dispersed material in the solution. He recommended that a filter standardization method using a toluene insoluble standard such as carbon-14 sucrose be implemented to construct a channels ratio curve. The channels ratio curve is constructed by recording counts on two channels and plotting their calculated ratio against the counting efficiency for a standard series of carbon-14 labeled algal filters. It was noted that as increasing amounts of algal material were filtered, efficiencies as determined by internal and external standardizations declined slightly. Using the filter standardization method and channels ratio counting, he found that large amounts of material on the filter actually resulted in an order of magnitude decrease in efficiency over that obtained from internal and external standards. Pugh concluded that the presence of the filter and cellular material had an absorptive effect which could not be detected by using external and internal standards. He stated that the filter standardization method apparently corrected for the self-absorption and quenching caused by the intact filter and cells within the vial.

It should be noted that Pugh (1970) was still working with a heterogeneous system consisting of intact algae on a membrane filter with a diameter of 50 mm. The filter standardization method works fairly well when small amounts of phytoplankton are present because self-absorption by algal cells is minimal. In a more recent paper, Pugh (1973) stated that the filter standardization method was accurate only when the weight of phytoplankton on the filter was less than 1 mg.

Bush (1968) proposed a double channels ratio technique to determine homogeneity within a sample based upon the fact that efficiency for counting a radioactive sample is dependent upon the degree of quenching and upon the extent to which the sample is in solution, whereas the efficiency of counting an external standard is dependent only upon quenching. An external standard or suitably quenched series of internal standards can therefore be used to measure quenching independent of the efficiency with which the sample is being counted. If the channels ratio of the sample counts indicates a counting efficiency equal to that of the external standard, the sample is a true solution, and efficiency can be accurately determined by using the double channels ratio. If part of the sample is not in solution, the emission spectrum will be degraded because of absorption and scattering, and the sample channels ratio will be shifted in a direction indicating greater quenching. It will not indicate the same efficiency as the external (or quenched) internal standards.

EXPERIMENTAL PROCEDURE

As part of a study on primary production in the Great Salt Lake, Utah (Stephens and Gillespie, 1976), several techniques were investigated that would produce homogeneous samples from filtered material consisting of extremely halophyllic algae. The suitability of the filter standardization method for the determination of counting efficiency within these samples was evaluated. The techniques that evolved were modifications of the double channels ratio techniques of Bush (1968) and the filter standardization technique of Pugh (1970, 1973).

The inoculation and incubation procedures presented in Slack and others (1973) were used to obtain the carbon-14 labeled phytoplankton. A subsample of 20 to 200 ml was removed from the BOD (biochemical oxygen demand) bottles and filtered to dryness using a microanalysis assembly stainless steel support screen and 25-mm Celotate filters (Millipore Corp., Bedford, Mass.) having a porosity of 0.5 μm. An alkali resistant filter such as Celotate was used to prevent digestion of the filter and resultant chemical quenching caused by filter fragments as reported by Pugh (1973). The algal-filter complex was then rinsed with 5 ml of 0.1 *N* hydrochloric acid allowing a 2-minute contact time. The final 5-ml rinse consisted of filtered lake water, again filtering to dryness. The filter was removed from the holder with forceps and placed, algal side up, in the bottom of a standard glass scintillation vial. One millilitre of NCS solubilizer was then added to the vial. The vials were capped with polyethylene-lined caps to prevent the reaction of aluminum-lined caps and the solubilizer which results in color quenching. Following a 24-hour period in which digestion of the algae occurred, 10 ml of a standard liquid scintillation cocktail consisting of 5 grams of PPO plus 0.2 g of POPOP per litre toluene were added and the samples dark-adapted 24 hours prior to counting.

A standard calibration curve was then prepared from a set of filter standards which were counted by using a double channels ratio method of quench determination. The filter standards were prepared by filtering varying amounts of an algal culture, similar to those in the wild population, onto 25-mm Celotate filters with a porosity of 0.5 μm. The filters were pulled to dryness but not allowed to air dry completely in order to prevent rapid volatilization of carbon-14 as reported by Wallen and Geen (1968). The damp filters were removed from the filter apparatus, and 50 μl of carbon 14-thymine or sucrose providing a specific activity of 5×10^4 dpm (disintegrations per minute) were added. Labeled thymine, sucrose, or the equivalent was used because they are insoluble in toluene and react to basic digestion in the same manner as algal cells. The damp filters were then placed algal side up in the bottom of standard liquid scintillation glass vials and covered with 1 ml of the quaternary ammonium base solubilizer, NCS. The vials were closed with polyethylene-lined caps, and the algae were allowed to digest at room temperature overnight. It was found that complete lysis of the majority of algal cells occurred over an 8-hour interval without damage to the filter. Following digestion, 10 ml of scintillation cocktail (5 g of PPO plus 0.2 g of POPOP per litre toluene) were added. Each of the vials was counted on a liquid scintillation spectrometer at 25°C for 5 to 10 minutes after dark-adapting in the counter for 24 hours. All counts are made in triplicate but not in succession, and their average was taken. The channels ratio curve was constructed by recording counts on two channels set to discriminate a band of approximately 95 percent of pulse energy using wide window settings. Several discriminator settings were tested to select a combination that would produce a linear channels

ratio calibration curve. A linear relationship for the Packard Tri-Carb instrument was obtained by setting the count monitoring channel for a very wide window of 50/1000 and the quench monitoring channel at a narrower window of 80/1000. A gain setting of 9 percent provided satisfactory counts per minute while not overly broadening the carbon-14 pulse peak. A plot of the channels ratio, (80/1000)/(50/1000), versus the counting efficiency (cpm/dpm) was constructed and counting efficiencies for subsequent samples were determined by comparison of their channels ratio with the standard curve. Once a suitable channels ratio calibration curve is prepared for a scintillation spectrometer, it should be valid until counting geometry, instrument settings, or sample preparation is altered.

DISCUSSION

This technique was evaluated by using laboratory cultures of the alga *Dunaliella viridis* isolated from the Great Salt Lake, Utah. Efficiencies as determined by the filter standardization method and the internal standardization method gave comparable results when either dry or wet filters were used (table 1). However, slight decreases in efficiency due to quenching produced by water in the wet filter were noted. Analyzing the results in terms of the double channels technique of Bush (1968) indicates that, over the entire range of digested weights of algae, the samples do not constitute homogeneous solutions and that the filter standardization method could not be used to accurately predict counting efficiencies. However, when less than 4 mg of algae are present on the filter, the self-absorption effects of the complex are negligible, and filter standardization does allow a fairly accurate determination of counting efficiency, a conclusion also substantiated by Pugh (1973).

Channels ratio curves (fig. 1) were constructed for the filter standardization samples and for a homogeneous solution. The channels ratio curve representing a homogeneous solution was prepared from the net counts resulting from the addition of carbon-14 toluene to the filter standardization samples. There is good agreement between the two curves until the channels ratio drops below 0.60. Self-absorption by the digested algae filter complex becomes very significant at this point, and counting efficiency cannot be accurately determined.

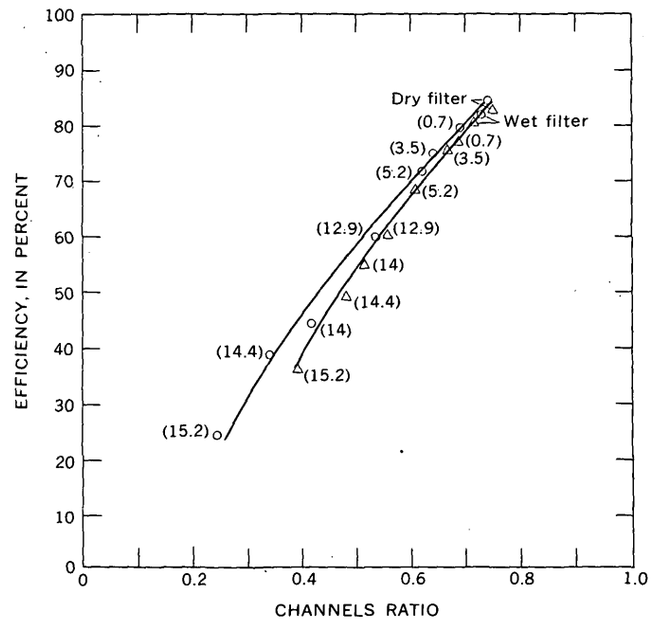

FIGURE 1.—Channels-ratio calibration curves. Filter standardization curve (o) is calculated from filtered and digested algae with carbon-14 thymine as the standard. Solution standardization curve (△) is calculated from filtered and digested algae with carbon-14 toluene standard added directly to scintillation cocktail. Numbers in parentheses refer to weights, in milligrams, of algae on the filters.

TABLE 1.—*Efficiency for liquid scintillation counting of carbon-14 thymine as a filter standardization and carbon-14 toluene as a solution standardization*

[Inert 25-mm diameter filters were coated with varying weights of the alga *Dunaliella viridis* and digested with a quaternary ammonium base]

Cell dry weight (mg)	Counting efficiency (percent)	
	Filter standardization	Solution standardization
Dry filter only: 0	84	83
Wet filter only:		
0	81	80
0.7	78	77
3.5	76	76
5.2	71	68
12.9	60	60
14.0	44	56
14.4	38	50
15.2	25	36

The limitations imposed upon the algal digestion technique by the need for accurate determination of the counting efficiency does not pose an extreme problem. The volume of subsample filtered should provide about 1,000 cpm for the light bottles and 100 cpm for the dark bottles; seldom does this volume result in a deposit of more than 3 mg of algae on the filter. With moderate algal populations, inoculation of 300-ml production bottles with 3 to 5 microcuries of carbon-14 carbonate followed by a 4- to 5-hour incubation period, and filtration of a 20-ml subsample yields suitable counts and allows an accurate determination of counting efficiency. Samples high in suspended solids such as sediments may require pretreatment to remove substances not susceptible to hydroxide digestion.

CONCLUSION

It is concluded that basic digestion of less than 4 mg of phytoplankton on small, inert filters produces a sample of almost homogeneous composition under most routine conditions. Use of an alkali resistant filter (such as Celotate) eliminates the excessive quenching noted by Pugh (1973) that results from the dissolution of the filters. The proposed filter standardization procedure and a double channels ratio method of quench determination would allow a more accurate calculation of counting efficiency than currently exists in techniques which count intact algae on large-diameter filters.

REFERENCES CITED

Bush, E. T., 1968, A double ratio technique as an aid to selection sample preparation procedures in liquid scintillation counting: Internat. Jour. Appl. Radiation and Isotopes, v. 19, p. 447–452.

Lind, O. T., and Campbell, R. S., 1969, Comments on the use of liquid scintillation for routine determination of ^{14}C uptake in production studies: Limnology Oceanography, v. 14, no. 5, p. 787–789.

Pugh, P. R., 1970, Liquid scintillation counting of ^{14}C-diatom material on filter papers for use in productivity studies: Limnology Oceanography, v. 15, no. 4, p. 652–655.

——— 1973, An evaluation of liquid scintillation counting techniques for use in aquatic primary production studies: Limnology Oceanography, v. 18, no. 2, p. 310–319.

Slack, K. V., Averett, R. C., Greeson, P. E., and Lipscomb, R. G., 1973, Methods for collection and analysis of aquatic biological and microbiological samples: U.S. Geol. Survey Techniques Water-Resources Inv., book 5, chap. A4., 165 p.

Stephens, D. W., and Gillespie, D. M., 1976, Phytoplankton production in the Great Salt Lake, Utah and a laboratory study of algal response to enrichment: Limnology Oceanography. v. 21, no. 1, p. 74–87.

Wallen, D. G., and Geen, G. H., 1968, Loss of radioactivity during storage of carbon-14 labeled phytoplankton on membrane filters: Jour. Fishery Res. Board., Canada, v. 25, no. 10, p. 2219–2224.

Ward, F. J., and Nakanishi, Masami, 1971, A comparison of Geiger-Mueller and liquid scintillation counting methods in estimating primary productivity: Limnology Oceanography, v. 16, no. 3, p. 560–564.

Wolfe, D. A., and Schelske, C. L., 1967, Liquid scintillation and geiger counting efficiencies for carbon-14 incorporated by marine phytoplankton in productivity measurements: Jour. du Conseil Internat. Exploration de la Mer, v. 31, no. 1, p. 31–37.

Jour. Research U.S. Geol. Survey
Vol. 4, No. 6, Nov.-Dec. 1976, p. 757–764

FIELD RECALIBRATION OF RADIOMETERS BY USING THE SHADING TECHNIQUE

By ALAN P. JACKMAN and RICHARD D. NOBLE, Menlo Park, Calif.

Abstract.—Use of radiometers to measure radiant energy components in energy budgets is widespread in water-resources studies. Previous experience has shown that readings of radiometers may contain substantial errors. These errors may be due to deterioration of the instrument during use and (or) inaccurate initial calibration. Both of these errors may be detected and corrected by proper field recalibration. After 10 months in the field, two Beckman-Whitley total hemispherical radiometers and one Eppley pyranometer were recalibrated by using the shading technique. The working standard was an Eppley pyrheliometer. Errors as great as 38 percent were discovered. New calibration constants were determined for all three field instruments. The shading technique is a rapid, accurate method of recalibrating under field conditions. It is important that the working standard be directly traceable to a primary standard which has participated in the International Comparisons of Pyrheliometers. With an accurate working standard and careful technique, very accurate field recalibration is possible.

Radiometers, devices used to measure the intensity of incident radiant energy, have been widely used in experimental water-resources investigations for the past 25 years. Evaporation of water from both soils and open water bodies may be estimated using the "energy-budget" technique (E. R. Anderson, 1954). With this technique, the heat lost by the system due to evaporation is calculated as the difference between the total energy gained by the system during a period of time and the net radiation and conduction gains by the system during the same period. Since conduction gain is usually calculated from the evaporation by means of Bowen's ratio, measurement of total energy gained by the system and net energy gained by radiation are crucial to the accuracy of the evaporation estimated. The former may be very accurately determined by simple temperature measurements. The latter must be determined using radiometers.

In addition to evaporation and evapotranspiration studies, radiometry is now being used to construct energy budgets for prediction of snowpack melt and for prediction of temperatures in rivers and streams. It is also used in studies of photosynthetic activity. Currently it is being used extensively in studies of solar heating and refrigeration.

There are several basic types of radiometers currently available. Most measure the radiation incident on a horizontal surface from all directions in the hemisphere above the horizon (hemispherical radiometers). Some measure the difference between incident radiation from the hemisphere above the horizon and that below the horizon (net radiometers). A few special-purpose radiometers measure radiation only from a very narrow cone rather than a hemisphere. Such radiometers are termed normal incidence radiometers or pyrheliometers.

With each of the above types it is possible to measure radiation within some specified band of wavelengths. Radiometers which respond to all frequencies are referred to as total radiometers. Frequently instruments are built to respond only to light in the visible range; that is, 300 to 1,000 nanometers. Such radiometers are referred to as "solar" radiometers since this is the band of wavelengths transmitted from the Sun through the atmosphere. Recently, instruments which measure only in the infrared part of the spectrum have become available.

For energy-budget studies, where one is interested in the difference between the incoming and outgoing radiation of all wavelengths, the net radiometer which senses all wavelengths is advantageous. This avoids the necessity of determining the reflectivity and emissivity of the surface being studied. Both reflectivity and emissivity may depend on wavelength and angle of incidence or emission.

For certain well-characterized surfaces such as water it is possible to use a hemispherical radiometer. In this case the amount of energy reflected from and emitted by the surface must be calculated. Emission follows the Stefan-Boltzmann law, $H_b = \sigma \epsilon T^4_w$ where $\sigma = 5.66961 \cdot 10^{-8}$ W m^{-2} K^{-4} ($8.14 \cdot 10^{-11}$ ly min^{-1} K^{-4}), $\epsilon \cong 0.97$ (E. R. Anderson, 1954), and T_w is the actual

temperature of the water surface.[1] Reflection is a very small fraction of the incident radiation at high solar angles and may be calculated theoretically from the Fresnel formula or empirically from charts prepared by E. R. Anderson (1954). It should be noted that these methods may be inadequate for shallow water bodies where substantial bottom reflection may occur.

There are a number of empirical formulas which allow the estimation of the incoming infrared (longwave) radiation. Such formulas have been discussed by Kondrat'ev (1965) and Sellers (1965) among others. If one is willing to accept the uncertainties inherent in such estimations, it becomes practical to calculate the radiation energy budget for a water surface measuring only the solar hemispherical radiation. The net radiation received by the water surface would be the solar hemispherical radiation corrected for reflection plus the calculated incoming infrared radiation corrected for reflection minus the infrared radiation emitted by the surface as calculated by the Stefan-Boltzmann law.

Because of their ability to measure the important infrared radiation component, total radiometers have been widely used in experimental water-resources investigations. These have generally been flat-plate radiometers of the Beckman-Whitley type (formerly Gier and Dunkle) which are available in models which measure either hemispherical or net radiation. Where necessary, infrared radiation has usually been determined either by taking the difference of readings from a total radiometer and a solar radiometer or by using empirical formulas. Solar radiometers have generally been of the Eppley type. These instruments were originally used in the evaporation studies at Lake Hefner (L. J. Anderson, 1954) and Lake Mead (Koberg, 1958) and their use continues to be popular today.

Concern about the accuracy of radiometers is by no means novel. N. Yotsukura (written commun., 1975) has reported that diurnal temperature fluctuations in the Savannah River and in a canal in Colorado were overestimated by approximately 25 percent by his stream-temperature model. He concludes that these errors probably stem from inaccurate radiometer calibrations. H. E. Jobson (written commun., 1975) has reported finding errors in results from flat-plate radiometers in Southern California, particularly during periods of peak insolation.

At an even more basic level, there are questions about the accuracy of the International Pyrheliometric Scale. This scale, established in 1956, is based on an angstrom electrical compensation pyrheliometer maintained at the Davos Observatory in Switzerland. In reporting on the Third International Comparison of Pyrheliometers organized by the World Meteorological Organization, Fröhlich and others (1973) discuss the development of new absolute radiometers. They note that differences of about 1.8 percent between these instruments and the standard instrument at the Davos Observatory raise serious questions about the absolute accuracy of the International Pyrheliometric Scale.

Ignoring considerations about the absolute accuracy of the International Pyrheliometric Scale, it would appear that problems with radiometer accuracy require that workers perform frequent field calibrations to assure obtaining reasonable radiation data. Errors of 5 percent or less are probably acceptable for most hydrologic purposes. Latimer (1972) reports that such accuracy can be obtained with careful work. But errors in excess of 10 percent, as have been reported, can lead to serious errors in heat balances.

CALIBRATION METHODS

Instructions for the International Geophysical Year (IGY) (Special Committee of the International Geophysical Year, 1958) discuss two methods of field calibration. One method employs a "working standard" pyrheliometer to measure the direct component of solar radiation and a theodolite to measure solar angle. The flux of direct beam radiation incident on a horizontal surface can thus be calculated. This value may be compared with the difference between the reading of the radiometer to be calibrated while fully exposed and the reading while only the direct beam radiation is shaded (occulted). The calibration constant of the field instrument is then adjusted to obtain agreement with the vertical component of flux found from the pyrheliometer. This technique may be applied to either net or hemispherical radiometers which sense either solar or total radiation. The IGY instructions recommend use of a shading disk which subtends the same included angle seen by the pyrheliometer, usually about 100 mm in diameter if held at 1 m from the surface to be shaded. This corresponds to a 5°43′ included angle. The included angle seen by the Eppley pyrheliometer, probably the most widely used working standard instrument, is 5°43′. The IGY instructions describe the Eppley instrument as very stable and say it may be used as a working standard with occasional restandardization.

The other field calibration method is a side-by-side comparison of the field instrument with another instrument of the same type which has been reserved for this purpose. The working standard for this method requires recalibration with a frequency dependent on the stability of the type of instrument being used.

[1] Abbreviations not defined in text are explained in list before "Reference Cited."

The authors are currently engaged in a data-collection program aimed at developing an adequate model of temperatures in natural river systems. In view of the above-mentioned written communications from Yotsukura and Jobson, it was decided to check the calibrations of radiometers being used for this study: two Beckman-Whitley (B–W) flat-plate total hemispherical radiometers (Model H–188, serial Nos. 240 and 321) and one Eppley precision spectral pyranometer (Model PSP, serial No. 13184F3).

Of the above-mentioned techniques, the shading technique was selected for several reasons. First, an Eppley pyrheliometer (Model NIP, serial No. 7816E6, calibration constant = 162.6 W m^{-2} mV^{-1} or 0.2326 ly min^{-1} mV^{-1}) which has been used only as a working standard for calibration of other radiometers was available along with a solar tracking mount, a shading device, and a theodolite from the Hydrometerological Field Station at the University of California, Davis. Further, standardized versions of the field instruments were not available. Finally, the shading technique is the method chosen by Eppley Laboratory for calibration of their working standards against their group of angstrom compensation pyrheliometers which serve as their primary standards.

Figure 1 is a schematic representation of the shading apparatus used. The shading tree itself is quite cumbersome, being fabricated principally from 1½-inch steel pipe. A much smaller, lighter device would greatly facilitate field calibration.

Calibrations reported here were performed on the flat roof of a three-story office building on the campus of the University of California, Davis. No obstacles were present which could block the Sun at angles greater than 10° above the horizon. Calibrations were performed only on clear, totally cloud-free days.

The pyrheliometer was placed in an Eppley solar tracking mount. The tracker was placed on the roof near the instruments to be calibrated. The main axis of the tracker was alined north-south and the base was leveled. This only served to eliminate the need for frequent adjustment of the tracker since the pyrheliometer has an alinement spot which indicates when the aperture is pointed at the Sun.

The radiometers to be calibrated were set on a table approximately 0.75 m high. The Eppley pyranometer was leveled by using the integral leveling bubble. With the Beckman-Whitley instruments it was found that the integral bubble indicated that the instrument was level when the plate was noticeably tilted. Therefore, these instruments were leveled by setting a small carpenter's level across and along the plate support arms.

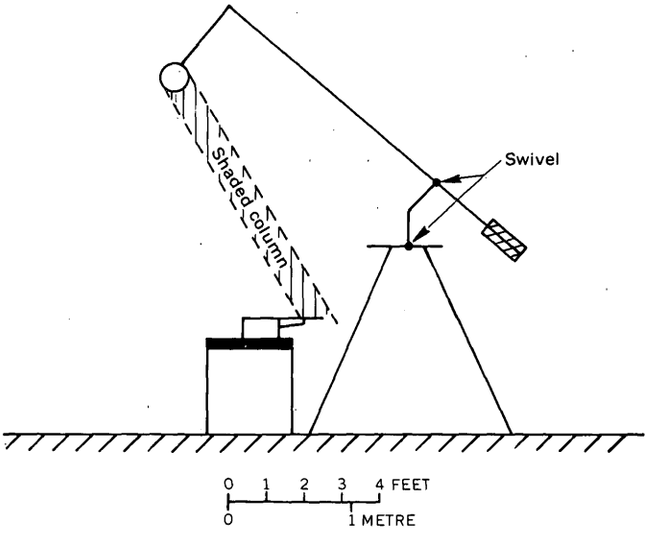

FIGURE 1.—Schematic diagram of shading apparatus.

It should be noted that improperly leveled radiometers can result in substantial errors at low solar angles.

All radiometer outputs were read on a Hewlett-Packard Model 7100B potentiometer. Zero drift was checked regularly but never required adjustment. The calibration was checked before and during data-collection runs with a Tektronix 067–502 standard amplitude calibrator. The potentiometer remained in excellent calibration throughout the studies. The flat-plate radiometers require measurement of plate temperature to calculate radiant emission from the plate and a temperature correction factor. This is done with an integral copper-constantan thermocouple. These thermocouples were read on a Honeywell Electronik 15 equipped with a cold-junction compensator.

For each observation the solar angle and the outputs of all radiometers were read as quickly as possible. The time required for this step was approximately 30 seconds. Each of the radiometers to be calibrated was then shaded in turn with the shading device. When the shaded instrument stabilized, its output was read and the next radiometer was shaded. This process required about 5 minutes where three radiometers were calibrated simultaneously. The flat-plate radiometers have considerable thermal mass and required about 90 seconds to stabilize.

With the direct radiation shaded out, only diffuse solar and atmospheric radiation is incident. Both of these components change very slowly during the day, and hence the 5-minute shading period introduces no appreciable error. The data show only small changes of the shaded reading with solar angle while unshaded reading changes considerably with solar angle.

Several checks were run to assure the adequacy of the shading disk. The pyrheliometer was shaded on several occasions and its output decreased to less than 7 W m^{-2} (0.01 ly/min). In addition, a steelplate about 0.40 by 0.60 m, held about 2 m from the radiometers, was used to shade all radiometers. This subtends a substantially greater included angle than the 5°43′ of the shading disk. There was no observable difference between the disk and the steelplate for shading the B–W radiometers. With the Eppley pyranometer, the steelplate reduced the output slightly from the output measured while shaded by the disk. This difference was less than 7 W m^{-2} (0.01 ly/min). If the steelplate was held at a distance of less than 1 m, substantial errors were observed.

RESULTS AND DISCUSSION

In comparing the radiometers to be calibrated with the pyrheliometer, it is assumed that the pyrheliometer measures that component of solar radiation which will be blocked by a shading device and further that such radiation is incident on a horizontal surface at an angle equal to the solar angle. Thus, if I_p is the flux measured by the pyrheliometer and I_s and I_u are the shaded and unshaded fluxes as measured by the hemispherical or net radiometer being calibrated, then a correctly calibrated radiometer will satisfy

$$I_p \sin \alpha = I_u - I_s \tag{1}$$

where α is the solar angle measured from the horizon.

The measured flux for a Beckman-Whitley total hemispherical radiometer is calculated as

$$I = \beta K V + \sigma T^4_p \tag{2}$$

where K is the calibration constant, V is the output voltage, σ is the Stefan-Boltzmann constant, and T_p is the plate temperature. The temperature correction factor, β, is given by

$$\beta = 1 - \frac{T_p - 80}{T_p + 675} \tag{3}$$

where T_p is measured in degrees Fahrenheit. The measured flux for an Eppley pyranometer is calculated as

$$I = K V. \tag{4}$$

If only a single observation is made, the calibration constant of the radiometer may be adjusted to force equation 1 to hold. If a larger number of observations are made, it is then necessary to use a technique such as least-mean-squares to establish the calibration factor. Least-mean-squares minimizes the sum of the squares of the deviation of measured radiation change from the measured direct radiation incident on a horizontal surface. Thus, while equation 1 will not hold exactly for any observation, it will nearly hold for all data.

On April 9-10, 1975, B–W No. 240 was calibrated against the Eppley pyrheliometer. The flat-plate radiometer had just been returned from 10 months of continuous service in the field. The plate was cleaned by washing with reagent-grade methanol but no further maintenance was attempted.

Table 1 contains the raw data along with the calculated values of direct solar radiation incident on a horizontal surface as measured by the pyrheliometer and as measured by the flat-plate radiometer (unshaded flux minus shaded flux) using the existing calibration. Figure 2 plots direct solar radiation on a horizontal surface as measured by the flat-plate radiometer versus that measured by the pyrheliometer. The solid line indicates the best least-mean-squares fit of the data.

On May 6, 1975, another calibration study was conducted. Included in this study were B–W Nos. 240 and 321, Eppley pyranometer No. 13184F3, and the Eppley pyrheliometer. Both flat-plate radiometers had been serviced before the calibration. This included cleaning the plates, cleaning the screens on the blower air intakes, and oiling the blower motors. The blower motor on No. 321 was found to have bad bearings and was replaced with another motor running at the same speed. The screens on the air intakes of both Nos. 240 and 321 were found to be seriously clogged, perhaps sufficiently to have been restricting airflow. The Eppley pyranometer received no servicing.

Results of the calibration on B–W No. 240, B–W No. 321, and the Eppley pyranometer are contained in

TABLE 1.—*Calibration data for Beckman-Whitley flat-plate radiometer. No. 240 obtained April 9–10, 1975*

[Calibration constants: 0.500 ly min^{-1} mV^{-1} for flat-plate radiometer and 0.2326 ly min^{-1} mV^{-1} for pyrheliometer]

Solar angle above horizon (degrees)	Eppley pyrheliometer reading (mV)	Beckman-Whitley				Calculated direct short-wave radiation	
		Unshaded reading		Shaded reading			
		Plate flux (mV)	Flat-plate temp (mV)	Plate flux (mV)	Flat-plate temp (mV)	Eppley pyrheliometer (ly/min)	Beckman Whitley (ly/min)
45.0	5.30	2.02	0.97	−0.20	0.83	0.87	1.14
34.0	4.85	1.35	.89	−0.28	.81	.71	.84
28.9	4.35	1.12	.47	−0.12	.40	.49	.66
35.8	4.80	1.60	.58	−0.08	.48	.65	.88
42.6	5.00	1.95	.65	−0.02	.55	.79	1.04
48.8	5.05	2.35	.73	0.05	.60	.88	1.20
54.2	5.05	2.30	.79	0.02	.63	.95	1.19
60.0	5.25	2.85	.88	0.08	.68	1.06	1.44
52.2	5.20	2.55	.87	−0.02	.69	.96	1.34
40.1	5.10	1.88	.82	−0.15	.71	.76	1.06
35.3	5.03	1.62	.81	−0.14	.71	.68	.92
29.5	4.80	1.20	.80	−0.10	.70	.55	.68
23.5	4.90	0.89	.75	−0.15	.69	.45	.54
17.5	3.93	0.52	.71	−0.14	.66	.27	.35
12.5	3.35	0.24	.66	−0.15	.64	.18	.20

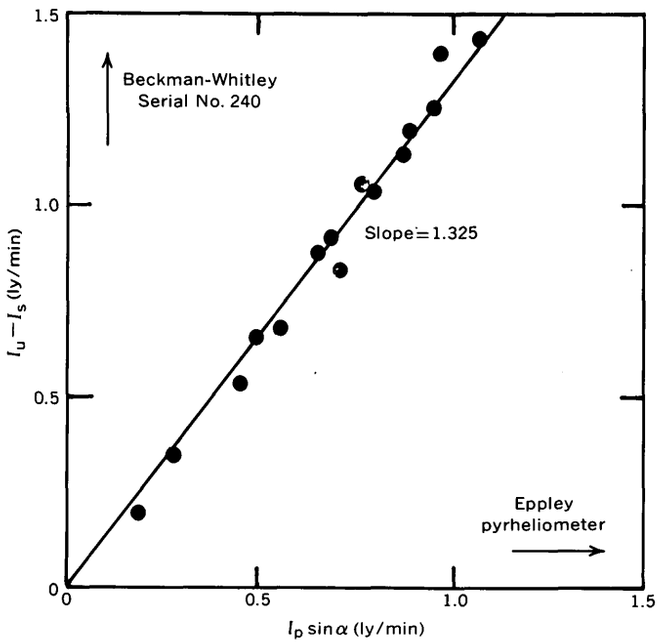

FIGURE 2.—Comparison of unshaded-minus-shaded flux observed by Beckman-Whitley radiometer No. 240 with direct flux measured by the working-standard radiometer. Data obtained April 9–10, 1975.

tables 2, 3, and 4, respectively. These results are plotted in figures 3, 4, and 5, respectively. The least-mean-squares fit of the data is shown in all figures.

The two flat-plate radiometers were last calibrated at the factory in December 1973. The calibration constants established at that time were $K=348.9$ W m^{-2} mV^{-1} (0.500 ly min^{-1} mV^{-1}) for No. 240 and $K=658.7$ W m^{-2} mV^{-1} (0.944 ly min^{-1} mV^{-1}) for No. 321. Both instruments had been in service for about 10 months. The Eppley pyranometer arrived new in May 1974 and also underwent 10 months of continuous service. It arrived with a calibration constant of 126.5 W m^{-2} mV^{-1} (0.192 ly min^{-1} mV^{-1}).

The least-mean-squares fitted lines of $I_u - I_s$ versus $I_p \sin\alpha$ give slopes of 1.336, 1.379, and 1.025 for B–W No. 240, B–W No. 321, and Eppley No. 13184F3, respectively. The slope for B–W No. 240 from the April 9–10 study was 1.325, in excellent agreement with the May 6 results, in spite of the fact that the intake screen had been clogged for the April 9–10 study.

The results from the B–W radiometers agree well with each other and from the Eppley pyrheliometer and pyranometer agree well with each other. Owing to the considerable discrepancy between the results for the two groups, it would appear that there exists a difference between the calibrations performed at the respective factories. This discrepancy raised the question of whether the pyrheliometer could be accepted

TABLE 2.—*Calibration data for Beckman-Whitley flat-plate radiometer No. 240 obtained May 6, 1975*

[Calibration constants: 0.500 ly min^{-1} mV^{-1} for flat-plate radiometer and 0.2326 ly min^{-1} mV^{-1} for pyrheliometer]

Solar angle above horizon (degrees)	Eppley pyrheliometer reading (mV)	Beckman-Whitley				Calculated direct short-wave radiation	
		Unshaded reading		Shaded reading			
		Plate flux (mV)	Flat-plate temp (mV)	Plate flux (mV)	Flat-plate temp (mV)	Eppley pyrheliometer (ly/min)	Beckman Whitley (ly/min)
53.1	4.60	2.48	.87	.25	.75	.86	1.16
65.4	4.88	3.00	1.05	.20	.89	1.03	1.44
69.8	4.98	3.00	1.12	.20	.98	1.09	1.43
65.9	4.92	2.95	1.19	.15	1.04	1.04	1.42
62.7	4.89	2.80	1.18	.19	1.04	1.01	1.32
56.8	4.80	2.54	1.15	.11	1.06	1.06	1.22
41.8	4.33	1.80	1.15	.02	1.03	.68	.91
36.2	4.25	1.50	1.08	.01	1.00	.58	.76
30.6	4.02	1.11	1.04	−.10	.98	.48	.62
24.3	3.41	.70	.98	−.12	.92	.33	.42
18.7	2.83	.35	.95	−.13	.92	.21	.25

TABLE 3.—*Calibration data for Beckman-Whitley flat-plate radiometer No. 321 obtained May 6, 1975*

[Calibration constants: 0.944 ly min^{-1} mV^{-1} for flat-plate radiometer and 0.2326 ly min^{-1} mV^{-1} for pyrheliometer]

Solar angle above horizon (degrees)	Eppley pyrheliometer reading (mV)	Beckman-Whitley				Calculated direct short-wave radiation	
		Unshaded reading		Shaded reading			
		Plate flux (mV)	Flat-plate temp (mV)	Plate flux (mV)	Flat-plate temp (mV)	Eppley pyrheliometer (ly/min)	Beckman Whitley (ly/min)
53.1	4.60	1.30	.88	.10	.77	.86	1.16
58.9	4.69	1.39	.92	.11	.79	.93	1.25
65.4	4.88	1.52	1.01	.10	.93	1.03	1.35
69.8	4.98	1.65	1.08	.10	.97	1.09	1.48
65.9	4.92	1.62	1.08	.12	.96	1.04	1.44
63.0	4.89	1.56	1.13	.12	.99	1.01	1.39
56.1	4.80	1.45	1.10	.10	1.00	.93	1.31
42.3	4.33	1.09	1.08	.05	1.03	.68	.99
35.4	4.25	.90	1.04	.01	.99	.58	.85
29.4	3.94	.67	.99	−.02	.93	.45	.68
23.4	3.40	.49	.95	−.02	.92	.31	.49
18.1	2.80	.29	.92	−.04	.89	.20	.33

TABLE 4.—*Calibration data for Eppley pyranometer serial No. 13184F3 obtained May 6, 1975*

[Calibration constants: 0.192 ly min^{-1} mV^{-1} for pyranometer and 0.2326 ly min^{-1} mV^{-1} for pyrheliometer]

Solar ange above horizon (degrees)	Eppley pyrheliometer reading (mV)	Eppley pyranometer plate flux (in millivolts)		Calculated direct short-wave radiation	
		Unshaded reading	Shaded reading	Eppley pyrheliometer (ly/min)	Eppley pyrheliometer (ly/min)
53.1	4.60	5.85	1.32	.86	.87
58.9	4.69	6.38	1.41	.93	.95
65.4	4.88	6.99	1.40	1.03	1.07
69.8	4.98	7.21	1.40	1.09	1.12
65.9	4.92	7.01	1.36	1.04	1.08
63.0	4.89	6.79	1.32	1.01	1.05
56.8	4.80	6.24	1.27	.93	.95
43.3	4.33	4.71	1.11	.68	.69
35.8	4.25	3.94	.93	.58	.58
29.8	4.02	3.18	.82	.46	.45
23.8	3.41	2.38	.74	.32	.31
18.3	2.80	1.62	.61	.20	.19

as a working standard based on its 5-year-old calibration at Eppley.

We conclude that the Eppley pyrheliometer can be accepted as a working standard. The most persuasive reason for this is the apparent overestimation of the direct beam radiation by both flat-plate radiometers. Based on factory calibrations, the direct beam flux ranges from 1.45 to 1.58 ly/min for No. 240 and No. 321 for all solar angles greater than 45°. Sellers (1965) reports values of direct beam flux ranging from 1.30 to 1.45 ly/min in Tucson, Ariz., measured on clear days at solar noon. Based on lower water vapor and dust concentrations and higher solar angles at Tucson, the values at Davis should be less than those at Tucson. Several other factors exerted lesser influence. The calibration facilities at Eppley have been described in published literature (Drummond and Greer, 1966). Eppley maintains a group of angstrom compensation pyrheliometers as primary standards and has regularly checked these against other such instruments at the International Comparisons of Pyrheliometers (see Fröhlich and others, 1973). Further, Eppley calibrates at a flux of about 700 W m^{-2} (1.0 ly/min) (Drummond and Greer, 1966) while Beckman-Whitley (Teledyne-Geotech) calibrations are performed at 70 W m^{-2} (0.1 ly/min) (R. K. Hammar, written commun., 1975).

Accepting the pyrheliometer results as the most accurate realization of the International Pyrheliometric Scale of 1956, the calibration constants of the two B–W flat-plate radiometers and the Eppley pyranometer must be adjusted so that a plot of $I_u - I_s$, calculated us-

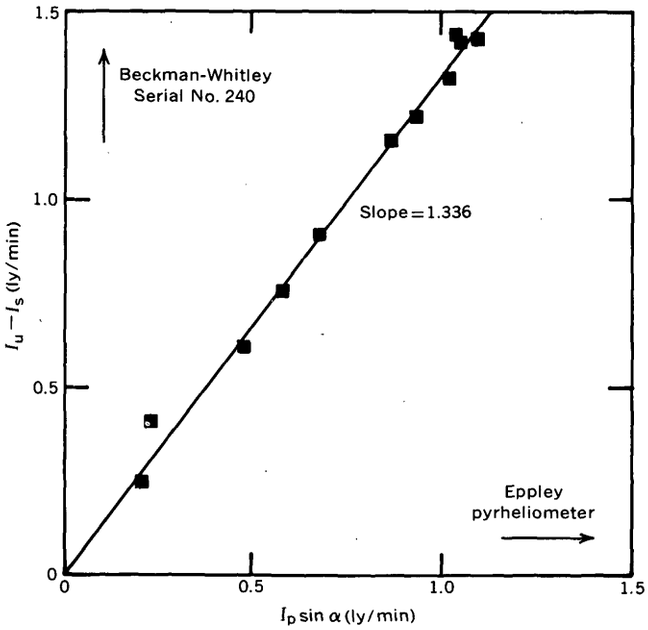

FIGURE 3.—Comparison of unshaded-minus-shaded flux observed by Beckman-Whitley radiometer No. 240 with direct flux measured by the working-standard radiometer. Data obtained May 6, 1975.

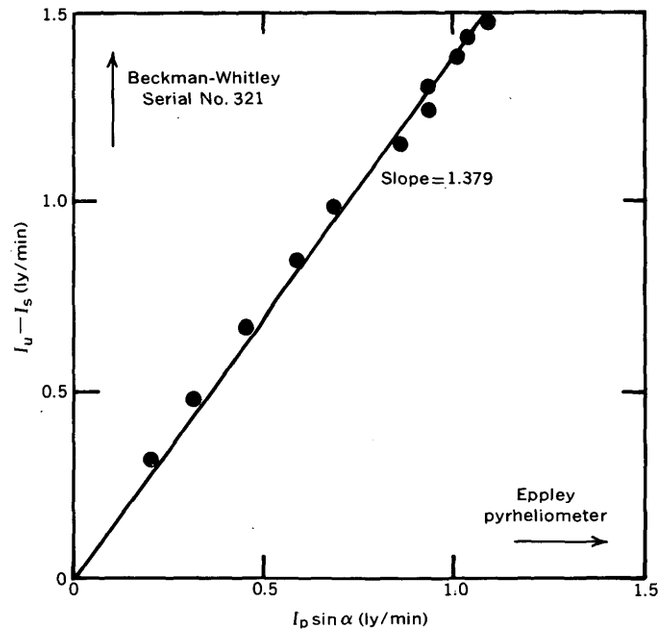

FIGURE 4.—Comparison of unshaded-minus-shaded flux observed by Beckman-Whitley radiometer No. 321 with direct flux measured by the working-standard radiometer. Data obtained May 6, 1975.

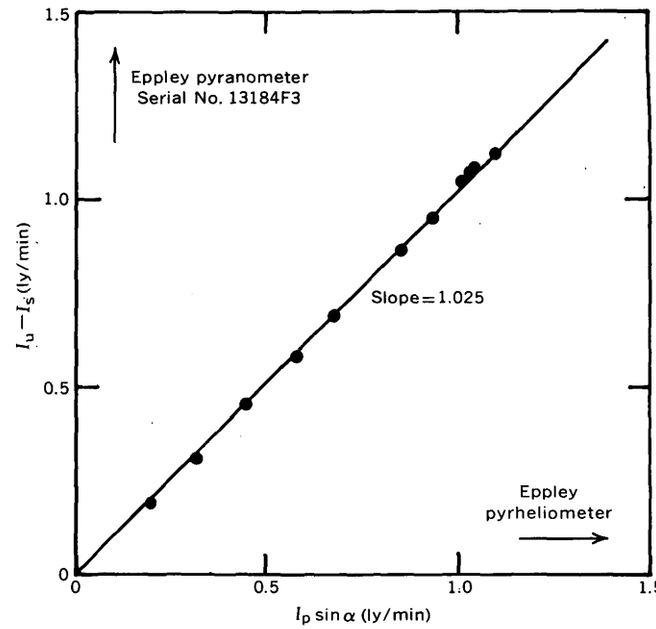

FIGURE 5.—Comparison of unshaded-minus-shaded flux observed by Eppley pyranometer No. 13184F3 with direct flux measured by the working-standard radiometer. Data obtained May 6, 1975.

TABLE 5.—*Calibration constants for three radiometers*

Instrument	Old calibration constant		New calibration constant	
B–W No. 240 ------	348.9 W m^{-2} mV^{-1}	(0.500 ly min^{-1}/mV^{-1})	258.2 W m^{-2} mV^{-1}	(0.370 ly min^{-1}/mV^{-1})
B–W No. 321 ------	658.7 W m^{-2} mV^{-1}	(0.944 ly min^{-1}/mV^{-1})	473.8 W m^{-2} mV^{-1}	(0.679 ly min^{-1}/mV^{-1})
Eppley No. 13184F3_	126.5 W m^{-2} mV^{-1}	(0.192 ly min^{-1}/mV^{-1})	130.5 W m^{-2} mV^{-1}	(0.187 ly min^{-1}/mV^{-1})

ing the new calibration constant, versus $I_p \sin \alpha$ would have a slope of 1.0. The old and new calibration constants for the three radiometers are given in table 5.

It should be noted that the calibration obtained using the shading technique is strictly valid only for radiation having the spectral characteristics of direct solar radiation. This is of particular concern with total radiometers which are expected to respond to both longwave and solar radiation. The response can be identical only if the absorptivity of the radiometer paint is the same for all wavelengths. Hall (1965) has studied the emissivity of the paint used on the Beckman-Whitley radiometers, Nextel Air Dry Black Velvet Coating made by Minnesota Mining and Manfacturing. His results show an average emissivity from 4 to 40 micrometres of 0.94 with a minimum of 0.86 and a maximum of 0.98. Kirchoff's law states that the hemispherical emissivity equals the hemispherical absorptivity if the emissivity and absorptivity are independent of angle (Siegel and Howell, 1972). Hall (1965) also found that the ratio of the normal emissivity to the hemispherical emissivity is 1.01. Therefore, it is reasonable to conclude that the hemispherical absorptivity is approximately 0.94 from 4 to 40 micrometres. Minnesota Mining and Manufacturing quotes a solar absorptivity of 0.98 for this paint. This would indicate that calibration using direct solar radiation may result in a 4-percent underestimation of the longwave radiation component.

CONCLUSIONS AND RECOMMENDATIONS

The results of this work as well as the work of others clearly indicate that radiation data collected under field conditions may be subject to considerable errors. In this study, among a sample of only four radiometers, a discrepancy of 38 percent existed between the lowest reading unit, the Eppley pyrheliometer, and the highest reading unit, B–W No. 321. Errors of this magnitude have a profound effect on the accuracy of a heat budget.

The source of the discrepancies that have been found is not clear. Discrepancies may be due to changes of calibration caused by such factors as paint deterioration, glass deterioration, thermopile deterioration, and so forth. They may be also due to incorrect factory calibrations. Or they may be due to a combination of deterioration and incorrect calibration.

In order to insure accurate data in the face of instrumental deterioration, routine field maintenance and frequent field recalibration are required. The shading technique is a quick, accurate, and widely accepted recalibration method. The Eppley pyrheliometer with solar tracking mount and theodolite is a good choice for a working standard to be used with the shading technique. The amount of equipment required could be reduced if a precision pyranometer were adopted as the working standard. This would eliminate the need for the solar tracking mount and the theodolite. It should be noted that both the U.S. National Weather Service and Eppley use pyranometers as working standards.

In order to avoid errors due to incorrect calibrations it is necessary to calibrate the working standard radiometer against a primary standard. Such a primary standard should be traceable to another primary standard which has participated in the International Pyrheliometer Comparisons or should participate itself.

Any organization making extensive use of radiometers in data collection programs should maintain a working standard radiometer for making field calibrations along with necessary shading equipment. The instrument should be used only for calibration of field instruments. The working standard should be calibrated regularly against a primary standard calibrated to reproduce the International Pyrheliometric Scale of 1956.

ABBREVIATIONS

K ---------- kelvin
ly ---------- langley
m ---------- metre
min ---------- minute
mV ---------- millivolt
W ---------- watt

REFERENCES CITED

Anderson, E. R., 1954, Energy-budget studies, *in* Water-loss investigations: Lake Hefner studies, technical report: U.S. Geol. Survey Prof. Paper 269, p. 71–119.

Anderson, L. J., 1954, Instrumentation for mass-transfer and energy budget studies, *in* Water-loss investigations: Lake Hefner studies, technical report: U.S. Geol. Survey Prof. Paper 269, p. 35–45.

Drummond, A. J., and Greer, H. W., 1966, An integrating hemisphere (artificial sky) for the calibration of meteorological pyranometers: Solar Energy, v. 10, no. 4, p. 7–11.

Fröhlich, C., Geist, J., Kendall, J., Sr., and Marchgrabers, R. M., 1973, The third international comparisons of pyrheliometers and a comparison of radiometric scales: Solar Energy, v. 14, no. 2, p. 157–166.

Hall, W. M., 1965, Effect of low temperature on the thermal emittance of three black paints; comparison of normal and hemispherical emittances: Jet Propulsion Lab. Space Programs Summary, v. 4, no. 37–31, p. 108–109.

Koberg, G. E., 1958, Instrumentation and methods, *in* Water-loss investigations: Lake Mead studies: U.S. Geol. Survey Prof. Paper 298, p. 11–20.

Kondrat'ev, K. I., 1965, Radiative heat exchange in the atmosphere: Oxford, Pergamon Press, 411 p.

Latimer, J. R., 1972, Radiation measurement: Ottawa, Information Canada, International Field Year for the Great Lakes tech. manual ser., no. 2, 53 p.

Sellers, W. D., 1965, Physical climatology: Chicago, University of Chicago Press, 272 p.

Siegel, Robert, and Howell, J. R., 1972, Thermal radiation heat transfer: New York, McGraw-Hill, 814 p.

Special Committee of the International Geophysical Year, 1958, Radiation instruments and measurements, *in* Annals of the International Geophysical Year: London, Pergamon Press, v. 5, pt. 6, p. 371– 466.

ANNUAL INDEX TO VOLUME 4

Journal of Research of the U.S. Geological Survey

[Issue number precedes colon; page number follows colon]

SUBJECT INDEX

AUTHOR INDEX

*U.S. GOVERNMENT PRINTING OFFICE: 1976 211-295/8 1-3

RECENT PUBLICATIONS OF THE U.S. GEOLOGICAL SURVEY

(The following books may be ordered from the Branch of Distribution, U.S. Geological Survey, 1200 South Eads Street, Arlington, VA 22202 (an authorized agent of the Superintendent of Documents, Government Printing Office). Payment is required. Remittances should be sent by check or money order payable to U.S. Geological Survey. Give series designation and number, such as Bulletin 1368–A, and the full title. Prices of Government publications are subject to change. Increases in costs make it necessary for the Superintendent of Documents to increase the selling prices of many publications offered. As it is not feasible for the Superintendent of Documents to correct the prices manually in all the previous announcements and publications stocked, the prices charged on your order may differ from the prices printed in the announcements and publications)

Professional Papers

P 486–A. Water resources of lower Colorado River—Salton Sea area as of 1971, summary report, by C. C. McDonald and O. J. Loeltz. 1976. A1–A34. 95¢.

P 576–E. Geologic history of the Slick Rock district and vicinity, San Miguel and Dolores Counties, Colorado, by D. R. Shawe. 1976. p. E1–E19. 55¢.

P 655–K. Effects of changes in an alluvial channel on the timing, magnitude, and transformation of flood waves, southeastern Arizona, by D. E. Burkham. 1976. p. K1–K25. 75¢.

P 853. Paleotectonic investigations of the Pennsylvanian System in the United States, by E. D. McKee, E. J. Crosby, and others. 1975 (1976). Pt. I, Introduction and regional analyses of the Pennsylvanian System, 349 p.; Pt. II, Interpretive summary and special features of the Pennsylvanian System, 192 p.; Pt. III, 17 plates in pocket. $41 per set.

P 859. Reconnaissance geology of the submerged and emerged Coastal Plain province, Cape Lookout area, North Carolina, by R. B. Mixon and O. H. Pilkey. 1976. 45 p; plates in pocket. $1.35.

P 872. Geology of the Golden quadrangle, Colorado, by Richard Van Horn. 1976. 116 p; plate in pocket. $3.65.

P 907–A,B. A, Grade and tonnage relationships among copper deposits, by D. A. Singer, D. P. Cox, and L. J. Drew. p. A1–A11; *and* B, Geochemical exploration techniques applicable in the search for copper deposits, by M. A. Chaffee. B1–B26. 1975. $1.60. (Reprinted 1976.)

P 910. Miocene marine diatoms from the Choptank Formation, Calvert County, Maryland, by G. W. Andrews. 1976. 26 p., 7 plates. $1.40.

P 913. A stochastic model for predicting the probability distribution of the dissolved-oxygen deficit in streams, by I. I. Esen and R. E. Rathbun. 1976. 50 p. $1.55.

P 916. Zoogeography of Holocene Ostracoda off western North American and paleoclimatic implications, by P. C. Valentine. 1976. 47 p.; 14 plates. $1.90.

P 927. Effect of irrigation pumping on desert pupfish habitats in Ash Meadows, Nye County, Nevada, by W. W. Dudley, Jr., and J. D. Larson. 1976. 52 p. $1.45.

P 954–A. Geochemical survey of Missouri—Methods of sampling, laboratory analysis, and statistical reduction of data, by A. T. Miesch, *with sections on* Laboratory methods, by P. R. Barnett, A. J. Bartel, J. I. Dinnin, G. L. Feder, T. F. Harms, Claude Huffman, Jr., V. J. Janzer, H. T. Millard, Jr., H. G. Neiman, M. W. Skougstad, and J. S. Wahlberg. 1976. p. A1–A39. $1.05.

P 954–D. Elemental composition of corn grains, soybean seeds, pasture grasses, and associated soils from selected areas in Missouri, by J. A. Erdman, H. T. Shacklette, and J. R. Keith. 1976. p. D1–D23. 65¢.

P 961. Petrology, mineralogy, and geochemistry of the East Molokai Volcanic Series, Hawaii, by M. H. Beeson. 1976. 53 p. $1.55.

P 966. The geologic retrieval and synopsis program (GRASP), by R. W. Bowen and J. M. Botbol. 1975. 87 p. $2.05. (Reprinted 1976.

P 967. Trioctahedral smectite in the Green River Formation, Duchesne County, Utah, by J. R. Dyni. 1976. 14 p. 55¢.

P 977. Stratigraphic distribution of some pollen types from the Campanian and lower Maestrichtian rocks (Upper Cretaceous) of the Middle Atlantic States, by J. A. Wolfe. 1976. 18 p., 4 plates. 85¢.

Bulletins

B 1385–D. Mineral resources of the South Warner Wilderness, Modoc County, California, by W. A. Duffield and R. D. Weldin, *with a section on* Aeromagnetic data, by W. E. Davis. 1976. p. D1–D31; plates in pocket. 75¢.

B 1391–D. Mineral resources of areas adjacent to the Cloud Peak Primitive Area, Wyoming, by Kenneth Segerstrom and R. C. Weisner, *with a section on* Aeromagnetic interpretation, by D. B. Jackson. 1976. p. D1–D37; plate in pocket. $1.55.

B 1400. Geology of the Michaud and Pocatello quadrangles, Bannock and Power Counties, Idaho, by D. E. Trimble. 1976. 88 p; plate in pocket. $2.30.

B 1405–D. Stratigraphy of the layered gabbroic Dufek intrusion, Antarctica, by A. B. Ford. 1976. p. D1–D36. 75¢.

Water-Supply Papers

W 1827–F. Reactions of aqueous aluminum species at mineral surfaces, by D. W. Brown and J. D. Hem. 1975 (1976). p. F1–F48. 85¢.

W 2107. Surface water supply of the United States, 1966–70—Part 3. Ohio River basin—Volume 1, Ohio River basin above Kanawha River. 1976. 668 p. $5.45.

W 2114. Surface water supply of the United States, 1966–70—Part 5, Hudson Bay and upper Mississippi River basins—Volume 2, Upper Mississippi River basin above Keokuk, Iowa. 1976. 785 p. $6.30.

W 2160. Quality of surface waters of the United States, 1970—Parts 12–16, North Pacific slope basins, Alaska, and Hawaii and other Pacific areas. 1976. 501 p. $4.70.